Dist: A

MICROSTRUCTURAL DESIGN FOR TOUGH CERAMICS

HELEN M. CHAN and BRIAN R. LAWN

Department of Materials Science and Engineering
Lehigh University
Bethlehem, PA 18015

With N.P. Padture, H. Cai, L.M. Braun, S.J. Bennison, E.R. Fuller, F. Guiberteau, B.M. Hooks, M.A. Stevens Kalceff, J. Rödel, J.L. Runyan

Final Technical Report
FY 92-94

AFOSR Contract No. F49620-92-J-0039

for

Air Force Office of Scientific Research
Bolling Air Force Base
Washington, DC 20332

October 1994

424468

14418

9

Dist: A

REPORT DOCUMENTATION PAGE

Form Approved
OMB No. 0704-0188

1. AGENCY USE ONLY *(Leave blank)*

2. REPORT DATE
October 1994

3. REPORT TYPE AND DATES COVERED
FINAL Report FY92-94

4. TITLE AND SUBTITLE
Microstructure Design for Tough Ceramics

5. FUNDING NUMBERS
AFOSR #
F49620-92-J-0039

6. AUTHOR(S)
Helen M. Chan and Brian R. Lawn

7. PERFORMING ORGANIZATION NAME(S) AND ADDRESS(ES)
Department of Materials Science and Engineering
Lehigh University
Bethlehem, PA

8. PERFORMING ORGANIZATION REPORT NUMBER
AFOSR-TR- 94 0653

9. SPONSORING/MONITORING AGENCY NAME(S) AND ADDRESS(ES)
Air Force Office of Scientific Research
Bolling Air Force Base
Washington, DC 20332
NA

10. SPONSORING/MONITORING AGENCY REPORT NUMBER
F49620-92-J-0039

11. SUPPLEMENTARY NOTES

12a. DISTRIBUTION/AVAILABILITY STATEMENT
Unlimited
Approved for public release,
distribution unlimited
A

12b. DISTRIBUTION CODE

13. ABSTRACT *(Maximum 200 words)*

Results of a program on the influence of microstructure on the toughness and fatigue properties of ceramics are presented. A theoretical analysis of toughness-curve behavior in two-phase ceramics has been completed. This analysis identifies particle size, volume fraction, and internal thermal expansion anisotropy stress as key microstructural variables in the toughness response. A simple contact fatigue methodology for investigating the accumulation of damage at stress concentrations in tough ceramics, using the Hertzian indentation test in cyclic loading, has been developed. This methodology offers several advantages over traditional long-crack fatigue testing, and relates directly to the stress states that occur in contact bearings. Optical and acoustic emission tests reveal fundamental departures from the classic cone fractures that form in homogeneous brittle materials. Instead, a new kind of damage, shear-initiated microfractures in a distributed zone directly beneath the contact area is observed. The damage thereby occurs in the short-crack region, and is most severe in those ceramics that show the highest long-crack toughness, underlying the need for compromise in materials design. The results bear strongly on such practical properties as bearing fatigue, and strength, wear and erosion of structural ceramics.

14. SUBJECT TERMS

15. NUMBER OF PAGES
140

16. PRICE CODE

17. SECURITY CLASSIFICATION OF REPORT
Unclassified

18. SECURITY CLASSIFICATION OF THIS PAGE
Unclassified

19. SECURITY CLASSIFICATION OF ABSTRACT
Unclassified

20. LIMITATION OF ABSTRACT

MICROSTRUCTURAL DESIGN FOR TOUGH CERAMICS

INTRODUCTION

1. *OBJECTIVES*

The aim of this program was to investigate the role of microstructure in the toughness, strength, fatigue and wear properties of ceramics, in particular ceramics that are characterized by *R*-curve or *T*-curve (toughness-curve) behavior. The term "*T*-curve" refers to materials whose toughness is an increasing function of crack size. The *T*-curve is governed principally by the material *microstructure*. It is pronounced in monophase ceramics, like aluminas, with coarse microstructures, and even more so in multiphase ceramic composites where residual mismatch stresses can be substantial. A primary feature of the *T*-curve is that it leads to a marked insensitivity of the strength to initial crack size, i.e. "flaw tolerance". This has a strong appeal to the structural engineer, because components may be designed to a specific stress without undue concern for variable flaw distributions, either pre-existing *or* service-induced. On the other hand, the same microstructural elements responsible for improved long-crack toughness can have a deleterious effect on short-crack properties, such as wear and contact fatigue. It was important to understand the subtle interrelations between materials characterization and *T*-curve micromechanics, in order that we may on the one hand be able to establish reliable design criteria and, on the other, tailor "superior" ceramics with maximum resistance to degradation and damage accumulation, especially in fatigue. Our principal goal was to investigate these interrelations.

In FY92, we focussed on *toughness* and *strength* properties. In FY93, our focus turned to the interrelation between *toughness* and *fatigue*, particularly in contact configurations. In FY94, we continued our emphasis on fatigue, and examined more closely the role of material *microstructure*. Our results may be summarized as follows:

(i) We completed a theoretical analysis of *T*-curve behavior in two-phase ceramics, including ceramics designed and fabricated in-house. This analysis identified particle size, volume fraction, and internal thermal expansion anisotropy stress, as key microstructural variable in the toughness curve. The analysis laid down guiding principles for designing ceramic microstructures with optimum toughness properties.

(ii) We developed a simple contact fatigue methodology for investigating the accumulation of damage at stress concentrations in tough ceramics, using the Hertzian indentation test in cyclic loading. This methodology offers several advantages over traditional long-crack fatigue testing, and relates strongly to the stress states that obtain in bearing configurations.

(iii) We carried out contact fatigue studies on several model ceramics, notably alumina and glass-ceramics, to investigate the nature of the damage incurred. We found fundamental departures from the classic cone fractures that form in homogeneous brittle materials. Instead, we observed a new kind of damage, shear-initiated microfractures in a distributed zone directly beneath the contact area. The damage thereby occured in the short-crack region, and was most severe in those ceramics that show the highest long-crack toughness.

(iii) We extended the toughness evaluation and contact fatigue methodology to more complex microstructures, including silicon nitride and silicon carbide composites. The first theoretical fracture mechanics models were developed to describe the fracture damage and fatigue processes, and thus to establish guidelines for designing and fabricating ceramic composites for optimum resistance to fatigue in concentrated (e.g. bearing) stress fields.

(2) *ACHIEVEMENTS*

Seventeen papers were published during FY92-94. The work in these papers is summarized by the following abstracts, and the papers themselves are appended:

Paper 1. Ceramics are notorious for their "brittleness", i.e. the sensitivity of mechanical strength to flaws on the microstructural scale. The associated notion of the "critical flaw" has dominated design considerations concerning structural reliability and materials processing of ceramic components. This accounts for the trend over the last decade toward a processing strategy of eliminating strength-degrading flaws at source. Here we propose a fundamentally different approach, that of processing ceramics with crack-impeding elements integrated into the indigenous microstructures, such that any pre-existing or service-induced flaws are effectively stabilized. Strength data on a tailored alumina/aluminium-titanate material demonstrate the capacity of our approach to produce simple ceramics with unique flaw insensitivity.

Paper 2. An *in situ* study is made of crack interfaces in alumina composites reinforced with silicon carbide whiskers during increasing applied loading. Both qualitative observations of the whisker bridging micromechanisms and quantitative measurements of the crack profile are made to assess the specific role of the whiskers on the toughness-curve (T-curve or R-curve). At small crack-wall separations the whiskers act as elastic restraints to the point of rupture. In some cases the whiskers remain in frictional contact with the alumina matrix over large pullout distances, up to 2 μm, corresponding to a bridging zone approaching 1 mm. The results are discussed in relation to existing models of whisker reinforcement and published long-crack T-curve data.

Paper 3. A procedure for evaluating short-crack toughness curves (*T*-curves) from quantitative *in situ* observations of Vickers indentation cracks during stressing is described. We demonstrate the procedure with results on an Al_2O_3–Al_2TiO_5 composite with strong *T*-curve behavior and attendant crack stabilization from grain-localized-crack-bridging. The stabilization allows the material to tolerate multiple damage accumulation during loading.

Paper 4. The intergranular phase in an alumina, containing 1 vol% anorthite glass, was crystallized in order to enhance internal residual stresses within the microstructure. The influence of crystallization on the mechanical behavior was investigated by the indentation-strength method. Such crystallization was found to result in a marked improvement in the flaw tolerance of this alumina, indicative of strong R- or T-curve behavior. These results are discussed in the light of a theoretical model which assumes grain-localized crack bridging to be the predominant toughening mechanism. Particular reference is made to the influence of residual stresses and interfacial properties on grain pullout across the crack walls in the wake of the crack tip.

Paper 5. To determine the influence of volume constraint, the crystallization behavior of bulk anorthite glass was compared with that of anorthite glass situated at intergranular pockets in an alumina ceramic. Near 100% crystallization of the glass was obtained in both cases. Examination of the crystallized microstructures using SEM and TEM revealed several interesting features. The resulting microstructures, together with the very high degree of crystallization, are discussed with reference to a thermodynamic model for the constrained crystallization of glass.

Paper 6. An objective methodology is developed for evaluating toughness-curves (*T*-curves) of ceramics using indentation flaws. Two experimental routes are considered: (i) conventional measurement of inert strength as a function of indentation load; (ii) *in situ* measurement of crack size as a function of applied stress. Central to the procedure is a proper calibration of the indentation coefficients that determine the *K*-field of indentation cracks in combined residual-contact and applied-stress loading, using data on an appropriate base material with single-valued toughness. Tests on a fine-grain alumina serve to demonstrate the approach. A key constraint in the coefficient evaluation is an observed satisfaction of the classical indentation strength–load$^{-1/3}$ relation for such materials, implying an essential geometrical similarity in the crack configurations at failure. *T*-curves for any alumina-based ceramic *without* single-valued toughness can then be generated objectively from inert-strength or *in situ* crack-size data. The methodology thereby circumvents the need for any pre-conceived model of toughening, or for any prescribed analytical representation of the *T*-curve function. Data on coarse-grained aluminas and an alumina-matrix material with aluminum titanate second-phase particles are used in an illustrative case study.

Paper 7. The microstructures of alumina-aluminum titanate (A-AT) composites have been tailored with the intent of altering their crack-resistance (R- or T-curve) behavior and resulting flaw tolerance. Specifically, two microstructural parameters which influence grain-localized crack bridging, viz: i) internal residual stresses, and ii) microstructural coarseness have been investigated. Particulate aluminum titanate was added to alumina to induce intense internal residual stresses from extreme thermal expansion mismatch. It was found that A-AT composites with uniformly distributed 20-30 vol% aluminum titanate ("duplex") showed significantly improved flaw tolerance over single-phase alumina. Coarsening of the duplex microstructure via grain growth scaling was relatively ineffective in improving the flaw tolerance further. Onset of spontaneous microcracking precluded further exploitation of this scaling approach. Therefore, an alternative approach to coarsening was developed, in which a uniform distribution of large alumina grains was incorporated within a fine-grain A-AT matrix ("duplex-bimodal"), via a powder processing route. The duplex-bimodal composites yielded excellent flaw tolerance with steady-state toughness of ≈8 MPa.m$^{1/2}$. A qualitative model for microstructure development in these duplex-bimodal composites is presented.

Paper 8. Vickers indentation sites in ceramics have been examined after specimen failure from median/radial indentation cracks. Evolution of a new cracking pattern of "ortho-lateral" cracks originating at the intact corners of the Vickers indentation and running orthogonal to the classic lateral cracks and parallel to the new fracture surface, has been observed. In some instances post-failure extension of the classic lateral cracks towards the surface was also observed. Enhanced residual tensile stress from relaxation of constraints on the indentation-plastic cavity by the generation of a fracture surface is postulated to drive the subsidiary cracking. A simple qualitative model to explain this phenomenon is presented. Possible implications of such post-failure subsidiary cracking on residual-stress-driven flaws, post-mortem fractography, and wear in ceramics are discussed.

Paper 9. A fracture mechanics model is presented for the toughening of ceramics by bridging from second-phase particles, resulting in toughness-curve (*T*-curve) behavior. It is assumed that the second-phase particles are in a state of residual thermal expansion dilatational mismatch relative to the matrix. In the long-crack region these stresses augment frictional sliding stresses at the interphase boundaries, enhancing the crack resistance; in the short-crack region the same stresses drive the crack, diminishing the crack resistance. The principal manifestation of these countervailing influences is a reduced sensitivity of strength to initial flaw size, i.e. an increased flaw tolerance. In seeking to incorporate these key physical elements, our model opts for mathematical simplicity by assuming uniformly distributed stresses in two bridging domains: in the first, at small crack-wall separations, a constant opening stress; in the second, at larger separations, a constant closing stress. The uniform crack-plane distributions allow for simple closed-form solutions of the crack *K*-field equations, and thence an analytical formulation for the *T*-curve. Indentation–strength data on a "reference" Al_2O_3/Al_2TiO_5 ceramic composite are used to demonstrate the main theoretical predictions and to calibrate essential parameters in the *T*-curve formulation.

Paper 10. The fracture mechanics analysis of Paper I is here extended to consider the effects of volume fraction and scale of second-phase particles on the toughness-curve properties of ceramic matrix composites. Increasing these variables enhances the flaw tolerance of the material, but only up to certain limits, beyond which bulk microcracking occurs. These limits define domains of damage accumulation and potential strength degradation by microcrack coalescence. In the familiar approximation of elliptical crack-wall profiles, we show that the principal effects of increasing volume fraction (or expansion mismatch) and particle size is to enhance the *slope* and *scale* of the *T*-curve, respectively. We also derive expressions for the microcracking limits, and use these expressions to construct a simple design diagram for characterizing the effects of microstructural variation on mechanical behavior. Indentation–strength data on Al_2O_3/Al_2TiO_5 composites over a range of volume fractions and particles sizes are used to demonstrate the severe loss in mechanical integrity that can be suffered on entering the microcracking domains.

Paper 11. A simple Hertzian contact procedure for investigating cyclic fatigue damage in brittle polycrystalline ceramics is described. Repeat loading of a spherical indenter on a coarse alumina ceramic produces cumulative mechanical damage. The mode of damage is one of deformation-induced intergranular microfracture, leading ultimately at large numbers of cycles and high contact pressures to severe grain dislodgement. In contrast to the classical Hertzian cone cracks that form in more homogeneous materials in the regions of tensile stress *outside* the contact circle, the damage in the coarse-grain alumina develops in a zone of high shear stress and hydrostatic compression *beneath* the contact circle. The fatigue damage is evident in inert environments, confirming the mechanical nature of the process, although exposure to moisture accelerates the effect. The relatively modest degradation in failure stress with number of repeat contacts for indented flexure specimens suggests that conventional strength and toughness testing procedures may not always provide sensitive indications of the extent of damage that can be incurred in concentrated loading.

Paper 12. Flaw-tolerance and associated toughness-curve (*T*-curve) characteristics in SiC/glass particle/matrix composites are studied. Two glass compositions, chosen to produce composites at extremes of high (H) and low (L) thermal expansion mismatch relative to the SiC particles, are investigated. In situ observations of crack extension from indentation flaws reveal widely different responses: in the L composite the path is relatively undistorted from planar geometry, with trans-particle fractures; in the H composite the path deflects strongly around the particles, with consequent interfacial bridge formation and activity in the crack wake. Surface fracture patterns produced by spherical indenters confirm the implied transition from trans-particle to inter-particle fracture with increasing internal residual stress, and point to a potential degradation in *short*-crack properties like wear and fatigue. Indentation–strength measurements also show different characteristics in the two composites: minor flaw tolerance in the L material, consistent with a single-valued, "rule of mixtures" toughness; major tolerance in the H material, consistent with a pronounced *T*-curve. The *T*-curves themselves are objectively deconvoluted from the indentation–strength data for each composite and analyzed.

Paper 13. The role of microstructural scale on deformation–microfracture damage induced by contact with spheres is investigated in monophase alumina ceramics over a range 3 to 48 μm in grain size. Measurement of a universal indentation stress–strain curve indicates a critical contact pressure ≈ 5 GPa above which irreversible deformation occurs in alumina. A novel sectioning technique identifies the deformation elements as intragrain shear faults, predominantly crystallographic twins, within a confining subsurface zone of intense compression–shear stress. The twins concentrate the shear stresses at the grain boundaries and, above a threshold grain size, initiate tensile intergranular microcracks. Below this threshold size, classical Hertzian cone fractures initiate outside the contact circle. Above the threshold, the density and scale of subsurface-zone microcracks increases dramatically with increasing grain size, ultimately dominating the cone fractures.

The damage process is stochastic, highlighting the microstructural discreteness of the initial deformation field; those grains which lie in the upper tail of the grain-size distribution and which have favorable crystallographic orientation relative to local shear stresses in the contact field are preferentially activated. Initial flaw state is not an important factor, because the contact process creates its own flaw population. These and other generic features of the damage process will be discussed in relation to microstructural design of polycrystalline ceramics.

Paper 14. A new processing strategy based on atmospheric pressure sintering is presented for obtaining dense SiC-based materials with microstructures consisting of: (i) uniformly distributed elongate shaped α-SiC grains and (ii) relatively high amounts (20 vol%) of second-phase yttrium aluminum garnet (YAG). This strategy entails the sintering of β-SiC powder doped with α-SiC, Al_2O_3, and Y_2O_3. The Al_2O_3 and Y_2O_3 aid in the liquid-phase-sintering of SiC and form in situ YAG which has a significant thermal expansion mismatch with SiC. During a subsequent grain-growth heat treatment it is postulated that the α-SiC "seeds" assist in controlling in situ growth of the elongated α-SiC grains. The fracture pattern in the in situ toughened SiC is intergranular with evidence of copious crack-wake bridging, akin to toughened Si_3N_4 ceramics. The elongate nature of the α-SiC grains together with the high thermal-residual stresses in the microstructure enhance the observed crack-wake bridging. This bridging accounts for a measured twofold increase in the indentation toughness of this new class of in situ toughened SiC relative to a commercial SiC.

Paper 15. A new kind of irreversible deformation in otherwise brittle ceramics (specifically, silicon carbide and micaceous glass-ceramic) has been observed in Hertzian contacts. The deformation takes the form of an expanding microcrack damage zone below the contact circle, in place of the usual single propagating macrocrack (the so-called Hertzian cone fracture) outside. An important manifestation of this deformation is an effective "ductility" in the indentation stress–strain response. Control of the associated brittle–ductile transition is readily effected by appropriate design of weak interfaces, large and elongate grains, and high internal stresses in the ceramic microstructure.

Paper 16. The Hertzian indentation response of a machinable mica-containing glass–ceramic is studied. Relative to the highly brittle base glass from which it is formed, the glass–ceramic shows evidence of considerable "ductility" in its indentation stress–strain response. Section views through the indentation sites reveal a transition from classical cone fracture outside the contact area in the base glass to accumulated subsurface deformation–microfracture in the glass–ceramic. The deformation is attributed to shear-driven sliding at the weak interfaces between the mica flakes and glass matrix. Extensile microcracks initiate at the shear-fault interfaces and propagate into the matrix, ultimately coalescing with neighbors at adjacent mica flakes to effect easy material removal. The faults are subject to strong compressive stresses in the Hertzian field, suggesting that frictional tractions are an important element in the micromechanics. Bend-test measurements on indented specimens show that the glass–ceramic, although weaker than its base glass counterpart, has superior resistance to strength degradation at high contact loads. Implications of the results in relation to microstructural design of glass–ceramics for optimal toughness, strength, and wear and fatigue properties, are discussed.

Paper 17. A fracture mechanics model of damage evolution within Hertzian stress fields in heterogeneous brittle ceramics is developed. Discrete microcracks generate from shear faults associated with the heterogeneous ceramic microstructure; e.g. in polycrystalline alumina, they initiate at the ends of intragrain twin lamellae and extend along intergrain boundaries. Unlike the well-defined classical cone fracture that occurs in the weakly tensile region *outside* the surface contact in homogeneous brittle solids, the fault–microcrack damage in polycrystalline ceramics is distributed within a subsurface shear–compression zone *below* the contact. The shear faults are modelled as sliding interfaces with friction, in the manner of established rock mechanics descriptions but with provision for critical nucleation and matrix restraining stresses. This allows for constrained microcrack pop-in during the loading half-cycle. Ensuing stable microcrack extension is then analyzed in terms of a K-field formulation. For simplicity, only mode I extension is considered specifically here, although provision exists for including mode II. The compressive stresses in the subsurface field constrain microcrack growth during the loading half-cycle, such that enhanced extension occurs during unloading. Data from damage observations in alumina ceramics are used to illustrate the theoretical predictions. Microstructural scaling is a vital element in the microcrack description: initiation is unstable only above a critical grain size, and extension increases as the grain size increases. Internal residual stresses also play an important role in determining the extent of microcrack damage. Implications of the results in the practical context of wear and fatigue properties are discussed.

PHILOSOPHICAL MAGAZINE LETTERS, 1991, VOL. 64, NO. 4, 191–195

Flaw-insensitive ceramics

By STEPHEN J. BENNISON†, NITIN P. PADTURE†,
JULIE L. RUNYAN‡, and BRIAN R. LAWN
Ceramics Division, National Institute of Standards and Technology,
Gaithersburg, Maryland 20899, USA

[*Received 25 March 1991 and accepted 19 June 1991*]

ABSTRACT

Ceramics are notorious for their 'brittleness', i.e. the sensitivity of mechanical strength to flaws on the microstructural scale. The associated notion of the 'critical flaw' has dominated design considerations concerning structural reliability and materials processing of ceramic components. This accounts for the trend over the last decade towards a processing strategy of elimination strength-degrading flaws at source. Here we propose a fundamentally different approach, that of processing ceramics with crack-impeding elements integrated into the indigenous microstructures, such that any pre-existing or service-induced flaws are effectively stabilized. Strength data on a tailored alumina/aluminium-titanate material demonstrate the capacity of our approach to produce simple ceramics with unique flaw insensitivity.

Our strategy for flaw insensitivity springs from recent studies on the strength properties of monophase aluminas and other common ceramics, using indentations to introduce flaws of controlled initial size (Cook, Lawn and Fairbanks 1985, Cook, Fairbanks, Lawn and Mai 1987, Bennison and Lawn 1989; Chantikul, Bennison and Lawn 1990). Figure 1 reproduces data for strength as a function of indentation load or corresponding indentation flaw size for aluminas of two extreme grain sizes, 2·5 and 80 μm (Chantikul, Bennison and Lawn 1990). Observe that the coarser material has a markedly reduced sensitivity to indentation load, i.e. has a greater 'flaw tolerance', albeit at the cost of a considerable loss in strength in the small flaw domain. This flaw tolerance correlates with a systematic increase in toughness as the crack extends from microstructural to macroscopic dimensions, widely known as crack-resistance, or R-curve, behaviour (Hübner and Jillek 1977, Mai and Lawn 1986, Bennison and Lawn 1989). (We emphasize that the data points in fig. 1 represent breaks exclusively from indentation flaws, so the plateau at low load reflects the intrinsic toughness characteristics and not a 'cutoff' from natural flaws.) In the case of alumina-based ceramics the R-curve is due to bridging behind the advancing tip by interlocking grains in persistent, frictional sliding contact (Knehans and Steinbrech 1982, Steinbrech, Knehans and Schaarwächter 1983, Swanson, Fairbanks, Lawn, Mai and Hockey 1987, Swanson 1988, Steinbrech and Schmenkel 1988; Vekinis, Ashby and Beaumont 1990,

---

† Guest scientist from the Department of Materials Science and Engineering, Lehigh University, Bethlehem, Pennsylvania 18015, USA.

‡ Summer student from the Department of Materials Engineering, Virginia Polytechnic Institute and State University, Blacksbury, Virginia 24061, USA.

Fig. 1

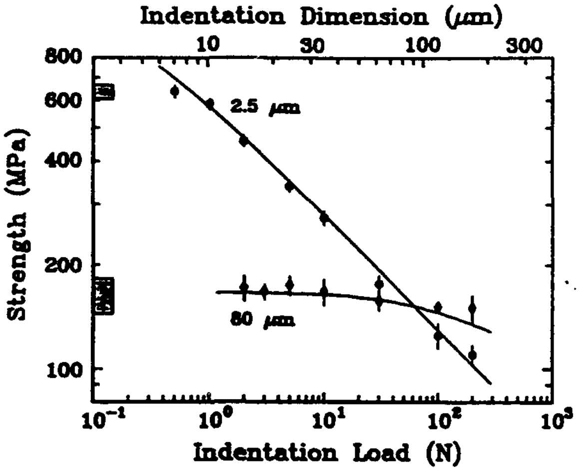

Plot of strength versus indentation load or indentation size (indentation diagonal from hardness impression) for alumina at two extreme grain sizes. Data points (from Chantikul, Bennison and Lawn 1990) represent breaks from indentation flaw sites, and indicate standard deviation limits. Solid curves are theoretical fracture mechanics fits to bridging R-curve theory (Chantikul, Bennison and Lawn 1990). Shaded areas at left represent breaks for specimens without indentation flaws.

Rōdel, Kelly and Lawn 1990). There is a loose analogy here to the toughening mechanism in fibre-reinforced composites. Crack extension is impeded such that microstructural flaws, *regardless of initial size*, undergo stable extension to a critical length prior to failure. In fig. 1 the solid curves are data fits from a theoretical fracture mechanics analysis of the bridging R-curve (Chantikul, Bennison and Lawn 1990).

The above results suggest that flaw insensitivity in ceramics may be achieved by judiciously tailoring the microstructure. However, there is a limit to the benefits that may be obtained with monophase materials. Increasing the grain size scales up the crack-opening displacements over which the frictional tractions remain intact, enhancing the R-curve. It also scales up the bridge spacing, enlarging the extent flaws may grow before bridges are activated. The net result is a tradeoff: the curves in fig. 1 cross each other. An alternative, more radical route suggested by bridging theory (Bennison and Lawn 1989) is to build strong internal compressive stresses into the microstructure so as to enhance grain–grain contacts during slide-out, thereby augmenting frictional restraining forces. This brings us to our hypothesis for microstructural design of fine-grained, flaw-tolerant ceramics: *incorporate heterogeneities into the matrix using a second phase with large thermal expansion mismatch.*

The notion of manipulating microstructures for high toughness through additive phases is not new (Claussen 1990). What is new is the specific intent of tailoring for flaw tolerance. Here we demonstrate the hypothesis with some results on an alumina matrix containing 20 vol% aluminium titanate as a second phase. Aluminium titanate was chosen because its thermal expansion coefficients show extreme anisotropy, and differ dramatically from those of alumina: Al_2O_3 (hexagonal), $\alpha_a = 9 \times 10^{-6}\,°C^{-1}$, $\alpha_c = 10 \times 10^{-6}\,°C^{-1}$; Al_2TiO_5 (orthorhombic), $\alpha_a = 12 \times 10^{-6}\,°C^{-1}$, $\alpha_b = 20 \times 10^{-6}\,°C^{-1}$, $\alpha_c = -3 \times 10^{-6}\,°C^{-1}$ (Bayer 1971). Fabrication was by a conventional pressureless sintering route (Runyan and Bennison 1991). A colloidal suspension of high-purity powders (α-Al_2O_3, Sumitomo AKP-HP grade, 99·995% pure, 0·5 μm

Fig. 2

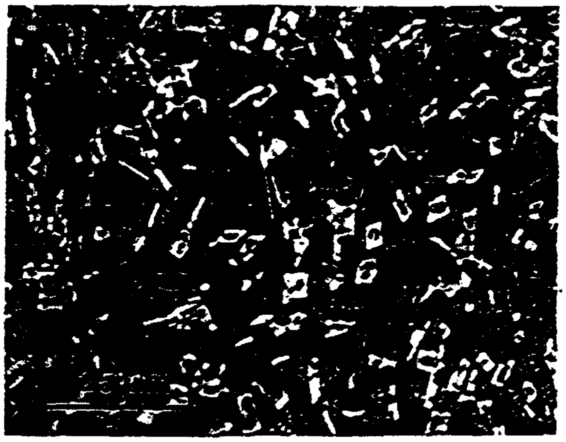

Scanning electron micrograph of Al_2O_3/Al_2TiO_5(20 vol%) composite. Polished section, surface thermally etched at 1490°C for 6 min in air to reveal grain structure. Backscattered electron imaging: white phase Al_2TiO_5; grey phase Al_2O_3; black phase porosity.

Fig. 3

SEM micrograph showing bridging in Al_2O_3/Al_2TiO_5(20 vol%) composite. Observations made during stressing of indentation crack using *in situ* flexural loading fixture. Backscattered electron image, revealing phase structure. Second phase attracts and deflects the primary crack, thereby establishing strong friction points at grain facets for effective bridging. As the crack advances, more bridges are activated, thus increasing the toughness and stabilizing the crack.

crystallites; β-Al_2TiO_5, Trans-Tech, 99·9% pure, 1–5 μm crystallites) in water (pH ~ 3) was dried, and formed into green discs by single-end die pressing (63 MPa) followed by isostatic pressing (350 MPa). The discs were calcined in air at 1050°C for 12 h and sintered at 1600°C for 1 h, to produce high-density (~ 99% theoretical limit) specimens with a matrix grain size of 6 μm. Figure 2 shows the microstructure. The material has an equiaxed structure with the aluminium titanate particles distributed mainly at the matrix grain boundary junctions, with occasional agglomerates of 5–10 particles. Scanning electron microscopy examination of extended indentation cracks during actual loading to failure (Braun, Bennison and Lawn 1991) revealed evidence for copious grain-interlock bridging at crack interfaces. The example shown in fig. 3 indicates that the aluminium titanate particles play a highly active role in the bridging process.

Figure 4 plots strength versus indentation load and indentation flaw size for our 'composite' material. The solid curve through the data set is an empirical fit. For comparison, we include as the dashed curves the responses for the two homogeneous aluminas in fig. 1, plus the interpolated response for an alumina of the same base grain size as the composite (6 μm) using an analysis from an earlier study (Chantikul, Bennison and Lawn 1990). The strengths of the composite are significantly higher than for the monophase aluminas in the large-flaw size domain, although this is offset somewhat by lower strengths in the small-flaw size domain. Again, the trade-off renders the strength of the composite almost completely independent of the flaw size. Note especially that the strength level is well in excess of that for the coarsest alumina, attesting to the increased efficacy of the bridging.

Flaw insensitivity is a highly desirable property in structural ceramics from the standpoint of component design. Primarily, it enables an engineer to design to a single, well-defined stress level, without regard to the size of a critical flaw. It also provides inbuilt protection for the component against in-service damage (e.g. from impacts with errant particles in the atmosphere), and does not place undue onus on the ceramics manufacturer to resort to unconventional, expensive, ultra-clean processing routes. The implications are that incorporation of heterogeneities with high internal stresses, properly controlled via sintering and heat-treatment processes, can suitably modify the microstructure and confer great benefits on strength and toughness properties of structural ceramics. A special attraction is the likelihood that the underlying bridging process responsible for the flaw tolerance is widespread in common ceramics (Swanson 1988); similar tolerance can be achieved by the much discussed process of phase-transformation toughening (Garvie, Hannink and Pascoe 1975, Marshall 1986), but

Fig. 4

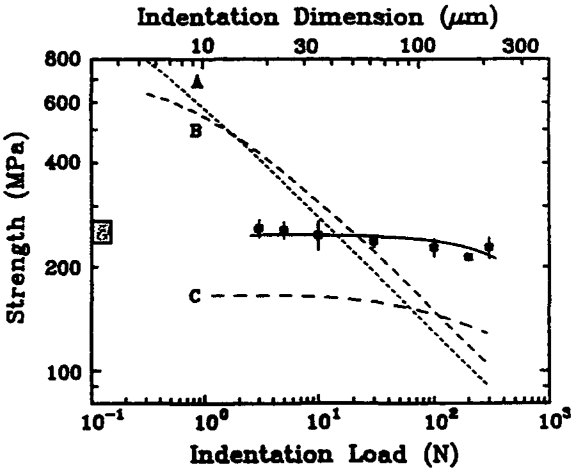

Plot of strength versus indentation load for alumina/aluminium-titanate composite (data points, solid curve). Shaded area at left represents breaks for specimens without indentation flaws. Dashed curves for alumina of different grain sizes included for comparison: (A) 2·5 μm and (C) 80 μm, from fits in fig. 1; (B) 6 μm, theoretical prediction.

that mechanism has thus far been demonstrated in only one material, zirconia. Again, we would stress that our strategy is counterintuitive to the more traditional procedures that seek to remove all flaws by progressively refining the microstructure (Lange 1983; Lange and Metcalf 1983, Lange, David and Aksay 1983, Alford, Birchall and Kendall 1987, Kendall, Alford, Clegg and Birchall 1989). Those procedures certainly produce materials of higher laboratory strength: but the processing is exacting and costly; the fine scale of the defect structure does not lend itself to nondestructive evaluation; and, most important, the materials are highly susceptible to subsequent in-service strength degradation.

The future challenge is to tailor heterogeneous ceramics which preserve the quality of flaw insensitivity displayed here and at the same time attain even higher strength levels.

Acknowledgments

The authors thank Linda Braun for fig. 3. Funding was provided by the U. S. Air Force Office of Scientific Research and E. I. duPont de Nemours and Co. Inc.

References

Alford, N. McN., Birchhall, J. D., and Kendall, K., 1987, *Nature*, **330**, 51.
Bayer, G., 1971, *J. less common Met.*, **24**, 129.
Bennison, S. J. and Lawn, B. R., 1989, *Acta metall.*, **37**, 2659.
Braun, L. M., Bennison, S. J., and Lawn, B. R., 1991, to be published.
Chantikul, P., Bennison, S. J., and Lawn, B. R., 1990, *J. Am. Ceram, Soc.*, **73**, 2419
Claussen, N., 1990, In: *Structural Ceramics—Processing, Microstructure and Properties*, edited by J. J. Bentzen, J. B. Bilde-Sørenson, N. Christiansen, A. Horsewell and B. Ralph (Roskilde, Denmark: Risø National Laboratory), p. 1.
Cook, R. F., Fairbanks, C. J., Lawn, B. R., and Mai, Y.-W., 1987, *J. Mater. Res.*, **2**, 345.
Cook, R. F., Lawn, B. R. and Fairbanks, C. J., 1985, *J. Am. Ceram. Soc.*, **68**, 604.
Garvie, R. C., Hannink, R. H. J., and Pascoe, R. T., 1975, *Nature*, **258**, 703.
Hübner, H., and Jillek, W., 1977, *J. Mater. Sci.*, **12**, 117.
Kendall, K., Alford, N. McN., Clegg, W. J. and Birchall, J. D., 1989, *Nature*, **339**, 130.
Knehans, R., and Steinbrech, R. W., 1982, *J. Mater. Sci. Lett.*, **1**, 327.
Lange, F. F., 1983, *J. Am. Ceram. Soc.*, **66**, 396.
Lange, F. F., David, B. I., and Aksay, I. A., 1983, *J. Am. Ceram. Soc.*, **66**, 407.
Lange, F. F., and Metcalf, M., 1983, *J. Am. Ceram. Soc.*, **66**, 398.
Marshall, D. B., 1986, *J. Am. Ceram. Soc.*, **69**, 173.
Mai, Y-W., and Lawn, B. R., 1986, *Ann. Rev. Mater Sci.*, **16**, 415.
Rödel, J., Kelly, J. F., and Lawn, B. R., 1990, *J. Am. Ceram. Soc.*, **73**, 3313.
Runyan, J. L., and Bennison, S. J., 1991, *J. Europ. Ceram. Soc.*, **7**, 93.
Steinbrech, R. W. and Schmenkel, O., 1988, *J. Am. Ceram. Soc.*, **71**, C271.
Steinbrech, R. W., Knehans, R., and Schaarwächter, W., 1983 *J. Mater. Sci.*, **18**, 265.
Swanson, P. L., 1988, In: *Advances in Ceramics, Vol. 22: Fractography of Glasses and Ceramics* (Columbus, OH: American Ceramic Society), p. 135.
Swanson, P. L., Fairbanks, C. J., Lawn, B. R., Mai, Y-W., and Hockey, B. J., 1987, *J. Am. Ceram. Soc.*, **70**, 279.
Vekinis, G., Ashby, M. F., and Beaumont, P. W. R., 1990, *Acta metall.*, **38**, 1151.

Reprinted from the Journal of the American Ceramic Society, Vol. 74, No. 12, December 1991

journal

J. Am. Ceram. Soc., 74 [12] 3154–57 (1991)

In Situ Observations of Toughening Processes in Alumina Reinforced with Silicon Carbide Whiskers

Jürgen Rödel,[*] Edwin R. Fuller, Jr.,[*] and Brian R. Lawn[*]

Ceramics Division, National Institute of Standards and Technology, Gaithersburg, Maryland 20899

An in situ study is made of crack interfaces in composites of alumina reinforced with silicon carbide whiskers. Both qualitative observations of the whisker-bridging micromechanisms and quantitative measurements of the crack profile are made to assess the specific role of the whiskers on the toughness curve (*T*-curve or *R*-curve). At small crack-wall separations the whiskers act as elastic restraints to the point of rupture. In some cases the whiskers remain in frictional contact with the alumina matrix over large pullout distances (more than 1 μm) corresponding to a bridging zone approaching 1 mm. The results are discussed in relation to existing models of whisker reinforcement and published long-crack *T*-curve data. [Key words: bridging, composites, cracks, pullout, toughness.]

I. Introduction

The incorporation of silicon carbide whiskers ($\approx$1 μm in diameter) into alumina can lead to considerable toughening.[1-8] A typical composite shows a monotonic toughness increase (toughness *T*-curve or crack-resistance *R*-curve) relative to $\approx$2.5 MPa$\cdot$m$^{1/2}$ for the base alumina, and maximum reported toughness values are 5 to 9 MPa$\cdot$m$^{1/2}$ (Refs. 8 to 11) depending on the properties and volume fraction of whiskers. It is generally accepted that the *T*-curve mechanisms involve some form of crack-interface bridging.[8] However, the precise nature of these mechanisms remains an issue of much debate. Many argue, e.g., from near-tip observations using transmission electron microscopy,[4,7] that the bridging primarily entails debonding and subsequent elastic deformation of the whiskers to abrupt rupture immediately (within 20 μm) behind the advancing crack tip. Those observations have been used as the basis for most micromechanics modeling.[8] Few efforts have been made to reconcile such small-scale bridging zones with long-crack *T*-curve data (typical crack extension range $\approx$100 μm to 1 mm),[9-11] e.g., by invoking an artificially enhanced "tail" in the fiber–matrix constitutive stress-displacement function (associated with a distribution in whisker strengths) or secondary bridging from the alumina grains in a coarse-grained matrix.[12,13]

In this communication we describe the results of some in situ experiments on crack growth in fine-grained alumina matrix materials reinforced with silicon carbide whiskers. The fine grain size minimizes potential bridging from the alumina grains themselves,[12,13] in order that we may investigate more clearly the micromechanisms of whisker toughening. Observations of whisker-bridging sites under load enable identification of these micromechanisms and, together with measurements of crack-opening displacements over the crack interface, indicate that the bridging which contributes to the toughness can indeed occur over substantial distances, i.e., up to 1 mm behind the crack tip. The results reveal the following features in the whisker-toughening process: (i) a considerably greater role of extended whisker pullout than hitherto proposed, (ii) identification of the *T*-curve baseline with the matrix (grain boundary) toughness, and (iii) enhancement of the bridge-formation processes from internal residual stresses.

I. Experimental Procedure

Two composites of silicon carbide whiskers[†] and alumina powder[‡] were hot-pressed as 50-mm-diameter disks at 1700°C for 1 h at a pressure of 42 MPa. Composite A was fabricated with 20 vol% whiskers that were 0.3 to 0.6 μm in diameter and 5 to 15 μm in length and composite B with 30 vol% whiskers that were 1.1 μm in diameter and 50 μm in length. The resultant composites achieved a density >99% with a random distribution of whiskers (except for slight alignment perpendicular to the hot-pressing direction) in matrices of grain size 1 to 2 μm.

The disks were surface ground to 1 mm in thickness and one surface of each was polished with diamond paste to 1-μm finish. Compact tension specimens with a notch of 7 mm in length and a tip radius of 150 μm were sawed from the disks.[14] A tapered cut was made ahead of the notch from the back (unpolished) surface to produce a chevron guide $\approx$2 mm in length.[14] This latter process was to provide extra stability in the ensuing crack extension. A Vickers indentation flaw (load 50 N) placed immediately ahead of the notch tip in the polished surface was then subjected to a preliminary load cycle to induce pop-in. The notch was finally resawed through the indentation, leaving a starter precrack $\approx$100 μm long.

The specimens were mounted into a fixture for in situ experiments in the scanning electron microscope (SEM)[15] with the polished side facing the electron beam for direct observation of the crack trace. Loads applied externally to the specimen in the SEM enabled the crack to be stably propagated (if sometimes discontinuously) for distances up to $\approx$1 mm within the chevron. Individual bridging sites were monitored during the crack growth. Crack-opening displacements (COD) were measured behind the crack tip, to determine the bridged interface profiles.[14]

After running the crack through the chevron the specimens were withdrawn and resawed for repeat experiments.

K.T. Faber—contributing editor

Manuscript No. 196531. Received July 18, 1991; approved October 10, 1991.

Supported by the U.S. Air Force Office of Scientific Research and the U.S. Department of Energy.

[*] Member, American Ceramic Society.

[*] Guest scientist from the Department of Material Science and Engineering, Lehigh University, Bethlehem, PA. Now at the Technical University, Hamburg-Harburg, Hamburg, Germany.

[†] TWS 100 (0.3 to 0.6 μm in diameter and 5 to 15 μm in length) and TWS 400 (1.1 μm in diameter, 50 μm in length), Tokai Carbon, Ltd., Tokyo, Japan.

[‡] High-purity Reynolds alumina grade RC-HP DBM alumina powder with 0.05% MgO, mean particle size 0.5 μm and surface area 7.6 m^2/g, Reynolds Metals Co., Richmond, VA.

III. Results

(1) *Crack Propagation and Whisker Bridge Evolution*

Specific examples of whisker bridging sites monitored in the SEM are shown in Figs. 1 and 2. Generally, the fracture followed an intergranular path in the alumina matrix with markedly abrupt deflections along or around the whiskers, although not always exactly along the whisker–matrix interfaces. These abrupt deflections appeared to be a most effective precursor to bridge formation. A majority of the whisker bridges ruptured at a distance <100 μm behind the crack tip, but some remained active over much greater distances. No detached microcracking at whisker–matrix interfaces more than a few grain diameters from the primary crack plane was observed.

Immediately behind the crack tip the walls begin to separate, but the whiskers remain mechanically connected across the interface. Figure 1(a) shows one such whisker ≈10 μm behind the tip, i.e., in the range ordinarily considered appropriate for "elastic" bridges.[4,7] Many of the whiskers observed in our materials disengaged from the matrix within this range with little indication of pullout. However, the particular whisker in Fig. 1(a) remained intact prior to abrupt rupture until the tip had progressed ≈120 μm beyond the site, corresponding to a COD of ≈300 nm. Other bridges showed even longer range effects. Figure 1(b) shows one such site where the debonding and stress buildup was sufficient to cause secondary, off-plane matrix fragmentation around the embedded whisker ≈350 μm behind the crack tip. This implies a long tail to the bridging stress-separation function.

An even more striking example of a whisker with long-range interaction across the interface is shown in the sequence of Fig. 2. In this case the whisker is located only ≈70 μm from the mouth of the extending crack (i.e., from the notch tip). The whisker ruptures well away from the crack plane and pulls out (in apparently sustained frictional contact with the matrix over this distance) during monotonic loading, as shown in Figs. 2(a) to (c). The whisker is slightly inclined to the separation plane and, therefore, is subjected to increasing bending stresses during its pullout. As shown in Fig. 2(d), disengagement is ≈830 μm behind the crack tip, corresponding to a COD ≈1 μm. The now unconstrained whisker rotates at its free end, so that, on unloading (Figs. 2(e) and (f)) the whisker does not re-enter its "socket" without some misfit, leaving the "closed" crack interface in a residual state of internal wedge loading.

(2) *Crack-Opening Displacement (COD)*

The COD measurements at the loaded crack interfaces allow us to construct the *K*-field plots in Fig. 3. We start with the Irwin relation[14] for COD in terms of the stress-intensity factor K and coordinate x behind the crack tip:

$$u(x) = (8x/\pi)^{1/2}(1 - \nu^2)K/E \tag{1}$$

with Young's modulus $E \approx 400$ GPa and Poisson's ratio $\nu \approx 0.25$. This relation may reasonably be expected to hold in the region $x \leq \Delta c \ll c_0$ (recall crack extension $\Delta c \approx 1$ mm and notch length $c_0 \approx 7$ mm in our experiments) if the crack walls are stress free (i.e., zero bridging). In reality, the bridging *K*-field acts to restrain the crack walls from opening as wide as Eq. (1) predicts.

The $K[u(x)]$ data points shown in Fig. 3 are accordingly obtained by inversion of Eq. (1). The data in this figure indicate the *K*-field an "Irwinian" observer would measure on traversing the crack plane from crack tip ($x = 0$) to mouth ($x = \Delta c$). At $x = \Delta c$, $K = 5.1$ MPa·m$^{1/2}$ is an approximate (under)estimate of the unshielded, applied stress-intensity factor, corresponding to the limiting toughness at the long-crack plateau of the *T*-curve. At the extrapolated limit $x \rightarrow 0$, $K = 2.5$ MPa·m$^{1/2}$ represents the shielded, crack-tip stress-intensity factor and is close to the intrinsic grain-boundary toughness of the matrix alumina. This extrapolated value lies well below the minimum (≈5 MPa·m$^{1/2}$) measured by more conventional *T*-curve methods.[8-11] We note that the *K*-field is slightly greater for material B, i.e., the material with the higher density of coarser fibers. We also note that the *K*-field increases up to $x \approx 500$ μm, indicating a broad bridging zone and a corresponding long-range *T*-curve.[14,§]

IV. Discussion

The present in situ observations enable us to identify more closely the bridging micromechanics of silicon carbide-whisker reinforcement in an alumina matrix, and to ascertain the range of the bridging zone.

For the bridging micromechanics, we see evidence for the short-range elastic component proposed in most analytical models.[8] Local matrix stress is transferred to the progres-

---

[§] A complete, self-consistent analysis of the profile over the bridging zone is a complex numerical procedure,[16] requiring (among other things) knowledge of the complete bridging-stress-separation function.

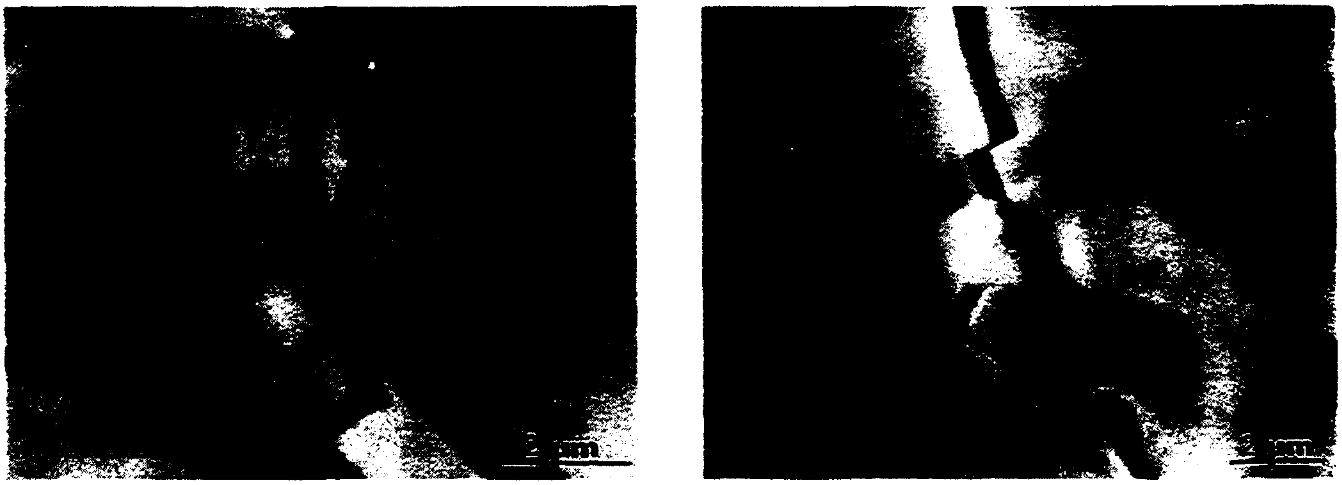

(a) (b)

Fig. 1. In situ SEM micrographs of bridging silicon carbide whiskers in alumina for material B (crack direction downward). (a) Elastic bridge (central whisker) 10 μm behind crack tip. Note strong deflections at this bridge, not exactly along the whisker–matrix interface. (b) Mechanically interlocked whisker 350 μm behind the crack tip. Note adjoining microfracture in surrounding matrix at bridge site.

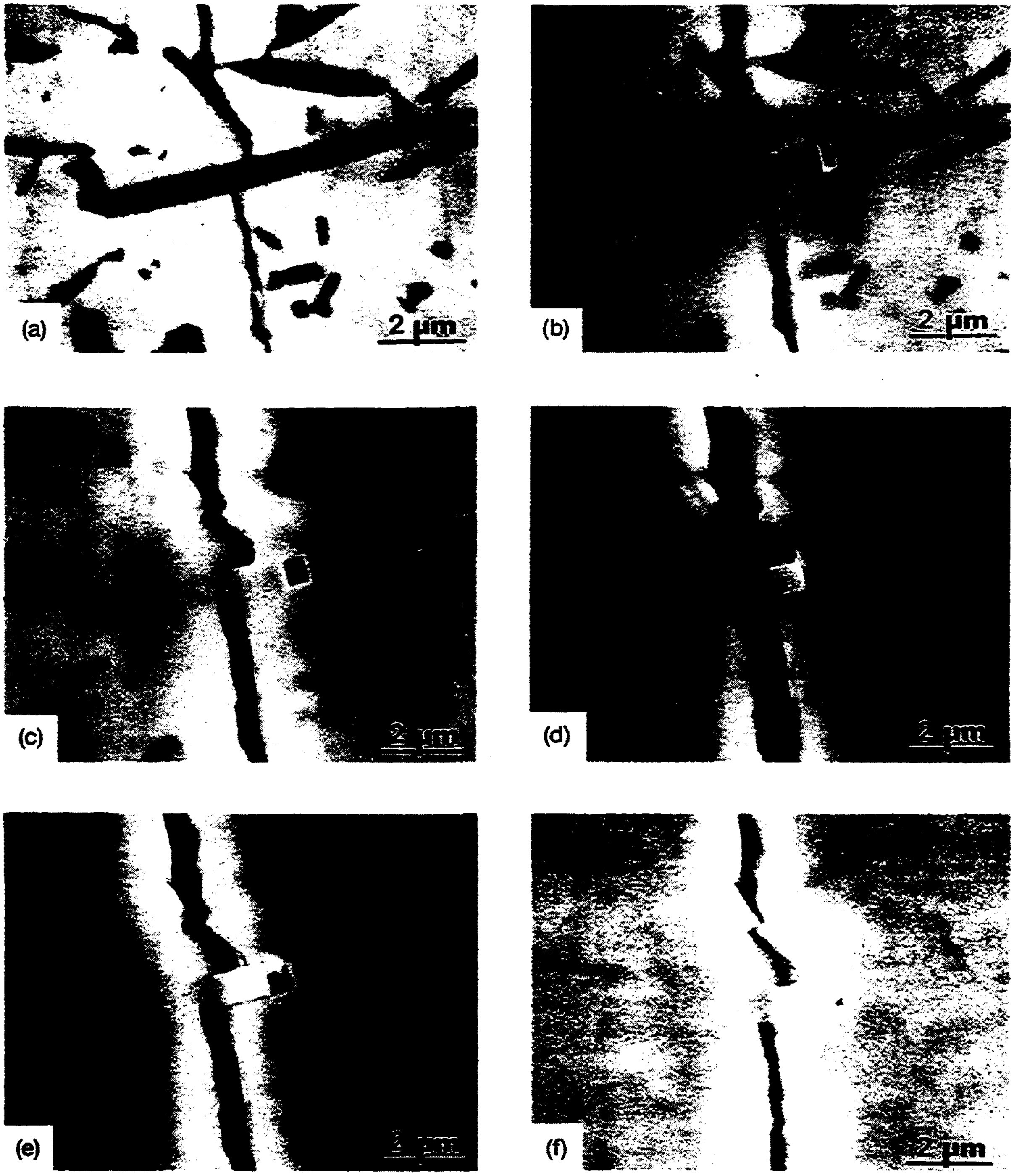

Fig. 2. In situ SEM sequence showing evolution of bridge whisker pullout for material A (crack direction downward). Distance x behind crack tip and force P on compact-tension load points: (a) $x = 100$ μm, $P = 167$ N; (b) $x = 110$ μm, $P = 209$ N; (c) $x = 330$ μm, $P = 213$ N; (d) $x = 830$ μm, $P = 233$ N; (e) $x = 830$ μm, $P = 101$ N; and (f) $x = 830$ μm, $P = 0$ N.

sively debonding whisker, until abrubt rupture occurs (whisker or matrix or both) in the near-crack plane. This rupture occurs most frequently at distances $x < 100$ μm from the crack tip in our materials, with attendant energy dissipation by acoustic waves. However, in many instances, such as in Fig. 1, the rupture point is located much farther behind the crack tip than previously supposed.

However, even these unusually strong elastic bridges cannot account for the crack extension range of 1 mm or so that are apparent in the reported *T*-curve measurements.[8–11] Additionally, as may be deduced from indentation-flaw studies,[17] the alumina grain size (≈ 2 μm) is far too small for a significant contribution from *matrix* grain–grain interlocking. Any explanation would require the extended cracks in our experiments to be bridged over their entire lengths. Figure 2(c), where the bridge site remains active some 330 μm behind the crack tip, demonstrates the viability of such an extensive zone. An essential ingredient of persistent bridge activity is the substantial pullout that can occur well after whisker rupture. Although such pullout bridges constitute only a small fraction (perhaps 1 in 20) of observed sites in our observations, and the ensuing frictional tractions are unlikely to be as intense as those that build up at the rupture point, the toughness may be considerably enhanced by the relatively large crack-wall separation over which energy can be dissipated (corresponding to a large area under the stress-separation function). This frictional component of the work expenditure may be further augmented by enhanced wall-contact

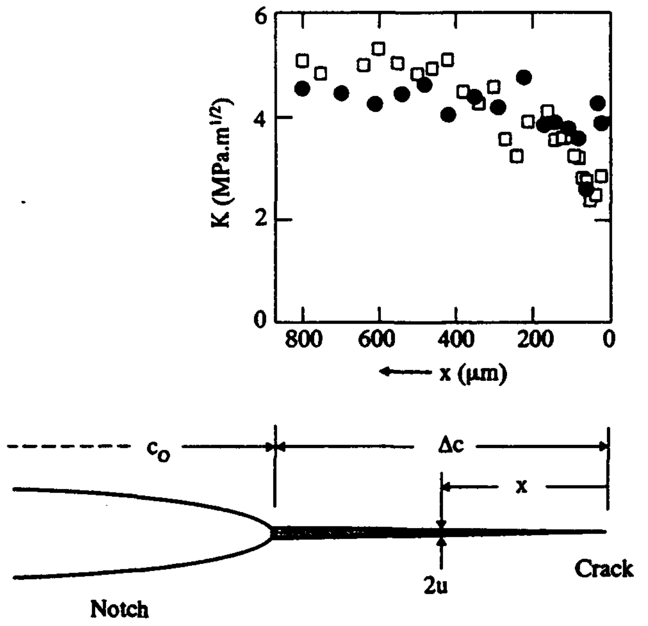

Fig. 3. *K*-field evaluated from crack-opening displacements along crack interface in silicon carbide-whisker-reinforced alumina for materials A (closed symbols) and B (open symbols). Cracks remain bridged (hatched region in schematic) in propagation through $\Delta c \approx 1000$ μm (notch length $c_0 = 7$ mm). Data points are *K*-field evaluations from inverted form of Irwin relation (Eq. (1)).

stresses associated with the oblique pullout in Fig. 2.[18,19] On the other hand, the resulting bending moments on the bridges could cause premature failure of the whisker or matrix, e.g., Figs. 1(b) and 2(d), in part negating some of the potential benefits.

The importance of long-range whisker pullout interactions is also reflected in the measured crack-interface profile. We see from the COD data in Fig. 3 that the transition from crack tip to far-field bounding *K*-fields occurs most rapidly between $x = 0$ to 300 μm, and more slowly thereafter between $x \approx 300$ to 1000 μm. This implies a bridging stress-separation function with rapid falloff from a strong, short-range peak into a weak, long-range tail.

In this context, we may note some implications in our observations concerning fatigue. On unloading the crack the bridges are unlikely to restore to their original configuration at the interface, e.g., Fig. 2. At the very least, this may be expected to prevent complete closure, with resultant enhancement of the mean crack-tip *K*-field during cyclic loading.[20] More importantly, the bridges may suffer progressive and irreparable damage, thereby degrading the intrinsic toughening processes and reducing the lifetime.[21]

We reemphasize that the COD measurements provide a more accurate measure of the lower limit of the *T*-curve than do conventional fracture mechanics techniques. These latter techniques are restricted by the scale of the pop-in starter cracks (typically 100 μm) used in the crack extension measurements. Here, extrapolation of our data to the crack tip ($x = 0$) in Fig. 3 yields $K \approx 2.5$ MPa·m$^{1/2}$, corresponding to the grain-boundary toughness, whereas the more conventional fracture mechanics methods are generally unable to obtain data below $K \approx 5$ MPa·m$^{1/2}$.[8-11]

Finally, we may recall our observations in Section I(1) of markedly abrupt crack deflections in the proximity of whiskers. Such behavior may be attributed to either weak interphase boundaries or strong local internal stresses. Recall again, however, that the deflections do not always occur exactly along the whisker–matrix interfaces (Fig. 1(a)). Direct measurements of internal stresses in our composites using neutron diffraction techniques reveal substantial thermal expansion mismatch stresses in the alumina ($\approx +200$ MPa in composite A and +430 MPa in composite B) and silicon carbide (≈ -1330 MPa in composite A and −1050 MPa in composite B).[22] We conclude that residual stresses play an important role not only in the *energetics* but also in the *formation* of bridging, by enhanced crack deflection.

Acknowledgments: We thank Ralph F. Krause, Jr., for hot-pressing the samples and James F. Kelly for assistance with the SEM imaging.

References

[1] P. F. Becher and G. C. Wei, "Toughening Behavior in SiC-Whisker Reinforced Alumina," *J. Am. Ceram. Soc.*, **67** [12] C-267–C-269 (1984).

[2] J. Homeny, W. L. Vaughn, and M. K. Ferber, "Processing and Mechanical Properties of SiC-Whisker-Al$_2$O$_3$-Matrix Composites," *Am. Ceram. Soc. Bull.*, **66** [2] 333–38 (1987).

[3] J. Homeny and W. L. Vaughn, "Whisker-Reinforced Ceramic Matrix Composites," *MRS Bull.*, **7** [7] 66–71 (1987).

[4] P. F. Becher, C.-H. Hsueh, P. Angelini, and T. N. Tiegs, "Toughening Behavior in Whisker-Reinforced Ceramic Matrix Composites," *J. Am. Ceram. Soc.*, **71** [12] 1050–61 (1988).

[5] P. F. Becher, "Recent Advances in Whisker-Reinforced Ceramics," *Annu. Rev. Mater. Sci.*, **20**, 179–95 (1990).

[6] J. Homeny, W. L. Vaughn, and M. K. Ferber, "Silicon Carbide Whisker/Alumina Matrix Composites: Effect of Whisker Surface Treatment on Fracture Toughness," *J. Am. Ceram. Soc.*, **73** [2] 394–402 (1990).

[7] G. H. Campbell, M. Rühle, B. J. Dalgleish, and A. G. Evans, "Whisker Toughening: A Comparison Between Aluminum Oxide and Silicon Nitride Toughened with Silicon Carbide," *J. Am. Ceram. Soc.*, **73** [3] 521–30 (1990).

[8] P. F. Becher, "Microstructural Design of Toughened Ceramics," *J. Am. Ceram. Soc.*, **74** [2] 255–69 (1991).

[9] R. F. Krause, E. R. Fuller, and J. F. Rhodes, "Fracture Resistance Behavior of Silicon Carbide Whisker-Reinforced Alumina Composites with Different Porosities," *J. Am. Ceram. Soc.*, **73** [3] 559–66 (1990).

[10] J. Homeny and W. L. Vaughn, "*R*-Curve Behavior in a Silicon Carbide Whisker/Alumina Matrix Composite," *J. Am. Ceram. Soc.*, **73** [7] 2060–62 (1990).

[11] S. V. Nair, "Crack-Wake Debonding and Toughness in Fiber- or Whisker-Reinforced Brittle-Matrix Composites," *J. Am. Ceram. Soc.*, **73** [10] 2839–47 (1990).

[12] P. L. Swanson, C. J. Fairbanks, B. R. Lawn, Y-W Mai, and B. J. Hockey, "Crack-Interface Grain Bridging as a Fracture Resistance Mechanism in Ceramics: I. Experimental Study on Alumina," *J. Am. Ceram. Soc.*, **70** [4] 279–89 (1987).

[13] P. F. Becher, E. R. Fuller, Jr., and P. Angelini, "Matrix-Grain-Bridging Contributions to the Toughness of Whisker-Reinforced Ceramics," *J. Am. Ceram. Soc.*, **74** [9] 2131–35 (1991).

[14] J. Rödel, J. F. Kelly, and B. R. Lawn, "In Situ Measurements of Bridged Crack Interfaces in the SEM," *J. Am. Ceram. Soc.*, **73** [11] 3313–18 (1990).

[15] J. Rödel, J. F. Kelly, M. R. Stoudt, and S. J. Bennison, "A Loading Device for Fracture Testing of Compact Tension Specimens in the SEM," *Scanning Micros.*, **5** [1] 29–35 (1991).

[16] B. N. Cox and D. B. Marshall, "Determination of Crack Bridging Forces," *Int. J. Fract.*, in press.

[17] P. Chantikul, S. J. Bennison, and B. R. Lawn, "Role of Grain Size in the Strength and *R*-Curve Properties of Alumina," *J. Am. Ceram. Soc.*, **73** [8] 2419–27 (1990).

[18] J. Bowling and G. W. Groves, "The Debonding and Pullout of Ductile Wires from a Brittle Matrix," *J. Mater. Sci.*, **14** [2] 431–42 (1979).

[19] V. C. Li, Y. Wang, and S. Backer, "Effect of Inclining Angle, Bundling and Surface Treatment on Synthetic Fibre Pull-Out From a Cement Matrix," *Composites (Guildford U.K.)*, **21** [2] 132–40 (1990).

[20] R. O. Ritchie, "Mechanisms of Fatigue Crack Propagation in Metals, Ceramics and Composites: Role of Crack Tip Shielding," *Mater. Sci. Eng.*, **A103** [2] 15–28 (1988).

[21] S. Lathabai, J. Rödel, and B. R. Lawn, "Cyclic Fatigue from Frictional Degradation at Bridging Grains in Alumina," *J. Am. Ceram. Soc.*, **74** [6] 1340–48 (1991).

[22] H. Prask, C. Choi, E. R. Fuller, R. F. Krause, A. Krawitz, and J. Richardson, "Micro-Stresses in Ceramic Composites," Annual Report, NIST Reactor Radiation Division, 1990. □

SHORT-CRACK *T*-CURVES AND DAMAGE TOLERANCE IN ALUMINA-BASED COMPOSITES

Linda M. Braun, Stephen J. Bennison & Brian R. Lawn, Materials Science and Engineering Laboratory, National Institute of Standards & Technology, Gaithersburg, MD 20899

ABSTRACT

A procedure for evaluating short-crack toughness curves (*T*-curves) from quantitative *in situ* observations of Vickers indentation cracks during stressing is described. We demonstrate the procedure with results on an Al_2O_3–Al_2TiO_5 composite with strong *T*-curve behavior and attendant crack stabilization from grain-localized-crack-bridging. The stabilization allows the material to tolerate multiple damage accumulation during loading.

INTRODUCTION

Rising toughness with crack extension (*T*-curve or *R*-Curve) underlies the mechanical properties of many ceramic materials [1-5]. Two issues are central to optimizing the *T*-curve characteristics for structural applications. The first involves identification and manipulation of the microstructural parameters that control the *T*-curve. The second involves evaluation of the *T*-curve in the "short-crack" domain, i.e. on a scale comparable to the microstructure. The short-crack *T*-curve controls the strength [1,5,6], flaw sensitivity [1,5,6], and reliability [5] of ceramics and is, therefore, highly pertinent to engineering design.

In this paper we present a strategy for improving the *T*-curve properties of Al_2O_3-based ceramics through enhancement of residual thermal expansion (TEA) mismatch stresses via incorporation of a second phase, β-Al_2TiO_5. These stresses augment the frictional grain-bridging mechanism responsible for the *T*-curves and associated flaw tolerance in Al_2O_3 (and many other nontransforming) ceramics [7-9]. We describe a procedure for evaluating the short-crack *T*-curve from quantitative *in situ* observations of Vickers indentation cracks during stressing [10], in conjunction with indentation–strength data [9], on the tailored Al_2O_3–Al_2TiO_5 composite.

EXPERIMENTAL

The Al_2O_3–Al_2TiO_5 composite was fabricated by pressureless sintering [8]. A colloidal suspension of high purity powders (α-Al_2O_3, Sumitomo AKP-HP grade, 99.995% pure, 0.5 μm crystallites; β-Al_2TiO_5, Trans-Tech., 99.9% pure, 1-5 μm crystallites) in water (pH ~3) was dried and formed into green disks by single-end die pressing (63 MPa) in high-purity graphite followed by wet-bag isostatic pressing (350 MPa). The disks were calcined in air at 1050°C for 12 hr and sintered at 1600°C for 1 hr. The density was measured using the Archimedes method [11], and grain size using a linear intercept technique [12] on thermally etched (1490°C, 6 min. air) polished sections.

The short-crack *T*-curve characteristic of the composite was determined from quantitative observations of crack growth from a Vickers indentation during loading [6,13-15]. This was accomplished using a custom-made biaxial stressing fixture, punch (diam 6mm) on six-ball support (diam 23mm). A force was applied using a piezoelectric translator and measured using a strain gage load cell. The fixture could be placed on an inverted optical microscope with long working-distance lenses, or in a scanning electron microscope (SEM). Crack evolution and crack-microstructure interactions were taped on a video cassette recorder. The experimental procedure consisted of: (i) indenting the center of a polished disk (diam 30mm, thickness 4mm) at a specified peak contact load (20-300 N); (ii) covering the indentation site with a drop of dry silicone oil and a glass cover slide for optical imaging; (iii) loading the specimen and simultaneously recording the applied stress (calculated from the force and geometry using thin-plate formulas) and crack growth during evolution to failure; (iv) measuring the crack lengths at jump and arrest points during loading directly from the video tape.

Indentation-strength tests were carried out using a universal testing machine, to determine the flaw tolerance characteristics. Vickers indentations at specified loads were made in the center of each polished specimen (diam 20mm, thickness 3mm). The disks were broken in biaxial flexure using a punch (diam 4mm) on three-ball support (diam 15mm). These tests were conducted with a drop of dry silicone oil on the indentation site and broken in fast loading (<10 ms) to maintain "inert" conditions. Post-mortem examinations were made of all broken specimens to confirm failure initiation from the indentation sites. A minimum of 4 specimens per contact load were fractured. Comparative *in situ* and strength tests were also carried out on a control fine-grain (6 μm) Al_2O_3.

RESULTS

Figure 1 shows the microstructure of the Al_2O_3–Al_2TiO_5 (20 vol.%) composite. The microstructure has a density >99% and a matrix grain size of 6 μm. The grain structure is equiaxed with the Al_2TiO_5 particles distributed mainly at the matrix grain boundaries, with occasional clusters of 5-10 particles. These clusters are probably remnant agglomerates from the starting powder.

The indentation crack patterns in the composite were well formed at all indentation loads. During stressing both of the mutually orthogonal radial crack systems were observed to extend stably, with discrete jumps. At approximately 80% of the failure stress one set of radial cracks began to extend at the expense of the other. The total extension of this dominant set relative to the initial crack length exceeded the factor 2.5 characteristic of indentation flaws in materials with single-valued toughness. Such enhanced extension indicates the presence of an additional stabilizing contribution (i.e. above and beyond that of the residual contact field) to the crack-tip *K*-field [1,5,16], consistent with a rising *T*-curve.

The *in situ* testing fixture also facilitated detailed observations of crack-microstructure interactions in the SEM. Examinations of extended cracks during loading to failure revealed evidence for copious grain-interlock bridging at crack interfaces. Figure 2 indicates that the Al_2TiO_5 particles play a highly active role in the bridging process responsible for the strong *T*-curve in this material [5,7,9].

The stabilization imparted by the *T*-curve is strong enough to allow the development of multiple macro-crack systems from natural flaws in the tensile surface of the specimen. Figure 3, an optical micrograph recorded at slight overfocus, reveals the presence of general damage in the form of multiple "macro-cracks", i.e. cracks typically 30-300 grain diameters in length. The incidence of these cracks corresponded to a significant nonlinearity in the measured load-deflection curve in this material [8]; interactions with the macro-crack damage therefore influences the strength and damage tolerance characteristics. Failure of the specimen nevertheless still occurred from the indentation cracks. In unindented specimens, strength is controlled by percolation of the macro-cracks.

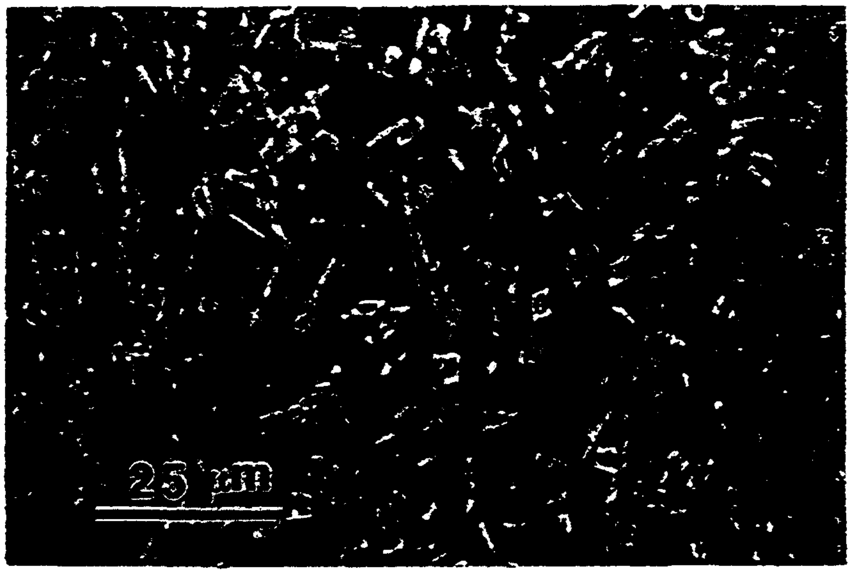

Figure 1 SEM micrograph (backscattered) of the Al_2O_3–Al_2TiO_5 (20 vol.%) composite. White phase Al_2TiO_5; grey phase Al_2O_3; black phase porosity.

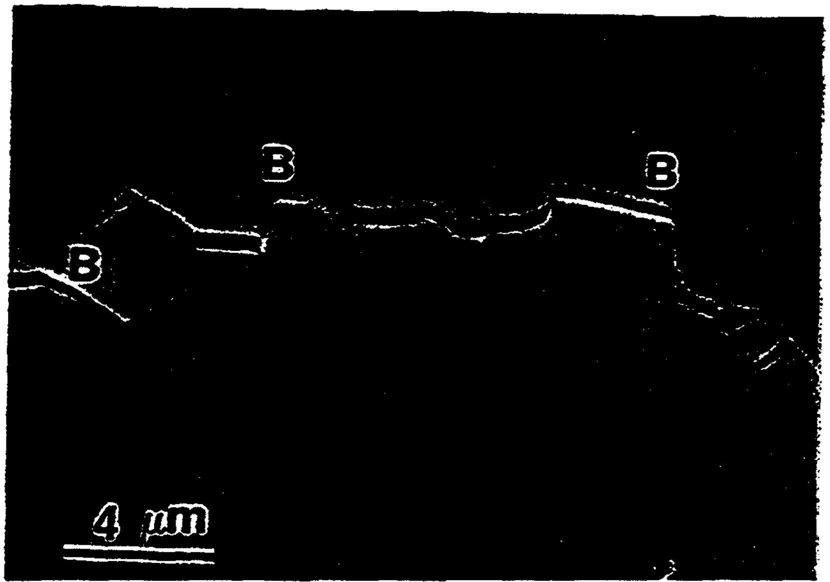

Figure 2 SEM micrograph (backscattered electrons) of a loaded indentation crack showing bridging in Al_2O_3–Al_2TiO_5 composite. B marks grain-grain bridge sites.

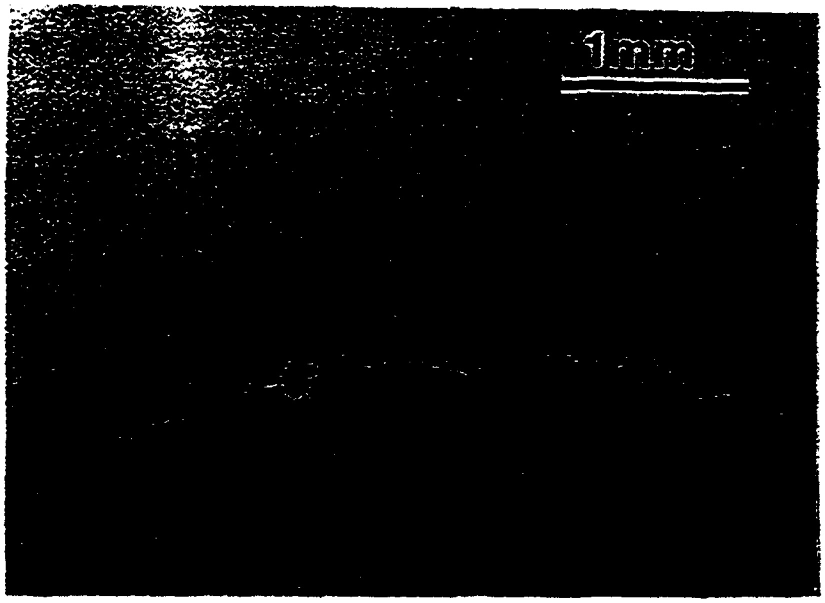

Figure 3 Optical micrograph (bright field) of damage in Al_2O_3–Al_2TiO_5 composite. Multiple cracks are present and stable during loading. The image is deliberately overfocused to enhance contrast.

T-CURVE ANALYSIS AND STRENGTH

The T-curve is determined from the stress-intensity field governing growth of indentation cracks subject to microstructural closure forces. The crack-tip K-field, K_*, as a function of radial crack size c is [1,5-7]

$$\begin{aligned} K_*(c) &= K_A + K_R + K_\mu \\ &= \psi\sigma_A c^{1/2} + \chi P/c^{3/2} + K_\mu(c) = T_0 \end{aligned} \qquad (1)$$

at equilibrium. K_A is the stress-intensity factor associated with the applied stress field σ_A, K_R with the residual contact field at an indentation load P, and K_μ with microstructural shielding (the source of the T-curve); $\psi = 0.75$ [10] is a geometrical coefficient that characterizes the half-penny-like crack configuration, and $\chi = 0.076$ [10] is a coefficient that characterizes the intensity of the residual contact field; T_0 is the intrinsic material toughness, governed by the grain boundary fracture energy for intergranular fracture. Eqn. 1 may be transposed into a form appropriate to a "global" (i.e. externally measured) K-field

$$\begin{aligned} K_A'(c) &= \psi\sigma_A c^{1/2} + \chi P/c^{3/2} \\ &= T_0 - K_\mu(c) = T_0 + T_\mu(c) = T(c) \end{aligned} \qquad (2)$$

where $K_A'(c)$ is an effective applied stress-intensity factor, $T_\mu(c) = -K_\mu(c)$ is a shielding toughness term, and $T(c)$ defines the T-curve. Measurements of σ_A and c at given load P are substituted into Eqn. 2 to evaluate $T(c)$.

A quantitative evaluation of the short-crack T-curve for our composite material is accordingly presented in fig. 4. The $\sigma_A(c)$ data used in this evaluation were taken before the onset of nonlinear load-deflection behavior. The toughness increases monotonically from $T \approx 1.8$ MPa.m$^{1/2}$ at $c \approx 100$ µm to $T \approx$ MPa.m$^{1/2}$ at c ≈ 2 mm. The maximum measured toughness does not achieve the steady-state value $T \approx 9$ MPa.m$^{1/2}$ estimated from long-crack (disk-compact-tension geometry) measurements [17]. Note that the initial toughness falls below the intrinsic toughness for a fine-grain control Al_2O_3, $T_0 = 2.75$ MPa.m$^{1/2}$ [7,18]. At very small crack sizes local residual tensile TEA stresses *drive* crack growth ($T < T_0$); at large crack sizes, closure stresses from bridging dominate, and *inhibit* growth ($T > T_0$).

The pronounced crack stabilization imparted by the strong T-curve in the Al_2O_3–Al_2TiO_5 composite is evident in the indentation-strength response shown in fig. 5. The strength of the composite is relatively insensitive to indentation load, and shows a marked deviation from the ideal $P^{-1/3}$ behavior for the control Al_2O_3 [6,16,18]. In contrast to the composite, the control material is highly flaw-sensitive, with relatively low strengths in the domain of intermediate cracks (high indentation loads).

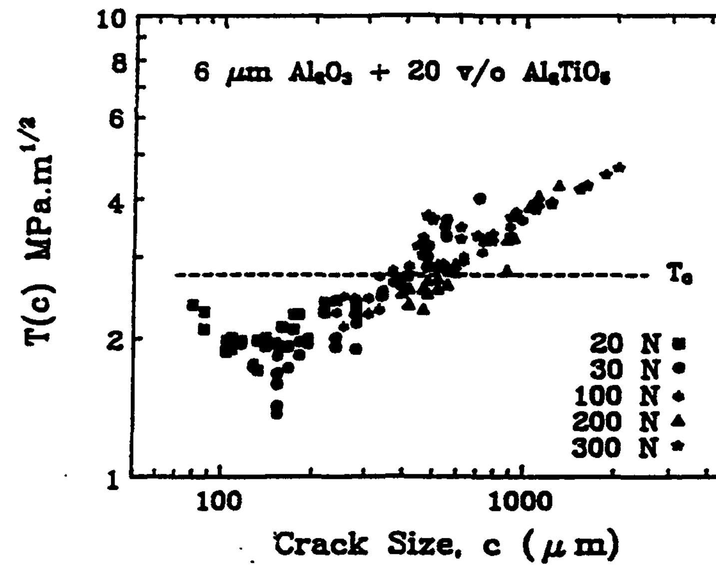

Figure 4 *T*-curve of Al_2O_3–Al_2TiO_5 composite as evaluated by *in situ* observations of Vickers indentation cracks (P = 20, 30, 100, 200, 300N) during loading. The baseline toughness T_0 = 2.75 MPa.m$^{1/2}$ is for fine-grain control Al_2O_3.

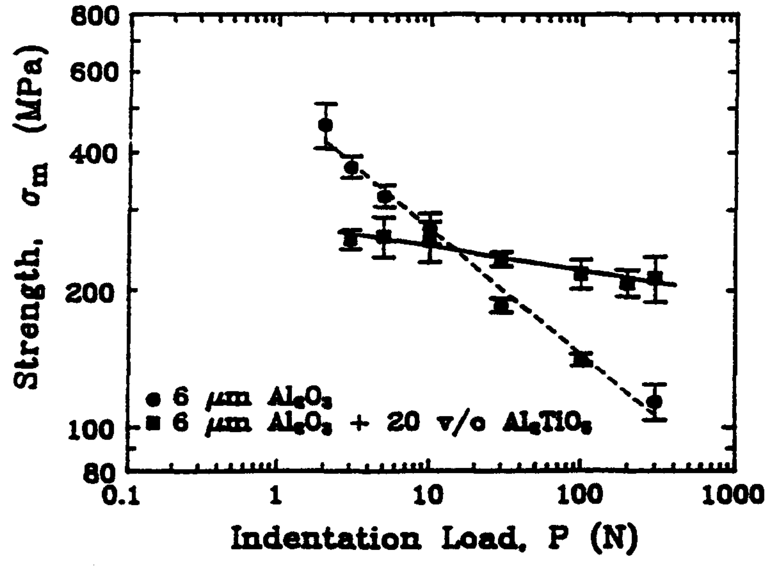

Figure 5 Plot of $\sigma_M(P)$ for Al_2O_3–Al_2TiO_5 composite and control Al_2O_3. The composite shows superior flaw tolerance.

We have shown that optimization of grain-localized crack bridging in Al_2O_3 can be achieved by incorporation of an Al_2TiO_5 second-phase, via enhancement of local TEA stresses. The attendant crack stabilization yields a composite that is highly damage resistant (fig. 3), with strong *T*-curve characteristics (fig. 4) and high flaw tolerance (fig. 5). With regard to the *T*-curve in fig. 4, scatter in the *in situ* data arises from uncertainties in crack-size measurements, and from crack-size variations in the crack-geometry and indentation coefficients ψ [14] and χ [15]. Slow crack growth can also lead to an underestimate of the toughness level [10]. The data range using indentation flaws is limited by the contact loads at which well-formed, dominant radial crack systems are obtainable. Notwithstanding these qualifications, the *in situ* technique presents itself as a powerful means of *T*-curve evaluation in the critical short-crack region that determines strength and other (e.g. wear) properties of structural ceramics; and, moreover, provides valuable information on the crack-microstructure interactions fundamentally responsible for the *T*-curve.

ACKNOWLEDGEMENTS

The authors acknowledge discussions with E.R. Fuller Jr. and N.P. Padture, and experimental assistance from J.L. Runyan. Funding was provided by the U.S. Air Force Office of Scientific Research and E.I. duPont de Nemours and Co. Inc.

REFERENCES

1. Y-W. Mai and B.R. Lawn, "Crack Stability and Toughness Characteristics in Brittle Materials," *Ann. Rev. Mater. Sci.* 16 415-39 (1986).

2. R.W. Steinbrech and O. Shmenkel, "Crack Resistance Curves of Surface Cracks in Alumina," *J. Amer. Ceram. Soc.* 71[5] C-271-73 (1988).

3. D.J. Green, R.H.J. Hannink and M.V. Swain, *Transformation Toughening of Ceramics*. CRC Press, Boca Raton, Florida, 1989.

4. A.G. Evans, "Perspective on the Development of High-Toughness Ceramics" *J. Amer. Ceram. Soc.* 73[2] 187-206 (1990).

5. B.R. Lawn, *Fracture of Brittle Solids*, second edition. Cambridge University Press, Cambridge, UK, 1991.

6. R.F. Cook, C.J. Fairbanks, B.R. Lawn and Y-W. Mai, "Crack Resistance by Interfacial Bridging: Its Role in Determining Strength Characteristics," *J. Mater. Research* 2[3] 345- 56 (1987).

7. S.J. Bennison and B.R. Lawn, "Role of Interfacial Grain-Bridging Sliding Friction in the Crack-Resistance and Strength Properties of Nontransforming Ceramics," *Acta Metall.* 37[10] 2659-71 (1989).

8. J.L. Runyan and S.J. Bennison, "Fabrication of Flaw-Tolerant Aluminum-Titanate-Reinforced Alumina," *J. Europ. Ceram. Soc.* 7 93-99 (1991).

9. S.J. Bennison, N.P. Padture, J.L. Runyan and B.R. Lawn, "Flaw-Insensitive Ceramics," *Philos. Mag. Letters* 64[4] 191-95 (1991).

10. L.M. Braun, S.J. Bennison and B.R. Lawn, "Objective Evaluation of Short-Crack Toughness-Curves Using Indentation Flaws: Case Study on Alumina-Based Ceramics," Submitted *J. Amer. Ceram. Soc.*

11. E.C.M. Pennings and W. Grellner, "Precise Nondestructive Determination of the Density of Porous Ceramics," *J. Amer. Ceram. Soc.*, 72 [2] 1268-70 (1989).

12. J.C. Wurst and J.A. Nelson, "Lineal Intercept Technique for Measuring Grain Size in Two-Phase Polycrystalline Ceramics," *J. Amer. Ceram. Soc.,* 55 [2] 109 (1972).

13. N. Ramachandran and D.K. Shetty, "Rising Crack-Growth-Resistance (*R*-Curve) Behavior of Toughened Alumina and Silicon Nitride," *J. Amer. Ceram. Soc.* 74[10] 2634-41 (1991).

14. S.M. Smith and R.O. Scattergood, "Crack Shape Effects in Fracture Toughness Measurements," *J. Am. Ceram. Soc.*, in press.

15. C-W. Li, D-J. Lee and S-C. Lui, "*R*-Curve Behavior and Strength of *In Situ* Reinforced Silicon Nitride with Different Microstructures," *J. Amer. Ceram. Soc.*, submitted.

16. D.B. Marshall, B.R. Lawn and P. Chantikul, "Residual Stress Effects in Sharp-Contact Cracking: II. Strength Degradation," *J. Mater. Sci.* 14[9] 2225-35 (1979).

17. J. Rödel and S.J. Bennison, unpublished work.

18. P. Chantikul, S.J. Bennison and B.R. Lawn, "Role of Grain Size in the Strength and *R*-Curve Properties of Alumina," *J. Am. Ceram. Soc.* 73[8] 2419-27 (1990).

Reprinted from the Journal of the American Ceramic Society, Vol. 75, No. 7, July 1992

journal

J. Am. Ceram. Soc., 75 [7] 1870-75 (1992)

Improved Flaw Tolerance in Alumina Containing 1 vol% Anorthite via Crystallization of the Intergranular Glass

Nitin P. Padture[*,†] and Helen M. Chan[*]

Department of Materials Science and Engineering and Materials Research Center,
Lehigh University, Bethlehem, Pennsylvania 18015

The intergranular phase in an alumina containing 1 vol% anorthite glass was crystallized in order to enhance internal residual stresses within the microstructure. The influence of crystallization on the mechanical behavior was investigated by the indentation–strength method. Such crystallization was found to result in a marked improvement in the flaw tolerance of this alumina, indicative of strong *R*- or *T*-curve behavior. These results are discussed in the light of a theoretical model which assumes grain-localized crack bridging to be the predominant toughening mechanism. Particular reference is made to the influence of residual stresses and interfacial properties on grain pullout across the crack walls in the wake of the crack tip. [Key words: alumina, anorthite, crystallization, microstructure, *R*-curve.]

I. Introduction

It is now well established that crack resistance (commonly referred to as *R*- or *T*-curve) behavior in alumina-based and some other nontransforming ceramics results from the microstructural crack tip shielding process of grain-localized crack bridging.[1-6] Such *R*-curve behavior, in which the toughness increases with the crack length, arises from frictional tractions associated with the pullout of intact grains (bridges) in the wake of an advancing crack tip.[4] One of the most important consequences of a rising *T*-curve is the stabilization of crack growth, in that the initial flaw undergoes stable extension several times its original dimension prior to failure. This imparts the ceramic with the highly desirable property of "flaw tolerance," i.e., it exhibits a strength which is relatively insensitive to the initial flaw size or subsequent in-service damage.[7]

The bridging process has been theoretically modeled in which the grain-bridging elements are considered to be "clamped" within the matrix by compressive internal residual stresses arising from thermal expansion anisotropy/mismatch.[8,9] More generally, various models have been developed which describe the incremental toughening in terms of microstructural parameters, such as grain size, internal residual stresses, and sliding friction coefficient.[5,8-11] Since these microstructural parameters which affect the bridging process would be expected to have a marked effect on the *T*-curve behavior, the potential exists for tailoring of the ceramic microstructure for enhanced flaw tolerance. In several instances, this has indeed been shown to be the case. For example, some researchers have demonstrated that an increase in the grain size of single-phase aluminas results in an improvement in the degree of flaw tolerance.[3,12] This result has been interpreted as a direct consequence of the larger grain size resulting in an increase in both the size of the crack wake over which bridging is active, and the bridge pullout distance. A similar effect of grain size was obtained for liquid-phase-sintered (LPS) aluminas.[13,14] Other parameters of interest are those which influence the magnitude of residual stresses in the microstructure, as this is thought to control the clamping forces against which the bridges pull out. In single-phase alumina, the magnitude of the grain boundary residual stresses is limited by the degree of thermal expansion anisotropy. By adding a second phase of different thermal expansion coefficient, it is possible to further enhance the residual stresses and hence the flaw-tolerant behavior. This has been clearly demonstrated in the case of alumina–aluminum titanate composites, where the thermal expansion behavior of aluminum titanate is both extremely anisotropic and shows significant mismatch with the alumina matrix.[7,15-18]

Another (related) approach is to incorporate a *continuous* grain boundary second phase, as opposed to discrete particles (as in the case of alumina–aluminum titanate). This could be achieved, for example, by devitrification of a glassy grain boundary phase in LPS aluminas. It would appear that commercial aluminas might be readily amenable to this approach, since their microstructures invariably contain glassy phases at grain boundaries and triple points. Although there have been several studies concerning the effect of crystallization of the glassy intergranular phase on the mechanical properties of LPS aluminas[13,14,19-23] (to some extent in SiAlONs[24]), the results have been somewhat conflicting. Thus, some researchers[19-22] have reported significant increases in the toughness values of LPS aluminas containing 10 to 28 vol% intergranular glass. The toughness improvements resulted from simple postsintering heat treatments and were attributed to the crystallization of the intergranular glass. However, it should be noted that there was no mention of the degree of crystallization in the aforementioned studies. Further, the toughness measurements in those studies were performed at a single crack length, which possibly precluded the detection of *T*-curve behavior. The only exception to this was the work by Zdaniewski and Kirchner,[21] who measured the toughness using the indentation-crack length method at increasing indentation loads.

In contrast to this, Bennison *et al.*[13] showed that for a commercial fine-grain alumina containing ≈18 vol% second phase, crystallization of the second phase had very little effect on the crack-resistance curve. A similar null result was obtained by Powell-Doğan and Heuer,[23] again for a commercial alumina, but where the glass content was ≈7 vol%. Most recently, work by the present authors on fine-grain as well as coarse-grain LPS aluminas (containing ≈28% vol% glass) showed that the mechanical properties were essentially not affected by the crystallization heat treatment.[14] In view of the significant increase in the residual stresses which was estimated to result from the crystallization heat treatment, it seemed difficult to reconcile this finding with reference to the

---

R. F. Cook—contributing editor

Manuscript No. 196434. Received August 23, 1991; approved March 5, 1992.
Supported by a grant from the U.S. Air Force Office of Scientific Research and Coors Ceramics Company.

[*] Member, American Ceramic Society.

[†] Now at Materials Science and Engineering Laboratory, National Institute of Standards and Technology, Gaithersburg, Maryland 20899.

bridging model. However, transmission electron microscope (TEM) examination of the heat-treated specimens revealed that crystallization of the glassy phase was incomplete. This led us to believe, therefore, that viscous flow of the residual glass was allowing *relaxation* of the residual stresses, thus accounting for the lack of change in the mechanical properties.

The challenge, therefore, was to identify and study an alumina-based system where complete crystallinity in the intergranular glassy phase could be readily achieved, and to determine unambiguously whether the crystallinity of the second phase affects the mechanical properties. Note that in many instances complete crystallization of the glass is often not possible, because the chemical composition of the intergranular glass, especially for commercial materials, is different from that of the crystallizing phase(s). A further complication which can hinder complete crystallization is the physical constraint imposed by the surrounding alumina grains.[25] Clearly, for the purposes of the present investigation, the ability to tailor the glass composition is highly desirable. For this reason, it was decided to study specimens processed in the laboratory, rather than commercially available materials. In order to minimize the physical constraint effect, 1 vol% anorthite ($CaO \cdot Al_2O_3 \cdot SiO_2$) glass was chosen as the intergranular second phase. The alumina–anorthite system seemed particularly suited to this study, because previous work from our laboratory had already demonstrated that, because of the relatively small change in the volume associated with the crystallization of anorthite glass,[†] near-100% crystallization[‡] of the intergranular anorthite composition glass could be achieved.[27] Furthermore, the mismatch in the thermal expansion coefficients between crystalline anorthite and alumina is sufficiently great to induce high residual stresses (a factor of ≈4 greater than that in single-phase alumina[14] and a factor of ≈2.5 greater than that in alumina with glassy anorthite), making anorthite an ideal choice in this case.

Therefore, the purpose of the study was (i) to experimentally study the influence of crystallization of the intergranular glass on the flaw tolerance, as measured using the indentation–strength technique, of tailored alumina–1 vol% anorthite (A–An) materials, and (ii) to apply the bridging model by Bennison and Lawn[9] to deconvolute theoretical T-curves from the experimental indentation–strength data.

II. Experimental Procedure

(1) *Materials Processing*

Alumina specimens containing 1 vol% anorthite glass were fabricated using the following method. High-purity alumina powder (α-Al_2O_3, AKP-HP (≈0.5-μm crystallites), Sumitomo Chemical America, New York) was mixed with 1 vol% anorthite glass frit[§] and wet-ball-milled in methanol using zirconia (Y-TZP) grinding media for 24 h. The alumina–anorthite slurry was then gently stirred while drying on a hot plate. Individual powder batches (≈3.5 g) were placed in polyethylene bags, crushed between a roller and plate assembly, and subsequently placed in a graphite die. Approximately 80 disks (25-mm diameter × 5-mm thickness) were fabricated by uniaxial pressing at 50 MPa. These disks were then wet-bag isostatically pressed at 350 MPa. The green disks were then packed in loose alumina powder inside a high-purity alumina crucible and calcined at 800°C for 12 h, followed by sintering at 1600°C for 1 h. Specimens subjected only to this heat treatment will be referred to as A–An(G), since (as will be shown later) the anorthite is in the form of an intergranular glass. Approximately half of the above specimens were then subjected to an additional heat treatment of 25 h at 1200°C to fully crystallize the glassy phase.[27] These specimens will be referred to as A–An(C)

(2) *Materials Characterization*

Cross sections of A–An(G) and A–An(C) pellets were mounted in epoxy and were polished to 1-μm grade. The polished sections were then removed from the mounts and thermally etched at 1500°C for 0.5 h to reveal the microstructures. These microstructures were then observed in the scanning electron microscope (SEM) (AUTOSCAN, Etec Corp., Hayward, CA) in the secondary electron mode. The average grain size ($\bar{\ell}$) was determined using the linear intercept method,[28] and the grain aspect ratio (α_L) was estimated by measuring the long (L) and the and the short (ℓ) grain dimensions for at least 100 random grains for each material (where, $\alpha_L = L/\ell$). Specimens for TEM were prepared using the standard procedures for ceramic materials. Disks, 3 mm in diameter and ≈150-μm thickness, were ultrasonically cut from polished thin sections and dimpled to a thickness of ≈20 μm in the center. These disks were then ion-beam-milled to perforation, and evaporation-coated with a thin layer of carbon. The TEM specimens were observed in a TEM (400T, Philips Electronic Instruments, Inc., Mahwah, NJ) operated at 120 keV. The densities of the two materials (A–An(G) and A–An(C)) were measured by the Archimedes method, using deionized water as the immersion medium.[29] The measured densities were compared with the respective calculated theoretical densities.

Mechanical testing of the A–An(G) and A–An(C) disk samples was carried out using the indentation–strength technique.[3,12] In each case, ≈40 disk specimens were machined to a thickness of 2.5 mm and polished to 1-μm grade on the prospective tensile surface. For most of the disk specimens, a Vickers indentation was made at the center of the polished surface with contact loads ranging from 3 to 300 N. Some specimens, however, were left unindented. These disk specimens were then broken in biaxial flexure, using a three-point support and punch fixture in a servohydraulic testing machine (Model 1350, Instron Corp., Canton, MA). Vacuum grease was applied to the indentation site before testing, and the failure time was maintained to be less than 20 ms, to minimize any environmental effects. The strength was determined, using the breaking load and specimen dimensions.[30] Great care was taken to examine the indentation site for each specimen after failure to ensure that the failure originated from the indentation. The specimens that did not fail from the indentation were incorporated in the data pool for unindented controls.

On separate polished surfaces of A–An(G) and A–An(C) specimens, five indentations for each contact load (3 to 300 N) were made. The average size of the radial cracks emanating from these indentations was measured, using an optical microscope.

III. Results

(1) *Microstructure*

Figures 1(a) and (b) show representative SEM micrographs of the A–An(G) and A–An(C) microstructures, respectively. As would be expected, given the relatively low temperature of the crystallization heat treatment, the grain size distribution and grain morphology of A–An(C) are unchanged from those of A–An(G). Note the elongated nature of the grain structures, which is a commonly observed characteristic of aluminas containing glassy phase.[31] Examination of the samples in the TEM confirmed that in A–An(G) the intergranular phase was completely glassy, whereas in A–An(C), near-100% crystallization of the anorthite had occurred. Representative TEM micrographs showing the intergranular anorthite are given in Figs. 2(a) and (b). Table I summarizes the various heat

---

[†] The densities of crystalline and glassy anorthite are 2.763 g/cm^3 (Ref. 26) and 2.700 g/cm^3 (Ref. 27), respectively.

[‡] We refer to the degree of crystallinity as "near-100%" since very narrow glassy films may be present at the alumina–anorthite grain boundaries.[27]

[§] Details of the experimental procedures for melting of the anorthite glass and the subsequent comminution and classification to produce the glass frit (≈1.0-μm particles) have been described elsewhere.[27]

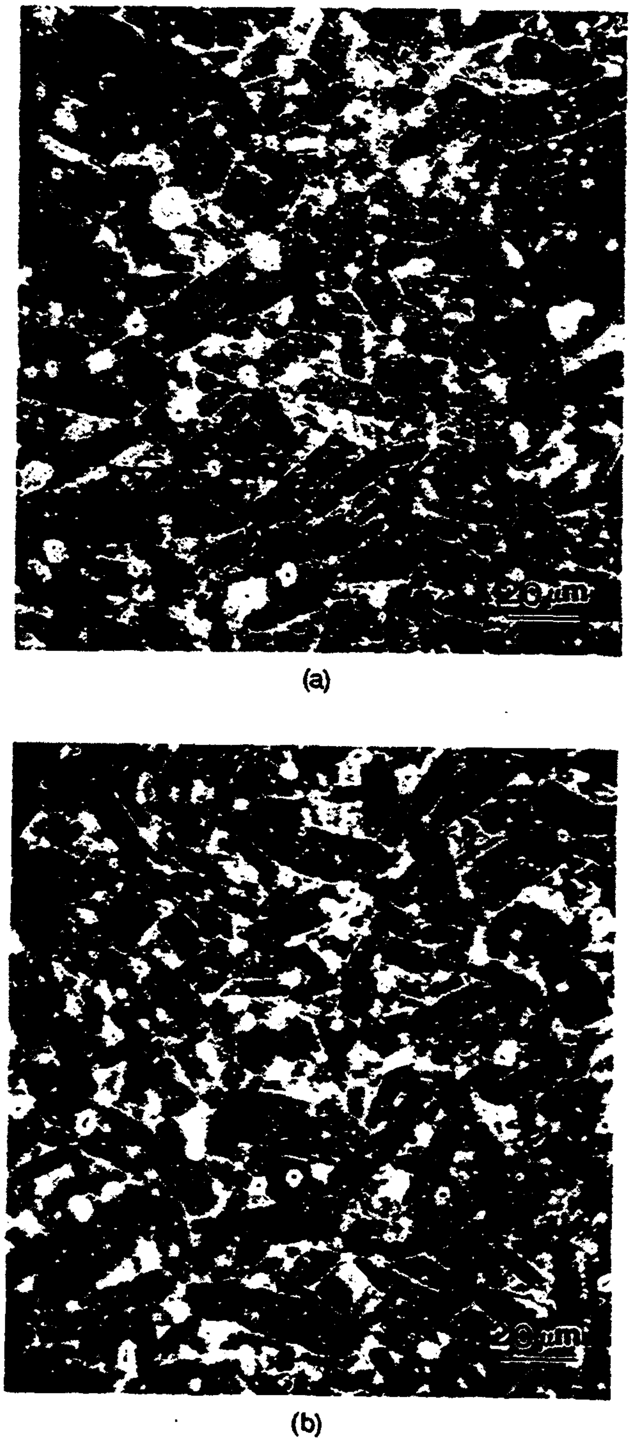

Fig. 1. SEM secondary electron images of polished and thermally etched sections of (a) A–An(G) and (b) A–An(C). Note the elongated grains in both the microstructures.

treatments and the resulting microstructures for the A–An materials.

(2) Mechanical Behavior

The plots of indentation load (P) versus strength (σ_M) for both sets of A–An specimens are shown in Fig. 3. For reference, the theoretically calculated $\sigma_M(P)$ response for an equivalent grain size (11 μm) single-phase equiaxed alumina[12] has been included as the dashed curve in Fig. 3. It can be seen that for A–An(C) there is a distinct *flattening* of the curve relative to that of A–An(G), which is indicative of improved flaw tolerance (note that an ideal $P^{-1/3}$ behavior indicates no T-curve). Thus, crystallization of the anorthite produces a strength *increase* at high flaw sizes, but a strength *decrease* at small flaw sizes. It is perhaps worth mentioning that the base-

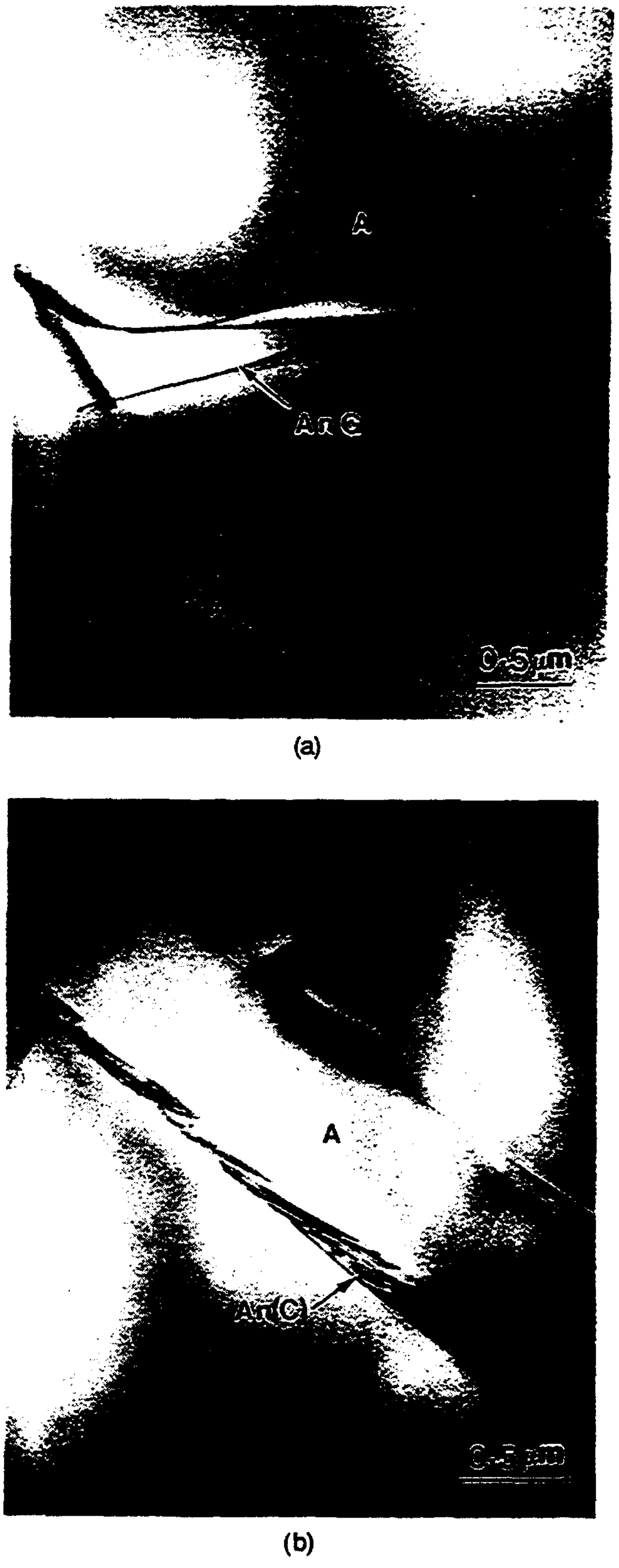

Fig. 2. TEM bright-field images of (a) A–An(G), showing intergranular glassy anorthite, and (b) A–An(C), showing intergranular crystalline anorthite.

Table I. Heat-Treatment Schedules and Resulting Microstructural Parameters for Alumina–Anorthite (A–An) Materials

		Resulting microstructure			
Material	Heat treatment	Al_2O_3 Grain size, $\bar{\ell}$ (μm)	Al_2O_3 aspect ratio, α_L	Intergranular phase	Density (g/cm^3) [% theoretical]
A–An(G)	1600°C, 1 h	11	≈2	Glassy anorthite	3.845 [96.8%]
A–An(C)	1600°C, 1 h, 1200°C, 25 h	11	≈2	Crystalline anorthite	3.850 [96.9%]

material A–An(G) is seen to possess marginally better flaw tolerance than equiaxed alumina of the same average grain size (11 μm).

In order to demonstrate the dependence of strength on the initial flaw size, Fig. 4 plots the same strength data from Fig. 3, but now against indentation crack length ($2c$) as the abscissa instead of the customary independent variable of indentation load. (In this case note that an ideal $(2c)^{-1/2}$ behavior indicates no T-curve.) However, a word of caution in the interpretation of such plots is in order. Since initial cracks in bridged ceramics undergo stable extension before failure, the system retains no memory of the initial crack size $2c$.[32] Therefore, not much significance should be attached to the initial crack size in bridged solids. However, such plots prove to be good intuitive guides to the understanding of the concept of flaw tolerance.

IV. Discussion

The results depicted in Fig. 3 clearly demonstrate that T-curve behavior, as evinced by the flattening of the $\sigma_M(P)$ response, is enhanced for A–An(C) by the postsintering crystallization heat treatment. In addition, microstructural examination of the A–An(G) and A–An(C) microstructures revealed that the alumina grain size and morphology were identical in the two samples, and that the only significant effect of the heat treatment was to produce crystalline anorthite at the grain boundaries. Since the influence on the strength was not uniform across the range of crack sizes (as evinced by the "rocking" of the $\sigma_M(P)$ curve for A–An(C) to A–An(G)), it cannot be argued that the change in mechanical properties was due solely to the replacement of the intergranular glass by a tougher or stronger crystalline phase. This leaves, therefore, the original premise as the most feasible explanation for the observed behavior; namely, the crystallization of the intergranular phase produces high internal residual stresses within the alumina–anorthite microstructure. This is believed to result in the bridging elements being more tightly clamped in the matrix. Consequently, there is an increase in the frictional tractions and more energy is dissipated in the process of grain pullout, hence enhancing the T-curve. It can also be argued that, because the second phase is distributed around the grains in A–An microstructures, the change in the nature of this intergranular phase can also affect the sliding friction properties of the bridge–matrix interface. Furthermore, upon comparing the $\sigma_M(P)$ data for A–An with that of the reference equiaxed alumina, it is suggested that the elongated nature of the grains, which increases the bridge pullout distance, is likely to augment the influence of the increased residual stresses and the interfacial sliding friction.

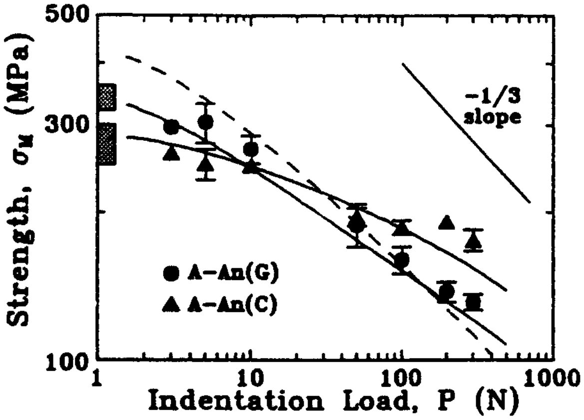

Fig. 3. Indentation load–strength responses for A–An(G) and A–An(C). Each datum point represents breaks from 4 to 5 specimens. Shaded regions to the left denote failures from natural flaws. Solid curves are fits from the bridging model. The dashed curve represents theoretically calculated $\sigma_M(P)$ response of an 11-μm grain size equiaxed alumina.[12]

As mentioned earlier, Bennison and Lawn[9] have derived a theoretical model describing the toughening due to grain bridging in nontransforming ceramics. The model incorporates several adjustable parameters which can be related to specific features of the ceramic microstructure. By allowing the parameters to vary between physically realistic boundary values, it is possible to fit the model to experimental data. In this manner, Chantikul *et al.*[12] have obtained excellent agreement between the model and their experimental data for single-phase alumina of differing grain sizes. We now apply this model to our experimental data for the A–An materials to obtain (i) quantitative estimate of the bridging parameters, (ii) fit to the experimental $\sigma_M(P)$ data, and (iii) deconvolution of the T-curves.[9,12,17]

First, consider the estimation of the bridging parameters. We began with assigning values to the microstructural parameters which were regarded as invariant: elastic modulus E = 393 GPa, Poisson's ratio ν = 0.2,[3] indentation flaw parameter χ = 0.022,[6,17] crack geometry coefficient ψ = 1.24 (pennylike crack),[6] grain aspect ratio α_L = 2, grain size ℓ = 7.3 μm,[¶] bridge spacing parameter α_D = 1,[12] distance to first bridge intersection $d_1 = \alpha_D \alpha_L \ell$,[17] and bridge perimeter factor α_λ = 4 (assumes rectangular bridges).[9] The fracture mechanics formulations and regression procedure described in Refs. 9 and 12 were then used to "search" for the "best fit" bridging parameters. This involved calculation of trial T-curves (toughness, T, as a function of crack length, c) followed by calculation of the corresponding $\sigma_M(P)$ response. The computed $\sigma_M(P)$ responses were then compared with the experimental data sets for A–An(G) and A–An(C) separately. The values for the bridging parameters were adjusted, within physically reasonable bounds, incrementally in an iterative algorithm until a minimum variance (standard deviation) between the theoretical and the experimental strength values (σ_M) was obtained. The best-fit parameters for A–An(G) and A–An(C) thus obtained are given in Table II, where T_0 is the grain boundary toughness, μ is the friction coefficient, σ_R is the residual stress, and ε is the strain to rupture.

The results from modeling (Table II) are consistent with the experimental findings in that, as expected, the magnitude of the residual stress σ_R is seen to increase as a result of crystallization of the intergranular anorthite (from 250 to 400 MPa). The results also showed a marginal increase in the

---

[¶] ℓ = 7.3 μm was estimated from the measured values of the average grain size $\bar{\ell}$ = 11 μm and the aspect ratio $\alpha_L \approx 2$, using a simplistic assumption: $\bar{\ell} = (L + \ell)/2$ and $\alpha_L = L/\ell$ (Section II(2)).

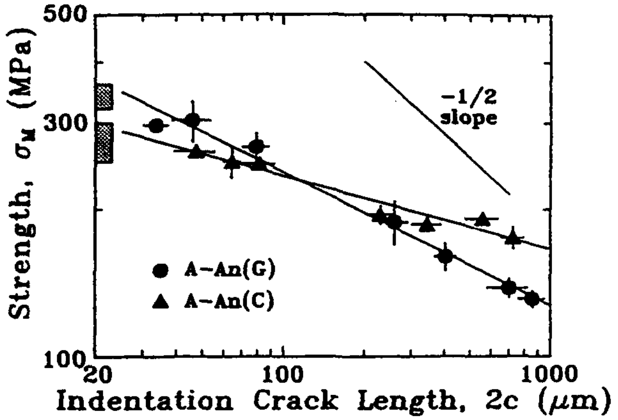

Fig. 4. The strength data for A–An(G) and A–An(C) from Fig. 3, now plotted against indentation crack size $2c$. The solid lines are empirical fits.

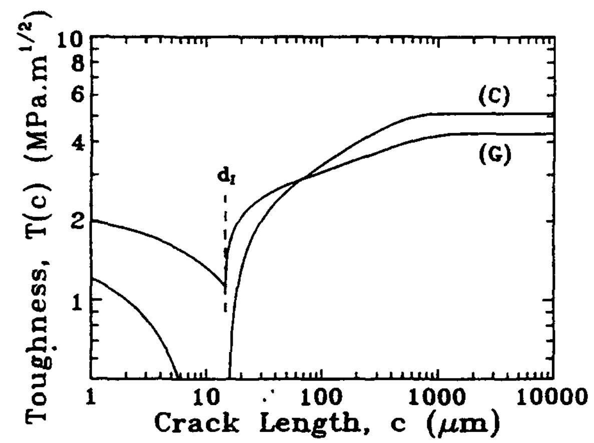

Fig. 5 Deconvoluted T-curves (G) and (C) from the A–An(G) and A–An(C) $\sigma_M(P)$ data sets, respectively (Fig. 3), using the grain-bridging model. d_I is the distance to the first bridge intersection.

friction coefficient, μ. Note that the intrinsic grain boundary toughness, T_0, is found to decrease for A–An(C), which is a manifestation of the "crossover" of the $\sigma_M(P)$ curves for A–An(G) and A–An(C) (Fig. 3). However, it should be pointed out that the bridging model predicts such a change in T_0 only for materials whose $\sigma_M(P)$ curves cross over and possess the same microstructural scale (as is the case for A–An(G) and A–An(C)). It is suggested that the decrease in T_0 is possibly due to the combined effect of the increase in the residual stress, and the change in the crystallinity of the grain boundary phase. However, at this stage we do not have any definitive experimental evidence to support this hypothesis.

Using the best-fit parameters (Table II) in the Bennison–Lawn bridging model, we obtain the theoretical $\sigma_M(P)$ responses for A–An(G) and A–An(C), shown by solid curves in Fig. 3. Note that these theoretical curves fit reasonably well to the experimental data and predict the crossover at about 10-N indentation load. The theoretical T-curves for A–An(G) and A–An(C) were also calculated, and appear in Fig. 5. Note that the toughness decreases with increasing crack length at small crack sizes ($c < d_I$) in Fig. 5, which is a result of the local tensile component of the residual stresses acting on the flaw before bridge intersection. However, after bridge intersection the toughness is seen to increase rapidly with the crack length. It is this rising part of the T-curve that essentially determines the characteristics of the "tangency condition" (instability) and hence the strength properties.[32] It was also seen that the calculated toughness for A–An(C) assumes negative values for crack lengths in the vicinity of d_I (Fig. 5), which represents the theoretical spontaneous microcracking limit.[12]

At this point, it is perhaps worth emphasizing that any "goodness of fit" of the grain-bridging model to the experimental data cannot be construed as evidence for the model's validity. Nonetheless, it is encouraging that the theoretically predicted increase in the residual stress was found to be consistent with the experimental crystallization heat treatments.

So far, we have discussed the experimentally observed improvement in the flaw tolerance of A–An(C) material based on enhanced residual stresses affecting the frictional grain pullout. It should be noted that the bridging model[9,12] we have used here is based on highly simplistic bridged-interface geometry and considers only frictional bridging. In reality the crack–microstructure interactions are more complicated, and several other types of bridging mechanisms have been put forward.[10,11] Some recent in situ SEM studies of crack propagation in alumina,[10] in addition to confirming the existence of frictional bridges, have revealed that other processes such as geometrical interlocking, elastic bridging, and rotational bridging may also play a role. Nonetheless, consideration of the frictional grain-bridging mechanism has produced good correlation between theory and experiment. More importantly, the model based on frictional bridging allows us to predict how microstructural changes will affect the flaw tolerance behavior, enabling the tailoring of ceramic microstructures for optimum mechanical properties.

Table II. Bridging Parameters for Alumina–Anorthite (A–An) Materials

Material	T_0 (MPa·m$^{1/2}$)	μ	σ_R (MPa)	ε	SD in σ_M (MPa)
A–An(G)	2.3	0.9	250	0.07	15
A–An(C)	1.7	1.0	400	0.07	15

V. Summary

The results and finding of the above study can be summarized as follows:

(i) By fabricating LPS alumina using a tailored intergranular glass of anorthite composition, the glass can be crystallized to near-100% crystallinity (with appropriate heat treatments).

(ii) The crystallization of the intergranular anorthite glass resulted in a marked improvement in the flaw tolerance of alumina–anorthite, indicative of enhanced R- or T-curve behavior.

(iii) The frictional bridging model[9,12] fits the flaw tolerance data well and can be used to calculate theoretical T-curves for the materials studied.

Acknowledgments: The authors would like to thank S.J. Bennison and B.R. Lawn for many fruitful discussions and providing us with the computer programs used in the modeling aspect of this work.

References

[1] H. Hüber and W. Jillek, "Sub-Critical Crack Extension and Crack Resistance in Polycrystalline Alumina," *J. Mater. Sci.*, 12, 117–25 (1977).

[2] R. Knehans and R. Steinbrech, "Memory Effect of Crack Resistance During Slow Crack Growth in Notched Al_2O_3 Bend Specimens," *J. Mater. Sci. Lett.*, 1, 327–29 (1982).

[3] R. F. Cook, B. R. Lawn, and C. J. Fairbanks, "Microstructure–Strength Properties in Ceramics: I, Effect of Crack Size on Toughness," *J. Am. Ceram. Soc.*, 68 [11] 604–15 (1985).

[4] P. L. Swanson, C. J. Fairbanks, B. R. Lawn, Y.-W. Mai and B. J. Hockey, "Crack-Interface Grain Bridging as a Fracture Resistance Mechanism in Ceramics: I, Experimental Study on Alumina," *J. Am. Ceram. Soc.*, 70 [4] 279–89 (1987).

[5] Y.-W. Mai and B. R. Lawn, "Crack-Interface Grain Bridging as a Fracture Resistance Mechanism in Ceramics: *II*, Theoretical Fracture Mechanics Model," *J. Am. Ceram. Soc.*, **70** [4] 289–94 (1987).

[6] R. F. Cook, C. J. Fairbanks, B. R. Lawn and Y.-W. Mai, "Crack Resistance by Interfacial Bridging: Its role in determining Strength Characteristics," *J. Mater. Res.*, **2** [3] 345–56 (1987).

[7] S. J. Bennison, N. P. Padture, J. L. Runyan, and B. R. Lawn, "Flaw-Insensitive Ceramics," *Philos. Mag. Lett.*, **64** [4] 191–95 (1991).

[8] M. V. Swain, "*R*-Curve Behavior in a Polycrystalline Alumina Material," *J. Mater. Sci. Lett.*, **5**, 1313–15 (1986).

[9] S. J. Bennison and B. R. Lawn, "Role of Interfacial Grain-Bridging Sliding Friction in the Crack-Resistance and Strength Properties of Non-Transforming Ceramics," *Acta Metall.*, **37** [10] 2659–71 (1989).

[10] R. F. Cook, "'Segregation Effects in the Fracture of Brittle Materials: Ca–Al_2O_3," *Acta Metall. Mater.*, **38** [6] 1083–100 (1990).

[11] G. Vekinis, M. F. Ashby, and P. W. R. Beaumont, "*R*-Curve Behavior of Al_2O_3 Ceramics," *Acta Metall. Mater.*, **38** [6] 1151–62 (1990).

[12] P. Chantikul, S. J. Bennison, and B. R. Lawn, "Role of Grain Size in the Strength and *R*-Curve Properties of Alumina," *J. Am. Ceram. Soc.*, **73** [8] 2419–27 (1990).

[13] S. J. Bennison, H. M. Chan, and B. R. Lawn, "Effect of Heat Treatment on Crack-Resistance Curves in a Liquid-Phase-Sintered Alumina," *J. Am. Ceram. Soc.*, **72** [4] 677–79 (1988).

[14] N. P. Padture and H. M. Chan, "Influence of Grain Size and Degree of Crystallization of Intergranular Glassy Phase on the Mechanical Behavior of a Debased Alumina," *J. Mater. Sci.*, **29**, 2711–15 (1991).

[15] J. L. Runyan and S. J. Bennison, "Fabrication of Flaw Tolerant Aluminum Titanate-Reinforced Alumina," *J. Eur. Ceram. Soc.*, **7**, 93–97 (1991).

[16] N. P. Padture, S. J. Bennison, J. L. Runyan, J. Rödel, H. M. Chan, and B. R. Lawn, "Flaw-Tolerant Al_2O_3–Al_2TiO_5 Composites"; pp. 715–21 in Ceramic Transactions, Vol. 19, *Advanced Composite Materials.* Edited by M. D. Sacks. American Ceramic Society, Westerville, OH, 1991.

[17] N. P. Padture, "Crack Resistance and Strength Properties of Some Alumina-Based Ceramics with Tailored Microstructures"; Ph.D. Thesis. Lehigh University, Bethlehem PA, 1991.

[18] N. P. Padture, S. J. Bennison, and H. M. Chan, "Crack Resistance and Strength Properties of Alumina–Aluminum Titanate Composites with Tailored Microstructures," *J. Am. Ceram. Soc.* (in review).

[19] N. A. Travitzky, D. G. Brandon, and E. Y. Gutmanas, "Toughening of Commercial 85 wt% Al_2O_3 by Controlled Heat Treatments," *Mater. Sci. Eng.*, **71**, 65–70 (1985).

[20] Y. Yeshrun, Z. Rosenberg, D. G. Brandon, and N. A. Travitzky, "Effect of Heat Treatment on the Dynamic Response of Commercial 85 wt% Al_2O_3," *Mater. Sci. Eng.*, **71**, 71–75 (1985).

[21] W. A. Zdaniewski and H. P. Kirchner, "Toughening of a Sintered Alumina by Crystallization of the Grain-Boundary Phase," *Adv. Ceram. Mater.*, **1** [1] 99–103 (1986).

[22] H. Tomaszewski, "Effect of the Intergranular Phase Structure on the Thermomechanical Properties of Alumina Ceramics," *Ceram. Int.*, **14**, 93–99 (1988).

[23] C. A. Powell-Dogan and A. H. Heuer, "Microstructure of 96% Alumina Ceramics: III, Crystallization of High-Calcia Boundary Glasses," *J. Am. Ceram. Soc.*, **73** [12] 3684–91 (1990).

[24] D. A. Bonnell, T.-Y. Tien, and M. Rühle, "Controlled Crystallization of the Amorphous Phase in Silicon Nitride Ceramics," *J. Am. Ceram. Soc.*, **70** [7] 460–65 (1987).

[25] R. Raj and F. F. Lange, "Crystallization of Small Quantities of Glass (or a Liquid) Segregated in Grain Boundaries," *Acta Metall.*, **29**, 1993–2000 (1981).

[26] W. F. Cole, H. Sørum, and W. H. Taylor, "The Structure of Plagioclase Feldspars I," *Acta Crystallog.*, **4**, 20–29 (1951).

[27] N. P. Padture and H. M. Chan, "On the Constrained Crystallization of Synthetic Anorthite ($CaO \cdot Al_2O_3 \cdot 2SiO_2$)," *J. Mater. Res.*, **7** [1] 170–77 (1992).

[28] J. C. Wurst and J. A. Nelson, "Lineal Intercept Technique for Measuring Grain Size in Two-Phase Polycrystalline Ceramics," *J. Am. Ceram. Soc.*, **55** [2] 109 (1972).

[29] E. C. M. Pennings and W. Grellner, "Precise Nondestructive Determination of the Density of Porous Ceramics," *J. Am. Ceram. Soc.*, **72** [2] 1268–70 (1989).

[30] D. B. Marshall, "An Improved Biaxial Flexure Test for Ceramics," *Am. Ceram. Soc. Bull.*, **59** [5] 551–53 (1980).

[31] W. A. Kaysser, M. Sprissler, C. A. Handwerker, and J. E. Blendell, "Effect of Liquid Phase on the Morphology of Grain Growth in Alumina," *J. Am. Ceram. Soc.*, **70** [5] 339–43 (1987).

[32] B. R. Lawn, *Fracture of Brittle Solids.* Cambridge University Press, Cambridge, U.K., 1992 (in press). □

On the constrained crystallization of synthetic anorthite ($CaO \cdot Al_2O_3 \cdot 2SiO_2$)

Nitin P. Padture and Helen M. Chan
Department of Materials Science and Engineering, Lehigh University, Bethlehem, Pennsylvania 18015

(Received 11 March 1991; accepted 26 August 1991)

To determine the influence of volume constraint, the crystallization behavior of bulk anorthite glass was compared with that of anorthite glass situated at intergranular pockets in an alumina ceramic. Near-100% crystallization of the glass was obtained in both cases. Examination of the crystallized microstructures using SEM and TEM revealed several interesting features. The resulting microstructures, together with the very high degree of crystallization, are discussed with reference to a thermodynamic model for the constrained crystallization of glass.

I. INTRODUCTION

Over a period of the last 40 years or so, the development of glass-ceramics in which select glass compositions are fabricated in the glassy state and subsequently crystallized, has proven to be of great scientific and technological importance (for reviews see Refs. 1 and 2). More recently, interest has developed in the area of crystallization of glassy phases present as intergranular pockets within liquid-phase-sintered (LPS) ceramics.[3–10] In both these cases, the major goal has been to achieve very high degrees of crystallinity. As will be seen from the following, the importance of this topic lies in the fact that the degree of crystallinity can have a significant influence on the mechanical properties.

Silica-based oxides are used as sintering aids during the processing of many LPS ceramics; these oxides form a liquid at the sintering temperature, which upon cooling is retained as a glassy phase at the grain boundaries.[11] The volume percent of the residual glass may be significant, and can be as high as 30 vol. % in some commercial aluminas. The presence of such intergranular residual glass is known to degrade the high temperature creep resistance of LPS alumina[12] and silicon nitride.[13] However, crystallization of the intergranular glass (either during creep or through post-sintering heat-treatments) results in improved mechanical properties at elevated temperatures.[12,14–16] Unfortunately, in many glass-ceramic systems, complete crystallization of the glass cannot be achieved. One explanation for this behavior lies in the volume constraint of the surrounding grains.

It has been known for some time that the complete crystallization of a glassy phase is very difficult when it is constrained within intergranular pockets surrounded by crystalline grains. Note that such glassy intergranular pockets can arise during the final stages of crystallization of a bulk glass, as well as in LPS ceramics (as described earlier). Raj and Lange[17] have proposed a thermodynamical model in order to explain the lack of complete crystallization of constrained glass. Figure 1(a) shows a schematic illustration of an intergranular pocket, which has been approximated by a sphere surrounded by a rigid crystalline body [Fig. 1(b)]. The essence of the Raj–Lange model is as follows. Consider the growth of a crystal nucleus within an intergranular pocket; as the glass transforms into crystalline material, its volume decreases. Since the crystallizing phase is physically bonded to the surrounding glass, strain is generated in the glass, setting up hydrostatic tension. As the crystal grows, the magnitude of the strain energy increases, thus offsetting the corresponding decrease in chemical free energy (which is the driving force for crystal growth). At some critical crystal size, therefore, it is possible for a balance to occur between the opposing energy terms. At this point, the crystal ceases to grow, resulting in a partially crystallized intergranular pocket. It follows that the actual degree of crystallinity achieved depends on several parameters, the values of which are particular to the geometry and the system in question.

Perhaps surprisingly, there has been very little detailed work aimed at studying the influence of volume constraint on the crystallization behavior of glass. Isolated observations exist on constrained crystallization in commercial LPS aluminas; however, in these systems there is the added consideration that the composition of the intergranular glass is different from that of the crystallizing phase.[6–9,18] This lack of control over the composition of the intergranular glass further complicates the constrained-crystallization problem, invariably leading to incomplete crystallization in commercial materials.[6–9,18,19] A notable exception is in the case of silicon nitride ceramics, commonly referred to as SiAlON materials (solid-solutions), where 100% crystallization of the intergranular glass has been reported.[10] This has been attributed to the dissolution of the constituent oxides of the residual glass in the SiAlON constraining grains.[10]

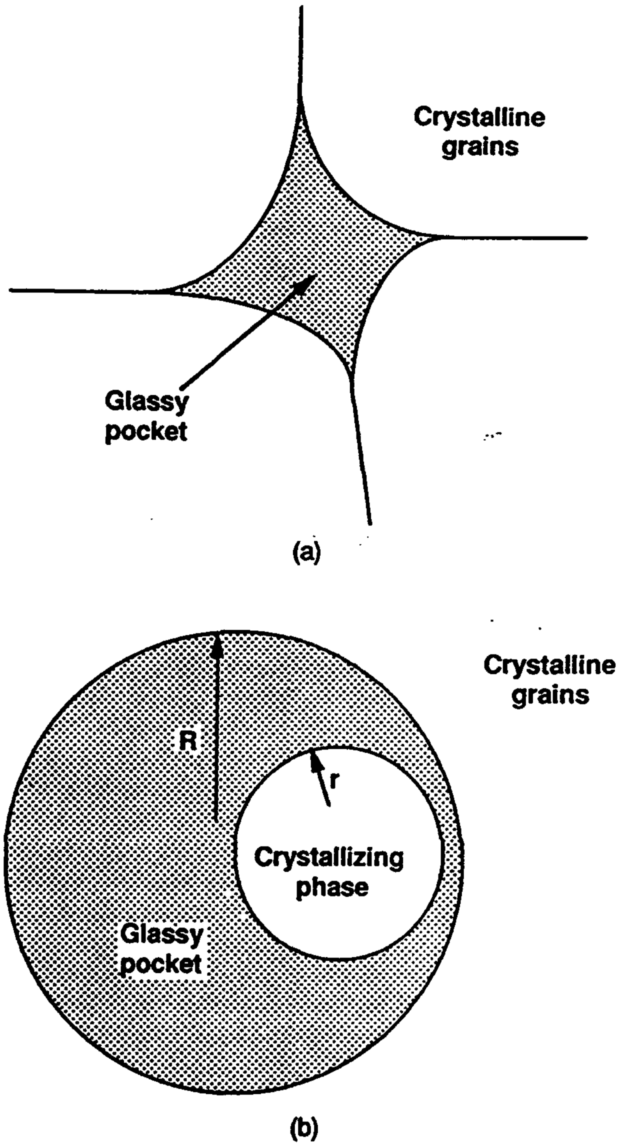

FIG. 1. Schematic illustrations of (a) an intergranular pocket containing glass surrounded by crystalline grains and (b) spherical representation of the above intergranular pocket. *R* represents the radius of the pocket and *r* represents the radius of the crystallizing phase. Reproduced with modifications from Ref. 17.

The purpose of the present study was to compare the crystallization behavior of anorthite ($CaO \cdot Al_2O_3 \cdot 2SiO_2$), a feldspar mineral, crystallized from the same composition glass present in two different physical situations, viz: (a) bulk glass and (b) glass constrained within intergranular pockets of LPS alumina. Anorthite was chosen for this study for the following reasons. Firstly, anorthite composition glass is relatively easy to form; also the glass-formation behavior, structure, and properties of anorthite glass have been documented by several researchers.[20,21] Anorthite has the additional advantage that its nucleation[22] and crystal growth[23,24] behavior from the bulk anorthite glass is relatively well understood. Finally, anorthite is of some practical significance in that it has been reported to be the major crystallizing phase in several commercial LPS aluminas.[8,9,18] Our aim in this paper, therefore, was to determine the crystallization behavior of anorthite glass in both bulk anorthite and alumina-anorthite, and to examine the results in the light of the Raj–Lange model.

II. EXPERIMENTAL

A. Materials processing

1. Bulk anorthite

Reagent grade (Fisher Scientific Company) $CaCO_3$, Al_2O_3, and SiO_2 were mixed in appropriate proportions and dry-blended for 12 h. This batch was then melted at 1600 °C for 24 h in a covered platinum crucible heated by an electrical resistance furnace. The resulting glass was then quenched, crushed, and remelted. (To ensure good chemical homogeneity, the preceding steps were repeated several times.) Next, the glass was cast into a steel mold and subsequently annealed at 800 °C for 1 h and cooled very slowly. This base glass will be referred to as specimen BULK-G (G refers to Glassy). (For a similar melting procedure of anorthite glass the deviation of the composition of the glass from the starting batch was reported to be less than 0.2 wt.% of any of the principal constituents.[23]) Crystallization of the bulk glass was carried out by heat-treating at 1200 °C for 30 min in a platinum enclosure (1200 °C corresponds to the temperature at which Klein and Uhlmann[23] reported a maximum in the crystallization rate). A short heat-treatment duration was chosen to avoid excessive grain growth and hence prevent severe microcracking of the crystallized specimen. This specimen will be referred to as specimen BULK-C (C refers to Crystalline).

2. Alumina-anorthite

Some of the above glass was crushed and ball-milled into a glass frit (<1.0 μm particle size as classified by sedimentation[25]). This glass frit was mixed with high-purity α-alumina powder (Sumitomo Chemical Company) in the volumetric proportion of anorthite glass frit: alumina, equal to 1:3. This mixture was then wet-ball-milled in methanol using zirconia ball-grinding media for 24 h. The resulting slurry was subsequently transferred to a teflon beaker where it was continuously stirred during drying and deagglomerated by crushing. A disk 10 mm in diameter and 2 mm in thickness was fabricated from this powder by uniaxial pressing at 50 MPa followed by wet-bag isostatic pressing at 350 MPa. The green disk was packed in loose alumina powder in a high purity alumina crucible and calcined at 800 °C for 12 h, followed by sintering at 1600 °C for 60 min. This sintered specimen will be referred to as INTER-G (since anorthite is in the form of an INTERgranular Glass). Note that because of the short sintering duration the composition of the intergranular glass is assumed to be unchanged from that of anorthite. A piece of the sintered specimen was heat-treated at 200 °C for 25 h in order to crystallize the intergranular glass. The relatively long crystallization heat-treatment used in this case was to try to overcome any kinetic effects. This specimen will be referred to as specimen INTER-C (C refers to Crystalline INTERgranular phase).

B. Materials characterization

Specimens BULK-C and INTER-C were subjected to x-ray powder diffraction analysis and the product of crystallization was confirmed to be anorthite (triclinic, space group $P\bar{1}$, at room temperature). The densities of all the specimens were measured using the Archimedes method with water as the immersing medium.[25] Sections of specimens BULK-C and INTER-C were polished to 1 μm grade using standard ceramographic techniques for microstructural observations in the scanning electron microscope (SEM). The microstructures of the specimens were revealed by thermal etching (BULK-C at 1300 °C for 30 min, and INTER-C at 1500 °C for 30 min). All SEM specimens were sputter-coated with Au–Pd to avoid charging in the microscope. Transmission electron microscopy (TEM) specimens were prepared from disks (diameter $\approx$3 mm, thickness $\approx$100 μm) cut ultrasonically from polished sections of BULK-C and INTER-C. The centers of the disks were dimpled to 20 μm, followed by ion-beam milling until perforation. Prior to examination in the TEM (Philips 400T at 120 keV, Philips 430 at 250 keV), specimens were coated with amorphous carbon.

III. RESULTS

Table I gives the nomenclatures, heat treatments, and densities for the materials fabricated. The theoretical densities of the specimens were calculated taking the density of anorthite glass to be 2.700 g/cm^3, and the theoretical densities of crystalline anorthite and α–alumina to be 2.763 g/cm^3 [27] and 3.987 g/cm^3, respectively.[28]

A. Bulk anorthite

Figure 2 shows the microstructure of the specimen BULK-C as seen in the SEM. The grain size distribution in this material was found to be very broad with grain diameters ranging from 0.5 μm to 25 μm. The most novel feature in this microstructure was the wavy and jagged nature of the grain boundaries. Consistent with this was the large amount of surface relief exhibited by the fracture surface of the BULK-C specimen (Fig. 3). TEM examination of BULK-C showed that the degree of crystallinity was close to 100%. Furthermore, it was observed that the anorthite grains were highly twinned (Fig. 4). It was also found that the twin density within a single grain increased with a decrease in the grain size. However, no attempt was made to establish a detailed quantitative relationship between twin density and grain size in this material.

Figure 5 shows a high resolution TEM (HRTEM) image of (010) twin boundaries (indicated by the arrows) in anorthite taken from specimen BULK-C. These boundaries were confirmed to be twin boundaries by optical (LASER) diffraction. No evidence of any imperfections along the twin boundaries was observed. The inset in Fig. 5 shows the corresponding selected area electron diffraction pattern (SAEDP) ([001] beam direction); spot splitting (indicated by the arrow) due to the numerous twin planes within the selected area aperture is clearly visible.

B. Alumina-anorthite

In the alumina-anorthite specimen INTER-C the average grain size of the alumina was estimated to be $\approx$5 μm, whereas the average size of the intergranular pockets was $\approx$1 μm. An SEM micrograph depicting the microstructure of specimen INTER-C is given in Fig. 6. An anorthite grain (which was identified by the presence of strong Ca and Si peaks in the x-ray energy dispersive spectrum) is shown situated at an alumina multi-grain junction. The corresponding TEM image of

TABLE I. Heat-treatments and properties of the anorthite and alumina-anorthite materials investigated.

Specimen	Composition and heat-treatments	Measured densities g/cm^3	Theoretical densities g/cm^3
BULK-G	Anorthite composition base-glass	2.700[a]	...
BULK-C	Crystalline anorthite crystallized at 1200 °C for 0.5 h	2.730	2.763
INTER-G	Alumina with 25 vol.% anorthite glass as the intergranular phase, as-fired at 1600 °C for 1 h	3.385	3.664
INTER-C	Alumina with crystalline anorthite as the intergranular phase, crystallized at 1200 °C for 25 h	3.387	3.680

[a] A value of 2.704 g/cm^3 has been reported in the literature for the density of anorthite glass.[26]

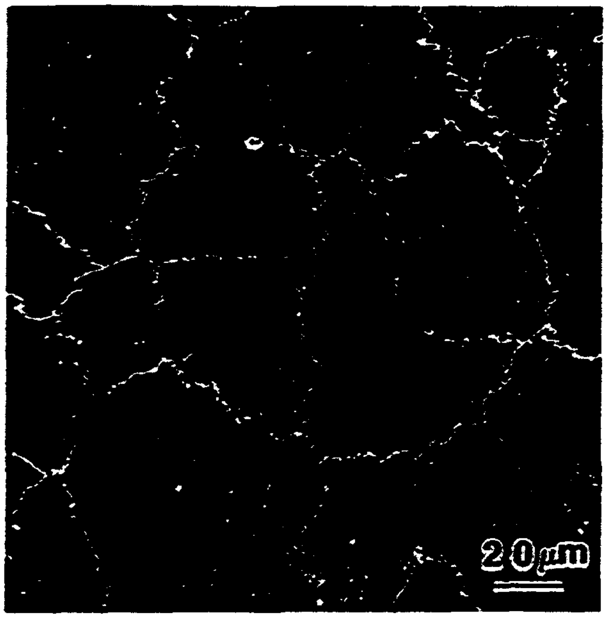

FIG. 2. SEM secondary electron image of a polished and etched section of anorthite (specimen BULK-C).

an intergranular pocket of crystalline anorthite is shown in Fig. 7. The highly twinned nature of anorthite and the near-100% crystallinity are clearly evident from this micrograph. The twinned phase was identified to be anorthite by SAEDP and x-ray energy dispersive spectroscopy (XEDS).

FIG. 3. SEM secondary electron image of the fracture surface of anorthite (specimen BULK-C).

FIG. 4. TEM bright-field image of anorthite (specimen BULK-C). The arrows indicate the wavy nature of the grain boundaries.

IV. DISCUSSION

Grain boundary waviness is clearly evident in the SEM micrograph of bulk crystalline anorthite (Fig. 2). The distribution of the microstructural scale of the waviness (facet length) is seen to be wide, ranging from several nm (Fig. 4) to several μm (Fig. 2). Such waviness is believed to be due to the intersection of the numerous twins within each grain with the grain boundaries. The wide distribution of the scale of the waviness is consistent with the variation in the width of the twin bands. It is postulated that the existence of such wavy grain boundaries may be partially responsible for the excellent high temperature hardness behavior of anorthite.[9]

The observation of extensive twinning in anorthite is consistent with the results of previous workers. Anorthite is known to twin readily during crystal growth and/or mechanical deformation.[29] Twinning in anorthite follows the albite twinning law in which the twin operation is given by a reflection across the (010) (twin) plane.[29] Confirmation that the twin plane in anorthite is indeed the (010) is clearly shown in Fig. 7. The aforementioned twinning operation is equivalent to rotation of 180° about

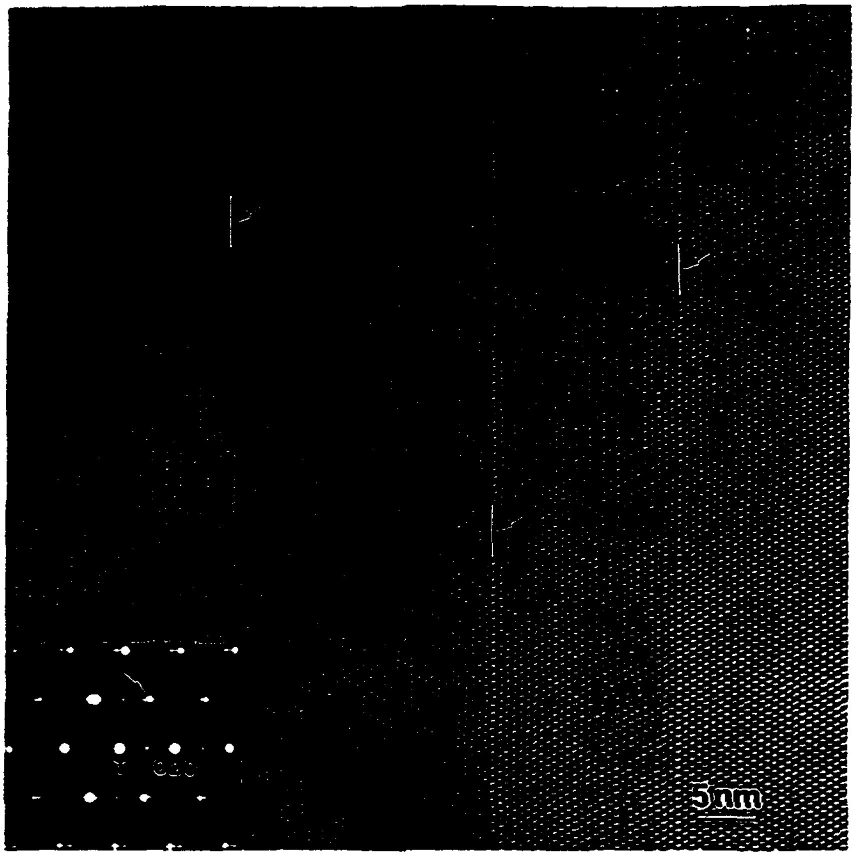

FIG. 5. HRTEM image of (010) twin boundaries in anorthite (specimen BULK-C) indicated by arrows. Inset: corresponding SAEDP ([001] beam direction); arrows indicate streaking due to twins.

b^*, the normal to (010). It is perhaps worth mentioning that in anorthite, the angle, ϕ, between b and b^* is equal to 3.7°, hence the deviation in crystallographic directions across the twin boundary is relatively small.[29]

As mentioned earlier, near-100% crystallinity occurs in specimens BULK-C and INTER-C. (It should be noted that we refer to degree of crystallization as "near-100%", since very thin glassy films may be present at the grain boundaries.) Such high degrees of crystallinity are quite uncommon in glass-ceramics due to the strain energy considerations embodied in the Raj–Lange model mentioned in Sec. I. For an in-depth analysis of the problem in question, the reader is referred to the original paper by Raj and Lange.[17] Here, our aim is simply to apply the Raj–Lange model to the problem of anorthite crystallizing from severely constrained glass in a LPS alumina. The following assumptions are made in this analysis: (a) the intergranular pocket is spherical, (b) nucleation of the crystallizing phase occurs homogeneously, (c) the constraining crystalline grains are rigid and chemically inert, (d) the crystallizing phase is also rigid, and (e) the compositions of the glass and the crystallizing phase are identical. The expression derived by Raj and Lange[17] for the normalized free energy change, Δg, during constrained crystallization is as follows:

$$\Delta g = a\rho^{15} + b\rho^{12} - \rho^3 + 3/2\rho_0\rho^2 \qquad (1)$$

where a, b, ρ, and ρ_0 are nondimensional parameters. After substituting suitable values for the parameters pertinent to the alumina-anorthite system, we can arrive at the following expression for g (the details of the calculations entailed in this analysis are deferred to the Appendix):

$$\Delta g = 0.221\rho^{15} + 0.083\rho^{12} - \rho^3 + 0.0075\rho^2 \qquad (2)$$

Figure 8 plots Δg as a function of ρ, where $\rho = r/R$. As seen from Fig. 1(b), ρ is a measure of the crystal size relative to the pocket size. It can be seen that the minimum in this curve occurs at $\rho = 0.97$. The prediction, therefore, is that the crystallizing phase will grow to 97% of the pocket size. This compares very favorably with the experimental observations of near-100% crystallinity, especially given the simplifying assumptions made in the analysis and the possible errors

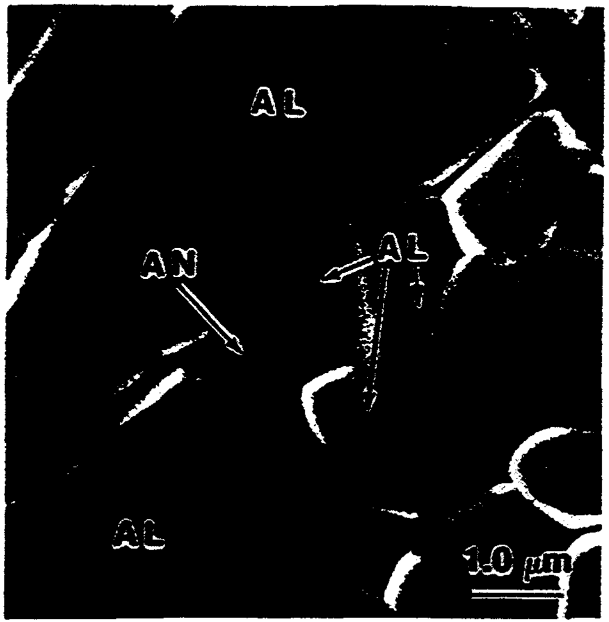

FIG. 6. SEM secondary electron image of a polished and etched section of LPS alumina containing anorthite (specimen INTER-C). AL represents alumina and AN represents anorthite.

in the values of the physical parameters. It should be emphasized, however, that prediction of such a high degree of crystallinity is very specific to the anorthite system. This is primarily because the densities of glassy and crystalline anorthite do not differ to a great extent, rendering the value of δV to be very small ($\delta V = 0.023$). As indicated by the dashed lines in Fig. 8, the $\Delta g - \rho$ function appears to be quite sensitive to δV; thus minima in the dashed curves for $\delta V = 0.05$ and 0.10 occur at 0.85 and 0.74, respectively. This comparison reinforces the argument that a small δV value plays a significant role in the high degree of crystallinity in anorthite.

FIG. 7. TEM bright-field image of anorthite within LPS alumina (specimen INTER-C). AL represents alumina and AN represents anorthite.

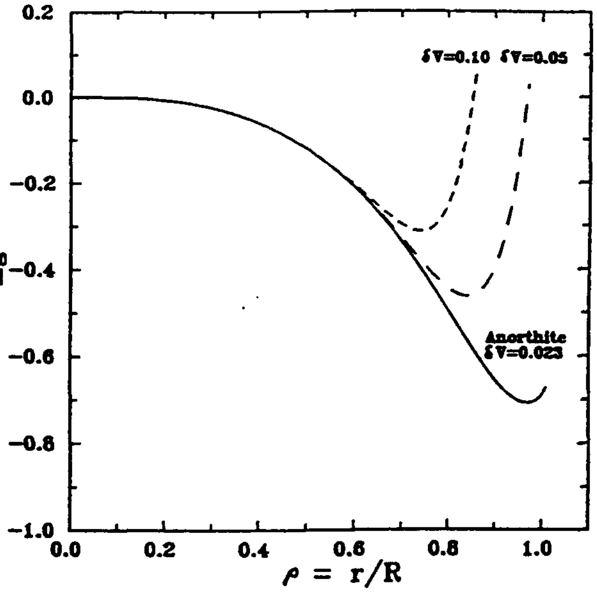

FIG. 8. A plot of Δg as a function of ρ, using Eq. (2) for different values of δV.

Some other factors, again specific to the anorthite system, may also be contributing to the high degree of crystallinity observed. Firstly, in violation of one of the assumptions of the Raj–Lange model, the crystallizing phase anorthite is not perfectly rigid. As pointed out earlier, profuse twinning has been observed in anorthite in both specimens BULK-C and INTER-C. Although it is not possible to distinguish between deformation twins and growth twins purely by observation, it is reasonable to assume that deformation twinning does occur. This would partially relieve the elastic strain energy and hence enhance the degree of crystallization. Next, let us consider the assumption that the crystalline matrix surrounding the intergranular pocket is completely rigid. Clarke[30] has discussed the existence of very thin intergranular glassy films in ceramics which may be thermodynamically stable. If such films were to exist in the alumina-anorthite, it is plausible that they would facilitate creep of matrix grains, thus allowing accommodation of the volume change during crystallization. Such accommodation would be expected to lead to an increase in density after crystallization. An attempt was made to correlate the measured densities of INTER-G

INTER-C with their respective theoretical densities (see Table I). However, due to the very small difference in the densities of glassy and crystalline anorthite, and the large fraction of porosity in the bulk alumina specimen, the results were inconclusive.

Finally, we wish to emphasize that achieving a high degree of crystallinity in glass-ceramics and LPS ceramics is of great technological value in terms of their improved physical properties. Our study of the anorthite system has clearly shown that near-100% crystallinity can be achieved in both bulk anorthite and alumina-anorthite. Further, the applicability of existing models for constrained crystallization to real systems has been demonstrated.

V. CONCLUSIONS

It can be concluded that near-100% crystallinity can be achieved when anorthite is crystallized from the same composition glass in (a) bulk form and (b) situated in an intergranular pocket constrained by four or more alumina grains in a LPS alumina. Such a high degree of crystallinity can be attributed to the following reasons: (i) the composition of the glass was the same as the crystallizing phase and (ii) the density of crystalline anorthite is very close to that of glassy anorthite. Other reasons that also possibly contributed are strain energy relief due to twinning of anorthite, and creep of the constraining matrix (anorthite grains in BULK-C and alumina grains in INTER-C) at the crystallization temperature.

ACKNOWLEDGMENTS

The authors would like to thank V. P. Dravid for his help with the HRTEM work and A. Owens for his help with the SEM work. Funding for this work was provided by the United States Air Force Office of Scientific Research and Coors Ceramics Company.

REFERENCES

1. P. W. McMillan, *Glass-Ceramics* (Academic Press, London, 1979).
2. Z. Strnad, *Glass Science and Technology (Glass-Ceramic Materials*, Vol. 8, Elsevier, New York, 1986).
3. N. A. Travitzky, D. G. Brandon, and E. Y. Gutmanas, Mater. Sci. Eng. 71, 65 (1985).
4. H. Tomaszewski, Ceram. Int. 14, 93 (1988).
5. W. A. Zdaniewski and H. P. Kirchner, Adv. Ceram. Mater. 1, 99 (1986).
6. S. J. Bennison, H. M. Chan, and B. R. Lawn, J. Am. Ceram. Soc. 72, 677 (1989).
7. C. A. Powell-Doğan and A. H. Heuer, J. Am. Ceram. Soc. 73, 3677 (1990).
8. C. A. Powell-Doğan and A. H. Heuer, J. Am. Ceram. Soc. 73, 3684 (1990).
9. N. P. Padture and H. M. Chan, J. Mater. Sci. 26, 2711 (1991).
10. D. A. Bonnell, T-Y. Tien, and M. Rühle, J. Am. Ceram. Soc. 70, 460 (1987).
11. W. D. Kingery, H. K. Bowen, and D. R. Uhlmann, *Introduction to Ceramics* (John Wiley & Sons, New York, 1976).
12. S. M. Wiederhorn, B. J. Hockey, and R. F. Krause, Jr., *Ceramic Microstructures '86*, edited by J. Pask and A. G. Evans (Plenum Press, New York, 1988), p. 795.
13. F. F. Lange, J. Am. Ceram. Soc. 61, 53 (1978).
14. R. A. Page and K. S. Chan, J. Mater. Sci. Lett. 8, 938 (1989).
15. A. Tsuge, K. Nashida, and M. Komatsu, J. Am. Ceram. Soc. 67, 323 (1984).
16. D. S. Wilkinson, J. Am. Ceram. Soc. 71, 562 (1988).
17. R. Raj and F. F. Lange, Acta Metall. 29, 1993 (1981).
18. Y. Yeshurun, Z. Rosenberg, N. A. Travitzky, and D. G. Brandon, Mater. Sci. Eng. 71, 71 (1985).
19. C. A. Powell-Doğan and A. H. Heuer, J. Am. Ceram. Soc. 73, 3684 (1990).
20. M. Cukierman and D. R. Uhlmann, J. Geophys. Res. 78, 4920 (1973).
21. M. Yamane and M. Okuyama, J. Non-Cryst. Solids 52, 217 (1982).
22. D. Cranmer, R. Salomaa, H. Yinnon, and D. R. Uhlmann, J. Non-Cryst. Solids 45, 127 (1981).
23. L. Klein and D. R. Uhlmann, J. Geophys. Res. 79, 4869 (1974).
24. M. S. Y. Bhatty, J. A. Gard, and F. P. Glasser, Miner. Mag. 37, 780 (1970).
25. J. S. Reed, *Introduction to Principles of Ceramics Processing* (John Wiley & Sons, New York, 1988).
26. N. Bansal and R. H. Doremus, *Handbook of Glass Properties* (Academic Press, Orlando, FL, 1986).
27. W. F. Cole, H. Sørum, and W. H. Taylor, Acta Cryst. 4, 20 (1951).
28. National Bureau of Standards Circular 3, 1 (1959).
29. J. V. Smith and W. L. Brown, *Feldspar Minerals* (Springer-Verlag, Berlin, 1988), Vol. 1.
30. D. R. Clarke, J. Am. Ceram. Soc. 70, 15 (1987).
31. D. Turnbull, *Solid State Physics* (Academic Press, New York, 1956), Vol. 3.
32. J. Hoffman, J. Chem. Phys. 29, 1192 (1958).

APPENDIX

The expression derived by Raj and Lange for the normalized free energy change during constrained crystallization is given by[17]:

$$\Delta g = a\rho^{15} + b\rho^{12} - \rho^3 + 3/2\rho_0\rho^2 \qquad \text{(A1)}$$

The constituent terms are defined as follows[17]:
(1) ρ is a measure of the crystal size relative to the pocket size [see Fig. 1(b)] and is given by:

$$\rho = r/R \qquad \text{(A2)}$$

(2) ρ_0 is related to the critical radius of the crystal (r_0) by:

$$\rho_0 = r_0/R \qquad \text{(A3)}$$

Assuming homogeneous nucleation, r_0 is given by:

$$r_0 = 2\gamma/\Delta G_v \qquad \text{(A4)}$$

where γ is the interfacial energy between the crystal and the glass, and ΔG_v is the decrease in the free energy per unit volume of the crystallized glass.[31]

(3) a is a measure of the strain energy per unit volume in the crystallizing phase relative to the chemical free energy during the transformation, and is given by:

$$a = \delta V^2 K_c / 2\Delta G_v \qquad \text{(A5)}$$

where δV is the change in the volume during transformation per unit volume of the crystal and K_c is the bulk modulus of the crystallizing phase.

(4) b is a measure of the strain energy per unit volume in the glass phase relative to the chemical free energy during the transformation, and is given by:

$$b = \delta V^2 K_g / 2\Delta G_v \qquad \text{(A6)}$$

where K_g is the bulk modulus of the glass.

By substituting reasonable values for the aforementioned variables, we may now obtain $\Delta g(\rho)$. The value of ΔG_v can be estimated using the following relation:

$$\Delta G_v = \Delta H_f (\Delta T \cdot T / T_m^2) \qquad \text{(A7)}$$

where ΔH_f is the heat of fusion per unit volume of the crystallizing phase, T is the crystallization temperature, T_m is the equilibrium melting temperature of the crystallizing phase, and ΔT is the undercooling $(T_m - T)$.[32] Taking $T_m = 1826$ K,[29] $T = 1473$ K ($\Delta T = 353$ K) and $\Delta H_f = 1.04 \times 10^9$ J/m^3,[23] we obtain $\Delta G_v = 1.62 \times 10^8$ J/m^3. Using this value of ΔG_v and $\gamma = 0.19$ J/m^2 [22] we obtain $r_0 = 2.3 \times 10^{-9}$ m (23 Å) [Eq. (A4)]. Taking $R = 0.5 \times 10^{-6}$ m (≈ 1 μm pocket size) we may now obtain $\rho_0 = 0.005$ [Eq. (A3)]. From values for the density of anorthite composition glass and the theoretical density of crystalline anorthite, we obtain $\delta V = 0.023$. Finally, taking values from the literature for the bulk moduli ($K_c = 139$ GPa,[29] $K_g = 52$ GPa[26]) and substituting in Eqs. (A5) and (A6), respectively, we obtain $a = 0.221$ and $b = 0.083$. Equation (A1) can now be rewritten as:

$$\Delta g = 0.221\rho^{15} + 0.083\rho^{12} - \rho^3 + 0.0075\rho^2 \qquad \text{(A8)}$$

Reprinted from the Journal of the American Ceramic Society, Vol. 75, No. 11, November 1992
Copyright © 1992 by The American Ceramic Society

journal

J. Am. Ceram. Soc. 75[11] 3049–57 (1992)

Objective Evaluation of Short-Crack Toughness Curves Using Indentation Flaws: Case Study on Alumina-Based Ceramics

Linda M. Braun,*,† Stephen J. Bennison,*,‡ and Brian R. Lawn*

Materials Science and Engineering Laboratory, National Institute of Standards and Technology, Gaithersburg, Maryland 20899

An objective methodology is developed for evaluating toughness curves (*T*-curves) of ceramics using indentation flaws. Two experimental routes are considered: (i) conventional measurement of inert strength as a function of indentation load; (ii) in situ measurement of crack size as a function of applied stress. Central to the procedure is a proper calibration of the indentation coefficients that determine the *K*-field of indentation cracks in combined residual-contact and applied-stress loading, using data on an appropriate base material with single-valued toughness. Tests on a fine-grain alumina serve to demonstrate the approach. A key constraint in the coefficient evaluation is an observed satisfaction of the classical indentation strength–(load)$^{-1/3}$ relation for such materials, implying an essential geometrical similarity in the crack configurations at failure. *T*-curves for any alumina-based ceramic *without* single-valued toughness can then be generated objectively from inert-strength or in situ crack-size data. The methodology thereby circumvents the need for any preconceived model of toughening, or for any prescribed analytical representation of the *T*-curve function. Data on coarse-grained aluminas and alumina-matrix material with aluminum titanate second-phase particles are used in an illustrative case study.

I. Introduction

TOUGHNESS curves or resistance curves (*T*-curves, K_R-curves, *R*-curves), which describe a functional dependence of toughness on crack size, are now known to have a profound influence on the mechanical properties of ceramics.[1-3] Traditional *T*-curve measurements are made with *long* cracks in notched specimens. However, some of the most important mechanical properties, notably strength, are determined in the domain of *short* cracks, i.e., cracks on a scale comparable with that of the microstructure. As intimated in measurements of crack extension from natural[4,5] and controlled[6,7] surface flaws in several ceramics, the critical short-crack region of interest lies below the lower limits of valid extrapolation from long-crack data.

It is in this context that radial cracks from Vickers indentations have been widely used as a means for evaluating toughness properties in the short-crack region. In the most practical form of the method, inert strength is measured as a function of indentation load.[8,9] Materials with single-valued toughness are characterized by a classical indentation strength–(load)$^{-1/3}$ relation;[8] the existence of a *T*-curve may then be inferred by departures from this relation. Specifically, as the *T*-curve becomes more pronounced the strength tends to a weaker dependence on indentation load, and thence on initial flaw size.[10,11] This quality of *flaw tolerance* is attributed to stabilization of crack growth from a shielding *K*-field that increases with crack extension[1] (or, alternatively, an *anti*-shielding *K*-field that *decreases* with extension[1,10]), and is a desirable end result in structural design.

A second form of the indentation method entails piecewise measurement of radial crack extension under monotonically increasing applied loading, in much the same way as indicated above for natural flaws. This approach derives from early work on materials with single-valued toughness, notably soda–lime glass,[8] aimed at quantifying the stabilizing role of residual contact stresses in the fracture mechanics. With the indentation *K*-field thus calibrated one should, in principle, be able to evaluate any *K*-field increment (or decrement) due to microstructural shielding. This approach has recently been used to generate *T*-curves for certain alumina,[6] inhomogeneous (elongated grain) silicon nitride,[13] and zirconia ceramics.[14]

The indentation technique has not been without detractors. The most critical suggest that the presumed flaw tolerance in the measured strength–load response is not due to an intrinsic *T*-curve at all, but is an artifact of the technique. A common argument is that the tendency for the strength to indentation-size independence simply denotes a natural flaw "cutoff" at low loads. This is despite meticulous attempts to confirm that the failures occur from indentation sites.[11] Another school points out that artifacts in both indentation–strength and applied-stress/crack-extension data can arise from crack-size variations in the two coefficients that determine the combined applied-stress plus residual-contact indentation *K*-field.[12,13] Improper specification of those coefficients can result in *apparent* *T*-curves in materials which are unquestionably single-valued in toughness, including glass.[12] Yet other critics acknowledge the association of indentation–strength data with an underlying *T*-curve, but question the curve-fitting procedures used in quantitative deconvolutions of the latter from the former. Analyses based on specific microstructural shielding models,[10,11,15,16] regardless of how well they might be substantiated by physical observation,[17,18] typically require the specification of several adjustable microstructural parameters, some of which can be determined only from elaborate data fits. Slight variations in these adjustable parameters can significantly alter the characteristics of the deconvoluted *T*-curve. Conversely, procedures that represent the *T*-curve by simplistic empirical functions[19-21] are open to objection for inconsistencies with physical reality. All such criticisms must be answered if indentation–strength is to be retained as a viable means of *T*-curve evaluation.

In light of this background, we endeavor here to establish a sound scheme for evaluating *T*-curves of ceramics *objectively* from indentation–strength and/or applied-stress/crack-extension data. We illustrate with results from previous indentation–strength studies on alumina-based ceramics, one on monophase aluminas covering a wide range of grain sizes[22] and the other on an alumina-matrix composite with aluminum titanate second-phase particles.[23] In the first of these earlier studies a detailed

K. T. Faber—contributing editor

Manuscript No. 196065. Received January 8, 1992; approved June 24, 1992.
Supported by the U.S. Air Force Office of Scientific Research, U.S. Office of Naval Research, and E. I. du Pont de Nemours and Co., Inc.

*Member, American Ceramic Society.

†Guest Scientist from the Department of Materials Science and Engineering, Lehigh University, Bethlehem, PA 18015.

‡Now at E. I. du Pont de Nemours and Co., Wilmington, DE 19898.

fracture-mechanics grain–grain bridging model[16] was used to deconvolute the *T*-curves. Those *T*-curves were found to deviate negligibly from the baseline toughness of alumina at the finest grain size (2.5 μm), but became progressively more pronounced with increasing coarsening. Here, we devise a much simpler methodology for generating the *T*-curves, without any need for specific models of the underlying shielding mechanism or for parametric deconvolutions. Our evaluation centers around an appropriate determination of the two coefficients that quantify the indentation *K*-field. We ensure self-consistency in this determination by noting that the ideal indentation strength–(load)$^{-1/3}$ relation is well satisfied for the finest grain-size (control) alumina, and use this relation to constrain the two coefficients. An integral part of our strategy is the use of in situ observations of crack growth during stressing to failure, to obtain essential information on the indentation-crack dimensions. These in situ observations reinforce our previous contention that failure does indeed occur from indentation sites, enable explicit calibration of the indentation coefficients, and (in favorable cases) provide an alternative route to evaluation of the *T*-curves.

II. The Problem of Analytically Deconvoluting *T*-Curves from Indentation Data

Let us consider how one might objectively determine the *T*-curve from indentation–strength and applied-stress/crack-extension data. Begin with the general relation for the "crack-tip" *K*-field as a function of radial crack size *c* relative to the contact center for equilibrium indentation cracks with residual deformation fields in a material with *T*-curve behavior:[1,2,11,16]

$$K_*(c) = K_A + K_R + K_\mu$$
$$= \psi\sigma_A c^{1/2} + \chi P/c^{3/2} + K_\mu(c) = T_0 \qquad (1a)$$

K_A *is the stress-intensity factor associated with the applied* stress σ_A, K_R with the residual contact field at indentation load *P*, and K_μ with microstructural shielding (the source of the *T*-curve); ψ *is a geometrical coefficent that characterizes the* pennylike crack configuration;[2] $\chi \propto (E/H)^{1/2}$ is a coefficient, ideally independent of *c*, that characterizes the intensity of the residual field in terms of indentation hardness *H* and Young's modulus *E*;[24,25] T_0 is a baseline toughness, *monocrystal* for transgranular fracture and *grain boundary* for intergranular fracture. Equation (1*a*) may be normalized to

$$K_*/T_0 = (\psi/T_0)\sigma_A c^{1/2} + (\chi/T_0)P/c^{3/2} + K_\mu/T_0 = 1 \qquad (1b)$$

For materials with no *T*-curve, $K_\mu = 0$. For materials *with* *T*-curve, $K_\mu \neq 0$, but in this study we make absolutely no statement as to what explicit functional form $K_\mu(c)$ might take. *Equation (1a) may be transposed into a form appropriate to a* "global" *K*-field

$$K'_A(c) = \psi\sigma_A c^{1/2} + \chi P/c^{3/2}$$
$$= T_0 - K_\mu(c) = T_0 + T_\mu(c) = T(c) \qquad (2)$$

where $K'_A(c)$ is an effective applied stress-intensity factor, $T_\mu(c) = -K_\mu(c)$ is a shielding toughness term, and $T(c)$ defines the *T*-curve for the material.[1,2]

Equation (2) may be solved for the applied stress as a function of equilibrium crack size:

$$\sigma_A(c) = (1/\psi c^{1/2})[T(c) - \chi P/c^{3/2}] \qquad (3)$$

Generally, because of the stabilizing influence of $K_R(c)$ and $K_\mu(c)$ in Eq. (1), the newly formed indentation cracks will extend stably prior to crack failure, so the critical failure configuration does *not* identify with spontaneous propagation from the initial crack size, c_0.[1,8] The inert strength identifies with the critical configuration $\sigma_A = \sigma_M$, $c = c_M > c_0$, at which $\sigma_A(c)$ passes through a dominant maximum, corresponding to a "tangency condition"

$$dK'_A(c)/dc = dT(c)/dc \qquad (4)$$

in Eq. (2).[1,2]

Since the explicit mathematical *form* of $T(c)$ is not specified a priori here, analytical solutions of the strength function $\sigma_M(P)$ for materials with *T*-curves are not generally obtainable from Eq. (3). (In fact, analytical solutions are not guaranteed even when the form of $T(c)$ *is* specifiable.) On the other hand, if the coefficients ψ and χ can be properly calibrated from $\sigma_A(c)$ data on a control material with single-valued toughness, the *T*-curve should, in principle, be calculable directly from Eq. (2).

III. Experimental Procedure

The basis of the experimental *T*-curve determinations is the analysis of inert strength data for specimens with indentation flaws, in combination with in situ measurements of the flaw evolution to failure. Here we use strength data from earlier studies,[22,23] but include a brief description of the test procedure for completeness. A description of the in situ crack-extension measurements is given in more detail.

(1) Materials

Alumina was chosen as a base for this study because of its extensive adoption as a model polycrystalline material in several previous indentation studies, as well as its common use as a practical ceramic. The starting material was a high-purity (500 at. ppm Mg/Al) alumina with equiaxed grains of mean grain size 2.5 μm.[22] At this fine grain size, alumina has a negligible *T*-curve,[22] and so serves as a convenient *control* for the materials described below. Specimens were machined into disks of thickness 3 mm.

Aluminas with significant *T*-curves were produced by heat-treating batches of the starting material to produce microstructures with enlarged grain sizes.[22] Here we consider grain sizes 15, 35, and 80 μm.

An alumina-matrix composite with especially pronounced flaw tolerance[23] was also investigated. This composite contains 20 vol% aluminum titanate as a second phase. Preparation was by sintering, via a conventional powder processing route.[26,27] The mean size of the matrix alumina and aluminum titanate grains was 6 μm, but with occasional agglomerates of the latter of 5 to 10 grains.[23] Specimens of this material were cut into disks 5 mm thick.

All specimens were polished on one side to remove spurious machining stresses, and to observe ensuing indentation cracks with minimum surface obstruction.

(2) Indentation–Strength Tests

Vickers indentations at specified loads were made in the center of each polished surface. The disks were broken in biaxial flexure, indentations centered on the tensile side, with 6-mm-diameter flat loading on three-ball support.[28] These tests were conducted with a drop of oil on the indentation site and broken in fast loading (within 10 ms), to maintain "inert" conditions. Stresses at the indentation site were calculated from the applied load using thin plate theory.[28] Post-mortem examinations were made of all polished specimens to confirm failure initiation from the indentation sites.

Some comparative tests were made on specimens with annealed indentations, to remove the crack-stabilizing influence of the contact field.[8]

(3) In Situ Observations of Crack Extension

In situ observations of indentation-crack growth to failure were made using a custom-built biaxial flexure fixture for placement on an optical microscope or in an SEM. A schematic is shown in Fig. 1. A piezoelectric translator was used to apply a load to the biaxial flexure specimen. Stable growth of the surface radial cracks could then be followed directly as a function of monotonically increasing load, measured using a load cell. Quantitative tests were carried out exclusively on the optical

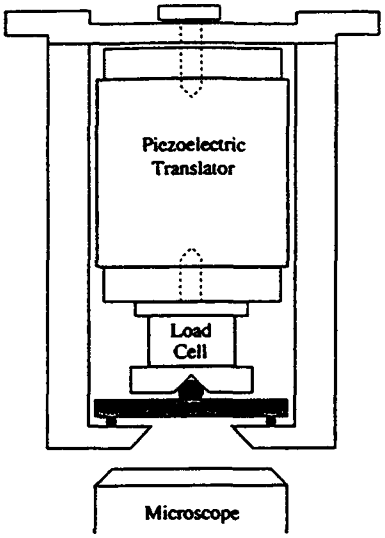

Fig. 1. Schematic of fixture for viewing indentation crack growth in situ during stressing to failure. Load is delivered to a biaxial flexure specimen by a piezoelectric translator and is measured by a load cell. The fixture can be located on the stage of an optical microscope or in an SEM.

microscope. Indentation sites were again covered with oil to reduce the influence of moisture, and covered with a glass cover slide to facilitate microscopic observation. In our tests a typical run to failure took ≈1–2 h. Crack sizes were measured at each stage of loading from video recordings of the crack evolution after failure was complete. Subsidiary observations were made in the SEM on the alumina-matrix composite to examine the crack-face morphology.

The immediate postindentation crack patterns in the fine-grain control alumina and the alumina-matrix composite were observed to be "well-developed," i.e., four radial arms extending symmetrically from the indentation corners, with each arm of length more than twice the Vickers impression half-diagonal.[29] Such was not the case for the coarsest aluminas, where the cracks deflected abruptly along local crack grain boundary facets in a more irregular fashion. In situ observations on the coarse aluminas were accordingly confined to semiquantitative estimates of the net crack extension to failure.[17]

(4) *Hardness and Modulus*

The indentation hardness (load/projected contact area) was evaluated directly from the impression diagonals of the Vickers indentations for each material. Young's modulus for the alumina was taken from a previous estimate,[29] and for the composite material determined by an independent acoustic technique.[30]

IV. Results and Analysis

(1) *Indentation–Strength Data*

Figure 2 is a plot of inert strength vs indentation load results for our as-indented 2.5-μm-grain-size control alumina, from an earlier study.[22] Figure 3 is a plot of corresponding results for 15, 35, and 80 μm for the coarse-grain test aluminas, from the same data source. All data points with error bars are means and standard deviations (logarithmic coordinates) for a minimum of four specimens at each prescribed load. These points exclusively represent confirmed failures from indentation sites. Any breaks *away* from indentations are included in a data pool for natural flaws, indicated at left by the shaded regions. Included in the plot for the control material in Fig. 2 are some additional individual results from the in situ runs (see Section IV(2)). The solid line in Fig. 2 is a least-squares data fit, in accordance with prediction for a material with single-valued toughness (Section IV(2)). This last fit is reproduced in Fig. 3 (dashed lines) as a reference baseline for evaluating flaw tolerance in the coarser aluminas.

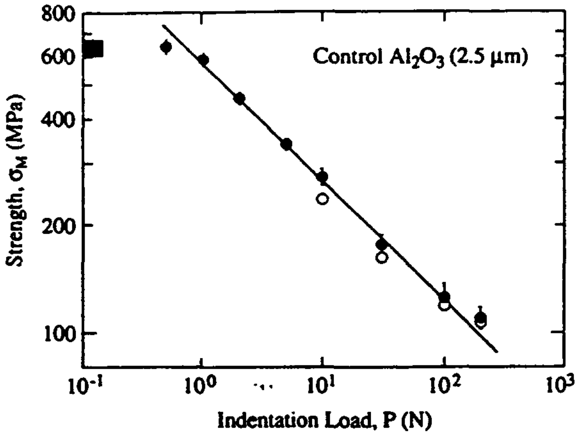

Fig. 2. Plot of $\sigma_M(P)$ inert strength data for control alumina, grain size 2.5 μm, with Vickers indentation flaws (closed symbols). Data from Ref. 22. Additional results from current individual in situ runs (open symbols). Solid straight-line fit of (slope)$^{-1/3}$ (logarithmic coordinates) allows determination of $(T_0/\psi)(T_0/\chi)^{1/3}$ in Eq. (6*b*) for alumina.

Figure 4 is a plot of corresponding inert strength vs indentation load results for the as-indented alumina-matrix/aluminum titanate composite.[23] In this case data points with error bars are means and standard deviations for 4–10 specimens at each prescribed load. Again, the dashed line is reproduced from Fig. 2 as a reference baseline.

The results in Figs. 3 and 4 indicate large matrix grains and second-phase particles as important microstructural elements contributing to high flaw tolerance.[31] We note the especially low sensitivity of the data to indentation load for the composite material in Fig. 4, i.e., enhanced strength at large *P* (approaching the long-crack region), counterbalanced by diminished strength at small *P* (short-crack region).

(2) *In Situ Measurements of Crack Growth in Control Fine-Grain Alumina*

As indicated earlier, the 2.5-μm-grain-size alumina was used as a *control* material for calibrating indentation coefficients. The indentations in this material were characterized by a well-formed radial crack system at each of the indentation loads *P*, with all four radial arms from the indentation corners equal in length to within 10% and with the radial surface traces exceeding twice the indentation half-diagonals (conditions for "well-developed" radial cracks[29]). The fracture was predominantly intergranular.

On application of an applied flexural stress σ_A the radial cracks in the *as-indented* ($\chi \neq 0$) specimens began to extend stably, but with discrete jumps in increments of one to three grains. Some persistent slow crack growth was observed at sustained stress after such jumps. After each such jump the load was ramped up until the next jump occurred. This piecewise extension proceeded relatively uniformly in all four radial directions until, at ≈80% of the failure stress, one pair of cracks began to develop at the expense of the other. Radial crack sizes $2c$ were measured at initial and final extremities of this dominant pair at each abrupt jump-arrest point. Figure 5 is a plot of the $\sigma_A(c)$ data for several values of *P*. Such precursor stable growth has been well documented in silicate glasses,[8] homogeneous silicon nitride,[32] and other fine-grain ceramics.

Let us now examine $\sigma_A(c)$ in Eq. (3) for the special case of a single-valued toughness, $T = T_0$. For inert environment it is readily shown[8] for this case that the crack begins stable growth from its immediate postindentation configuration at

$$\sigma_A = 0 \tag{5a}$$

$$c = c_0 = (\chi P/T_0)^{2/3} \tag{5b}$$

to instability at the maximum ($d\sigma_A/dc = 0$)

$$\sigma_A = \sigma_M = (3T_0/4\psi)(T_0/4\chi P)^{1/3} \tag{6a}$$

$$c = c_M = (4\chi P/T_0)^{2/3} \tag{6b}$$

Thus we have a stable branch of relative size $c_M/c_0 = 4^{2/3} = 2.52$. Constancy of the experimental quantity $\sigma_M P^{1/3}$ implies invariance in the compound parameter $\psi\chi^{1/3}$ with P at failure; similarly, constancy in $c_M P^{-2/3}$ implies invariance in χ. Using σ_M and c_M in Eq. (6) as normalizing parameters, Eq. (3) may be reduced to the universal function

$$\sigma_A/\sigma_M = (1/3)(c_M/c)^{1/2}[4 - (c_M/c)^{3/2}] \tag{7}$$

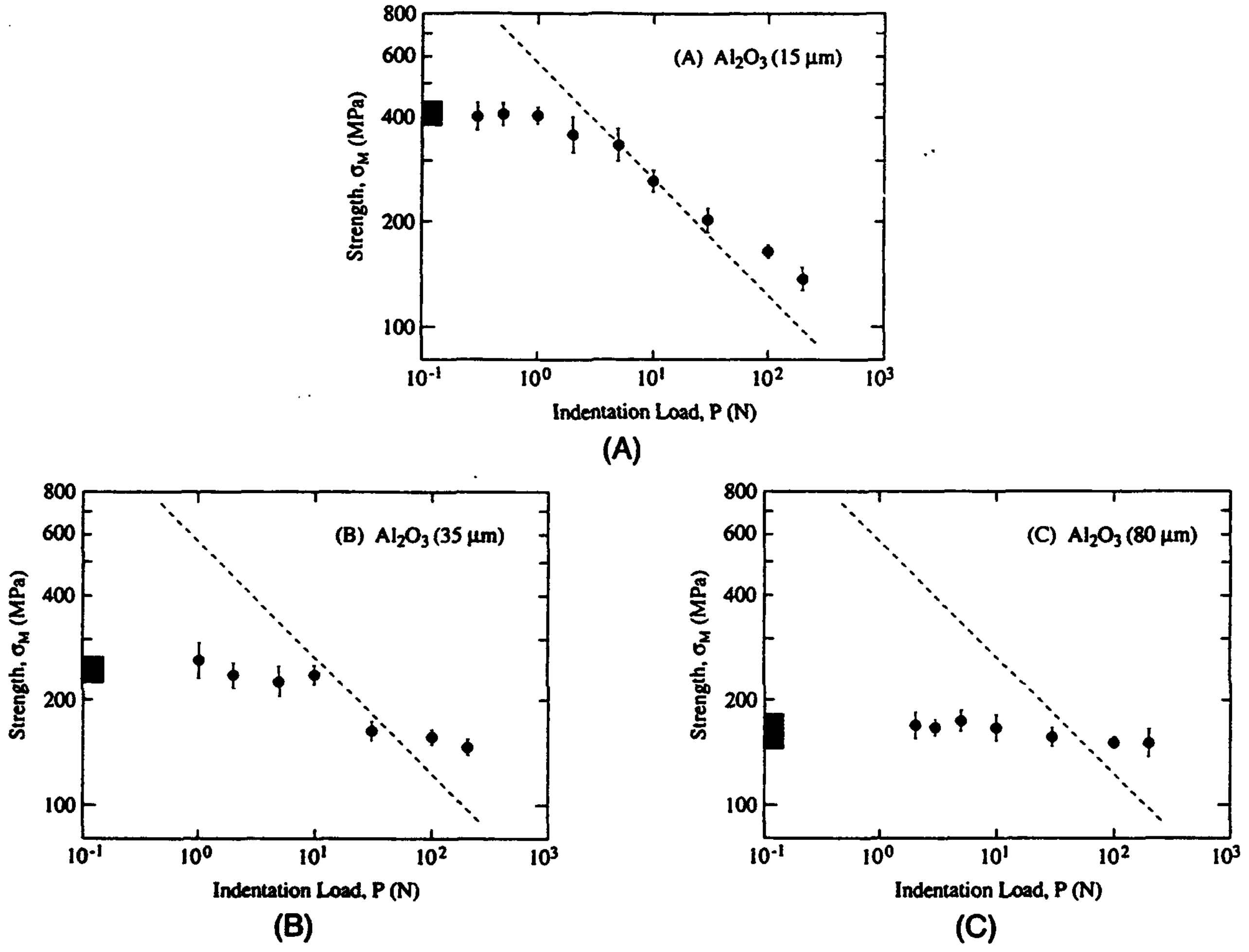

Fig. 3. Plot of $\sigma_M(P)$ inert strength data for coarse-grain test aluminas with Vickers indentation flaws.[22] Grain size: (A) 15, (B) 35, and (C) 80 µm. Fit to control data in Fig. 2 is reproduced as the dashed lines. Note higher flaw tolerance at larger grain size.

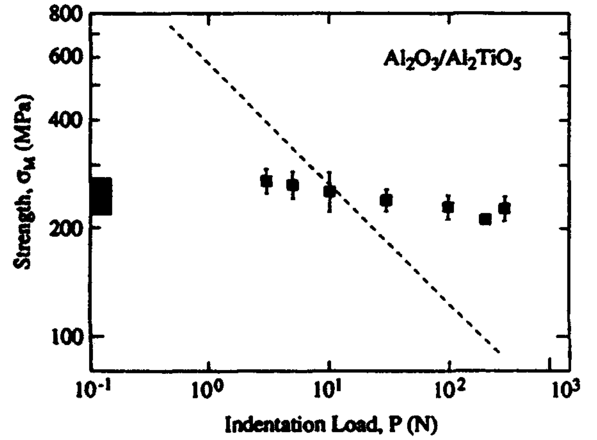

Fig. 4. Plot of $\sigma_M(P)$ inert strength data for aluminum titanate/alumina-matrix composite with Vickers indentation flaws. Dashed line is fit to 2.5-µm alumina control from Fig. 2.

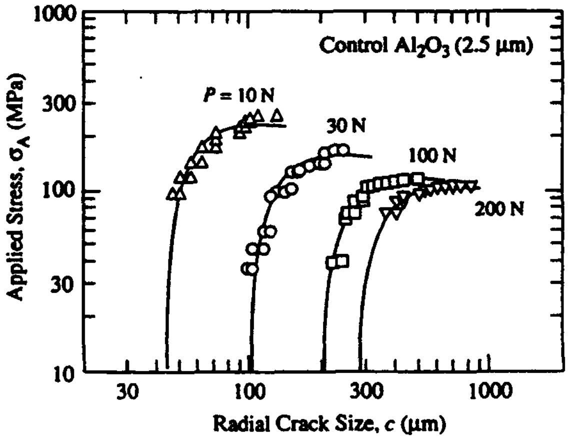

Fig. 5. Plot of in situ Vickers radial crack growth $\sigma_A(c)$ data (logarithmic coordinates) for 2.5-µm-grain-size alumina control, at specified values of P. Solid curves are fit to Eq. (3) at $T = T_0$ using calibrated coefficients from Section IV(3).

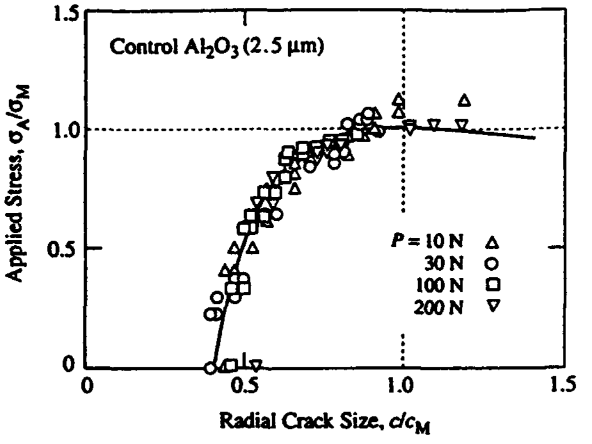

Fig. 6. Universal $\sigma_A(c)$ diagram (linear coordinates) for alumina control, Eq. (7), using collapsed data from Fig. 5. Fit allows determination of σ_M and c_M at each load P.

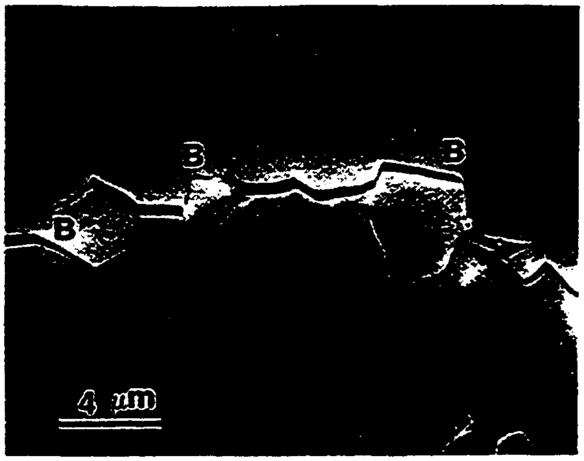

Fig. 8. SEM micrograph showing bridging in alumina-matrix composite. Aluminum titanate is light phase. B marks grain–grain bridge sites.

for materials with single-valued toughness.

In Fig. 6 we fit the data from Fig. 5 to this universal function by least-squares best-fitting values of σ_M and c_M at each load P. Note that this procedure makes full use of all the $\sigma_A(c)$ data, and does not rely exclusively on estimates of the actual maximum configuration.

(3) Calibration of Indentation Coefficients for Alumina-Based Systems

The quantities σ_M and c_M in Eq. (6) for as-indented specimens are most conveniently represented as functions of the independent test variable P. The $\sigma_M(P)$ evaluations from Fig. 6 are included in Fig. 2, to demonstrate overlap with the earlier inert strength results for the control alumina. In accordance with Eq. (6*a*), a best-fit to the data in Fig. 2 yields

$$\sigma_M P^{1/3} = 572.5 \pm 49.0\ \mathrm{MPa{\cdot}N^{1/3}} \qquad (8a)$$

Similarly, Fig. 7 is a plot of $c_M(P)$, and a best-fit to Eq. (6*b*) yields

$$c_M P^{-2/3} = 23.1 \pm 2.3\ \mathrm{\mu m{\cdot}N^{-2/3}} \qquad (8b)$$

Inserting the values from Eq. (8) back into Eq. (6), we evaluate

$$T_0/\chi = 36.0 \pm 3.6\ \mathrm{MPa{\cdot}m^{1/2}} \qquad (9a)$$

$$T_0/\psi = 3.68 \pm 0.34\ \mathrm{MPa{\cdot}m^{1/2}} \qquad (9b)$$

which, once T_0 is specified, provides us with "calibrated" indentation coefficients χ and ψ for our alumina.

Results from comparative tests on *postindentation-annealed* ($\chi = 0$) control alumina specimens allow a check on this calibration. In those tests failure occurred spontaneously from the initial flaws. Inserting $\sigma_A = \sigma_0$, $c = c_0$ into Eq. (3) at $T = T_0$, we obtain the critical stress

$$\sigma_A = \sigma_0 = (T_0/\psi c_0)^{1/2} \qquad (10)$$

Measurements of σ_0 and c_0 from 13 specimens over the indentation load range P = 0.2 to 200 N give $\sigma_0 c_0^{1/2} = 1.77 \pm 0.22$ MPa·m$^{1/2}$, corresponding to $T_0/\psi = 2.82 \pm 0.36$ MPa·m$^{1/2}$. This value is somewhat lower than that in Eq. (9*b*), suggesting that ψ, while invariant with P at the critical configuration (as implied by the strength–(load)$^{1/3}$ fit in Fig. 2), may well be a diminishing function of c in its evolution to failure.

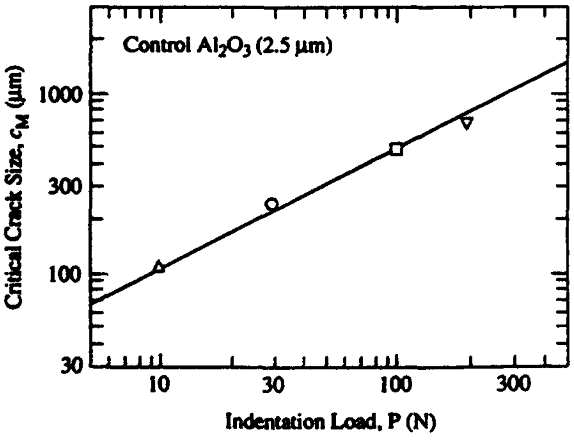

Fig. 7. Plot of c_M vs $P^{2/3}$ for alumina control. Fit allows determination of χ/T_0 in Eq. (6*b*).

(4) In Situ Observations of Crack Growth in Coarse-Grain Aluminas amd Alumina-Matrix/Aluminum Titanate Composite

As indicated in Section III(3), the indentations in the coarse-grain monophase aluminas showed considerably more irregular geometry than in the fine-grain control alumina. Explicit determination of $\sigma_A(c)$ curves of the kind plotted in Fig. 5 was therefore not undertaken for the coarse-grain aluminas. On the other hand, in line with previous observations,[17] the extent of stable crack growth prior to failure was observed to be substantially greater than the factor $c_M/c_0 = 2.52$ from Eqs. (5*b*) and (6*b*) for material of single-valued toughness, indicative of a shielding K-field.

For alumina-matrix/aluminum titanate composite, the relatively fine grain size produced reasonably well-defined radial crack patterns. Even so, some of the radial crack arms were larger than their neighbors. Especially strong deflections, presumably enhanced by strong *tensile* thermal expansion mismatch stresses,[26] occurred at alumina-matrix/aluminum titanate interphase boundaries (Fig. 8). The presumption of such tensile stresses was reinforced by the appearance of sporadic microcracking through the bulk of the composite material.[26,27,31] Countervailing *compressive* stresses at adjacent interphase facets augment frictional grain–grain contacts at the separating crack walls, thereby creating effective bridges and contributing to a shielding K-field.[16,23]

Quantitative in situ measurements of crack size as a function of applied stress were thereby made on composite specimens

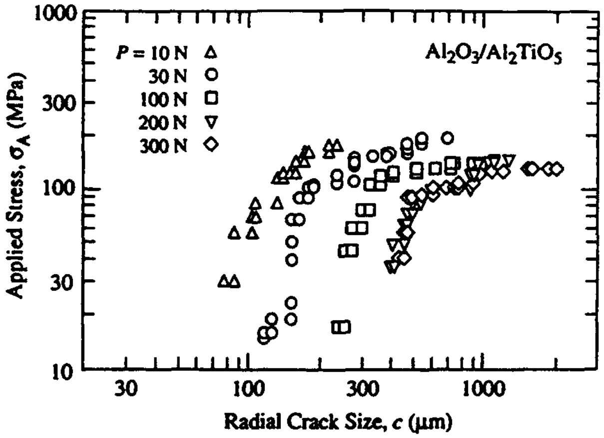

Fig. 9. Plot of $\sigma_A(c)$ in situ crack growth data for the aluminum titanate/alumina-matrix composite, at P = 10, 30, 100, 200, 300 N. Comparison with data for alumina fine-grain control at same loads (Fig. 5) shows much enhanced stable growth to failure in the composite, indicating an additional shielding K-field term.

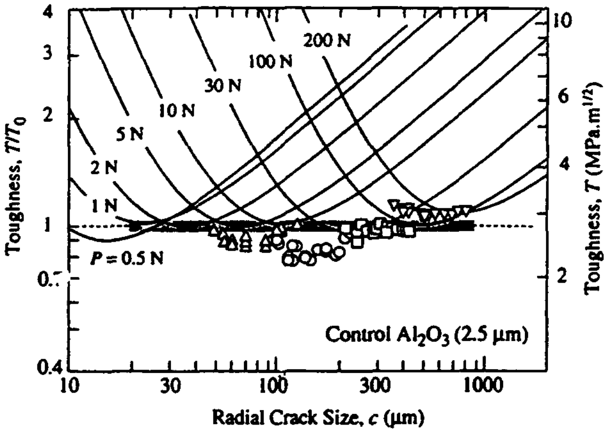

Fig. 10. T-curve diagram for fine-grain control alumina, grain size 2.5 μm. Left axis normalized T/T_0, right axis absolute T using T_0 = 2.75 MPa·m$^{1/2}$ as grain boundary toughness. Solid curves are plots of $K'_A(c)$ in Eq. (2) using alumina inert strengths σ_M at indentation loads P from Fig. 2. Data points are from in situ observations of $\sigma_A(c)$ in Fig. 5 at same loads. Shaded band is fitted T-curve at $T = T_0$.

indented at loads P = 10, 30, 100, 200, and 300 N. Crack extension was more erratic than in the fine-grain alumina control, with jumps of several grain dimensions during steady loading. Persistent slow growth after such jumps was noticeably more pronounced than in the control alumina. Where the crack pattern was asymmetrical, the longer of the two pairs of radial arms was measured. Figure 9 shows the ensuing $\sigma_A(c)$ data.

It is instructive to compare the data sets for the composite in Fig. 9 with those for the fine-grain alumina control material in Fig. 5. Observe first that the strength of the composite is relatively insensitive to indentation load, in accordance with Figs. 4 and 2. At the same time, the crack extension to failure at any given load is strongly enhanced. Such departures from the classical (Griffith) flaw response are indicative of a substantial stabilizing contribution to the K-field from the second phase.

(5) *Modulus/Hardness Ratio*

The modulus/hardness ratio for the base alumina material was determined as E/H = (395 ± 10 GPa)/(18.6 ± 1.0 GPa) = 21.3 ± 1.7, independent of grain size. The corresponding ratio for the alumina-matrix/aluminum titanate composite was E/H = (300 ± 25 GPa)/(13.2 ± 1.5 GPa) = 22.7 ± 4.5. Hence, within the experimental scatter, the indentation coefficient $\chi \propto (E/H)^{1/2}$ (Section II) may be considered essentially unchanged by addition of the second phase.

Accordingly, we may retain the calibrated parameters in Eq. (10) for our evaluations of the *normalized* T-curve in Eq. (1*b*) for the alumina-matrix composite material. Extension to evaluations of the *absolute* T-curve in Eq. (1*a*) is contingent on whether or not deflections along the interphase boundaries in the composite significantly alter the value of T_0.

(6) *T-Curve Constructions*

The calibration from the previous subsection allows us to construct $T(c)$ diagrams for our materials from indentation–strength and in situ applied-stress/crack-size data.

We begin with the alumina control, as a check on the assumption $T = T_0$ implicit in Eqs. (5)–(7). The family of solid curves in Fig. 10 represents generations of the *normalized* function $K'_A(c)/T_0$ in Eq. (1*b*) (left ordinate) using inert strengths $\sigma_A = \sigma_M$ at each load P from Fig. 2, and corresponding *absolute* function $K'_A(c)$ in Eq. (1*a*) (right ordinate) assuming T_0 = 2.75 MPa·m$^{1/2}$ (grain boundary toughness[16]). The T-curve is the locus of tangency points to these curves, as defined by $dK'_A(c)/dc = dT(c)/dc$ in Eq. (4). This locus effectively coincides with the horizontal line $T(c) = T_0$, as required for a material with single-valued toughness. The individual points in Fig. 10 are similar generations of $K'_A(c)/T_0$ or $K'_A(c)$ from the in situ $\sigma_A(c)$ data in Fig. 5. These points, representing equilibrium states in the growth evolution, are a *direct* measure of $T(c)$. Their tendency to fall below the dashed $T = T_0$ line may reflect the influence of slow crack growth, in addition to measurement uncertainties in the crack lengths. Notwithstanding such departures, the data substantiate the presumed invariance of toughness in the control alumina.

Figure 11 generates similar tangency constructions for the alumina test materials of grain sizes 15, 35, and 80 μm from the $\sigma_M(P)$ data sets in Fig. 3. Note that the $T(c)$ envelopes fall below the line $T = T_0$ at short crack sizes ($c < 400$ μm, approximately), and rise above this line at long crack sizes ($c > 400$ μm), reflecting the crossover in curves in Fig. 3. The steepness of the T-curve increases with grain size, again signifying a microstructural scaling effect in the shielding term. We note the absence of any firm indication that the toughness level has reached an upper plateau over the crack-size data range covered in these experiments.

Figure 12 is the T-curve construction for the alumina-matrix/aluminum titanate composite, generated from both inert strength (Fig. 4) and in situ (Fig. 9) data. Again, the data points from the in situ measurements are systematically displaced below and to the right of the $K'_A(c)$ inert-strength envelope, in keeping with the enhanced crack growth observed in this material. Nevertheless, the existence of a particularly steep T-curve for this material is manifest. An independent estimate of the long-crack toughness on a comparable composite material,[30] plotted as the upper dashed line at $T \approx 3T_0$ ($\approx$ 8 MPa·m$^{1/2}$) in Fig. 12, signifies that the cumulative effect of bridging is incomplete over >2 mm crack growth in our experiments. We point out that a crack size of 2 mm represents an appreciable fraction of the thickness of the composite disks (5 mm) so, by virtue of specimen geometry effects in the K-field relations,[6] any extrapolation of the data at extreme right in Fig. 12 becomes subject to considerable uncertainty.

V. Discussion

The present study offers an entirely objective strategy for evaluating short-crack T-curves from indentation–strength data. Underlying our evaluation for alumina-based ceramics is a proper calibration of the indentation–strength K-field coefficients for a fine-grain matrix material with negligible T-curve. With this calibration one may determine the T-curves from the K-field relation Eq. (2) in conjunction with the instability relation Eq. (4):[1,33] (i) by generating families of $K'_A(c)$ curves for

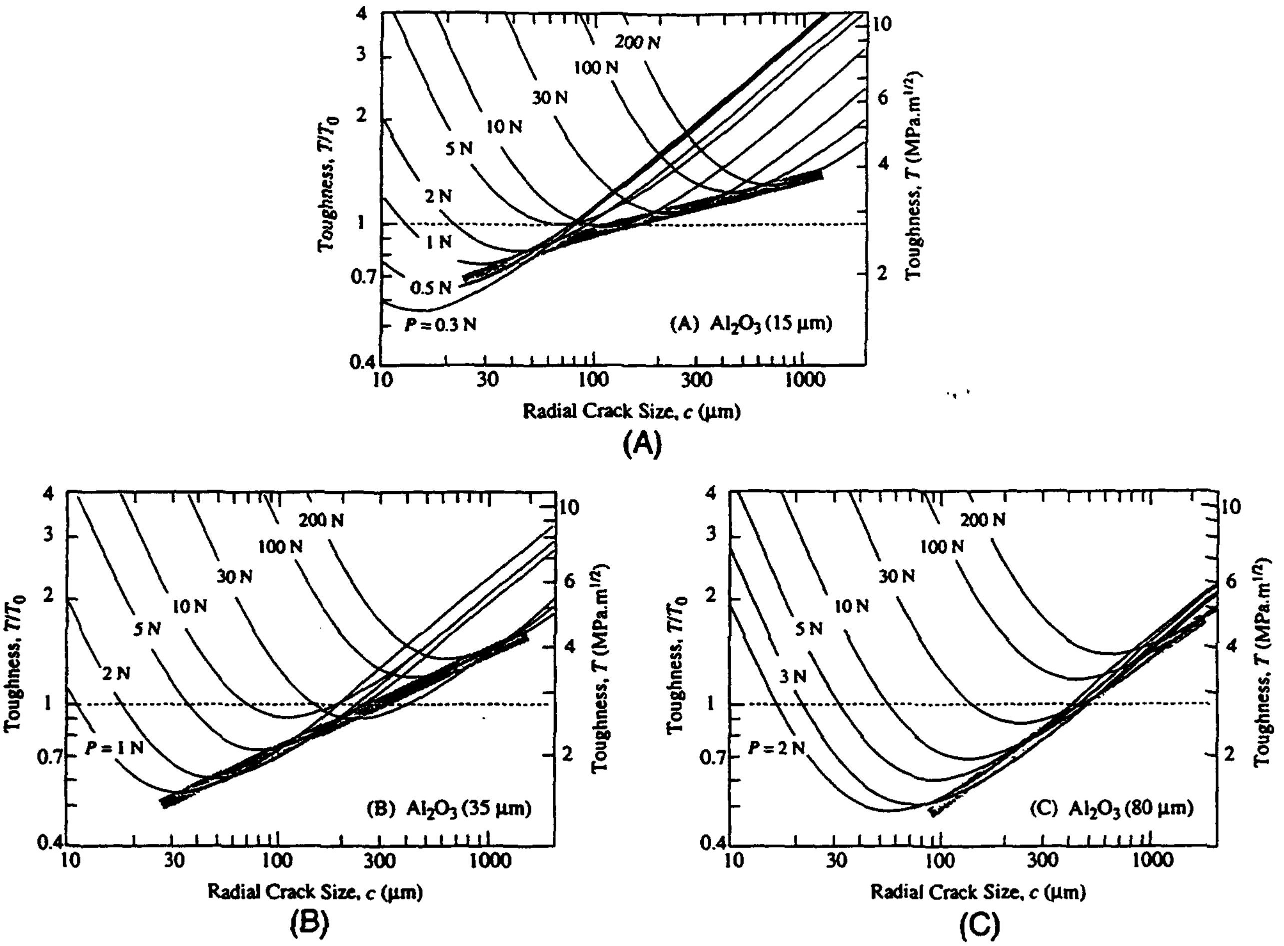

Fig. 11. T-curves for coarse-grain aluminas, grain sizes (A) 15, (B) 35, and (C) 80 μm. Left axis normalized T/T_0, right axis absolute T using T_0 = 2.75 MPa·m$^{1/2}$ as grain boundary toughness. Solid curves are plots of $K'_A(c)$ in Eq. (2) using alumina inert strengths σ_M at indentation loads P from Fig. 3. Shaded bands are arbitrarily fitted T-curves.

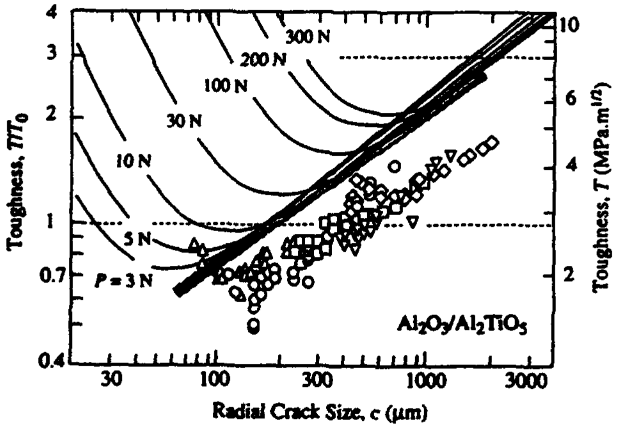

Fig. 12. T-curve for alumina-matrix/aluminum titanate composite. Left axis normalized T/T_0, right axis absolute T using T_0 = 2.75 MPa·m$^{1/2}$ as grain boundary toughness. Solid curves are plots of $K'_A(c)$ in Eq. (2) using inert strengths σ_M at indentation loads P from Fig. 4. Data points are from in situ observations of $\sigma_A(c)$ at same loads. Upper horizontal dashed line is independent measurement of long-crack toughness using a compact tension specimen.[30] Shaded band is arbitrarily fitted T-curve.

inert strengths σ_M at given indentation loads P, and fitting an envelope of tangency points to these curves; (ii) by generating $K'_A(c)$ data sets directly from in situ $\sigma_A(c)$ data. The $T(c)$ evaluations are limited only by restrictions in the crack-size range over which the indentations remain well-behaved,[29] ≈50 μm to 2 mm in Figs. 10–12.

Our strategy removes all the objections to the indentation methodology stated in Section I. In situ observations confirm failures from indentation sites, with distinctive stable crack growth prior to failure, so the observed flaw tolerance evident for the materials in Figs. 3 and 4 cannot be dismissed as strength cutoffs from natural flaws. No preconceptions concerning the analytical form of $T(c)$ are implied in our evaluations. It is not even necessary to identify a priori specific shielding mechanisms. The key to our calibration of the indentation coefficients is the invariance of $\sigma_M P^{1/3}$ over the load range for the control material, as in the inert indentation–strength data for the fine-grain alumina in Fig. 2. This corresponds to an equivalent load invariance in the compound coefficient $\psi\chi^{1/3}$ in Eq. (6*a*), implying self similarity in the radial crack configurations at failure. *Within* this constraint, uncertainties in absolute determinations of the individual parameters ψ and χ simply compress or expand the $K'_A(c)$ curves in Fig. 10 along the c-axis, affecting the steepness but not the existence of the T-curve. *Without* this constraint, independent calibrations of ψ and χ can lead to artificial T-curves, even in materials like silicate glass where none exist.[12] Such inadmissible results have prompted some workers to adopt ad hoc calibration procedures:

e.g., fixing χ at its ideal theoretical value while force-fitting $\psi(c)$ to match the requirement $T = T_0$;[6,12] or alternatively, fixing ψ while force-fitting $\chi(c)$.[13] A predisposition of ψ and χ to dependency on c during the evolution to failure has been acknowledged in our present evaluations of the former coefficient from Eq. (10) for annealed indentations, as well as in evaluations from earlier studies.[34,35] This potential complication is circumvented in the present procedure by the self similarity of the inert strength configurations implicit in Fig. 2.

The authenticity of the T-curves in Figs. 11 and 12 is supported by a weight of independent evidence. Experimental confirmation of a microstructural K-field shielding term, from frictional grain–grain bridging at the crack interface, has been documented in earlier microscopic studies on coarse aluminas and other ceramics.[17,18] In addition, direct measurements of the crack-opening profiles indicate a strong closure effect from the bridging tractions.[36] The trend to a steepening T-curve with increasing grain size in Fig. 11 reflects that reported by Knehans and Steinbrech[37] for long-crack tests in alumina. This same trend was also noted in deconvolutions of the inert strength data in Fig. 11 using a grain bridging fracture mechanics model with several adjustable parameters.[16] *Quantitative* comparisons with alternative T-curve evaluations are more tenuous, because of strong sensitivities to small errors in crack measurements (both technique- and material-related) and specimen geometry effects in the underlying fracture mechanics relations.

It is interesting to examine how the present calibration values of the K_A and K_R coefficients ψ and χ compare with previous estimates. Indentation flaws (and most natural flaws for that matter) tend to pennylike geometry.[2,38] In the ideal case of a single embedded penny crack in an infinite solid with axial symmetry, $\psi = 2/\pi^{1/2} = 1.27$.[2] Vickers radial cracks, however, depart from such ideal geometry in several ways, all of which may be expected to affect ψ. They are characterized by mutual intersections with the specimen free surface and orthogonal radial and lateral crack systems.[38] They tend also to an elliptical front, the more so as they extend through a greater fraction of the specimen thickness, and are annular about the deformation zone rather than center-point loaded.[8] For our as-indented base alumina, with $T_0 = 2.75$ MPa·m$^{1/2}$ (Section IV(6)), Eq. (9*b*) yields $\psi = 0.77$. A determination from the strength/crack-size measurements on postindentation-annealed specimens using Eq. (10) in Section IV(3) gives $\psi = 0.96$ for the same alumina; an analogous determination from an earlier study on glass gave $\psi = 0.89$.[34] The lower value for as-indented specimens is not inconsistent with a diminishing function $\psi(c)$ between c_0 and c_M.[6,12,14,39] On the other hand, a previous calibration, using a "dummy" indentation technique to determine the critical crack size c_M on several ceramics and invoking $\sigma_M c_M^{1/2} = 3T_0/4\psi$ from Eq. (6),[40] gave $\psi = 1.24$.[11]

Again using $T_0 = 2.75$ MPa·m$^{1/2}$ for our base alumina, Eq. (9*a*) yields $\chi = 0.076$. This value compares with $\chi = 0.071$ from measurements of immediate postindentation crack sizes in a fine-grain alumina,[29] but contrasts strongly with an earlier estimate $\chi = 0.018$[11] based on the dummy indentation method just mentioned (i.e., using $\psi = 1.24$ in Eq. (6*a*)). As with ψ, χ may be susceptible to relaxation with extending crack size. Also, in going from control material to test material, χ may be subject to variations from changes in indentation deformation, not least from changes in the modulus-to-hardness ratio, $\chi \propto (E/H)^{1/2}$ (Section II). This is not a factor in the "pure" aluminas, because changes in grain size have a negligible influence on the macroscopic elastic modulus and hardness of alumina. For aluminas with significant proportions of sintering additives, or alumina-based composites with additive second phases, changes in E and H will be the rule rather than the exception. In our aluminum titanate composite these changes are self-compensating, such that E/H, and presumably χ, remain unaltered (Section IV(5)). Very special caution needs to be exercised in those material systems in which the deformation in the second phase is not volume conserving, e.g., as with "anomalous glasses"[41] and phase-transforming zirconias,[42] where the relation $\chi \propto (E/H)^{1/2}$ may be modified.[25]

It is appropriate to weigh the advantages and limitations of the two variants of the indentation methodology advocated here for evaluating T-curves. Consider first the *indentation–strength* route, based on $\sigma_M(P)$ data for both test and control materials. The procedure is routine, fast, and free of potential complications from slow crack growth. However, several specimens (typically, a minimum of four) are required at each load over a wide range of indentation loads to generate an adequate data set. In addition, a complete calibration of the indentation coefficients requires some measurements of critical crack sizes, $c_M(P)$, on a representative number of control specimens. Here in situ observations on fine-grain alumina were used (Figs. 4 and 5) to determine $c_M(P)$. In principle, one could use the simpler "dummy" indentation technique[6,40] to measure c_M values, but at considerable potential sacrifice in certainty.[40]

With the alternative route, the roles are reversed. In situ, $\sigma_A(c)$ measurements on the actual test specimens then constitute the core of the T-curve evaluation—inert-strength data are needed only on the control material. From a quantitative standpoint, this route is not so practical for those materials that do not form well-defined indentation patterns, such as our coarsest-grain aluminas (Section IV(4)). Also, as noted for the composite material in Fig. 12 (and to a lesser extent for the control alumina in Fig. 10), the data are susceptible to slow crack growth. In relation to Eq. (2), such enhanced extension displaces the data to the right (enhanced crack size c) and downward (diminished K_A' at prescribed applied stress σ_A and indentation load P) relative to the equilibrium T-curve. On the other hand, the in situ procedure enables direct confirmation of failure from the indentations, and demonstrates enhancement of precursor stable growth in the more strongly bridged materials. It is this enhanced stabilization that is responsible for the flaw tolerance demonstrated in indentation–strength tests: the strength is no longer dependent on *initial* flaw size, but rather on some critical (history-independent) extended crack length to an instability (tangency) configuration.[10,15,16,31] The K_R-field from the residual contact stresses in as-indented specimens augments this stability, and thereby extends the range of crack sizes over which useful $T(c)$ data may be accumulated. Finally, in situ observations are able to provide clues to the underlying microstructural shielding processes (in our case, bridging) responsible for the T-curve behavior.

The indentation methodology proposed here for evaluating toughness properties of ceramics is pertinent to short-crack properties, clearly to *strength* but also to spontaneous microcracking, wear, thermal shock, and damage accumulation.

Acknowledgments: We acknowledge stimulating discussions with R. F. Cook, E. R. Fuller, Jr., C. W. Li, D. B. Marshall, N. P. Padture, R. O. Scattergood and S. M. Smith, and assistance with the design of the in situ crack growth device in Fig. 1 from D. T. Smith.

References

[1] Y.-W. Mai and B. R. Lawn, "Crack Stability and Toughness Characteristics in Brittle Materials," *Annu. Rev. Mater. Sci.*, **16**, 415–39 (1986).

[2] B. R. Lawn, *Fracture of Brittle Solids*, 2nd ed. Cambridge University Press, Cambridge, U.K., in press.

[3] D. J. Green, R. H. J. Hannink, and M. V. Swain, *Transformation Toughening of Ceramics*. CRC Press, Boca Raton, FL, 1989.

[4] D. B. Marshall, "Strength Characteristics of Transformation-Toughened Zirconia," *J. Am. Ceram. Soc.*, **69** [3] 173–80 (1986).

[5] R. W. Steinbrech and O. Schmenkel, "Crack Resistance Curves of Surface Cracks in Alumina," *J. Am. Ceram. Soc.*, **71** [5] C-271–C-273 (1988).

[6] N. Ramachandran and D. K. Shetty, "Rising Crack-Growth-Resistance (*R*-Curve) Behavior of Toughened Alumina and Silicon Nitride," *J. Am. Ceram. Soc.*, **74** [10] 2634–41 (1991).

[7] T. Fett and D. Munz, "Evaluation of *R*-curves in Ceramic Materials Based on Bridging Interactions," Report of the Nuclear Research Center Karlsruhe, Karlsruhe, Germany, 1991.

[8] D. B. Marshall, B. R. Lawn, and P. Chantikul, "Residual Stress Effects in Sharp-Contact Cracking: II. Strength Degradation," *J. Mater. Sci.*, **14** [9] 2225–35 (1979).

[9] R. F. Cook and B. R. Lawn, "Controlled Indentation Flaws for Construction of Toughness and Fatigue Master Maps"; pp. 22–42 in ASTM Special Technical

Publication No. 844, *Methods for Assessing the Structural Reliability of Brittle Materials*. Edited by S. W. Freiman and C. M. Hudson. American Society for Testing and Materials, Philadelphia, PA, 1984.

[10] R. F. Cook, B. R. Lawn, and C. J. Fairbanks, "Microstructure–Strength Properties in Ceramics: I, Effect of Crack Size on Toughness," *J. Am. Ceram. Soc.*, **68** [11] 604–15 (1985).

[11] R. F. Cook, C. J. Fairbanks, B. R. Lawn, and Y.-W. Mai, "Crack Resistance by Interfacial Bridging: Its Role in Determining Strength Characteristics," *J. Mater. Res.*, 2 [3] 345–56 (1987).

[12] S. M. Smith and R. O. Scattergood, "Crack Shape Effects in Fracture Toughness Measurements," *J. Am. Ceram. Soc.*, 75 [2] 305–15 (1992).

[13] C.-W. Li, D.-J. Lee, and S.-C. Lui, "*R*-Curve Behavior and Strength of In-Situ Reinforced Silicon Nitrides with Different Microstructures," *J. Am. Ceram. Soc.*, 75 [7] 1777–85 (1992).

[14] R. M. Anderson and L. M. Braun, "Technique for the *R*-Curve Determination of Y-TZP Using Indentation-Produced Flaws," *J. Am. Ceram. Soc.*, 73 [10] 3059–62 (1990).

[15] Y.-W. Mai and B. R. Lawn, "Crack-Interface Grain Bridging as a Fracture Resistance Mechanism in Ceramics: II, Theoretical Fracture Mechanics," *J. Am. Ceram. Soc.*, **70** [4] 289–94 (1987).

[16] S. J. Bennison and B. R. Lawn, "Role of Interfacial Grain-Bridging Sliding Friction in the Crack-Resistance and Strength Properties of Nontransforming Ceramics," *Acta Metall.*, 37 [10] 2659–71 (1989).

[17] P. L. Swanson, C. J. Fairbanks, B. R. Lawn, Y.-W. Mai, and B. J. Hockey, "Crack-Interface Grain Bridging as a Fracture Resistance Mechanism in Ceramics: I, Experimental Study on Alumina," *J. Am. Ceram. Soc.*, **70** [4] 279–89 (1987).

[18] P. L. Swanson, "Crack-Interface Traction: A Fracture-Resistance Mechanism in Brittle Polycrystals"; pp. 135–55 in Advances in Ceramics, Vol. 22, *Fractography of Glasses and Ceramics*. American Ceramic Society, Columbus, OH, 1988.

[19] R. F. Krause, "Rising Fracture Toughness from the Bending Strength of Indented Alumina Beams," *J. Am. Ceram. Soc.*, **71** [5] 338–43 (1988).

[20] R. F. Cook and D. R. Clarke, "Fracture Stability, *R*-Curves and Strength Variability," *Acta Metall.*, **36** [3] 555–62 (1988).

[21] D. K. Shetty and J. S. Wang, "Crack Stability and Strength Distribution of Ceramics That Exhibit Rising Crack-Growth (*R*-Curve) Behavior," *J. Am. Ceram. Soc.*, 72 [7] 1158–62 (1989).

[22] P. Chantikul, S. J. Bennison, and B. R. Lawn, "Role of Grain Size in the Strength and *R*-Curve Properties of Alumina," *J. Am. Ceram. Soc.*, 73 [8] 2419–27 (1990).

[23] S. J. Bennison, N. P. Padture, J. L. Runyan, and B. R. Lawn, "Flaw-Insensitive Ceramics," *Philos. Mag. Lett.*, **64** [4] 191–95 (1991).

[24] D. B. Marshall and B. R. Lawn, "Residual Stress Effects in Sharp-Contact Cracking: I. Indentation Fracture Mechanics," *J. Mater. Sci.*, **14** [8] 2001–12 (1979).

[25] B. R. Lawn, A. G. Evans, and D. B. Marshall, "Elastic/Plastic Indentation Damage in Ceramics: The Median/Radial Crack System," *J. Am. Ceram. Soc.*, **63** [9–10] 574–81 (1980).

[26] J. L. Runyan and S. J. Bennison, "Fabrication of Flaw-Tolerant Aluminum-Titanate-Reinforced Alumina," *J. Eur. Ceram. Soc.*, **7**, 93–99 (1991).

[27] N. P. Padture, S. J. Bennison, and H. M. Chan, "Flaw Tolerance and Crack Resistance Properties of Alumina-Aluminum Titanate Composites with Tailored Microstructures," *J. Am. Ceram. Soc.*, in review.

[28] D. B. Marshall, "An Improved Biaxial Flexure Test for Ceramics," *Am. Ceram. Soc. Bull.*, **59** [5] 551–53 (1980).

[29] G. R. Anstis, P. Chantikul, B. R. Lawn, and D. B. Marshall, "A Critical Evaluation of Indentation Techniques for Measuring Fracture Toughness: I, Direct Crack Measurements; II, Strength Method," *J. Am. Ceram. Soc.* **64** [9] 533–38, 539–43 (1981).

[30] N. P. Padture, "Crack Resistance and Strength Properties of Some Alumina-Based Ceramics with Tailored Microstructures"; Ph.D. Thesis. Lehigh University, Bethlehem, PA, 1991.

[31] S. J. Bennison, J. Rödel, S. Lathabai, P. Chantikul, and B. R. Lawn, "Microstructure, Toughness-Curves and Mechanical Properties of Alumina Ceramics"; pp. 209–33 in *Toughening Mechanisms in Quasi-Brittle Materials*. Edited by S. P. Shah. Kluwer Academic Publishers, Dordrecht, The Netherlands, 1991.

[32] D. B. Marshall, "Controlled Flaws in Ceramics: A Comparison of Knoop and Vickers Indentation," *J. Am. Ceram. Soc.*, **66** [2] 127–31 (1983).

[33] R. F. Cook, "Segregation Effects in the Fracture of Brittle Materials: Ca-Al_2O_3," *Acta Metall.*, **38** [6] 1083–100 (1990).

[34] D. B. Marshall and B. R. Lawn, "Flaw Characteristics in Dynamic Fatigue," *J. Am. Ceram. Soc.*, **63** [9–10] 532–36 (1980).

[35] B. R. Lawn, K. Jakus, and A. C. Gonzalez, "Sharp vs Blunt Crack Hypothesis in the Strength of Glass," *J. Am. Ceram. Soc.*, **68** [1] 25–34 (1985).

[36] J. Rödel, J. Kelly, and B. R. Lawn, "In Situ Measurements of Bridged Crack Interfaces in the SEM," *J. Am. Ceram. Soc.*, **73** [11] 3313–18 (1990).

[37] R. Knehans and R. Steinbrech, "Effect of Grain Size on the Crack Resistance Curves of Al_2O_3 Bend Specimens," *Sci. Ceram.*, **12**, 613–19 (1983).

[38] B. R. Lawn and T. R. Wilshaw, "Indentation Fracture: Principles and Applications," *J. Mater. Sci.*, **10** [6] 1049–81 (1975).

[39] R. Steinbrech, "Growth of Indentation Cracks in Al_2O_3 under Loading"; presented at the European Ceramic Society, Augsburg, FRG, 1991.

[40] R. F. Cook and B. R. Lawn, "A Modified Indentation Toughness Technique," *J. Am. Ceram. Soc.*, **66** [11] C-200–C-201 (1983).

[41] A. Arora, D. B. Marshall, B. R. Lawn, and M. V. Swain, "Indentation Deformation/Fracture of Normal and Anomalous Glasses," *J. Non-Cryst. Solids*, **31** [3] 415–28 (1979).

[42] R. F. Cook and L. M. Braun, "Trapped Cracks at Indentations: I. Experiments on Y-TZP; II. Fracture Mechanics Model," *J. Mater. Res.*, to be submitted. ☐

Reprinted from the Journal of the American Ceramic Society, Vol. 76, No. 9, September 1993

journal

J. Am. Ceram. Soc. 76 [9] 2312–20 (1993)

Flaw-Tolerance and Crack-Resistance Properties of Alumina–Aluminum Titanate Composites with Tailored Microstructures

Nitin P. Padture,[*,•] Stephen J. Bennison,[*,†] and Helen M. Chan[*,‡]

Department of Materials Science and Engineering, Lehigh University, Bethlehem, Pennsylvania 18015

Ceramics Division, National Institute of Standards and Technology, Gaithersburg, Maryland 20899

The microstructures of alumina–aluminum titanate (A–AT) composites have been tailored with the intent of altering their crack-resistance (*R*- or *T*-curve) behavior and resulting flaw tolerance. Specifically, two microstructural parameters which influence grain-localized crack bridging, viz., (i) internal residual stresses and (ii) microstructural coarseness, have been investigated. Particulate aluminum titanate was added to alumina to induce intense internal residual stresses from extreme thermal expansion mismatch. It was found that A–AT composites with uniformly distributed 20–30 vol% aluminum titanate ("duplex") showed significantly improved flaw tolerance over single-phase alumina. Coarsening of the duplex microstructure via grain growth scaling was relatively ineffective in improving the flaw tolerance further. Onset of spontaneous microcracking precluded further exploitation of this scaling approach. Therefore, an alternative approach to coarsening was developed, in which a uniform distribution of large alumina grains was incorporated within a fine-grain A–AT matrix ("duplex-bimodal"), via a powder processing route. The duplex-bimodal composites yielded excellent flaw tolerance with steady-state toughness of ≈8 MPa·m$^{1/2}$. A qualitative model for microstructure development in these duplex-bimodal composites is presented.

I. Introduction

Over the past decade or so it has been convincingly demonstrated that the macroscopic toughness of alumina-based ceramics increases with crack extension.[1,2] Such *T*-curve or *R*-curve behavior[§] arises from crack tip shielding due to grain-localized crack bridging.[2,3] In this mechanism, intact microstructural units pull out in the crack wake during propagation, providing frictional closure tractions across the crack walls. One of the most important manifestations of strong rising *T*-curves behavior is the *stabilization* of crack growth during external loading, in which an initial flaw undergoes equilibrium stable extension several times its original size en route to failure.[3] This stabilization imparts the ceramic with the highly desirable property of "flaw tolerance," in which the strength is insensitive to the initial flaw size or subsequent in-service damage.[4]

Theoretical modeling of the bridging process has identified two important microstructural variables that influence the *T*-curve characteristics of alumina-based ceramics,[5–9] viz., (i) grain size and (ii) internal residual stresses. The grain size controls the bridge pullout distance, which in turn determines the energy dissipated as frictional heating during pullout, and hence governs the length of the bridging zone. The magnitude of internal residual stresses from thermal expansion anisotropy or mismatch influences the intensity of the bridge-clamping stress which also plays a key role in determining the frictional dissipation of energy. This microstructural dependence of the *T*-curve characteristics and the resulting mechanical properties gives us the opportunity to tailor the microstructures of a ceramic component for optimum structural performance.[10]

The influence of grain size on the *T*-curve behavior of alumina-based ceramics has been investigated by several researchers. Direct measurements of the *T*-curve using long-crack testing geometries (crack size >> microstructural scale) have shown that increasing the grain size enhances the *T*-curve.[11] Indentation–strength measurements have demonstrated that increasing grain size imparts improved flaw tolerance to alumina as expected from an enhanced *T*-curve.[12,13] The influence of increased internal residual stresses on the *T*-curve characteristics and flaw tolerance has also been studied to some extent in two-phase ceramics.[¶] Enhanced *T*-curve and improved flaw tolerance have been observed in alumina matrix (and other ceramics) where internal residual stresses are intensified by deliberate addition of a second phase (distributed as an intergranular phase[14,15] or as discrete particles[16–18]).

In the present work we have systematically tailored both (i) internal residual stresses and (ii) microstructural coarseness in two-phase alumina–aluminum titanate (A–AT) composites. The internal residual stresses are adjusted by addition of uniformly distributed aluminum titanate particles to alumina. Aluminum titanate is chosen as the second phase because its thermal expansion coefficients both are extremely anisotropic and show large mismatch with alumina.[4] In addition, aluminum titanate and alumina can coexist as two distinct stable phases with limited solid solubility at the firing temperature employed.[19,20] Microstructural coarseness was adjusted by both (a) uniform coarsening (scaling in the classic sense to produce self-similar microstructures) via grain growth heat treatments (referred to as "duplex") and (b) nonuniform coarsening via an alternative powder processing route (referred to as "duplex-bimodal"), as illustrated in Fig. 1. Individual and combined influences of the above two microstructural variables on flaw tolerance of tailored A–AT composites were then investigated

---

R. Cook—contributing editor

Manuscript No. 195911. Received May 21, 1992; approved December 7, 1992.
Presented at the 94th Annual Meeting of the American Ceramic Society, Minneapolis, MN, April 14, 1992 (Symposium on Tailoring of Multiphase Ceramics for Optimum Mechanical Properties).
Supported by the U.S. Air Force Office of Scientific Research, E. I. du Pont de Nemours & Co., and the National Institute of Standards and Technology.

[*] Member, American Ceramic Society.

[•] Lehigh University; now at the Materials Science and Engineering Laboratory, National Institute of Standards and Technology, Gaithersburg, Maryland 20899.

[†] NIST; guest scientist on leave from the Department of Materials Science and Engineering, Lehigh University, Bethlehem, Pennsylvania 18015. Now with the Central Research and Development Experimental Station, E. I. du Pont de Nemours & Co. Inc., Wilmington, Delaware 19880–0356

[‡] Lehigh University.

[§] *T*, in the *T*-curve, refers to the toughness (stress intensity), and *R*, in the *R*-curve, refers to the fracture resistance (energy release rate). These two terms are used interchangeably in this paper. They are related through $R = T^2/E'$, where E' is the elastic modulus (plane strain).

[¶] In single-phase ceramics the magnitude of the internal residual stresses, for a given heat treatment, is limited by the thermal expansion anisotropy. Therefore, in order to obtain further increase in the residual stresses one has to resort to two-phase or polyphase ceramics for such studies.

using the indentation–strength technique.[12,13] In some instances direct *T*-curve (long-crack) measurements were also carried out.

II. Experimental Procedure

(1) *Processing*

(A) Powder Preparation: Commercially available alumina (A) (α-Al_2O_3, ≈0.5 μm crystallites, AKP-HP, Sumitomo Chemical, New York, NY) and aluminum titanate (AT) (β-Al_2TiO_5, ≈1.0 μm crystallites, Trans-Tech, Adamstown, MD) powders were used as raw materials. These powders were mixed in volumetric proportions of 80A:20AT (one batch) and 70A:30AT (four batches) in methanol. Individual powder batches were blended intimately by ball-milling using zirconia (Y-TZP) balls in polyethylene bottles for 24 h and the resulting slurries poured into Teflon beakers. Spray-dried alumina powder (α-Al_2O_3, ≈0.5 μm crystallites, ≈100 μm agglomerates, E4-3-85, GTE, Waltham, MA) was added to three of the 70A:30AT slurries in the following proportions: 20, 30, and 50 vol%. All individual slurries were then gently stirred while drying on a hot-plate. The resulting powder cakes were partially deagglomerated by crushing and stored. The three powder blends containing spray-dried agglomerates were used for processing duplex-bimodal composites. The rest were used for duplex composites. Flow charts in Fig. 2 outline the powder preparation procedures.

The entire powder processing was carried out in a laminar-flow hood within a class A-100 clean room. The following density values were used to calculate the volumetric proportions of the powders: α-Al_2O_3 = 3.987 g/cm^3 (Ref. 21) and β-Al_2TiO_5 = 3.700 g/cm^3 (Ref. 22).

(B) Powder Consolidation: Individual powder batches (≈3.5 g) were placed in polyethylene bags, crushed between a roller and plate assembly, and subsequently placed in a graphite die. Cylindrical pellets (2.5-mm diameter × 5-mm thickness) were fabricated by uniaxial pressing at 50 to 63 MPa. Several larger pellets (60-mm diameter × 5-mm thickness, ≈30 g powder per pellet) were also pressed using the procedure described. The uniaxially pressed pellets were placed in latex bags which were then sealed, evacuated, and subsequently isostatically pressed at 350 MPa. Isostatic pressing was carried out to remove any textural defects associated with the uniaxial pressing.

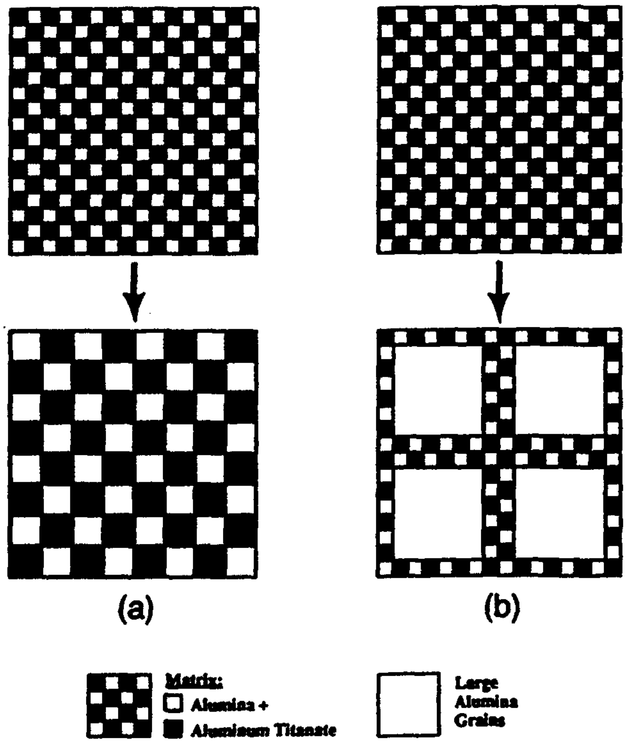

Fig. 1. Schematic diagram contrasting the two different approaches of microstructure coarsening: (a) duplex microstructures—uniform coarsening via grain-growth heat treatments (scaling in the classic sense), and (b) duplex-bimodal microstructures—nonuniform coarsening via powder processing.

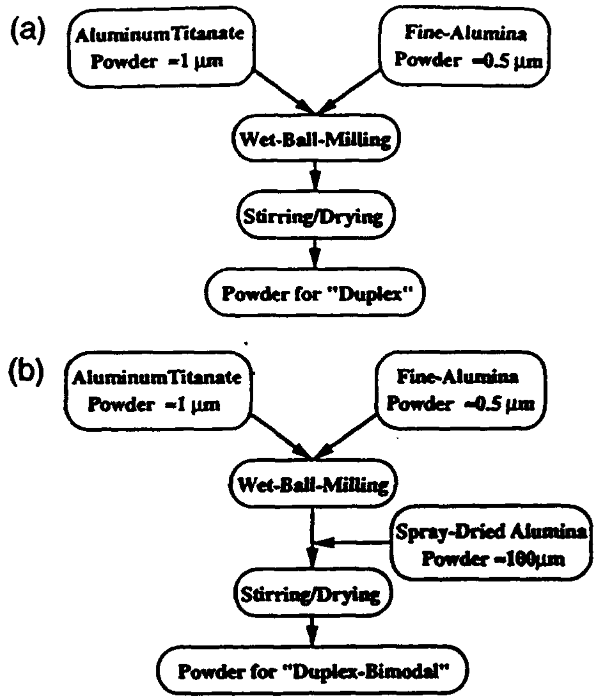

Fig. 2. Flow charts outlining powder processing procedures used for (a) duplex composites and (b) duplex-bimodal composites.

(C) Calcination and Sintering: Green pellets were packed in loose alumina powder in high-purity alumina crucibles and calcined in air using an electrical resistance-heated furnace at 1050°C for 12 h; a heating rate of 1°C/min and a cooling rate of ≈30°C/min were employed. These calcined pellets (packed in loose alumina powder in high-purity alumina crucibles) were *pressureless sintered in air* at temperatures in the range 1550° to 1600°C for times 5 to 1170 min with a heating rate of 8°C/min and a cooling rate of ≈30°C/min.

The powder compositions and heat treatments for the eight different materials processed in the present work are listed in Table I. The following scheme for material nomenclature is adopted: the number before AT refers to the volume percent of aluminum titanate in the A–AT mixture; D or DB in parentheses refer to duplex or duplex-bimodal, respectively; the letter after (D) refers to the grain size, S small, M medium, L large; the number after (DB) refers to the volume percent of spray-dried alumina agglomerates (relative to the A–AT mixture) in the starting powder. For example, for A–30AT(DB)-50, the matrix composition is 30 vol% aluminum titanate, and the composite is duplex-bimodal and contains 50 vol% alumina agglomerates.

(2) *Characterization*

Cross sections of as-sintered specimens were ground and polished to 1-μm grade using routine ceramographic techniques. These sections were thermally etched at 1500°C in air for 30 min, and subsequently sputter-coated with Au or Au–Pd. The microstructures were observed in an SEM (AUTOSCAN, Etec Corp., Hayward, CA; Model 1830, Amray Inc., Bedford, MA) using secondary and backscattered electrons.

Table I. Compositions, Processing Parameters, and Microstructural Parameters of A–AT Composites

Material*	Powder composition (vol%)			Sintering heat treatment	Resulting microstructure		
	Matrix		Spray-dried Al_2O_3		Grain size (μm)		Density (g/cm³) [% theoretical]
	Fine Al_2O_3	Fine Al_2TiO_5			Matrix Al_2O_3/Al_2TiO_5	Large Al_2O_3	
A–20AT(D)-S	80	20		1550°C, 2.5 h	4.0		3.896 [99.2%]
A–20AT(D)-M	80	20		1550°C, 17.5 h	6.4		3.888 [99.0%]
A–20AT(D)-L	80	20		1550°C, 19.5 h	6.6		3.825 [97.4%]
A–30AT(D)-S	70	30		1600°C, 0.08 h	2.5		3.814 [97.8%]
A–30AT(D)-L	70	30		1600°C, 1 h	8.0		3.788 [97.1%]
A–30AT(DB)-20	70	30	20	1600°C, 1 h	≈4	≈20	3.835 [97.9%]
A–30AT(DB)-30	70	30	30	1600°C, 1 h	≈4	≈24	3.858 [98.2%]
A–30AT(DB)-50	70	30	50	1600°C, 1 h	≈5	≈25	3.883 [98.5%]

*The number before AT refers to the volume percent of aluminum titanate in the A–AT mixture; D or DB in parentheses refers to duplex or duplex-bimodal, respectively; the letter after (D) refers to the grain size, S = small, M = medium, L = large; the number after (DB) refers to the volume percent of spray-dried alumina agglomerates (relative to the A–AT mixture) in the starting powder.

The grain size of the duplex microstructures was measured using a linear-intercept method[23] on representative SEM micrographs, where the average value for the grain size included *both* alumina and aluminum titanate grains. In the case of duplex-bimodal microstructures, the grain sizes of the A–AT matrix and the large alumina grains were evaluated separately.

The bulk densities of all the materials were measured using the Archimedes method, with deionized water as the immersion medium.[24] The measured densities were then compared with the theoretically calculated values. The elastic moduli of some of the A–AT composites were measured using an acoustic technique (Ultran Laboratories, State College, PA).

(3) Mechanical Testing

(A) Indentation–Strength: As-sintered disk specimens (≈23-mm diameter × ≈3.5-mm thickness) were ground to ≈2.5 mm thickness and polished to 1 μm grade (≈40 specimens per material). The centers of the polished side of most of the disks were indented with a Vickers diamond at contact loads P ranging from 3 to 300 N. Some disks were left unindented as controls. The indented specimens were allowed to sit in air for 10 min before a drop of dry silicone oil was placed on the indentation site.

The specimens were broken at room temperature in biaxial flexure using a three-point support and circular-flat fixture with the indentation side in tension using a universal testing machine (Models 1350 and 1122, Instron, Canton, MA). To avoid any environmental effects the failure times were maintained below 20 ms. Strengths, σ_M, were calculated from the failure loads and the specimen dimensions using thin plate and beam formulas.[25] Care was taken to examine the broken specimens to ensure that failure originated from the indentation. Those specimens that did not fail from the indentation were included in the data pool for unindented controls (see Refs. 12 and 13 for details).

(B) Long-Crack T-Curve: Large disks (≈50-mm diameter × ≈3.5-mm thickness) were ground to 2-mm thickness and one side was polished to 1-μm grade. The polished disks were machined into compact-tension specimens according to ASTM E-399 specifications.[26] A through-thickness sharp crack (≈300 μm in length) ahead of a 7-mm-long notch was generated using a precracking procedure.[27,28] The total crack length, c (distance from the loading axis to the crack tip), and the crack extension, Δc (distance between the notch tip and the crack tip), were measured (± 10 μm) using an optical microscope. A clip strain gauge was attached to the mouth of the notch, and the specimen was loaded in tension using a servo-hydraulic testing machine (Model 8502, Instron). The load, the crack opening displacement from the strain gauge, and the location of the crack tip were monitored continuously. In the event of any visible crack growth the specimen was unloaded. The toughness, T, was then calculated using the K-field solution from the ASTM E-399 standard.[26] The specimen was removed from the Instron machine and the new crack length measured. This entire procedure was repeated several times to obtain a T-curve for c/w values ranging from 0.2 to 0.35, where w is the distance between the loading axis and the rear of the specimen. All the T-curve measurement experiments were carried out at room temperature in laboratory air (≈55% relative humidity).

Similar compact tension specimens (1.2-mm thickness) were loaded in a miniaturized loading device[29] housed in the SEM (Model 1830, Amray Inc., Bedford, MA) for *in situ* observations. All such specimens were polished on one side, thermally etched, and sputter-coated with Au prior to the *in situ* SEM experiments. Loading of the specimen was achieved by activating the piezoelectric translator in the loading device from outside the SEM chamber. Events occurring at the bridging sites during crack propagation were monitored and recorded on film and/or video tape, in both secondary and backscattered electron modes.

III. Results

(1) Processing and Characterization

(A) Microstructures: Figure 3 shows representative microstructures of small- and large-grain duplex materials. Note that the aluminum titanate grains are distributed uniformly within the microstructure. Isolated spontaneous microcracks were observed in the finer-grain materials; however, in the coarser-grain materials profuse spontaneous microcracking was observed as indicated by the arrows in Fig. 3(b). Table I outlines the results from the microstructural characterization of the five different duplex materials. The grain sizes reported in Table I are those of the bulk microstructure (i.e., alumina and aluminum titanate grains combined). It was observed that the mean grain size of aluminum titanate was approximately half of that of alumina in each of these materials. As seen from Table I and Fig. 3 the densities of all these materials were found to be high, in excess of ≈97% of the theoretical limit (porosity visible in the micrographs is predominantly due to grain pullout during polishing).

Figure 4 shows representative microstructures of the three duplex-bimodal materials. The *bimodal* nature of the grain size, and the uniformity of the distribution of the large alumina grains, are clearly evident from these micrographs. Note also the successive increase in the relative number of large alumina grains (commensurate with the relative amounts of spray-dried agglomerates in the starting powders) in Figs. 4(a) to (c). Figure 5 is a backscattered-electron SEM image of the microstructure of an A–30AT(DB)-30 specimen, showing large alumina grains embedded within a fine-grain A–AT matrix. Table I outlines the results from the microstructural characterization of the three duplex-bimodal materials. Because of the bimodal nature of the microstructures, the grain sizes of the large alumina grains measured for these composites should be regarded only as approximate values. Again the densities of all the materials were found to be in excess of ≈97% of the theoretical limit.

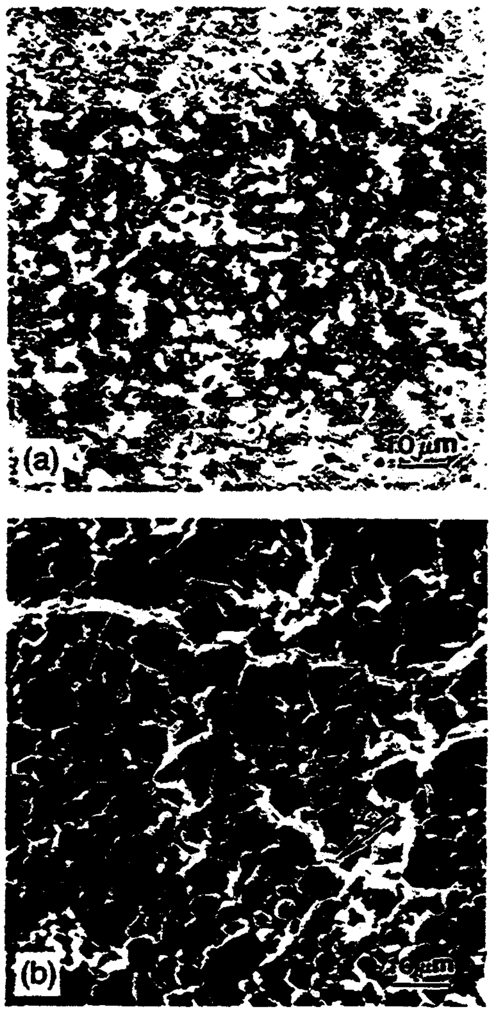

Fig. 3. Microstructures of duplex composites as seen in the SEM: (a) A–20AT(D)-S using backscattered electrons (gray phase is alumina, the white phase is aluminum titanate, and the dark regions represent porosity or grain pullout), and (b) A–30AT(D)-L using secondary electrons (arrows indicate spontaneous microcracks).

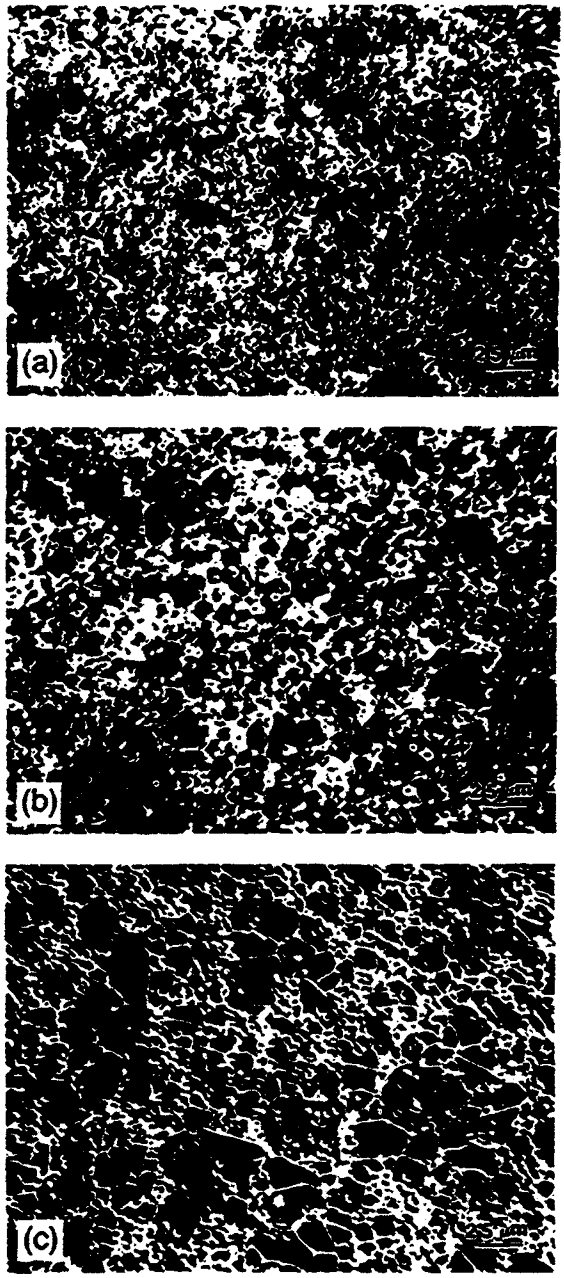

Fig. 4. Microstructures of duplex-bimodal composites as seen in the SEM using secondary electrons: (a) A–30AT(DB)-20, (b) A–30AT (DB)-30, and (c) A–30AT(DB)-50. Note the increasing number of large alumina grains from (a) to (c).

(B) In Situ SEM Observations: Now we examine some of the observations made during the *in situ* SEM crack growth experiments on the duplex-bimodal composites. Figures 6 and 7 are sequences taken with loads increasing between a and b (note the increase in the crack openings). In these two figures the load was applied in mode I tension horizontally and the direction of crack propagation is from top to bottom. Figure 6 shows a sequence for an A–30AT(DB)-30 specimen using secondary electrons in the SEM. Observe the alumina grains, both small and large, acting as bridges in this material, exerting frictional tractions at points P, Q, and R. On several occasions "clusters" of several grains (alumina and aluminum titanate) were also found to be active bridges. Figure 7 shows such an example in an A–30AT(DB)-50 specimen.

The density of bridging elements, comprising individual large alumina, small alumina/aluminum titanate grains, and "grain clusters," in the duplex-bimodal composites was found to be greater than single-phase alumina, approximately every three to four grains apart. It was also observed that the propagating crack tip was attracted toward the alumina/aluminum titanate interfaces. It is perhaps worth mentioning that within the limits of the resolution of our *in situ* experiments, no direct evidence of a stress-induced microcrack cloud ahead of the crack tip and in the wake was observed, in either the duplex or duplex-bimodal material. However, solitary microcracks were often observed to open immediately ahead of the tip causing the primary crack to deflect into the microcrack and thus setting up a potential frictional bridging unit.

(2) *Mechanical Properties*

(A) Indentation–Strength: The indentation load–strength, $\sigma_M(P)$, responses of the duplex A–20AT composites are plotted in Fig. 8. The $\sigma_M(P)$ response of a 6-µm-grain-size single-phase alumina[10] has been included in Fig. 8 for comparison. (Note that the strength of the 6-µm alumina shows close to $P^{-1/3}$ dependence, i.e., little *T*-curve behavior.[12] Within experimental error, the $\sigma_M(P)$ responses for single-phase aluminas of grain sizes 5 to 7 µm fall on the same curve.[13] The A–20AT(D)-S material possesses improved flaw tolerance over the single-phase alumina. It is also seen that uniform coarsening of

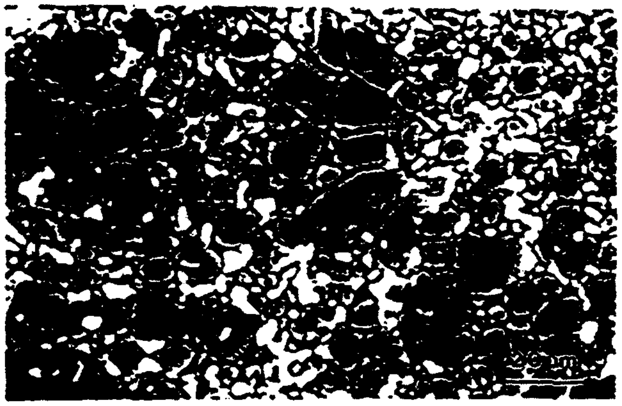

Fig. 5. Microstructure of material A–30AT(DB)-30 as seen in the SEM using backscattered electrons. Observe the duplex nature of the matrix (e.g., region on the top left) and the remnants of the spray-dried alumina agglomerates in the form of large alumina grains (bimodal nature of the entire microstructure). (Phase denotation is same as in Fig. 3.)

the microstructure over 4 to 6 µm does not lead to further significant improvement in the flaw tolerance of A–20AT(D)-M. On the other hand, additional increase in the grain size (A–20AT(D)-L) is seen to result in a relatively weak material. A dramatic decrease in strength (≈90%) is seen to occur over an extremely narrow grain size window (≈3% increase in grain size).

Consider now the $\sigma_M(P)$ response of the duplex A–30AT(D)-S material (Fig. 9). The A–30AT(D)-S material also shows

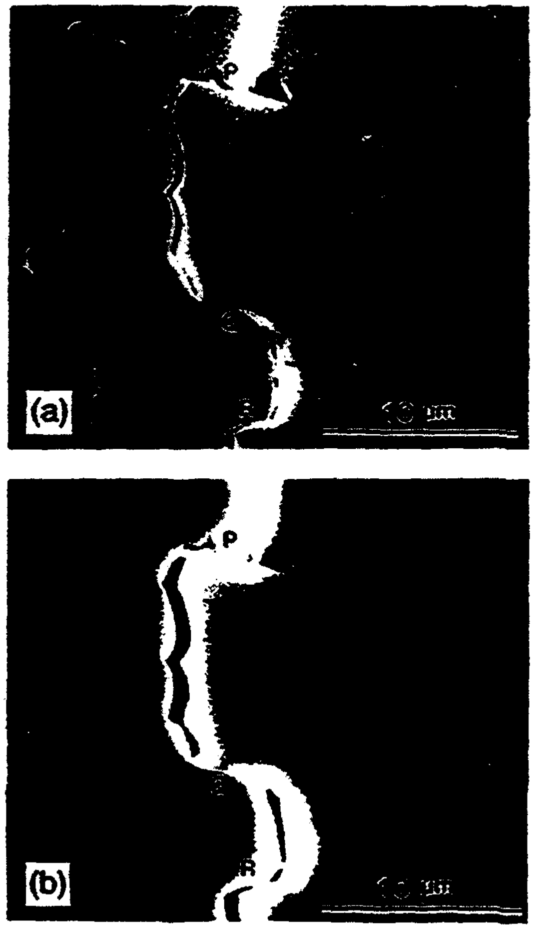

Fig. 6. Sequence of micrographs of a bridging site taken *in situ* in the SEM (secondary electrons) during crack propagation in a A–30AT(DB)-30 specimen. P, Q, and R denote friction points.

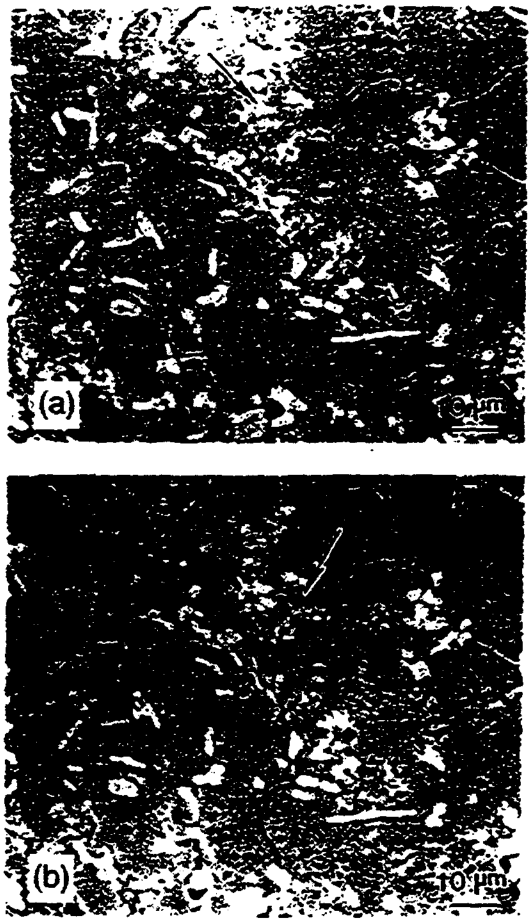

Fig. 7. Sequence of micrographs of a bridging site taken *in situ* in the SEM (backscattered electrons) during crack propagation in a A–30AT(DB)-30 specimen showing a cluster of grains acting as a bridging unit (arrows indicate a friction point). (Phase denotation is same as in Fig. 3.)

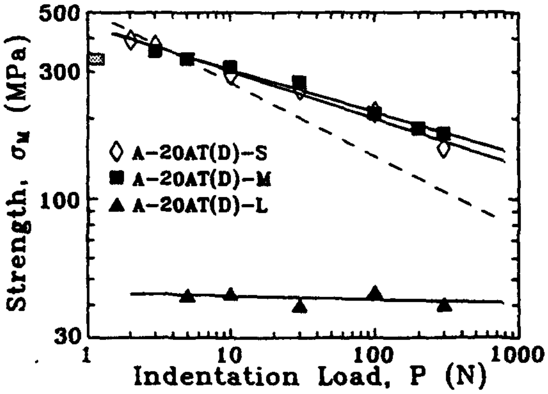

Fig. 8. Indentation load–strength responses of materials: A–20AT(D)-S, A–20AT(D)-M, and A–20AT(D)-L. The solid lines are empirical fits to the data. The dashed line is a fit to the 6-µm single-phase alumina data after Ref. 30. (For Figs. 8 to 10, each datum point represents breaks from four to five specimens; shaded region to the left denotes failures from natural flaws; error bars are ≈1.5 times the size of the symbols, and are omitted for clarity.)

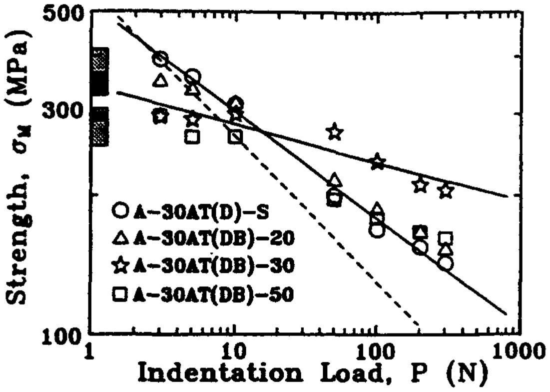

Fig. 9. Indentation load–strength responses of materials: A–30AT(D)-S, A–30AT(DB)-20, A–30AT(DB)-30, and A–30AT(DB)-50. Empirical fits (solid lines) only for the A–30AT(D)-S and A–30AT(DB)-30 data have been included for clarity. The dashed line is a fit to the 2.5-µm single-phase alumina data after Ref. 13.

improved flaw tolerance over the same grain size alumina (dashed curve). The $\sigma_M(P)$ responses of A–20AT(D)-S and A–30AT(D)-S materials were observed to be similar (Figs. 8 and 9). Upon uniform coarsening of the microstructures, a dramatic decrease in the strength, similar to that in A–20AT(D)-L material, was observed in the A–30AT(D)-L material (data not included in Fig. 9).

The $\sigma_M(P)$ responses of the duplex-bimodal composites are also plotted in Fig. 9. It is seen that the A–30AT(DB)-20 material has marginally better flaw tolerance over the base material, A–30AT(D)-S. However, further additions of large alumina grains are seen to result in a distinct improvement in the flaw tolerance of the A–30AT(DB)-30 material, while maintaining a higher plateau strength level, in excess of 210 MPa. Still further additions of large alumina grains in material A–30AT(DB)-50, in spite of maintaining good flaw tolerance, reduced the overall strengths at high indentation loads. Figure 10 compares the $\sigma_M(P)$ responses for duplex-bimodal composites with that of single-phase aluminas of grain sizes corresponding to that of the A–AT matrix (4 µm), and the large alumina grains (25 µm).[13] Note that the flaw-tolerance behavior of all of the duplex-bimodal composites is more pronounced (albeit different degrees) than either of the single-phase aluminas (4 and 25 µm). Note also that the $\sigma_M(P)$ response of the A–30AT(DB)-50 material is seen to be the closest to that of the 25-µm single-phase alumina.

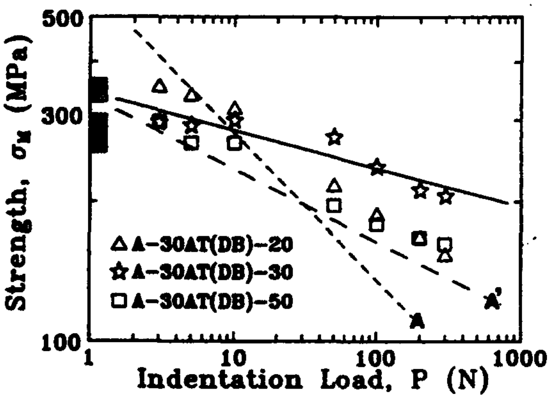

Fig. 10. Indentation load–strength responses of materials: A–30AT(DB)-20, A–30AT(DB)-30, and A–30AT(DB)-50 from Fig. 9, now plotted to compare with the theoretically calculated $\sigma_M(P)$ responses of 4-µm (A) and 25-µm (A') single-phase aluminas (dashed curves after Ref. 13).

(B) *Long-Crack T-Curve*: Figure 11 plots result from direct *T*-curve measurements on A–30AT(DB)-30 and A–30AT(DB)-50 specimens. It can be seen that the *T*-curves for both of these materials are similar, with high steady-state toughness values of up to ≈ 8 $\mathrm{MPa\cdot m^{1/2}}$. *T*-curves for A–30AT(D)-S and A–30AT(DB)-20 could not be measured because of the inability to obtain a stable through-thickness starter crack. However, the toughness value of A–30AT(D)-S estimated during the precracking step has been included in Fig. 11, which serves as a baseline toughness for the A–30AT matrix. The *T*-curve for a single-phase alumina with an average grain size of ≈ 20 µm (wide grain size distribution), measured using a compact tension specimen,[6] is included in Fig. 11 for comparison. (Alumina with grain size 4 µm, corresponding to the grain size of the A–30AT matrix, has a constant toughness of ≈ 4 $\mathrm{MPa\cdot m^{1/2}}$ measured using a compact-tension specimen.[11])

IV. Discussion

(1) *Processing and Characterization*

Consider first the results from processing and microstructure characterization of the duplex A–AT composites (Table I and Fig. 3). It is clear that duplex A–AT composites attain high densities and have well-controlled microstructures with uniform distributions of the aluminum titanate phase. It appears that the aluminum titanate second phase retards grain growth in alumina by a "pinning" mechanism, also found in other two-phase ceramics,[31-32] and is responsible for the well-controlled morphology of these microstructures. It has also been suggested that grain growth in the A–AT system is prevented by the lack of pore–grain boundary separation.[17] Therefore, densification, which competes with grain growth during sintering,[33] is favored. The densification process is believed to be further enhanced by dissolution of trace titania from the aluminum titanate in alumina, in a manner similar to that reported by Bagley *et al.*[34] The bluish color of the as-sintered A–AT specimens, believed to be due to color centers,[35] provides circumstantial evidence for the dissolution of titania in alumina.

It was noted in Table I and Figs. 4 and 5 that duplex-bimodal composites possess high densities and well-controlled grain structures. In order to explain the formation of the well-controlled duplex-bimodal microstructures we propose the following phenomenological model. Recall from Section II(1)(A) and Fig. 2(b) that the powder blends used for the processing of duplex-bimodal composites consisted of spray-dried alumina

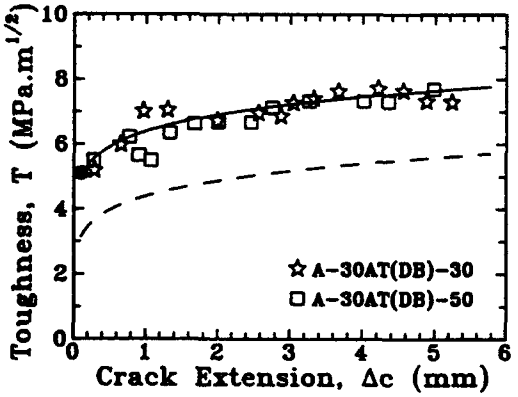

Fig. 11. Long-crack *T*-curves of materials: A–30AT(DB)-30 and A–30AT(DB)-50, measured using ASTM E-399 compact tension specimen geometry. (Estimated error in the *T* measurement is ±0.25 $\mathrm{MPa\cdot m^{1/2}}$.) The solid curve is an empirical fit to the A–30AT(DB)-30 data. The filled symbol represents an estimated toughness value for material A–30AT(D)-S (baseline toughness for the A–30AT matrix). *T*-curve for a 20-µm (wide grain size distribution) single-phase alumina after Ref. 6, represented by the dashed curve, included for comparison.

powder added to a mixture of fine-alumina and fine-aluminum titanate powders. Figure 12(a) is a schematic illustration of a green compact made up of such a powder blend. Note the three different kinds of powder particles in the hypothetical compact, and the absence of aluminum titanate powder particles in the agglomerates. It is believed that because of the relatively compliant nature of the spray-dried alumina agglomerates, efficient powder packing can be achieved in these compacts during consolidation.[36] The ensuing microstructure, shown schematically in Fig. 12(b), consists of large alumina grains embedded within a fine-grain A–AT matrix. It is suggested that upon sintering, the spray-dried powder agglomerates produce the large alumina grains in Fig. 12(b). It is postulated that the A–AT matrix and the spray-dried agglomerates sinter at approximately the same rate, thereby avoiding defects associated with differential sintering (e.g., constrained sintering). Grain growth can occur within the agglomerate because of the lack of a grain-growth-inhibiting second phase. However, the matrix remains relatively fine-grained because of grain-boundary "pinning" by the aluminum titanate second phase, and thus avoiding the microcracking problem. The result is the duplex-bimodal microstructures seen in Figs. 4 and 5.**

Consider now the interaction of cracks with the microstructures in A–AT composites observed *in situ* in the SEM. Figures 6 and 7 provide evidence of grain-localized crack bridging in duplex-bimodal composites. A high number density of the bridging sites, and the large dimensions of the bridging elements (relative to the crack opening displacements), are demonstrated. The *in situ* observations also suggest that high residual stresses play an important role in the process of bridge formation in the A–AT composites. Deflection of the primary crack into solitary microcracks in close proximity to the tip, and attendant formation of frictional interlocking points, are strongly influenced by intense residual stresses.[38] The lack of evidence for an extensive stress-induced microcrack cloud ahead of the crack tip from our *in situ* SEM experiments suggests that this mechanism does not play a significant role in the toughening of our A–AT composites.

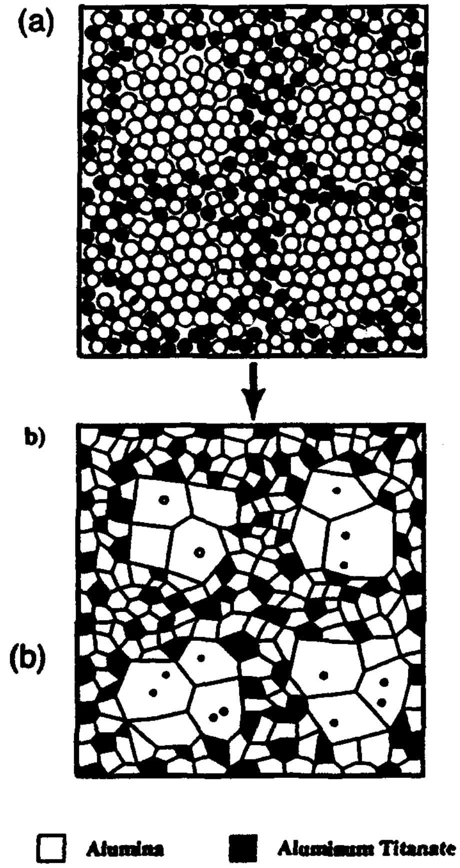

Fig. 12. Schematic illustration of the model for duplex-bimodal microstructures: (a) green compact (note the absence of second phase particles within the agglomerates), and (b) sintered body showing large alumina grains embedded within a duplex matrix.

(2) Mechanical Properties

At this point it is worth reiterating the interpretation of the indentation load–strength ($\sigma_M(P)$) plots. A $P^{-1/3}$ dependence of the strength, σ_M, indicates single-valued toughness (i.e., no *T*-curve). On the other hand, a decreasing dependence of the strength on the indentation load *P* indicates *T*-curve behavior.[12]

(A) Duplex: Compare the $\sigma_M(P)$ responses of A–20AT-(D)-S and 6-μm single-phase alumina in Fig. 8, and A–30AT-(D)-S and 2.5-μm single-phase alumina in Fig. 9. It is observed that addition of aluminum titanate to alumina results in better flaw-tolerance properties. Since aluminum titanate is weaker than alumina,[39] it cannot be argued that the improvement in the flaw tolerance is a "rule-of-mixtures" effect. It is believed that the high level of residual stresses due to the presence of aluminum titanate is responsible for enhancing the closure stresses during bridge pullout in the A–20AT(D)-S material. This was, in fact, the original rationale behind adding aluminum titanate to alumina.

Now consider the influence of microstructural scaling of the A–AT composites on the flaw tolerance. From Fig. 8 it is seen that, within experimental error, the $\sigma_M(P)$ responses of A–20AT(D)-S and A–20AT(D)-M materials are the same. A likely explanation is that the increase in the grain size from A–20AT(D)-S to A–20AT(D)-M is relatively small (Table I), and not sufficient to alter the *T*-curve behavior significantly despite the high level of residual stresses. Note that in single-phase aluminas the microstructural scale must be increased by an order of magnitude to observe an appreciable effect on the flaw tolerance.[13] Upon further scaling of the microstructure a dramatic decrease in strength is observed (see behavior of A–20AT(D)-L in Fig. 8). This is attributed to profuse spontaneous microcracking as a result of high residual stresses and relatively large grain size. A similar strength drop was also observed in the A–30AT(D)-L composite. The micrograph in Fig. 3(b) presents direct evidence for the presence of spontaneous microcracks. The low elastic modulus (≈100 GPa) for this weak A–AT material compared to a value of ≈300 GPa for the fine-grain A–AT material further supports the microcracking argument. Note that the window of grain size over which the strength drop occurred is extremely narrow (Table I) and results in the existence of a spontaneous microcracking limit in terms of a critical grain size.[40]

The $\sigma_M(P)$ responses of A–20AT(D)-S and A–30AT(D)-S were observed to be similar. Note that the grain sizes of these two materials are slightly different (Table I). But as we saw from Fig. 9, slight differences in the grain sizes of nonmicrocracked A–AT materials do not significantly influence their $\sigma_M(P)$ responses. This implies that the volume percent of the aluminum titanate has a relatively small effect on the *T*-curve behavior of duplex A–AT composites in the microstructural and volume percent range investigated. At this juncture we do not have a definite explanation for this observation. However, volume percent does determine the inter-aluminum titanate particle distance, thereby influencing the critical grain size governing the onset of spontaneous microcracking.[40]

The above discussion demonstrates the limit to which the scaling approach can be exploited. This was the reason that we resorted to nonuniform coarsening in the duplex-bimodal A–AT composites.

(B) Duplex-Bimodal: Consider the $\sigma_M(P)$ responses of the duplex-bimodal composites in Fig. 9. The A–30AT(DB)-30

**Ironically, grain growth within agglomerated inclusions during the sintering of two-phase ceramics was regarded as a "processing problem."[17]

material is seen to exhibit the best flaw-tolerance property, indicating enhanced *T*-curve behavior. Comparison of the $\sigma_M(P)$ responses of the A–30AT(D)-S and A–30AT(DB)-30 materials suggests that the improved flaw tolerance can be attributed to the presence of large alumina grains in the A–30AT(DB)-30 microstructure (Fig. 4(b)). *In situ* SEM observations of such large alumina grains (Fig. 6) and "grain clusters" (Fig. 7) acting as bridging units in the A–30AT(DB)-30 material support this argument. From Table I we note that the grain sizes of A–30AT(D)-S and the matrix of A–30AT(DB)-30 are slightly different. However, scaling in duplex A–AT composites does not affect their $\sigma_M(P)$ responses appreciably (Section IV(2)(A)). Therefore, it cannot be argued that such improvement in the flaw tolerance of A–30AT(DB)-30 is due to the difference in the matrix grain sizes. Further confirmation of enhanced *T*-curve in A–30AT(DB)-30 material over its duplex counterpart A–30AT(D)-S comes from the direct *T*-curve measurements (Fig. 11).

Compare now the $\sigma_M(P)$ responses of the A–30AT(DB)-30 material and those of the single-phase aluminas (Fig. 10). It is evident that the duplex-bimodal material exhibits improved flaw-tolerance properties over both of the single-phase alumina materials. The improvement over the 25-μm alumina is attributed to the enhanced efficacy of bridging in A–30AT(DB)-30 as a result of high internal residual stresses (due to AT in the matrix) on the frictional closure force coupled with enhanced bridge formation. On the other hand, the improvement over the 4-μm alumina is attributed to the combined influences of high residual stresses and large alumina grains on bridging in the duplex-bimodal material. From Fig. 11 improved *T*-curve behavior of the duplex-bimodal material over the coarse-grain single-phase alumina is evident.

At this point we do not know why the A–30AT(DB)-20 material, in spite of containing large alumina grains (Fig. 4(a)), exhibits only a marginal improvement in flaw tolerance over its duplex counterpart A–30AT(D)-S (Fig. 9). A possible explanation might be that the number density of large alumina grains intersected by a crack in the A–30AT(DB)-20 is not sufficient to cause significant improvement in its *T*-curve behavior.

Still further addition of large alumina grains (A–30AT(DB)-50), in spite of maintaining good flaw tolerance, was seen to degrade the strength properties somewhat (Fig. 9). However, its long-crack *T*-curve was seen to be similar to that of the A–30AT(DB)-30 material (Fig. 11). The good flaw-tolerance properties and high toughness values of the A–30AT(DB)-50 material can be rationalized using the same arguments of microstructural coarsening and residual stresses used to explain the mechanical behavior of the A–30AT(DB)-30 material.

Finally, we come to the question, Why do A–30AT(DB)-30 and A–30AT(DB)-50 materials show the same plateau toughness (Fig. 11) but different $\sigma_M(P)$ responses (Figs. 9 and 10)? The reason for similar *T*-curves for these two materials is possibly due to a tradeoff between (i) the area fraction of bridges which increases with an increase in the number of large alumina grains and (ii) residual stresses which are postulated to decrease with an increase in the number of large alumina grains. This trade-off argument is consistent with the *T*-curve predictions from a theoretical fracture mechanics model for grain-localized crack bridging in materials with bimodal microstructures.[28,41]

To explain the $\sigma_M(P)$ responses of the two materials we take a closer look at the microstructure of A–30AT(DB)-50 material in Fig. 4(c). It is seen from this micrograph that the large alumina grains in the microstructure of A–30AT(DB)-50 are well-interconnected; this makes it difficult to tell whether the matrix is composed of large alumina grains or the A–AT mixture. From the similarity in the $\sigma_M(P)$ response of the A–30AT(DB)-50 material and the 25-μm single-phase alumina in Fig. 10, we postulate that because of the high interconnectivity, the constituent large alumina grains essentially govern the strength behavior of the A–30AT(DB)-50 material.

An alternative answer to the afore-stated question might lie in the fundamentally different nature of the two techniques used to investigate *T*-curve behavior. The indentation–strength technique probes the toughness characteristics of short and intermediate pennylike cracks whereas the direct *T*-curve measurement technique pertains to through-thickness cracks on a scale large compared to the microstructure. Such crack systems show disparate behavior due in part to fundamental differences in their intrinsic crack profile characteristics.[42] Resolution of this issue awaits further *T*-curve determination in the short and intermediate crack size domains.

As a final point it is worth noting that our philosophy of deliberately introducing heterogeneities to ceramic microstructures is in direct contrast to the processing strategies based on the premise that flaws must be eliminated. In our scheme it is accepted that processing flaws exist and further damage is likely to be introduced during service. The aim, therefore, becomes one of stabilizing the growth of these preexisting flaws by introducing a strong *T*-curve in the material, and not that of striving to eliminate them. We have demonstrated the effectiveness of this strategy by fabricating composites with strong rising *T*-curve and impressive flaw tolerance through judicious but less exacting ceramics processing. Remaining challenges include the stabilization of multiple damage[30] and improvement of the strength properties of these flaw-tolerant ceramics.

V. Conclusions

The major findings and conclusions from our study of the alumina–aluminum titanate (A–AT) composites can be summarized as follows:

(a) Composites with microstructures containing (i) uniformly distributed 20–30 vol% aluminum titanate in alumina (duplex), and (ii) large alumina grains embedded within a fine-grain A–AT matrix (duplex-bimodal), can be tailored to high densities using conventional ceramics processing. A proposed phenomenological model accounts for the processing of the duplex-bimodal microstructures.

(b) For both duplex-bimodal and duplex composites, *in situ* SEM observation of crack growth provides direct evidence for grain-localized bridging in the crack wake.

(c) Addition of aluminum titanate to alumina results in an improvement in flaw tolerance of the duplex A–AT composites over single-phase aluminas, indicative of a strong *T*-curve. In the A–AT composites the combined influence of intense thermal-expansion-mismatch-induced internal residual stresses on both the bridge-clamping stress and bridge formation is responsible for the enhanced *T*-curve behavior. Coarsening of duplex A–AT microstructures by grain growth scaling results in a negligible effect on the flaw tolerance in the microstructural range investigated. However, further microstructural scaling results in a relatively weak material due to profuse spontaneous microcracking.

(d) Composites with duplex-bimodal microstructures exhibit impressive flaw tolerance and *T*-curve properties. The improved mechanical behavior is attributed to the combined influences of increased internal residual stresses (due to the presence of aluminum titanate in the matrix) and increased microstructural coarseness due to the presence of the large alumina grains.

Acknowledgments: We thank M. P. Harmer and B. R. Lawn for many stimulating discussions. Experimental assistance from S. Darby, J. Rödel, J. L. Runyan, and L. M. Braun at NIST, and J. D. French and C. J. Russo at Lehigh University, is gratefully acknowledged.

References

[1] H. Hübner and W. Jillek, "Sub-Critical Extension and Crack Resistance in Polycrystalline Alumina," *J. Mater. Sci.*, 12, 117–25 (1977).

[2] R. Knehans and R. W. Steinbrech, "Memory Effect of Crack Resistance During Slow Crack Growth in Notched Al_2O_3 Bend Specimens," *J. Mater. Sci. Lett.*, 1, 327–29 (1982).

[3] P. L. Swanson, C. J. Fairbanks, B. R. Lawn, Y.-W. Mai, and B. J. Hockey, "Crack-Interface Grain Bridging as a Fracture Resistance Mechanism in Ceramics: I, Experimental Study on Alumina," *J. Am. Ceram. Soc.*, 70 [4] 279–89 (1987).

[4] S. J. Bennison, N. P. Padture, J. L. Runyan, and B. R. Lawn, "Flaw-Insensitive Ceramics," *Philos. Mag. Lett.*, **64** [4] 191–95 (1991).

[5] Y.-W. Mai and B. R. Lawn, "Crack-Interface Bridging as a Fracture Resistance Mechanism in Ceramics: II, Theoretical Fracture Mechanics Model," *J. Am. Ceram. Soc.*, **70** [4] 289–94 (1987).

[6] M. V. Swain, "*R*-Curve Behavior in a Polycrystalline Alumina Material," *J. Mater. Sci. Lett.*, **5**, 1313–15 (1986).

[7] S. J. Bennison and B. R. Lawn, "Role of Interfacial Grain-Bridging Sliding Friction in the Crack-Resistance and Strength Properties of Nontransforming Ceramics," *Acta Metall.*, **37** [10] 2659–71 (1989).

[8] R. F. Cook, "Segregation Effects in the Fracture of Brittle Materials: Ca-Al_2O_3," *Acta Metall. Mater.*, **38** [6] 1083–100 (1990).

[9] G. Vekinis, M. F. Ashby, and P. W. R. Beaumont, "*R*-Curve Behavior of Al_2O_3 Ceramics," *Acta Metall. Mater.*, **38** [6] 1151–62 (1990).

[10] B. R. Lawn, *Fracture of Brittle Solids*, 2nd ed. Cambridge University Press, Cambridge, U.K., in press.

[11] F. Deuerler, R. Knehans, and R. W. Steinbrech, "Testing Methods and *R*-Curve Behavior of Al_2O_3," *J. Phys. (Les Ulis, Fr.)*, **47** [C1] 617–21 (1986).

[12] R. F. Cook, C. J. Fairbanks, and B. R. Lawn, "Microstructure–Strength Properties in Ceramics: I, Effect of Crack Size on Toughness," *J. Am. Ceram. Soc.*, **68** [11] 604–15 (1985).

[13] P. Chantikul, S. J. Bennison, and B. R. Lawn, "Role of Grain Size in the Strength and *R*-Curve Properties of Alumina," *J. Am. Ceram. Soc.*, **73** [8] 2419–27 (1990).

[14] W. A. Zdaniewski and H. P. Kirchner, "Toughening of a Sintered Alumina by Crystallization of the Grain-Boundary Phase," *Adv. Ceram. Mater.*, **1** [1] 99–103 (1986).

[15] N. P. Padture and H. M. Chan, "Improved Flaw Tolerance in Alumina Containing 1 vol% Anorthite via Crystallization of the Intergranular Glass," *J. Am. Ceram. Soc.*, **75** [7] 1870–75 (1992).

[16] C. H. McMurty, W. D. G. Boecker, S. G. Sheshadri, J. S. Zanghi, and J. E. Garnier, "Microstructure and Material Properties of SiC–TiB_2 Particulate Composites," *Am. Ceram. Soc. Bull.*, **66** [2] 325–29 (1987).

[17] J. L. Runyan and S. J. Bennison, "Fabrication of Flaw-Tolerant Aluminum Titanate Reinforced Alumina," *J. Eur. Ceram. Soc.*, **7**, 93–99 (1991).

[18] N. P. Padture, S. J. Bennison, J. L. Runyan, J. Rödel, H. M. Chan, and B. R. Lawn, "Flaw Tolerant Al_2O_3–Al_2TiO_5 Composites"; pp. 715–21 in Ceramic Transactions, Vol. 19, *Advanced Composite Materials*. Edited by M. D. Sacks. American Ceramic Society, Westerville, OH, 1991.

[19] S. M. Lange, C. L. Fillmore, and L. H. Maxwell, "The System Beryllia–Alumina–Titania: Phase Relations and General Properties of Three-Component Porcelains," *J. Res. Natl. Bur. Stand. (U.S.)*, **48** [4] 298–301 (1952).

[20] D. Goldberg, "On the Systems Formed by Alumina with Several Trivalent and Tetravalent Metal Oxides, in Particular Titanium Oxide (in Fr.)," *Rev. Int. Hautes Temp. Refract.*, **5**, 181–94 (1968).

[21] H. E. Swanson, M. I. Cook, T. Isaacs, and E. H. Evans, "*Standard X-ray* Diffraction Powder Patterns," NBS Circular No. 539, Vol. 9, National Bureau of Standards, Washington, DC, 1959.

[22] B. Morosin and R. W. Lynch, "Structure Studies on Al_2TiO_5 at Room Temperature and at 600°C," *Acta Crystallogr.*, **B28**, 1040–46 (1972).

[23] J. C. Wurst and J. A. Nelson, "Lineal Intercept Technique for Measuring Grain Size in Two-Phase Polycrystalline Ceramics," *J. Am. Ceram. Soc.*, **55** [2] 109 (1972).

[24] E. C. M. Pennings and W. Grellner, "Precise Nondestructive Determination of the Density of Porous Ceramics," *J. Am. Ceram. Soc.*, **72** [2] 1268–70 (1989).

[25] D. B. Marshall, "An Improved Biaxial Flexure Test for Ceramics," *Am. Ceram. Soc. Bull.*, **59** [5] 551–53 (1980).

[26] "Standard Test Method for Plane-Strain Fracture Toughness of Metallic Materials," ASTM E-399; pp. 480–504 in *Annual Book of ASTM Standards*, Vol. 3.01. American Society for Testing and Materials, Philadelphia, PA, 1983.

[27] S. Lathabai, J. Rödel, and B. R. Lawn, "Cyclic Fatigue from Frictional Degradation at Bridging Grains in Alumina," *J. Am. Ceram. Soc.*, **74** [6] 1340–48 (1991).

[28] N. P. Padture, "Crack Resistance and Strength Properties of Some Alumina-Based Ceramics with Tailored Microstructures"; Ph.D. Thesis. Lehigh University, Bethlehem, PA, 1991.

[29] J. Rödel, J. F. Kelly, M. R. Stoudt, and S. J. Bennison, "A Loading Device for Fracture Testing of Compact Tension Specimens in the Scanning Electron Microscope," *Scanning Microsc.*, **5** [1] 29–35 (1991).

[30] L. M. Braun, S. J. Bennison, and B. R. Lawn, "Short-Crack *T*-Curves and Damage Tolerance in Alumina-Based Composites," *Ceram. Sci. Eng. Proc.*, **13** [7–8] 156–63 (1992).

[31] R. J. Brook, "Controlled Grain Growth"; pp. 331–64 in *Treatise on Materials Science and Engineering*, Vol. 9. Edited by F. F. Y. Wang. Academic Press, New York, 1976.

[32] J. D. French, M. P. Harmer, H. M. Chan, and G. A. Miller, "Coarsening-Resistant Dual-Phase Interpenetrating Microstructures," *J. Am. Ceram. Soc.*, **73** [8] 2508–10 (1990).

[33] M. P. Harmer, "Use of Solid-Solution Additives in Ceramics Processing"; pp. 679–96 in Advances in Ceramics, Vol. 10, *Structure and Properties of MgO and Al_2O_3 Ceramics*. Edited by W. D. Kingery. American Ceramic Society, Westerville, OH, 1984.

[34] R. D. Bagley, I. B. Cutler, and D. L. Johnson, "Effect of TiO_2 on Initial Sintering of Al_2O_3," *J. Am. Ceram. Soc.*, **53** [2] 136–41 (1970).

[35] E. R. Winkler, J. F. Sarver, and I. B. Cutler, "Solid Solution of Titanium Dioxide in Aluminum Oxide," *J. Am. Ceram. Soc.*, **49** [12] 634–37 (1966).

[36] S. J. Lukasiewicz and J. S. Reed, "Characterization and Compaction Response of Spray-Dried Agglomerates," *Am. Ceram. Soc. Bull.*, **57** [9] 798–805 (1978).

[37] F. F. Lange, "Powder Processing Science and Technology for Increased Reliability," *J. Am. Ceram. Soc.*, **72** [1] 3–15 (1989).

[38] J. Rödel, "Crack Closure Forces in Ceramics: Characterization and Formation," *J. Eur. Ceram. Soc.*, **9**, 323–34 (1992).

[39] H. Okamura, E. A. Barringer, and H. K. Bowen, "Preparation and Sintering of Narrow-Sized Al_2O_3–TiO_2 Composites," *J. Mater. Sci.*, **24**, 1867–80 (1989).

[40] N. P. Padture, J. L. Runyan, S. J. Bennison, L. M. Braun, and B. R. Lawn, "Model for Toughness Curves in Two-Phase Ceramics: II, Microstructural Variables," *J. Am. Ceram. Soc.*, in review.

[41] N. P. Padture and B. R. Lawn, "Toughness Curves in Bimodal Microstructures: A Fracture Mechanics Model," unpublished work.

[42] R. W. Steinbrech, R. M. Dickerson, and G. Kleist, "Characterization of the Fracture Behavior of Ceramics through Analysis of Crack Propagation Studies"; pp. 287–311 in *Toughening Mechanisms in Quasi-Brittle Materials*, Vol. 195. Edited by S. P. Shah. Kluwer Academic Publishers, Dordrecht, Netherlands, 1991. □

Postfailure subsidiary cracking from indentation flaws in brittle materials

Nitin P. Padture[a)]

Materials Science and Engineering Laboratory, National Institutes of Standards and Technology, Gaithersburg, Maryland 20899

(Received 20 July 1992; accepted 10 February 1993)

Vickers indentation sites in ceramics have been examined after specimen failure from median/radial indentation cracks. Evolution of a new cracking pattern of "ortho-lateral" cracks, originating at the intact corners of the Vickers indentation and running orthogonal to the classic-lateral cracks and parallel to the new fracture surface, has been observed. In some instances postfailure extension of the classic-lateral cracks toward the surface was also observed. Enhanced residual tensile stress from relaxation of constraints on the indentation-plastic cavity by the generation of a fracture surface is postulated to drive the subsidiary cracking. A simple qualitative model to explain this phenomenon is presented. Possible implications of such postfailure subsidiary cracking on residual-stress-driven flaws, postmortem fractography, and wear in ceramics are discussed.

I. INTRODUCTION

It is now well known that indentation of brittle solids by sharp indenters (such as Vickers) gives rise to the formation of cracks, in addition to the plastically deformed hardness impression. The recoverable (elastic) and the unrecoverable (residual) stress fields generated during the loading-unloading of the indenter are responsible for the ensuing cracking. In most brittle solids, the cracks, which are driven by the residual component of the stress field, develop during the unloading of the indenter. The resulting cracking patterns are broadly classified into radial and lateral. (For a detailed description of indentation fracture, see reviews by Lawn and Wilshaw[1,2] and Cook and Pharr[3] and references therein.)

In this paper we focus our attention on the lateral cracking pattern when the indenter is fully withdrawn. According to the elastic/plastic expanding-cavity model for indentation, the stress-free specimen surface relieves constraint on the indentation-induced plastic deformation zone giving rise to a residual tensile stress normal to the specimen surface.[4,5] This residual stress provides the driving force for classic laterals.[5,6] The residual stress reaches its maximum value at full contact load and persists at a constant value σ_r as the indenter is unloaded.[5,6] In most brittle solids classic laterals have been observed to initiate during the unloading cycle at the base of the plastic deformation zone below the contact and extend laterally on a plane closely parallel to the specimen surface.[1,7–10] Since these cracks lie subsurface, their detection is limited only to light optical inspection in transparent or highly translucent materials.

In this paper we report a modification of the classical cracking pattern associated with indentations which occurs after stressing of indented specimens to failure. New cracks were observed to originate from the intact corners of the Vickers indentation and run somewhat parallel to the new fracture surface and orthogonal to both the specimen surface and classic laterals. This new cracking pattern was found to closely resemble the cross-sectional view of classic laterals.[11] Therefore, we call these cracks "ortho-laterals". It appears that similar forces drive both ortho- and classic-lateral cracks.

Ortho-lateral cracking has certain implications in the postfailure role of residual-stress-driven flaws in ceramics and postmortem fractography. Also, in view of the great significance of lateral cracking in material removal in the erosion[12] and wear[13] of ceramic surfaces, study of ortho-lateral cracks might prove to be potentially useful in the understanding of general lateral fracture in optically opaque ceramics.

II. EXPERIMENTAL

Bars (3 × 3 × 15 mm) made of soda-lime-silica glass (pre-annealed commercial sheet glass), sapphire (Adolf Meller Co., Providence, RI), polycrystalline alumina (grain size 2.5 μm),[14] and polycrystalline MgO (grain size 20 μm; Ozark Technical Ceramics, Webb City, MO) were polished on one face and sputter-coated with gold. (Use of any products in this work does not imply their endorsement by the National Institutes of Standards and Technology.) The polycrystalline speci-

---

[a)] Guest scientist on leave from the Department of Materials Science and Engineering, Lehigh University, Bethlehem, Pennsylvania 18015.

mens, prior to gold-coating, were thermally etched (Al_2O_3–1500 °C for 0.5 h; MgO–1200 °C for 1.0 h). Centers of the prospective tensile polished faces were indented with a Vickers diamond using contact loads ranging from 3 to 100 N. Care was taken to align the pyramidal edges with the longitudinal axis of the bar specimens. In most specimens indentation was carried out in the presence of dry silicone oil with the intent of reducing environmental effects on fracture. A few indented glass specimens were annealed at 530 °C for 1 h followed by furnace cooling in order to remove the indentation-residual-contact field. The bar specimens were then broken in uniaxial flexure using a four-point bend fixture. In some cases centers of the prospective tensile faces of disk (25 mm diameter × 2 mm thickness) specimens were indented and broken in biaxial flexure using a flat punch on a three-ball-support fixture. For each of the materials investigated in this work, between 5 and 20 specimens were broken and examined for subsidiary cracking.

Two halves of the broken specimens were quickly removed from the testing fixture and carefully placed on a glass coverslip without damaging the indentation sites. Evolution of subsidiary crack growth (environmentally assisted) from the indentation sites was then observed under an optical microscope (Nikon Diaphot, New Haven, CT). In some instances fracture surfaces of the broken specimens were sputter-coated with gold and indentation sites observed in a scanning electron microscope (SEM) (Amray Inc., Bedford, MA).

III. RESULTS

Figure 1(a) shows a Vickers indentation site before failure in a soda-lime-silica glass specimen. Figures 1(b) to 1(d) are a sequence of micrographs recorded after failure of the same specimen from the indentation, where indentation and subsequent bending tests were carried out in the presence of dry silicone oil. For specimens broken without oil, the subsidiary cracks were found to develop fully within 1 min after failure, preventing us from following the evolution of the cracking pattern. The use of oil did not eliminate environmentally assisted crack growth, but significantly reduced the crack velocity,[15] enabling us to observe the evolution of subsidiary cracks over a period of hours. The new cracks seen in Fig. 1(d) are classified as ortho-laterals (OL) and extended laterals (EL), based on their origins. Ortho-lateral cracks can be observed from Figs. 1(b) to 1(d) to initiate at the indentation corners and subsequently run somewhat parallel to the fracture surface and orthogonal to both the specimen surface and classic laterals. On the other hand, extended-lateral cracks, from subsurface observation using transmitted light (not shown here), were found to result from the upward extension of the classic laterals to the surface. Partial closure of the radials was also observed as the ortho-laterals extended [compare Figs. 1(a) and 1(b) with Fig. 1(d)], suggesting a decay in the component of the residual stress driving the radials. The cracking sequence observed in Figs. 1(a) to 1(d) is typical of ≈20 glass specimens tested in our laboratory.

Figures 2(a) and 2(b) show a typical example of a pre- and postfailure indentation site in glass, in which the specimen was annealed after indentation. Note the absence of any subsidiary cracking in Fig. 2(b).

Figures 3(a) and 3(b) show a typical example of an indentation site in sapphire before and after failure, in which the specimen was broken in biaxial flexure. In sapphire the postfailure cracking was found to be predominantly in the form of extended laterals. Figures 4(a) and 4(b) are pre- and postfailure SEM micrographs of an indentation site in fine-grain polycrystalline Al_2O_3, showing evidence of ortho-lateral cracking. Partial closure of the radials was also observed in the case of polycrystalline Al_2O_3 [Fig. 4(b)]. Pre- and postfailure optical micrographs of an indentation site in polycrystalline MgO appear in Figs. 5(a) and 5(b). No evidence of postfailure subsidiary cracking was observed in MgO. (Table I summarizes all the results from the present study.)

IV. DISCUSSION

Consider the expanding-cavity model for indentation in which a spherical cavity under pressure produces a spherical plastic zone embedded within an elastic continuum.[5] Creation of a zero-stress plane (free surface S) in this system relaxes the constraint on the plastic zone, resulting in a tensile stress σ_r at full indenter unload acting normal to the free surface [see Fig. 6(a)].[5] This residual tensile stress provides a driving force for classic-lateral cracking. Consider now the creation of a new stress-free plane (fracture surface S') orthogonal to the plane S. This new fracture surface further removes the constraint on the plastic zone, and results in a residual tensile stress σ_r', acting normal to the plane S' [Fig. 6(b)]. It is postulated that some complex stress field produced by the combination of tensile stresses σ_r and σ_r' drives the ortho-lateral (OL) and the extended-lateral (EL) cracks. Lack of any postfailure subsidiary cracking in indented glass specimens with the residual contact field removed by annealing [Fig. 2(b)] supports this argument. It is also suggested that this cracking problem may not be confined to a mode I loading and may well be a complex mixed-mode problem,[16] which is beyond the scope of this paper.

Possibility of postfailure subsidiary cracking arising from any testing artifacts was ruled out by testing specimens in both four-point bend and biaxial flexure (see

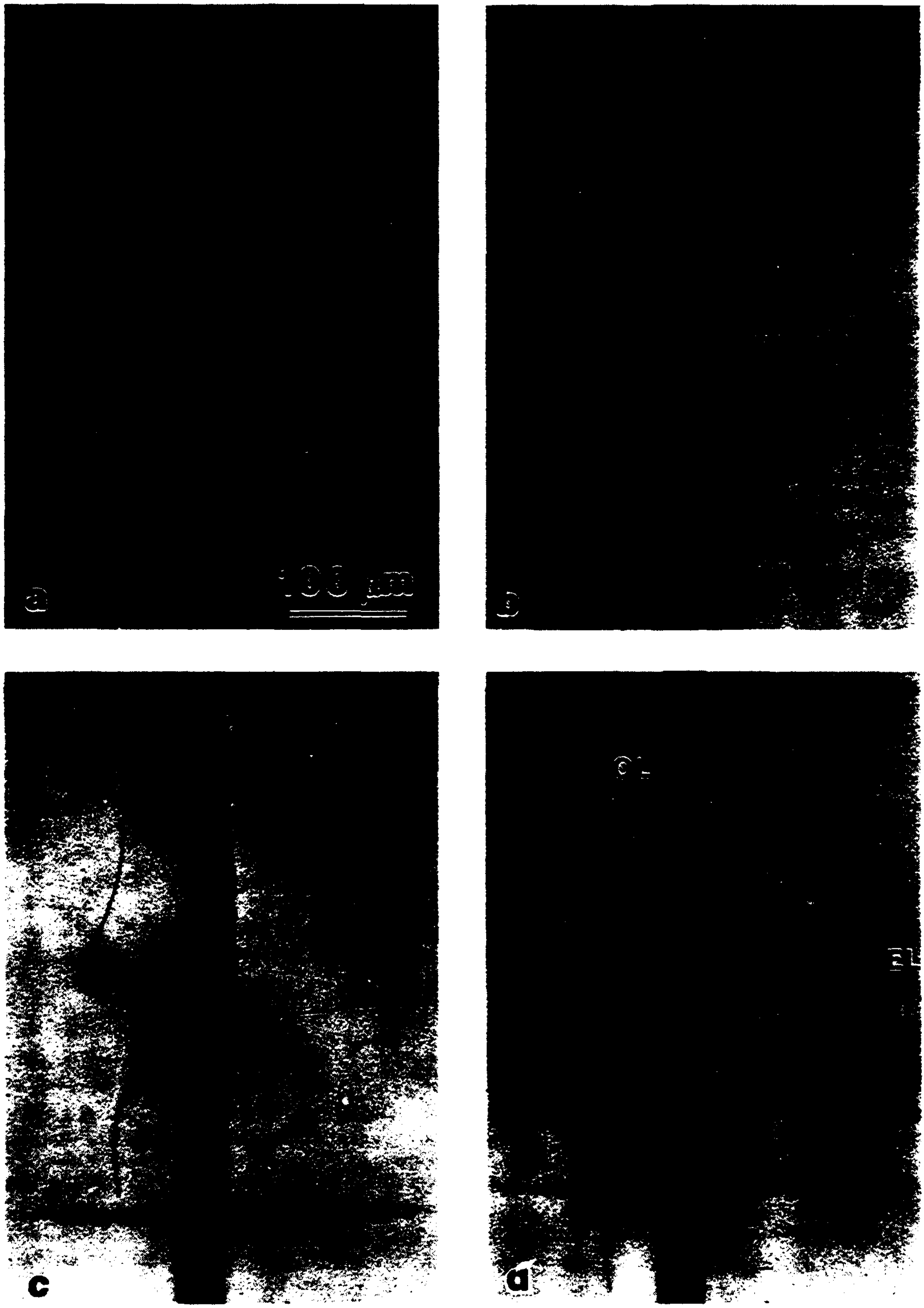

FIG. 1. Reflected-light micrographs showing the evolution of ortho-lateral (OL) and extended-lateral (EL) cracks after failure from a 20 N indentation in a soda-lime-silica glass bar specimen: (a) as-indented, (b) 2 min after failure in four-point bend, (c) 30 min, and (d) 24 h. Indentation and subsequent bending tests were carried out in the presence of dry silicone oil.

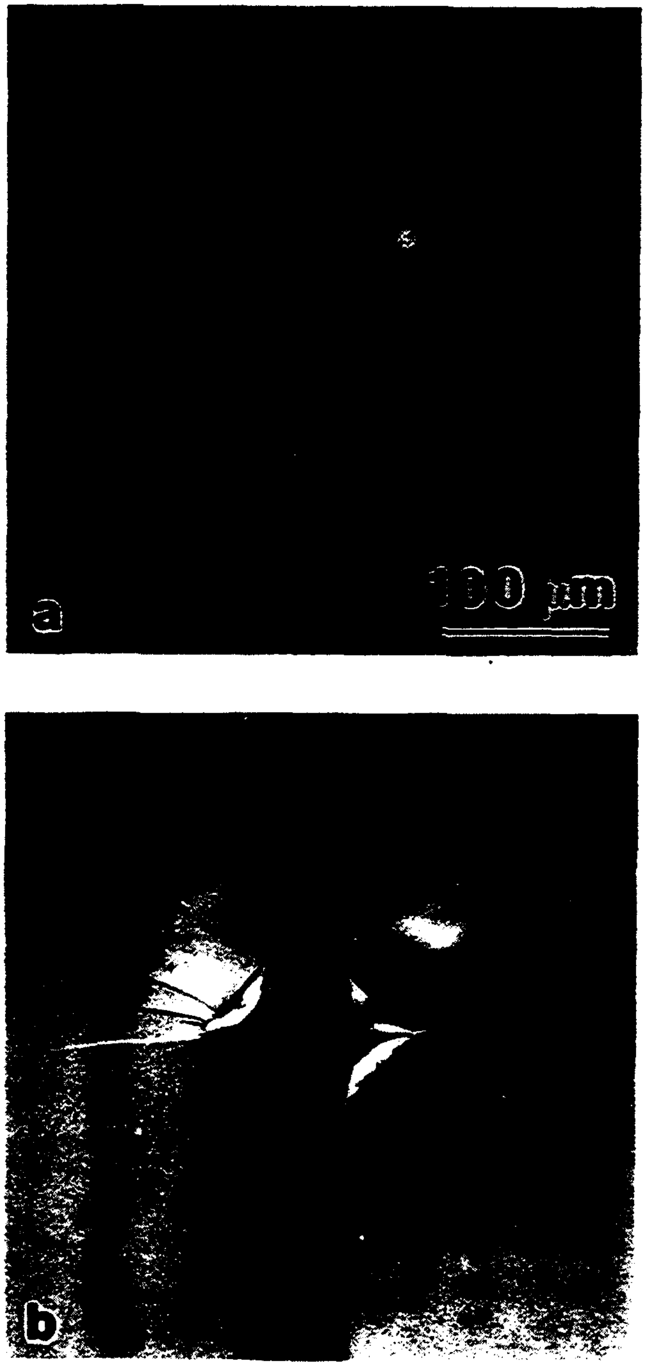

FIG. 2. Reflected-light micrographs of annealed 20 N indentation in a soda-lime-silica glass bar specimen: (a) as-annealed and (b) 24 h after failure in four-point bend.

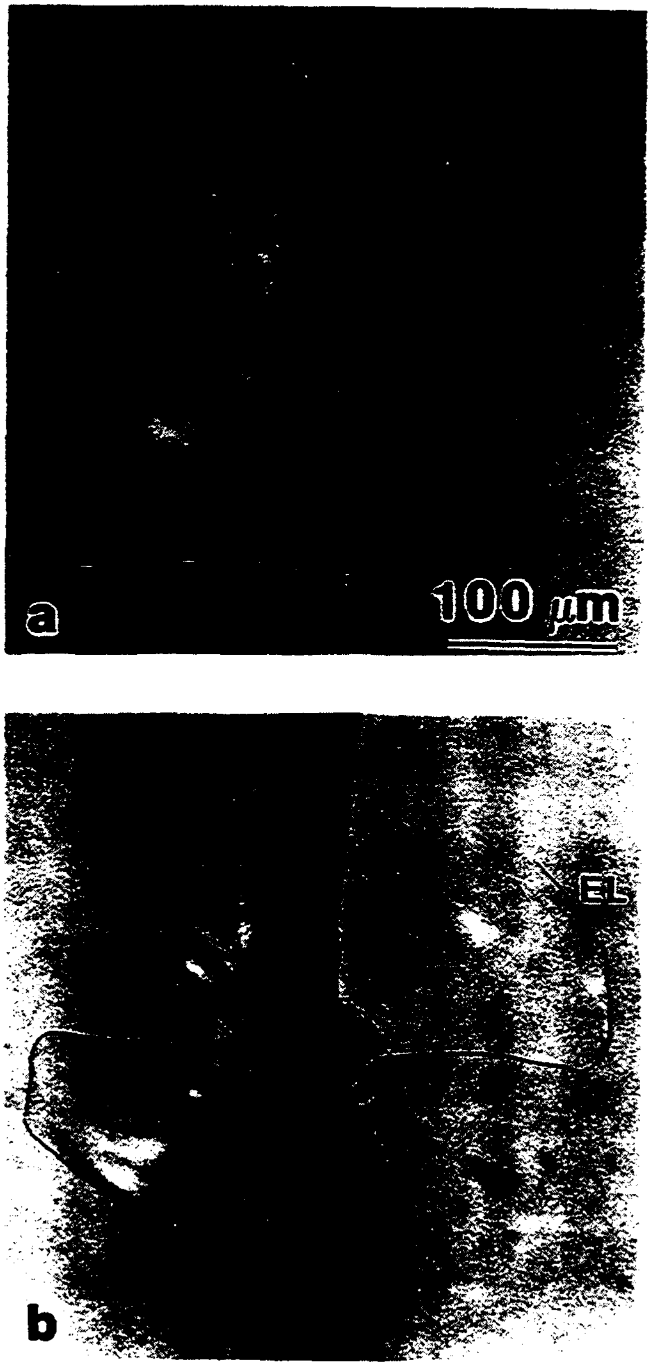

FIG. 3. Reflected-light micrographs of a 30 N indentation in a sapphire disk specimen: (a) as-indented and (b) 24 h after failure in biaxial flexure.

Table I). Comparative experiments with Al_2O_3 (single-crystal and polycrystalline), which have a relatively higher elastic modulus to hardness ratio (E/H) and thus a greater magnitude of the indentation-contact-field stress,[4] suggest that the phenomenon of ortho-lateral cracking is not limited to glass (see Table I).

On the other hand, in spite of an even higher E/H value, lack of any postfailure subsidiary cracking in polycrystalline MgO is rather surprising. At this juncture we do not have a definite answer as to why this is so in the case of MgO. A possible explanation may lie in the fact that indentations in MgO do not produce well-behaved cracks; cracks forming at various angles to the indentation diagonals are evident from Fig. 5(a). Also, the cracks were observed to interact with the microstructure due to the coarse-grained nature of the

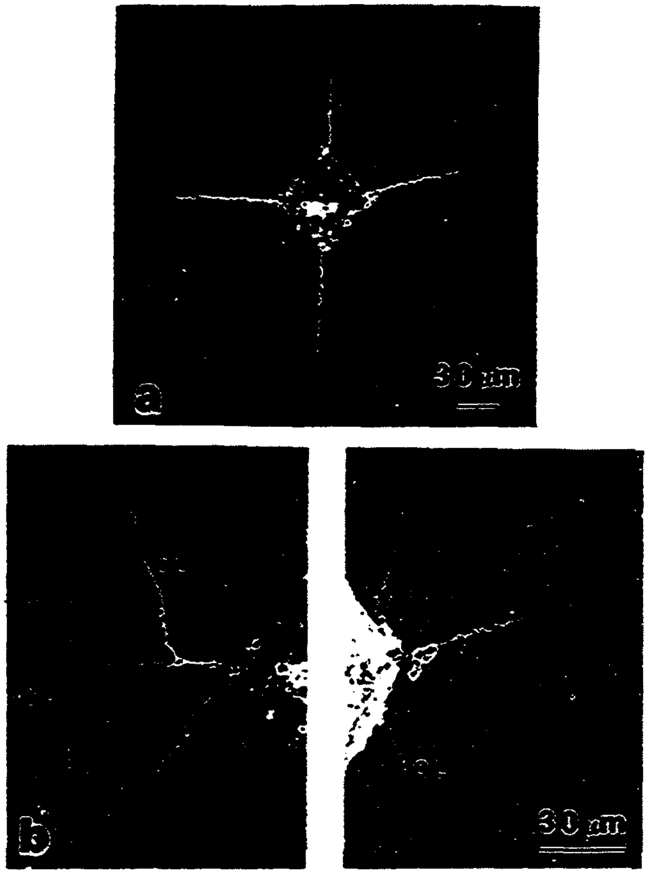

FIG. 4. Secondary electron SEM micrographs of a 50 N indentation in a polished and etched polycrystalline Al_2O_3 bar specimen: (a) as-indented and (b) 24 h after failure in a four-point-bend. Ortho-lateral cracks are denoted by OL.

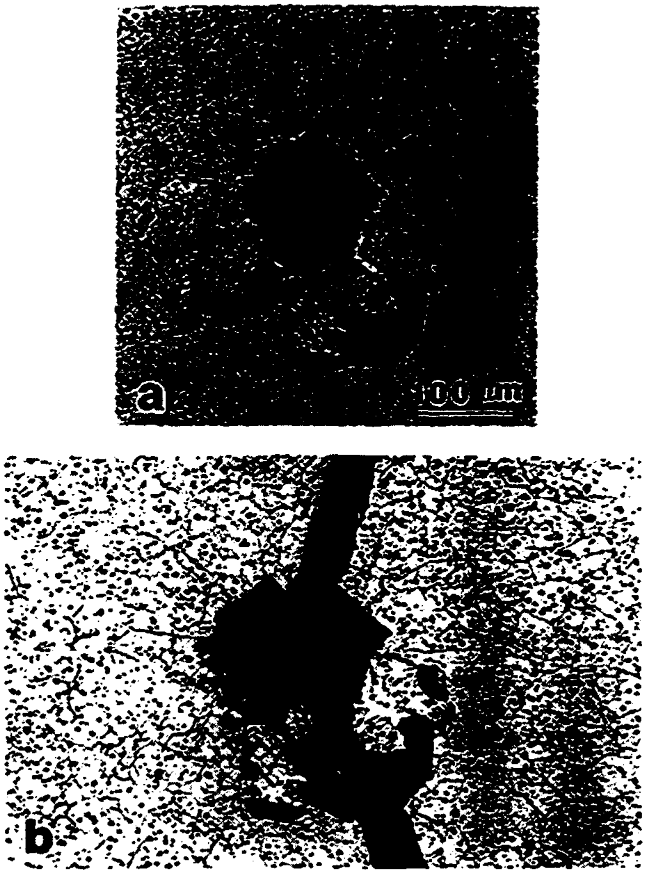

FIG. 5. Reflected-light micrographs of a 50 N indentation in a polished and etched polycrystalline MgO bar specimen: (a) as-indented and (b) 24 h after failure in four-point bend. Note the irregular cracking pattern around the indentation in (a).

MgO, precluding a clear picture of the cracking pattern (see also e.g., Cook and Liniger[17]).

Now we discuss some implications of postfailure subsidiary cracking in brittle solids: (a) Flaws in ceramics due to second-phase inclusions[2,18] and contact damage (e.g., indentation)[4] are usually accompanied by residual tensile stresses. The observation of postfailure subsidiary cracking from indentations suggests that residual-stress-driven flaws may remain active even after specimen failure from those flaws. (b) Our observation of the evolution of the subsidiary cracks from indentations beginning immediately after specimen-failure has led us to the conclusion that such a phenomenon is truly *postfailure*. Since the subsidiary cracks fully develop *soon* after specimen-failure, fractography of such failure-origin sites in ceramics long after failure is likely to lead to erroneous conclusions. There is a real danger of associating the subsidiary cracking from residual-stress-driven flaws with the propagation of the primary crack to failure, e.g., microcracking close to the fracture surface in two-phase ceramics. (c) Sliding contact with brittle surfaces can cause severe damage and result in microfracture from those contact-damage sites.[2] Repeated sliding is quite likely to result in the fracture of the previous contact-damage sites leading to subsidiary cracking, thereby further degrading wear properties. (d) In view of the great significance of classic-lateral cracking in erosion and wear, model experiments have been carried out to understand fracture behavior of classic laterals from indentations.[6,19] However, classic-lateral cracking occurs subsurface, limiting these studies only to transparent or highly translucent ceramics. On the other hand, ortho-laterals can be easily observed in opaque ceramics, and their fracture behavior appears to be quite similar to that of classic laterals. Therefore, the potential now exists to investigate the phenomenon of general lateral fracture in opaque brittle solids, which form the majority of technologically important ceramics.

V. SUMMARY

In summary, evolution of a new cracking pattern of "ortho-lateral" cracks which originate at the intact corners of the Vickers indentation after specimen-failure in brittle materials has been observed. In some instances

TABLE I. Summary of postfailure observations of subsidiary cracking in some brittle solids.

Material	E/H	OL and EL cracking
Soda-lime-silicate glass	$11.9^{2,3}$	
Four-point bend		Yes
Biaxial flexure		Yes
Annealed (four-point bend)		No
Sapphire	$18.0^{2,3}$	
Four-point bend		Yes[a]
Biaxial flexure		Yes[a]
Polycrystalline Al_2O_3 (four-point bend)	21.3^{3}	Yes
Polycrystalline MgO (four-point bend)	$52.6^{17,18}$	No

[a] Extended laterals were found to dominate.

postfailure extension of the classic laterals toward the surface has also been demonstrated. A simple model suggests that residual tensile stress from the combined effects of the indentation-plastic cavity and generation of a stress-free plane (fracture surface), similar to that in classic-lateral cracking, acting normal to the fracture surface is responsible for the subsidiary cracking. Lack of any postfailure subsidiary cracking from annealed indentation sites in glass supports this model. Postfailure subsidiary cracking has some implications concerning residual-stress-driven flaws, postmortem fractography, and wear in ceramics.

ACKNOWLEDGMENTS

The author thanks E. R. Fuller, Jr., B. R. Lawn, and R. F. Cook for fruitful discussions, and K. Meares for providing the MgO specimens. This work was supported by a grant from the United States Air Force Office of Scientific Research.

REFERENCES

1. B. R. Lawn and T. R. Wilshaw, J. Mater. Sci. **10**, 1049 (1975).
2. B. R. Lawn, *Fracture of Brittle Solids*, 2nd ed. (Cambridge University Press, Cambridge, 1993, in press).
3. R. F. Cook and G. M. Pharr, J. Am. Ceram. Soc. **73**, 787 (1990).
4. B. R. Lawn, A. G. Evans, and D. B. Marshall, J. Am. Ceram. Soc. **63**, 574 (1980).
5. S. S. Chiang, D. B. Marshall, and A. G. Evans, J. Appl. Phys. **53**, 298 (1982).
6. D. B. Marshall, B. R. Lawn, and A. G. Evans, J. Am. Ceram. Soc. **65**, 561 (1982).
7. B. R. Lawn and M. V. Swain, J. Mater. Sci. **10**, 113 (1975).
8. B. J. Hockey and B. R. Lawn, J. Mater. Sci. **10**, 1275 (1975).

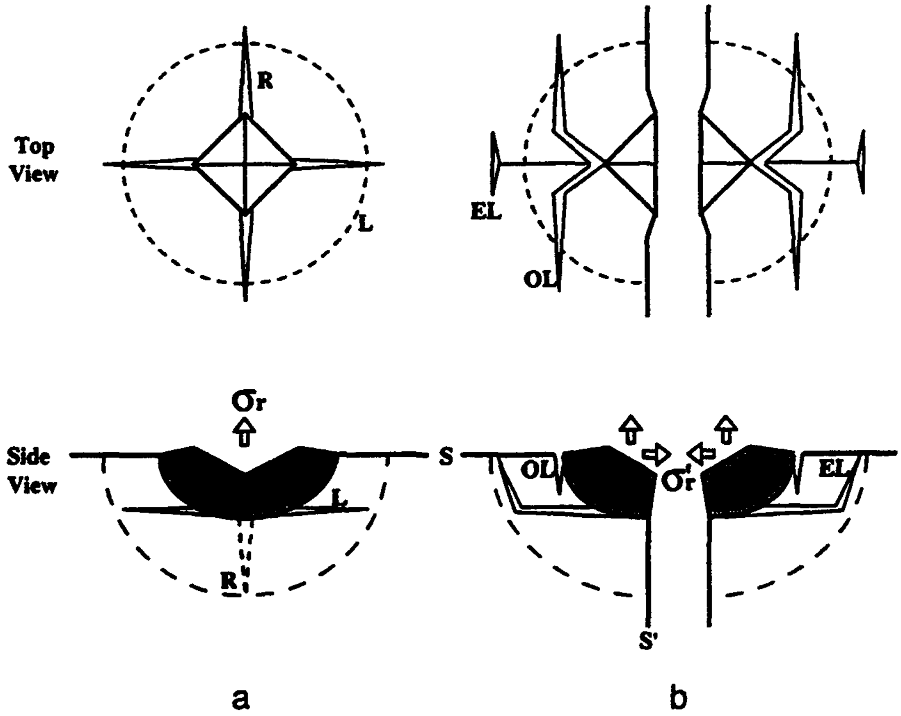

FIG. 6. Proposed model for postfailure subsidiary cracking: (a) top and side views of as-indented specimen (L denotes classic laterals; R denotes radials) and (b) top and side views of specimen after failure (OL and EL represent ortho and extended laterals, respectively; shaded region represents plastic cavity). Specimen surface and new fracture surfaces are denoted by S and S', respectively. σ_r represents the residual tensile stress before failure, and σ_r' represents the tensile stress generated by the fracture of the indentation cavity.

9. M. V. Swain and J. T. Hagan, J. Phys. D: Appl. Phys. **9**, 2201 (1976).
10. B. R. Lawn and D. B. Marshall, J. Res. Natl. Bur. Stand. **89**, 435 (1984).
11. A. G. Evans and T. R. Wilshaw, Acta Metall. **24**, 939 (1976).
12. A. W. Ruff and S. M. Wiederhorn, *Materials Erosion: Treatise on Materials Science and Technology*, edited by C. M. Preece (Academic Press, New York, 1979), Vol. 16.
13. B. R. Lawn, Wear **33**, 369 (1975).
14. P. Chantikul, S. J. Bennison, and B. R. Lawn, J. Am. Ceram. Soc. **73**, 2419 (1990).
15. B. R. Lawn, K. Jakus, and A. C. Gonzalez, J. Am. Ceram. Soc. **68**, 25 (1985).
16. M. D. Thouless, Acta Metall. et Mater. **38**, 1135 (1990).
17. R. F. Cook and E. G. Liniger, J. Mater. Sci. **27**, 4751 (1992).
18. R. W. Davidge, *Mechanical Behavior of Ceramics* (Cambridge University Press, Cambridge, 1979).
19. R. F. Cook and D. H. Roach, J. Mater. Res. **1**, 589 (1986).

Reprinted from the Journal of the American Ceramic Society, Vol. 76, No. 9, September 1993

journal

J. Am. Ceram. Soc., 76 [9] 2235–40 (1993)

Model for Toughness Curves in Two-Phase Ceramics: I, Basic Fracture Mechanics

Brian R. Lawn,[*] Nitin P. Padture,[*,†] Linda M. Braun,[*] and Stephen J. Bennison[*,‡]

Ceramics Division, Materials Science and Engineering Laboratory, National Institute of Standards and Technology, Gaithersburg, Maryland 20899

A fracture mechanics model is presented for the toughening of ceramics by bridging from second-phase particles, resulting in toughness curve (*T*-curve) behavior. It is assumed that the second-phase particles are in a state of residual thermal expansion dilatational mismatch relative to the matrix. In the long-crack region, these stresses augment frictional sliding stresses at the interphase boundaries, enhancing the crack resistance; in the short-crack region, the same stresses drive the crack, diminishing the crack resistance. The principal manifestation of these countervailing influences is a reduced sensitivity of strength to initial flaw size, i.e., an increased flaw tolerance. In seeking to incorporate these key physical elements, our model opts for mathematical simplicity by assuming uniformly distributed stresses in two bridging domains: in the first, at small crack-wall separations, a constant opening stress; in the second, at larger separations, a constant closing stress. The uniform crack-plane distributions allow for simple closed-form solutions of the crack *K*-field equations, and thence an analytical formulation for the *T*-curve. Indentation–strength data on a "reference" Al_2O_3/Al_2TiO_5 ceramic composite are used to demonstrate the main theoretical predictions and to calibrate essential parameters in the *T*-curve formulation. The utility of the model as a route to microstructural design is addressed in Part II.

I. Introduction

It is now acknowledged that the toughness of monophase ceramics can exhibit a crack-size dependence, the so-called *toughness curve* (*T*-curve) or *resistance curve* (*R*-curve).[1–7] In nontransforming ceramics the *T*-curve is attributable principally to a mechanism of "bridging" by frictional grain slideout, greatly enhanced in noncubic materials by thermal expansion anisotropy stresses.[6] A characteristic of such ceramics is "flaw tolerance",[3–5,7–17] i.e., a diminished dependence of strength σ_F on initial flaw size c_f, relative to traditional "Griffith" behavior ($\sigma_F \propto c_f^{-1/2}$). Flaw tolerance in monophase ceramics may be enhanced by scaling up the grain size.[18] Beyond a *limiting* grain size, however, microcracking occurs spontaneously through the bulk material, with a consequent degradation of strength. These characteristics imply an element of compromise in materials design, e.g., increased strength in the long-crack region at the potential expense of bulk microcracking and reduced wear resistance in the short-crack region.[19]

Additions of a second phase can augment the *T*-curve behavior, well beyond any "law of mixtures," by enhancing the effectiveness and density of bridges. This is the underlying philosophy of reinforced composites. An important element in the materials design is the control of volume fraction and particle size, as well as internal residual stress. Increasing the volume fraction enhances the density of active bridges; increasing the particle size enhances the scale of these bridges. It follows that, with a proper understanding of these factors, one may better tailor microstructures for specified structural applications.

In the present study we extend the theory of grain bridging from monophase ceramics to two-phase ceramics, with special reference to alumina-matrix composites containing aluminum titanate particulate reinforcement.[6,20,21] Aluminum titanate is chosen as a second phase because of its large thermal expansion mismatch relative to alumina, so as to maximize the intensity of internal residual stresses at the bridge sites. Our endeavor is to establish a simple fracture mechanics model for the *T*-curve in this class of ceramic. In emphasizing simplicity, we are prepared to sacrifice mathematical rigor in the model, but not at the expense of physical essentials. Thus, we retain our capacity to incorporate basic microstructural elements, volume fraction, particle size, and residual stress, as governing microstructural variables in the description. Experimental indentation–strength data on the composite materials will be used to illustrate the versatility of the model, most notably in the short-crack region.

The study is presented in two parts. In Part I we outline the basic theory and analyze the principal features of the *T*-curve for our composite material. In Part II we investigate the effects of microstructural variables on the *T*-curve and associated flaw tolerance, with consideration of restrictions imposed by bulk microcracking limits.

II. Theoretical *K*-Field Analysis

We begin by deriving *K*-field relations for cracks in an otherwise homogeneous ceramic matrix with bridging second-phase particles. In developing these relations we shall borrow from earlier theoretical treatments for monophase ceramics[13] and fiber-reinforced composites,[22] but with the simplification of continuous and uniformly distributed (Barenblatt–Dugdale) bridging stresses over the crack interface. The analysis will be used to determine *T*-curve and strength formalisms for materials with indentation short cracks.

(1) Stress-Separation Function

Consider two surfaces bridged by second-phase particles over a separation $2u$ (Fig. 1). We concern ourselves with crack areas large relative to that occupied by a single particle, so that a distribution of *discrete* force–separation functions may be replaced by a *continuous* stress–separation function, $s(u)$, say. We shall regard $s(u)$ as a positive quantity (shielding) when it acts to close the interface; this convention is consistent with an enhanced long-crack toughness. At the same time, we recognize the need to allow for the possibility of negative $s(u)$ (antishielding) at small separations, so as to allow for microcracking in the short-crack region.

D. K. Shetty—contributing editor

Manuscript No. 195174. Received October 27, 1992; approved May 28, 1993.

Supported by the U.S. Air Force Office of Scientific Research and E. I. duPont Nemours and Company Inc.

[*] Member, American Ceramic Society.

[†] Guest Scientist, from Department of Materials Science and Engineering, Lehigh University, Bethlehem, PA 18015.

[‡] Now at Experimental Station, E. I. DuPont Nemours and Company, Wilmington, DE 19880–0356.

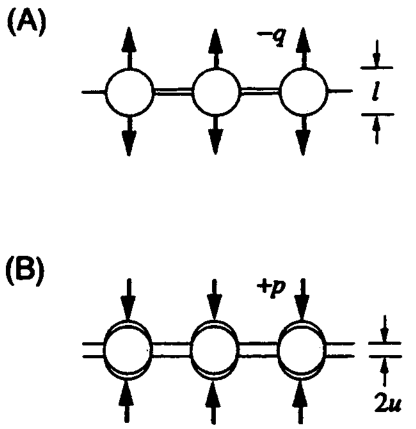

Fig. 1. Schematic diagram depicting interaction of second-phase particles with separating matrix walls. (A) Crack opening at small separations, due to residual outward pressure from compressed particles. (B) Bridging at large separations, from frictional tractions at sliding grain-matrix interphase boundaries.

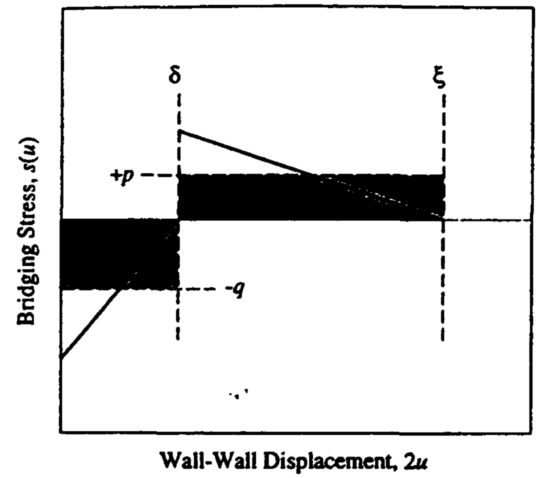

Fig. 2. Stress–separation function, $s(u)$, for system in Fig. 1. Shaded areas indicate approximations of uniform stress $s = +p$ and $s = -q$ in the two domains. (Positive sign denotes *closure* bridging stress.)

We therefore assume the bridging particles to exist in a state of residual compressive stress at the uncracked interface, so that they initially exert opening stresses on the matrix walls. As the walls separate, these opening stresses relax. At the same time, the particles debond from the matrix. At larger separations the particles begin to slide out of the constraining matrix but are restrained at those interphase boundary facets where the thermal expansion mismatch stresses are compressive. Resistance to sliding pullout then arises principally from Coulombic frictional tractions.[13] For simplicity, we assume that the transition to frictional sliding occurs when the precompressed springs are *just* relaxed, and neglect any resistance stresses due to debonding.

The function $s(u)$ at small u is then determined as the opening stress exerted on the matrix over the section area of a single particle, relative to the interface area occupied by that particle:

$$s(u) = -V_f(1 - V_f)(1 - 2u/\delta)\sigma_R \qquad (0 \leq 2u \leq \delta) \qquad \text{(1a)}$$

where V_f is the volume fraction, σ_R is the thermal expansion mismatch stress at the interphase boundary, and δ is the separation at which the residual elastic stresses are relaxed. (The factor $1 - V_f$ is to allow for a reduction in available matrix volume at increasing V_f, with $V_f < 0.5$.) Similarly, $s(u)$ at large u is determined as the closing stress exerted on the matrix over the interphase frictional contact area of the particle, again relative to the fractional interface area:[13]

$$s(u) = +V_f(1 - V_f)(1 - 2u/\xi)\eta\xi\mu\sigma_R/l \qquad (\delta \leq 2u \leq \xi) \qquad \text{(1b)}$$

where l is the particle diameter, η is a particle–matrix perimeter/area factor relative to l at the crack plane,[13] μ is the coefficient of sliding friction, and ξ is the separation at which the particle disengages ($\delta << \xi$, usually). The composite $s(u)$ function of Eq. (1) is plotted in Fig. 2.

While acknowledging the *physical* sensibility of the *linear* ("tail") stresses in the $s(u)$ function,[8,13] it is nevertheless *mathematically* expedient to replace these by *uniform* stresses over the pertinent bridging zones, as indicated in Fig. 1. Let us therefore define "averaged" values p and q over the two bridging zones:

$$s(u) = -q = -\frac{1}{2}V_f(1 - V_f)\sigma_R \qquad (0 \leq 2u \leq \delta) \qquad (2a)$$

$$s(u) = +p = \frac{1}{2}\eta\mu\varepsilon_\xi V_f(1 - V_f)\sigma_R \qquad (\delta \leq 2u \leq \xi) \qquad (2b)$$

with conjugate size-independent strain terms

$$\varepsilon_\delta = \delta/l \qquad (3a)$$

$$\varepsilon_\xi = \xi/l \qquad (3b)$$

(2) *K-Field and T-Curve*

Now consider the stress–separation function of Eq. (2) in the context of pennylike short cracks, to simulate the evolution of flaws (natural or artificially induced) under the action of an externally applied tensile stress. We assume that in their critical growth stages to failure the cracks traverse a large number of particles, so that we may be justified in using the *continuous* stress function $s(u)$ to describe the ensuing strength characteristics. (This assumption will be examined when we compute the cohesion-zone dimensions for our composite material later.)

Accordingly, the stress distribution along the coordinate r of a penny crack (Fig. 3) is

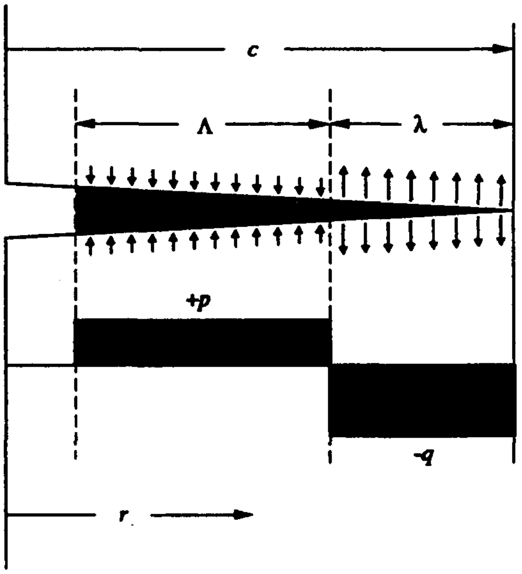

Fig. 3. Equivalent stress distribution, $s(r)$, for bridged crack.

$$s(r) = -q \qquad (c - \lambda \leq r \leq c) \tag{4a}$$

$$s(r) = p \qquad (c - \Lambda - \lambda \leq r \leq c - \lambda) \tag{4b}$$

with c the crack radius. The bridging zone dimensions λ and Λ scale with the crack-opening displacements δ and ξ of Fig. 1 via some crack profile relation (with $\lambda << \Lambda$, usually). In part I, the need for knowledge of the profile may be avoided, by simplistically treating λ and Λ as adjustable parameters; this will not be so in Part II, when we consider the role of microstructural variables.

The "crack-tip" K-field, K_*, for an equilibrium crack under applied stress σ_A in a bridging material contains a microstructural component, K_μ:

$$K_*(c) = \psi\sigma_A c^{1/2} + K_\mu(c) = T_0 \tag{5}$$

with T_0 the intrinsic toughness of the matrix material (grain boundary toughness in the case of intergranular fracture). Putting $-K_\mu = T_\mu$ (so that a true *shielding* term appears as a *positive* contribution to the toughness), we may write the "global" K-field as

$$K_A(c) = \psi\sigma_A c^{1/2} = T_0 - K_\mu(c)$$

$$= T_0 + T_\mu(c) = T(c) \tag{6}$$

which defines the toughness curve, or T-curve, $T(c)$.

To determine $T_\mu(c)$, we integrate the bridging stresses of Eq. (4) over the entire crack area, using the conventional Green's function expression for pennylike cracks:[23]

$$T_\mu(c) = 2\alpha/(\pi c)^{1/2}\int_0^c rs(r)\mathrm{d}r/(c^2 - r^2)^{1/2} \tag{7}$$

where α is a geometrical coefficient to allow for interactions with specimen and crack-neighbor free surfaces. For indentation radial cracks, one generally defines a coefficient $\psi = 2\alpha/\pi^{1/2}$, to allow for *half*-penny geometry, any ensuing distortions into elliptical fronts, and perturbations from orthogonal radial and lateral cracks. Integration within three different regions of crack size gives the microstructural function

$$T_\mu(c) = -\psi q c^{1/2} \qquad (0 \leq c \leq \lambda) \tag{8a}$$

$$T_\mu(c) = \psi q c^{1/2}\{1 - [1 - (1 - \lambda/c)^2]^{1/2}\}$$
$$- \psi q c^{1/2}[1 - (1 - \lambda/c)^2]^{1/2}$$
$$(\lambda \leq c \leq \Lambda + \lambda) \tag{8b}$$

$$T_\mu(c) = \psi p c^{1/2}\{[1 - (1 - \Lambda/c - \lambda/c)^2]^{1/2}$$
$$- [1 - (1 - \lambda/c)^2]^{1/2}\}$$
$$- \psi q c^{1/2}[1 - (1 - \lambda/c)^2]^{1/2}$$
$$(\Lambda + \lambda \leq c) \tag{8c}$$

The ensuing $T(c)$ function in Eq. (6) may be usefully simplified in certain regions of c by making some reasonable approximations. In the limit of a very small tensile zone, λ becomes independent of c ("small-zone," or "Barenblatt," approximation), and Eq. 8(b) results in a T-curve that is linear in $c^{1/2}$:

$$T(c) = T_0 - \psi(p + q)(2\lambda)^{1/2} + \psi p c^{1/2}$$
$$(\lambda << c \leq \Lambda + \lambda) \tag{9}$$

In the limit of very long cracks, Eq. (8c) results in

$$T(c) = T_0 - \psi(p + q)(2\lambda)^{1/2} + \psi p(2\Lambda)^{1/2}$$
$$(\Lambda + \lambda << c) \tag{10}$$

corresponding to the plateau toughness.

(3) *Indentation–Strength*

Now let us extend the analysis to Vickers indentation flaws, so that we may use indentation–strength data to evaluate the T-curve parameters in Eqs. (8–10) objectively for our test material (Sect. III).

It is necessary now to include one further term in our formulation, to allow for the residual K-field associated with the irreversible contact deformation at indentation load P. The equilibrium crack-tip K-field relation of Eq. (5) is modified to[13,24]

$$K_*(c) = \psi\sigma_A c^{1/2} + \chi P/c^{3/2} + K_\mu(c) = T_0 \tag{11}$$

corresponding to a global K-field

$$K_A'(c) = \psi\sigma_A c^{1/2} + \chi P/c^{3/2}$$

$$= T_0 - K_\mu(c) = T_0 + T_\mu(c) = T(c) \tag{12}$$

The residual-contact term provides additional stabilization to the crack. The inert strength for indentation flaws is the configuration $\sigma_A = \sigma_M$, $c = c_M$ at which the transposed function

$$\sigma_A(c) = (1/\psi c^{1/2})[T(c) - \chi P/c^{3/2}] \tag{13}$$

from Eq. (12) satisfies the requirement $\mathrm{d}\sigma_A(c)/\mathrm{d}c = 0$ for a maximum, corresponding to the "tangency condition"

$$\mathrm{d}K_A'(c)/\mathrm{d}c = \mathrm{d}T(c)/\mathrm{d}c \tag{14}$$

in a conventional T-curve construction.[25]

Equation (13) is not readily solved analytically for σ_M, c_M using the general $T_\mu(c)$ relations in Eqs. (6) and (8). However, an exact solution *is* obtainable in the region $\lambda << c \leq \Lambda + \lambda$, using Eq. (9). If we write $\sigma_A' = \sigma_A - p$, $T_0' = T_0 - \psi(p + q)(2\lambda)^{1/2}$, Eq. (11) then reduces to the exact same form as the standard relation for materials with single-valued toughness,[13,24]

$$K_*(c) = \psi\sigma_A' c^{1/2} + \chi P/c^{3/2} = T_0' \tag{15}$$

Solving for the instability configuration in Eq. (14), or by direct inspection of the standard solutions for such homogeneous materials,[26,27] one obtains

$$c_M = \{4\chi P/[T_0 - \psi(p + q)(2\lambda)^{1/2}]\}^{2/3} \tag{16a}$$

$$\sigma_M = p + 3[T_0 - \psi(p + q)(2\lambda)^{1/2}]^{4/3}/4\psi(4\chi P)^{1/3} \tag{16b}$$

We shall assert that, because of the long precursor extensions from initial size c_0 to final size c_M for indentation cracks, the specification $\lambda << c \leq \Lambda + \lambda$ poses no severe restriction to the validity of Eq. (16). Note that for large P the strength is enhanced relative to the homogeneous matrix material ($p = 0 = q$), because of the lower-limiting stress p; at small P the strength is reduced, because of the diminished effective toughness T_0' (square bracket term). Hence, the formalism embodies the essential quality of flaw tolerance.

III. Fits to Data for Two-Phase Al_2O_3/Al_2TiO_5 Composite

(1) *Experimental Procedure*

We illustrate the above formulation with indentation–strength data from a fine-grain alumina matrix reinforced by homogeneously distributed aluminum titanate particles (Al_2O_3/Al_2TiO_5). The fabrication procedure for this composite material has been described elsewhere.[20,21,28,29] Materials were fabricated with a starting grain size <2 μm, and the particles subsequently grown by a prescribed aging heat treatment.[21] Densities were measured using the Archimedes method, >98% in all cases, and the particle size by a lineal intercept method.[21] In Part I we focus on a reference composition with volume fraction V_f =

0.20 and mean second-phase particle size l = 4.0 μm. The alumina grain size is <7 μm, so that there is negligible contribution to the T-curve from the matrix itself.[18] A micrograph of the microstructure is shown in Fig. 4.

Additional batches of the alumina-matrix material were also fabricated with different values of V_f and l, for consideration in the scond part of this study (see Part II).

Specimens for strength testing were prepared as disks, 20-mm diameter and 2.5-mm thickness, with one surface polished to better than 1 μm. A Vickers indentation was made at the center of each polished surface, at prescribed load P, and covered with a drop of silicone oil. The disks were then broken in biaxial flexure, indentations on the tensile side, with 4-mm-diameter flat loading on a 15-mm-diameter three-ball support. These tests were run in "fast" loading (<10 ms failure time), to ensure "inert" conditions. Post-mortem examinations were made of all broken specimens to confirm failure initiation from the indentation sites.

The indentation–strength, $\sigma_M(P)$, results are plotted as the data points in Fig. 5. Error bars are standard deviation bounds for 4–6 tests at each indentation load.

(2) *Evaluation of T-Curve Parameters from Indentation–Strength Data*

Our approach is to evaluate the short-crack T-curve for our alumina-based composite from the $\sigma_M(P)$ data in Fig. 5, following a procedure developed in an earlier study.[24] Using coefficients ψ = 0.77 and χ = 0.076 calibrated on a fine-grain alumina reference material in that earlier study, we first generate $K'_A(c)$ functions (Eq. (12)) for each of the $\sigma_M(P)$ data points. The $T(c)$ function is then determined as the "envelope of tangency points" (Eqs. (12) and (14)) fitted to the family of $K'_A(c)$ functions, inserting a calibrated value of T_0 = 2.75 MPa·m$^{1/2}$ from the earlier study in Eq. (6) and adjusting the microstructural parameters in Eq. (8).

We do this in Fig. 6, as toughness T against crack-size quantity $c^{1/2}$. In this plot the $K'_A(c)$ functions are shown as the inverted solid curves. The heavy curve is a fit of the $T(c)$ function in Eqs. (6) and (8). To obtain this fit, we first used a least-squares procedure to evaluate the following parameters for the "reference state" at V_f = 0.20, l = 4.0 μm:

$$p = 325 \text{ MPa} \tag{17a}$$

$$(p + q)(2\lambda)^{1/2} = 3.51 \text{ MPa·m}^{1/2} \tag{17b}$$

$$\Lambda = 180\ \mu\text{m} \tag{17c}$$

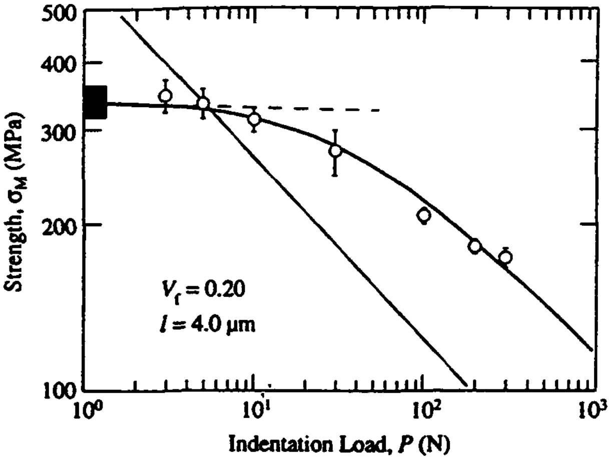

Fig. 5. Indentation–strength plot for reference Al_2O_3/Al_2TiO_5 composite (V_f = 0.20, l = 4.0 μm). Data points are means and standard deviations of 4–6 tests per load. Solid curve is generated theoretically from the condition $d\sigma_A(c)/dc = 0$ in Eq. (13) (using microstructural parameters evaluated from the T-curve fit in Fig. 6). Dashed curve is "plateau" approximation from Eq. (16b). Shaded line of slope −1/3 represents indentation–strength results for base fine-grain matrix alumina.

Recall from Eq. (9) that these parameters completely determine an approximate "linear" T–$c^{1/2}$ representation of $T(c)$, with slope p and T-axis intercept $T_0 - \psi(p + q)(2\lambda)^{1/2}$; this representation is included as the inclined dashed curve in Fig. 6. Observe the continuous rollover in the complete $T(c)$ function to saturation at $c >> \Lambda + \lambda$, as the fully developed bridging zone begins to translate with the crack.

Since the strength data in Fig. 6 do not extend down into the region $c < \lambda$, we need additional information to determine the full set of microstructural parameters in the T-curve function. Precise values of the remaining parameters are not crucial to our treatment at this juncture, so we take

$$\lambda = 7.0\ \mu\text{m} \tag{18a}$$

$$q = 613 \text{ MPa} \tag{18b}$$

to match estimates of the short-crack size ($c \approx 2\lambda$) at first microcracking in Al_2O_3/Al_2TiO_5 composites with scaled-up microstructures (see Part II). Observe also the minimum at

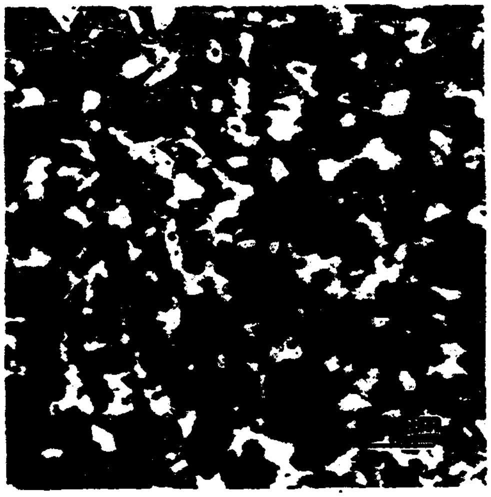

Fig. 4. Scanning electron micrograph showing Al_2TiO_5 particles (V_f = 0.20, white phase) in Al_2O_3 matrix (dark phase), for reference composite.

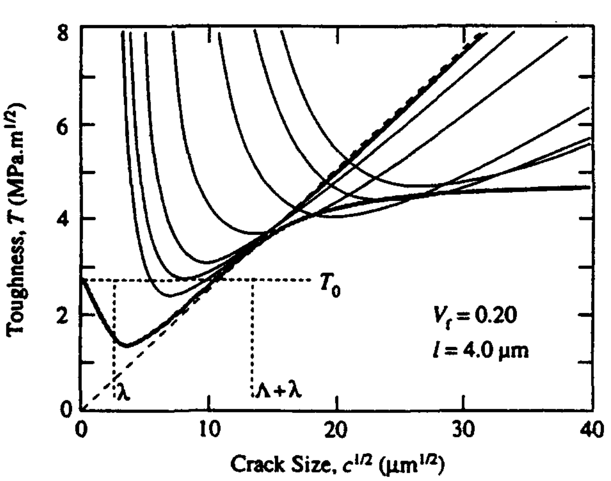

Fig. 6. T-curve constructions for reference Al_2O_3/Al_2TiO_5 composite. Family of inverted curves represents $K'_A(c)$ functions in Eq. (12) evaluated for (σ_M,P) data points in Fig. 5. Shaded curve is fitted envelope $T(c)$ function from Eqs. (6) and (8).

small c, signifying a degradation in toughness at $c < 2\lambda$ from the initial crack-opening action of second-phase particles.

With the estimates $\eta \approx 4$ (rectangular or circular cross-section particle) and $\varepsilon_{\xi} \approx 0.050$ (Sect. III(1)), we may use Eq. (2) to evaluate the composite material quantities

$$\sigma_R = 7.7 \text{ GPa} \qquad (19a)$$

$$\mu \approx 2.7 \qquad (19b)$$

Given the microstructural T-curve parameters in Eqs. (17) and (18), complete theoretical indentation–strength, $\sigma_M(P)$, curves may now be regenerated by seeking extremum solutions of Eq. (13). Figure 5 includes curves thus regenerated, using the full $T(c)$ function in Eqs. (6) and (8) (solid curve) and the "linear" T–$c^{1/2}$ approximation in Eq. (9) (dashed curve). The intersection of the solid curve through the data reinforces the validity of our fitting procedure in Fig. 6.

IV. Discussion

The above analysis allows us to analyze the T-curve response of two-phase ceramics in the short-crack region using indentation–strength data. A major feature of the analysis is its relative *simplicity*. Thus, although discrete microstructural parameters are used in defining the underlying bridging stress–separation function, Eqs. (1) and (2), we are nevertheless able to regard the same bridging stresses as *continuously* distributed along the crack plane, Eq. (4). The assumption of *uniform* stresses within the bridging zones (Figs. 1 and 2) allows for analytical solutions of the K-field integral equations. The exercise is thereby reduced to something akin to a Barenblatt–Dugdale crack problem. Moreover, by calibrating λ and Λ in Eqs. (8–10) directly from experimental data, our solutions can be determined *without at this stage specifying any crack-opening displacement relation* (see, however, Part II). In this context we may note that the estimated dimension $\lambda = 7.0$ μm (Sec. III(2)) is comparable to the Al_2TiO_5 interparticle separation in Fig. 4, so the continuum approximation is open to some question in the crack-size domain to the left of the $T(c)$ minimum in Fig. 6.

One of the advantages of the present model is the clear way it identifies essential T-curve and associated flaw tolerance characteristics with specific elements of the microstructure. Thus we note in Eq. (9) that the *slope* of the T-curve is proportional to the bridging stress p. From Eq. (2b), this stress increases monotonically with volume fraction V_f and residual stress σ_R. We also note in Eq. (9) that the *scale* of the T-curve is limited by the bridging zone length Λ. This dimension increases with particle size l (Part II). Hence we might expect to be able to enhance the relatively modest T-curve and flaw tolerance characteristics for our material in Figs. 5 and 6 by appropriately altering the microstructure. As we shall see in Part II, such potential enhancements are ultimately limited by the onset of general microcracking.

Our simple model is not without its limitations. Replacing the tail-dominated stress–separation functions in Fig. 1 by the uniform stresses p and q has inevitable consequences in the predicted shape of the T-curve. Nevertheless, our description contains the essence of microstructural scaling and internal stress influences, and will not affect the general physical conclusions drawn in either Parts I or II of this study.

Useful estimates of the controlling microstructural parameters emerge from the data fits in Figs. 5 and 6. The residual stress $\sigma_R \approx 7.7$ GPa (Eq. (19a)) is large but is of the order of computed thermal expansion anisotropy stresses for the Al_2O_3/Al_2TiO_5 system.[21] The friction coefficient $\mu \approx 2.7$ (Eq. (19b)) is also high but is nevertheless of the same order as that obtained in an earlier bridging analysis for pure alumina[13] and is not unreasonable for sliding contacts at *pristine* (freshly debonded) surfaces.[30]

There are interesting implications in the analysis concerning the stability of flaws that evolve through the residual bridging K-field in their initial state (cf. flaws with *no* residual K-field $\chi P/c^{3/2}$ in Eq. (11)), in response to an applied stress σ_A. The appropriate $K_A(c)$ function is a straight line through the origin of a T–$c^{1/2}$ plot, with slope $\psi\sigma_A$. For the particular Al_2O_3/Al_2TiO_5 composite in Fig. 6, the intercept of the extrapolated "linear" $T(c)$ function on the T-axis, $T_0 - \psi(p + q)(2\lambda)^{1/2}$ in Eq. (9), is *positive*. Hence in Fig. 6 the $K_A(c)$ line must always intersect the $T(c)$ curve with a slope $dK_A/d(c^{1/2}) > dT/d(c^{1/2})$. Under these conditions there is no T-curve "tangency" condition. This means that, whereas indentation flaws in our material show substantial precursor crack extension in a strength test, by virtue of the additional stabilizing influence of the residual contact K-field, natural flaws should propagate spontaneously to failure at their initial size, $c = c_f$ ("Griffith failure"). Our T-curve material in Fig. 6 does nevertheless exhibit a degree of flaw tolerance: the sensitivity of the strength σ_F for unindented specimens to c_f is manifestly reduced relative to a matrix base material at $T = T_0$.[3,5,7] Note that contrary to common practice $T(c)$ cannot, even in its oversimplified form of Eq. (9), be represented as a pure *power law*; the intercept term in the T-curve function is *vital* in determining the nature of the flaw response.

This last point will be made even more compellingly when we examine the effect of microstructural variations in Part II. The real power of the present model is that, once the controlling microstructural parameters for a given material system have been calibrated, in the manner of Sect. III(2), one may use the fracture mechanics to predict how the flaw tolerance characteristics vary with the microstructure. We will find that the T-axis intercept referred to above is depressed as volume fraction and particle size are increased, ultimately becoming negative and thereby altering the entire complexion of the flaw stability.

Acknowledgments: The authors acknowledge stimulating discussions with H. Cai, E. R. Fuller, Jr., and J. L. Runyan.

References

[1] H. Hübner and W. Jillek, "Subcritical Crack Extension and Crack Resistance in Polycrystalline Alumina," *J. Mater. Sci.*, 12, 117–25 (1977).

[2] R. Knehans and R. Steinbrech, "Memory Effect of Crack Resistance during Slow Crack Growth in Notched Al_2O_3 Bend Specimens," *J. Mater. Sci. Lett.*, I [8] 327–29 (1982).

[3] B. R. Lawn and C. J. Fairbanks, "Toughness and Flaw Response in Non-Transforming Ceramics: Implications for NDE"; pp. 1023–32 in *Review of Progress in Quantitative NDE*, Vol. 6B. Edited by D. O. Thompson and D. E. Chimenti. Plenum Press, New York, 1987.

[4] R. F. Cook, C. J. Fairbanks, B. R. Lawn, and Y.-W. Mai, "Crack Resistance by Interfacial Bridging: Its Role in Determining Strength Characteristics," *J. Mater. Res.*, 2 [3] 345–56 (1987).

[5] S. J. Bennison and B. R. Lawn, "Flaw Tolerance in Ceramics with Rising Crack-Resistance Characteristics," *J. Mater. Sci.*, 24, 3169–75 (1989).

[6] S. J. Bennison, J. Rödel, S. Lathabai, P. Chantikul, and B. R. Lawn, "Microstructure, Toughness Curves and Mechanical Properties of Alumina Ceramics"; pp. 209–33 in *Toughening Mechanisms in Quasi-Brittle Materials*. Edited by S. P. Shah. Kluwer Academic Publishers, Dordrecht, The Netherlands, 1991.

[7] S. J. Bennison, N. P. Padture, J. L. Runyan, and B. R. Lawn, "Flaw-Insensitive Ceramics," *Philos. Mag. Lett.*, 64 [4] 191–95 (1991).

[8] Y.-W. Mai and B. R. Lawn, "Crack-Interface Grain Bridging as a Fracture Resistance Mechanism in Ceramics: II, Theoretical Fracture Mechanics Model," *J. Am. Ceram. Soc.*, 70 [4] 289–94 (1987).

[9] P. L. Swanson, C. J. Fairbanks, B. R. Lawn, Y.-W. Mai, and B. J. Hockey, "Crack-Interface Grain Bridging as a Fracture Resistance Mechanism in Ceramics: I, Experimental Study on Alumina," *J. Am. Ceram. Soc.*, 70 [4] 279–89 (1987).

[10] A. Reichl and R. W. Steinbrech, "Determination of Crack Bridging Forces in Alumina," *J. Am. Ceram. Soc.*, 71 [6] C-299–C-301 (1988).

[11] P. L. Swanson, "Crack-Interface Traction: A Fracture-Resistance Mechanism in Brittle Polycrystals"; pp. 135–55 in Advances in Ceramics, Vol. 22, *Fractography of Glasses and Ceramics*. Edited by J. R. Varner and V. D. Frechette. American Ceramic Society, Westerville, OH, 1988.

[12] M. Sakai and R. C. Bradt, "The Crack Growth Resistance Curves of Non-Phase-Transforming Ceramics," *Nippon Seramikkusu Kyokai Gakujutsu Ronbunshi*, 96 [8] 801–809 (1988).

[13] S. J. Bennison and B. R. Lawn, "Role of Interfacial Grain-Bridging Sliding Friction in the Crack-Resistance and Strength Properties of Nontransforming Ceramics," *Acta Metall.*, 37 [10] 2659–71 (1989).

[14] E. K. Beauchamp and S. L. Monroe, "Effect of Crack-Interface Bridging on Subcritical Crack Growth in Ferrites," *J. Am. Ceram. Soc.*, 72, 1179–84 (1989).

[15] G. Vekinis, M. F. Ashby, and P. W. R. Beaumont, "*R*-Curve Behaviour of Al_2O_3 Ceramics," *Acta Metall.*, 38 [6] 1151–62 (1990).

[16] J. Rödel, J. Kelly, and B. R. Lawn, "*In Situ* Measurements of Bridged Crack Interfaces in the SEM," *J. Am. Ceram. Soc.*, 73 [11] 3313–18 (1990).

[17] P. F. Becher, "Microstructural Design of Toughened Ceramics," *J. Am. Ceram. Soc.*, 74 [2] 255–69 (1991).

[18] P. Chantikul, S. J. Bennison, and B. R. Lawn, "Role of Grain Size in the Strength and *R*-Curve Properties of Alumina," *J. Am. Ceram. Soc.*, 73 [8] 2419–27 (1990).

[19] S.-J. Cho, B. J. Hockey, B. R. Lawn, and S. J. Bennison, "Grain-Size and *R*-Curve Effects in the Abrasive Wear of Alumina," *J. Am. Ceram. Soc.*, 72 [7] 1249–52 (1989).

[20] N. P. Padture, H. M. Chan, S. J. Bennison, J. L. Runyan, J. Rödel, and B. R. Lawn, "Flaw Tolerant Al_2O_3–Al_2TiO_5 Composites"; pp. 715–21 in Ceramic Transactions, Vol. 19, *Advanced Composite Materials*. Edited by M. D. Sacks. American Ceramic Society, Westerville, OH, 1991.

[21] J. L. Runyan and S. J. Bennison, "Fabrication of Flaw-Tolerant Aluminum–Titanate-Reinforced Alumina," *J. Eur. Ceram. Soc.*, 7, 93–99 (1991).

[22] D. B. Marshall, B. N. Cox, and A. G. Evans, "The Mechanics of Matrix Cracking in Brittle-Matrix Fibre Composites," *Acta Metall.*, 23 [11] 2013–21 (1985).

[23] B. R. Lawn, *Fracture of Brittle Solids*. Cambridge University Press, Cambridge, U.K., 1993.

[24] L. M. Braun, S. J. Bennison, and B. R. Lawn, "Objective Evaluation of Short-Crack Toughness Curves Using Indentation Flaws: Case Study on Alumina-Based Ceramics," *J. Am. Ceram. Soc.*, 75 [11] 3049–57 (1992).

[25] Y.-W. Mai and B. R. Lawn, "Crack Stability and Toughness Characteristics in Brittle Materials," *Ann. Rev. Mater. Sci.*, 16, 415–39 (1986).

[26] D. B. Marshall and B. R. Lawn, "Residual Stress Effects in Sharp-Contact Cracking: I. Indentation Fracture Mechanics," *J. Mater. Sci.*, 14 [8] 2001–12 (1979).

[27] D. B. Marshall, B. R. Lawn, and P. Chantikul, "Residual Stress Effects in Sharp-Contact Cracking: II. Strength Degradation," *J. Mater. Sci.*, 14 [9] 2225–35 (1979).

[28] N. P. Padture, S. J. Bennison, and H. M. Chan, "Flaw-Tolerance and Crack-Resistance Properties of Alumina–Aluminum Titanate Composites with Tailored Microstructures," *J. Am. Ceram. Soc.*, 76 [9] 2312–20 (1993).

[29] N. P. Padture, "Crack Resistance and Strength Properties of Some Alumina-Based Ceramics"; Ph.D. Dissertation. Lehigh University, Bethlehem, PA, 1991.

[30] X. Dong, S. Jahanmir, and S. M. Hsu, "Tribological Characteristics of α-Alumina at Elevated Temperatures," *J. Am. Ceram. Soc.*, 74 [5] 1036–44 (1991). □

Reprinted from the Journal of the American Ceramic Society, Vol. 76, No. 9, September 1993

journal

J. Am. Ceram. Soc., 76 [9] 2241–47 (1993)

Model for Toughness Curves in Two-Phase Ceramics: II, Microstructural Variables

Nitin P. Padture,*,† Julie L. Runyan,‡ Stephen J. Bennison,*,§ Linda M. Braun,* and Brian R. Lawn*

Ceramics Division, Materials Science and Engineering Laboratory, National Institute of Standards and Technology,
Gaithersburg, Maryland 20899

The fracture mechanics analysis of Part I is here extended to consider the effects of volume fraction and scale of second-phase particles on the toughness-curve properties of ceramic-matrix composites. Increasing these variables enhances the flaw tolerance of the material, but only up to certain limits, beyond which bulk microcracking occurs. These limits define domains of damage accumulation and potential strength degradation by microcrack coalescence. In the familiar approximation of elliptical crack-wall profiles, we show that the principal effects of increasing volume fraction (or expansion mismatch) and particle size is to enhance the *slope* and *scale* of the *T*-curve, respectively. We also derive expressions for the microcracking limits and use these expressions to construct a simple design diagram for characterizing the effects of microstructural variation on mechanical behavior. Indentation–strength data on Al_2O_3/Al_2TiO_5 composites over a range of volume fractions and particles sizes are used to demonstrate the severe loss in mechanical integrity that can be suffered on entering the microcracking domains.

I. Introduction

In Part I,[1] we developed a simplified fracture mechanics toughness-curve (*T*-curve) model for two-phase ceramics. Experimental indentation–strength data on an alumina-matrix/aluminum titanate (Al_2O_3/Al_2TiO_5) particle-reinforced composite were used to confirm the essential features of the model and to calibrate controlling microstructural parameters for the *T*-curve. We are now placed to predict the effects of specified microstructural change on the toughness and strength properties of that composite system.

Accordingly, in Part II we investigate the predictive capacity of the model by analyzing the effects of volume fraction V_f and particle size l of the second phase, in addition to matrix/particle expansion mismatch stress σ_R, on the toughness. We shall show that increasing V_f (or σ_R) and l, respectively, enhances the slope and scaling characteristics of the *T*-curve, with profound consequences concerning crack stability. Beyond critical compositions the material is able to sustain multiple flaw extension prior to failure. This is the domain of microcrack damage accumulation and nonlinear stress–strain response. At even higher V_f and l, the strength is severely degraded, indicative of microcrack coalescence. Indentation–strength tests on Al_2O_3/Al_2TiO_5 composites with different volume fractions and particle sizes are used to validate these predictions.

The model will be discussed in special relation to microstructural strategies for optimum toughness characteristics, in terms of a simple design diagram.

II. Effect of Microstructural Variables on Toughness and Strength

Using the "calibrated" *T*-curve, $T(c)$, function for the reference composite material of Part I, we set out to predict the influence of two major microstructural variables, volume fraction V_f and particle diameter l, on the indentation–strength characteristics. Internal residual stress σ_R is also a parameter of potential interest, but that quantity is invariant for a given matrix–particle composite system. We again address the specific configuration of a half-penny crack in a semi-infinite medium.

(1) Microstructure Parametric Relations

In this subsection we seek relations between V_f and l and the controlling microstructural parameters in the $T(c)$ formalism of Section II, Part I: i.e., shielding stresses p and q, and bridging zone dimensions λ and Λ.

The microstructural dependence of the shielding stresses is given by Eqs. (2) and (3), Part I:

$$q = \frac{1}{2}V_f(1 - V_f)\sigma_R \qquad (0 \leq 2u \leq \varepsilon_\delta l) \qquad (1a)$$

$$p = \frac{1}{2}\eta\mu\varepsilon_\xi V_f(1 - V_f)\sigma_R \qquad (\varepsilon_\delta l \leq 2u \leq \varepsilon_\xi l) \qquad (1b)$$

with η a microstructural geometry parameter, μ a friction coefficient, and ε_δ and ε_ξ size-independent strains at which the bridging particle relaxes its elastic crack-opening stresses and disengages from the matrix, respectively. Eqs. (1*a*) and (1*b*) are basic microstructural *stress* relations for the *T*-curve. Observe that p and q depend on V_f (and σ_R), but not on l.

Analogous microstructural dependencies of λ and Λ can be obtained from Eq. (3), Part I, but less directly, requiring relations between λ and δ, Λ and ξ. It is now necessary to introduce appropriate crack-opening displacement relations. To maintain an equilibrium state, these relations must be solved simultaneously and self-consistently with the K-field condition $K_A(c) = T(c)$ in Eq. (6) of Part I, using Eq. (8) in Part I to evaluate $T(c)$ in the appropriate crack-size domains. Generally, such crack-opening displacement relations are couched in a nonlinear integral equation formalism.[2-4] In the present study, in the interest of maintaining simplicity, we use first-order solutions for strictly *uniform* stresses over the *entire* crack plane, i.e., elliptical profiles,[2] giving

$$\delta = (2\psi T_0/E')(2\lambda)^{1/2} \qquad (2a)$$

$$\xi = (2\psi T_0/E')(2\Lambda)^{1/2} \qquad (\lambda << \Lambda) \qquad (2b)$$

D. K. Shetty—contributing editor

Manuscript No. 195173. Received October 27, 1992; approved May 28, 1993.
Supported by the Air Force Office of Scientific Research and E. I. duPont Nemours and Company, Inc.

[*] Member, American Ceramic Society.

[†] Guest Scientist, from Department of Materials Science and Engineering, Lehigh University, Bethlehem, PA 18015.

[‡] Now at School of Materials Engineering, Georgia Institute of Technology, Atlanta, GA 30332.

[§] Now at Experimental Station, E. I. duPont Nemours and Company, Wilmington, DE 19880-0356.

with $E' = E(1 - \nu^2)$, E Young's modulus and ν Poisson's ratio, and T_0 the matrix (grain boundary) toughness, again regarding λ and Λ as constants for a given microstructure.

Of course, the actual internal stress distribution over the crack plane in Fig. 3, Part I, is highly *non*uniform, with discontinuities in stress and stress gradient at $r = \lambda$. In reality, relative to the profile solutions of Eq. (2), the walls will bulge open in the opening-stress domain $c - \lambda \leq r \leq c$ immediately behind the tip and, conversely, pinch down in the more remote closure-stress domain $c - \Lambda - \lambda \leq r \leq c - \lambda$.[5] Under such conditions, neither λ nor Λ will be strictly independent of p and q (hence V_f), or even of c (until one satisfies the requirements of the "small-zone" approximation $\lambda << \Lambda << c$[6]). Here, even though the displacement field equations are actually integrable for the stresses shown in Fig. 3 of Part I,[5,7,8] we choose to avoid such complexities in order to bring out the essential microstructural dependence of the T-curve more clearly.

Inversion of Eq. (2), in conjunction with Eq. (3) of Part I, yields relations

$$\lambda = \frac{1}{2}(\varepsilon_* E'/2\psi T_0)^2 l^2 \tag{3a}$$

$$\Lambda = \frac{1}{2}(\varepsilon_\xi E'/2\psi T_0)^2 l^2 \qquad (\lambda << \Lambda) \tag{3b}$$

which (neglecting any influence of the second phase on E') are independent of V_f (and also σ_R) and c, but scale with l. Equations (3a) and (3b) are basic microstructural *scaling* relations for the T-curve. Note that $\Lambda/\lambda = (\varepsilon_\xi/\varepsilon_*)^2 =$ constant, independent of V_f (and σ_R) and l; i.e., Λ and λ scale similarly with any change in the particle size.

(2) Damage Accumulation by General Microcracking

In our concluding remarks to Part I we alluded to a potential transition in flaw stability, depending on whether the extrapolated intercept of the "linear" T–$c^{1/2}$ function (Eq. (9), Part I) on the T-axis *is* positive or negative. The critical, *zero-intercept* transition condition is illustrated in the schematic of Fig. 1, where $T(c)$ is plotted as the solid curve. Let us consider intrinsic flaws that are free of spurious residual stresses (i.e., $\chi = 0$ in Eq. (11), Part I), and that have evolved fully through the bridging field from inception. Then the origin of the $K_A(c)$ function, $K_A' = K_A = \psi\sigma_A c^{1/2}$ in Eq. (12), Part I, plotted as the shaded line in Fig. 1, coincides with that of the linear T–$c^{1/2}$ function. Using this critical transition configuration as a reference state, and supposing the material to contain at least a proportion of flaws of initial size $c = c_f$ within the two vertical dashed lines in Fig. 1, we may usefully delineate the following regions of stability:

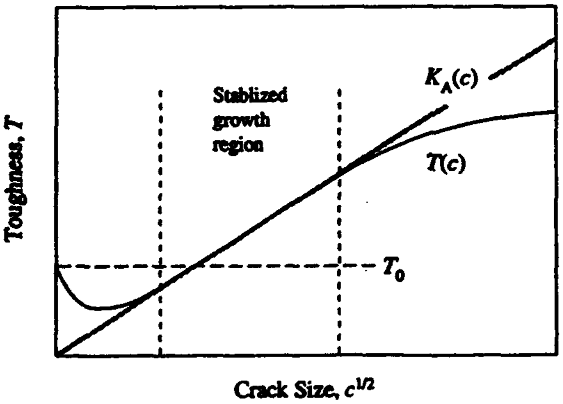

Fig. 1. Schematic diagram showing T-curve construction at limit of bulk microcrack activation. Solid curve is $T(c)$ at critical condition given by Eq. (6), shaded line is $K_A = \psi\sigma_A c^{1/2}$. Any flaw of initial size within the two vertical dashed lines will extend stably along the T-curve to failure at the extreme right dashed line.

(A) Positive Intercept, No Microcracking: For a material with positive intercept, such as our reference material in Fig. 6 of Part I, the equilibrium configuration $K_A = \psi\sigma_A c_f^{1/2} = T$ corresponds to a slope $\mathrm{d}K_A/\mathrm{d}(c^{1/2}) > \mathrm{d}T/\mathrm{d}(c^{1/2})$. Failure then occurs abruptly and unstably from a *single* critical flaw at $c = c_f$. Nevertheless, the material shows flaw tolerance, because the toughness T at failure effectively increases with c_f. For systems *just* at the transition in Fig. 1, the strength becomes altogether independent of c_f; i.e., the equilibrium is neutral. The applied stress–strain response is linear in this region.

(B) Negative Intercept, Activated Microcracking: For a material with negative intercept the condition $K_A = T$ at $c = c_f$ corresponds to a slope $\mathrm{d}K_A/\mathrm{d}(c^{1/2}) < \mathrm{d}T/\mathrm{d}(c^{1/2})$. The flaw then undergoes a precursor stage of stable extension with increasing σ_A, until a tangency condition $\mathrm{d}K_A/\mathrm{d}(c^{1/2}) = \mathrm{d}T/\mathrm{d}(c^{1/2})$ is met. The strength σ_F for breaks from natural flaws is now altogether independent of c_f. In this region, even though failure still occurs from a single critical flaw, other flaws may nevertheless undergo significant prefailure extension. This can result in accumulation of microcrack damage through the material prior to failure, the more so as the negative intercept increases. The applied stress–strain response of the material now becomes nonlinear.

(C) Negative Intercept, Spontaneous Microcracking: With still further depression of the negative intercept, such that the minimum in the T-curve falls below the c-axis, the system enters a severe-damage domain in which flaw pop-in can occur in the absence of applied stress, increasing the density of stable flaws and further enhancing the stress–strain nonlinearity.

The configuration of Fig. 1 delineating the transition between states (A) and (B) above corresponds to a critical volume fraction V_f^* (or residual stress σ_R^*) at fixed l, or to a critical particle size l^* at fixed V_f. This critical condition may be formalized by requiring $T = 0$ at $c = 0$ in the $T(c)$ function of Eq. (9) in Part I, yielding

$$[(p + q)(2\lambda)^{1/2}]^* = T_0/\psi \tag{4}$$

Invoking Eqs. (1) and (3) above allows us to express Eq. (4) in terms of microstructural variables,

$$[V_f(1 - V_f)l\sigma_R]^* = 4T_0^2/(1 + \eta\mu\varepsilon_\xi)\varepsilon_* E' \tag{5}$$

Hence, damage accumulation may be promoted by increasing the volume fraction (or residual internal stress) or scaling up the particle size.

An analogous condition for spontaneous microcracking may be obtained by requiring the minimum in the $T(c)$ function to intersect the c-axis. Approximating this minimum as the intersection point of the T–$c^{1/2}$ functions in Eqs. (8a) and (9) in Part I, i.e., $T = 0$ at $c \sim 2\lambda$, we have

$$[q(2\lambda)^{1/2}]^{**} = T_0/\psi \tag{6}$$

Again invoking Eqs. (1) and (3), we obtain

$$[V_f(1 - V_f)l\sigma_R]^{**} = 4T_0^2/\varepsilon_* E' \tag{7}$$

which is greater than $[V_f(1 - V_f)l\sigma_R]^*$ in Eq. (5) by a factor $1 + \eta\mu\varepsilon_\xi$ (neglecting any reduction in E' from the microcracking). The latter factor therefore defines a "window" of activated damage.

In the nonlinear region lower-bounded by Eq. (5), the prospect exists for coalescence of the stable microcracks, with attendant strength degradation. Coalescence is a "many-body" problem, depending on the characteristic spacing between neighboring, interactive microcrack sources in an actively evolving population. There is therefore a stochastic element in the mechanics of damage accumulation. Here we simply note that if the source–source spacing is less than the fully extended flaw size at the critical tangency condition, the strength drop will tend to be immediate. If the sources are more distantly spaced, the drop-off will be more gradual. Any remaining strength after coalescence will depend on the *variability* in the spatial distribution of the sources.

III. Microcracking Limits of Al_2O_3/Al_2TiO_5 Composites: Analysis Using Indentation–Strength Data

(1) *Experimental Procedure*

We now investigate the predictions of the T-curve analysis using indentation–strength data for Al_2O_3/Al_2TiO_5 composites of different volume fraction and particle size of the Al_2TiO_5 phase.

Materials were prepared as described in Section III(1) of Part I. Batches of material were fabricated with volume fractions $V_f = 0.10, 0.20, 0.30$, and 0.40, by altering the starting powder composition. Specimens from each batch were then heat-treated over a range of aging times[9] to grow the Al_2TiO_5 particles from their initial size, $l < 2$ μm, over a range of sizes up to a maximum $l = 12$ μm. The matrix grains were observed to scale similarly, but remained within a range of negligible influence on the T-curve.[10]

Strength tests were carried out as in Part I. Disks for strength testing were polished, then indented with a Vickers diamond at a prescribed load $P = 5$ N. This load is close to the intersection point of data sets for the reference composite and base alumina in Fig. 5 of Part I, i.e., in a region where the strength is relatively material-insensitive. The disks were then broken in biaxial flexure to obtain inert strength data. Post-mortem examinations were again made of all broken specimens to confirm failure initiation from the indentation sites. Means and standard deviations in strengths were evaluated from 4–6 tests at each value of V_f and l, where possible; beyond the strength falloff limits (Sect. III(2)), the success rate for breaks at indentations diminished rapidly, and the data were most often restricted to individual breaks.

Some of the specimen surfaces were examined for evidence of microcracking, both before and after strength testing.

(2) *Influence of Volume Fraction and Particle Size on Microcracking Limits*

Figure 2 plots the indentation–strength data as a function of particle size, $\sigma_M(l)$, at each of the volume fractions $V_f = 0.10, 0.20, 0.30, 0.40$. We see that, generally, σ_M falls off with l, initially slowly and thereafter, beyond a cutoff, precipitously. Increasing V_f shifts the "cliff" progressively to the left of the plots.

Surface examinations of the specimens showed a correlation between position on the strength plots in Fig. 2 and the incidence of microcracking. At the top of the cliff, the specimens gave no indication of multiple flaw extension. In this region the applied load–displacement curve remained essentially linear. Over the edge of the cliff, sporadic microcracking could be detected in the broken specimens using scanning electron microscopy. At the bottom of the cliff, microcracking was more prevalent, and the applied load–displacement curve showed nonlinearity[9]—in this domain the material may be considered to be "overaged". An example of spontaneous microcracking in a heavily overaged material is shown in Fig. 3. Materials subjected to even more overaging were so heavily microcracked that, on prolonged exposure (i.e., several days) to moist atmospheres, they began to crumble, with virtually total loss of strength.

The solid curves at left in each plot are calculated from the theoretical indentation–strength analysis (Sect. II(3), Part I). For these calculations, we use the previously defined indentation coefficients $\psi = 0.77$ and $\chi = 0.076$, and alumina matrix toughness $T_0 = 2.75$ MPa·m$^{1/2}$ (Ref. 11) (Sect. III(2), Part I). We also use the microstructural parameters $p = 325$ MPa, $(p + q)(2\lambda)^{1/2} = 3.51$ MPa·m$^{1/2}$ and $\Lambda = 180$ μm (Eq. (17), Part I) defined for our reference composite ($V_f = 0.20$, $l = 4.0$ μm); Eq. (1) is then invoked to scale the bridging stresses p and q for each new V_f, and Eq. (3) to scale bridging zone dimensions λ and Λ for each new l.

Beyond a critical particle size l^* at each V_f, evaluated by setting $V_f(1 - V_f)l^* = 0.672$ μm in accordance with Eq. (5), we approximate the strength degradation as an infinitely abrupt falloff, indicated by the *left*-hand vertical dashed lines in the plots. The falloff condition for the reference state at $V_f = 0.20$ may be used to evaluate the parameters λ and q (foreshadowed in Eq. (18), Part I), as follows. Inserting $\Lambda = 180$ μm at $l = 4.0$ μm (Eq. (17*c*), Part I) into Eq. (3*b*), we obtain $\varepsilon_\xi = 0.067$. Inserting ε_ξ into Eq. (5), along with $\eta = 4$ and $\mu = 2.7$ (Sect. III(2), Part I), plus $\sigma_R = 7.7$ GPa (Eq. (19*a*), Part I) and $E' = 300$ GPa[12] for our reference material, yields $\varepsilon_\delta = 0.013$. Then from Eq. (3*a*) (again neglecting any variation in E' with V_f) we have $\lambda/l^2 = 0.44$ μm^{-1}, which enables us to determine λ, and thence q (Eq. 17*b*), Part I), for each prescribed l.

With this parameter calibration, it is one further step to evaluate the limiting particle sizes l^{**} for spontaneous microcracking limits from Eq. (7). These limits are included as the *right*-hand vertical dashed lines for each V_f in Fig. 2.

IV. Implications Concerning Microstructural Design of Two-Phase Ceramics

(1) *Effect of Microstructural Variables on Toughness Curves*

It is apparent from the results in Sect. III of Part I and Sect. III above that incorporation of a second phase is an effective route to the control of toughness-curve behavior in ceramic composites. Using a reference composition to calibrate key crack bridging parameters in the T-curve relations, one may predict the effects of microstructural changes on the strength properties of a given material system. Here, we illustrate specifically with computed T-curves for a range of hypothetical volume fractions V_f and particle sizes l for our Al_2O_3/Al_2TiO_5 system. However, the generality of the theoretical analysis extends to potential variations in the internal mismatch stress σ_R (as modified, for instance, by incorporating a different second phase, or even changing the matrix).

(A) Volume Fraction (or Residual Stress): Consider first the influence of volume fraction V_f (or σ_R) on the T-curve. In Fig. 4 we generate $T(c)$ curves (Eqs. (6) and (8), Part I) by evaluating p and q for $V_f = 0.10, 0.20, 0.30$, and 0.40 in accordance with Eq. (1) above, keeping λ and Λ in Eq. (3) constant at the values determined for $l = 4.0$ μm (Eqs. (17*c*) and (18*a*), Part I). We see that the slope and upper plateau of the curves are enhanced, and the minimum simultaneously depressed, with increasing V_f. At the same time, the range of crack sizes over which $T(c)$ varies remains essentially constant. A conspicuous manifestation of this fixed range is the crossover of all curves through a common intersection point at $c = c_\dagger = 1100$ μm, $T = T_0 = 2.75$ MPa·m$^{1/2}$. Note that on substituting $T = T_0$ into Eq. (9) of Part I we obtain $c_\dagger = 2(1 + q/p)^2\lambda = 2(1 + 1/\eta\mu\varepsilon_\xi)^2\lambda$, which is indeed independent of V_f.

Now suppose a proportion of the natural flaw population to have initial sizes $c = c_f$ to the right of the minimum of any given curve in Fig. 4. The stability of such flaws under an applied stress σ_A is then determined by the disposition of $K_A(c) = \psi\sigma_A c^{1/2}$ relative to the shaded line passing through both the common intersection point ($c = c_\dagger$, $T = T_0$) and the origin (cf. Fig. 1). This "transition" line corresponds to a critical volume fraction $V_f = V_f^\ddagger = 0.21$ ($l = 4.0$ μm) in the zero-intercept linear T–$c^{1/2}$ function in Eq. (9) of Part I. In keeping with the description in Sect. II(2), we distinguish two regions of material response:

(i) At $0 < V_f < V_f^\ddagger$, the equilibrium configuration $K_A = \psi\sigma_A c_f^{1/2} = T$ is unstable; failure occurs from a single, critical flaw. Note, however, that as V_f approaches $V_f^\ddagger$ the strength becomes increasingly insensitive to c_f.

(ii) At $V_f^\ddagger < V_f$, the equilibrium at $K_A = T$, $c = c_f$ is stable, and extension proceeds up the T-curve with increasing stress until the tangency condition $dK_A/d(c^{1/2}) = dT/d(c^{1/2})$ is met. As V_f increases further beyond $V_f^\ddagger$ the potential increases for multiple flaw extension and coalescence, with consequent strength degradation.[9]

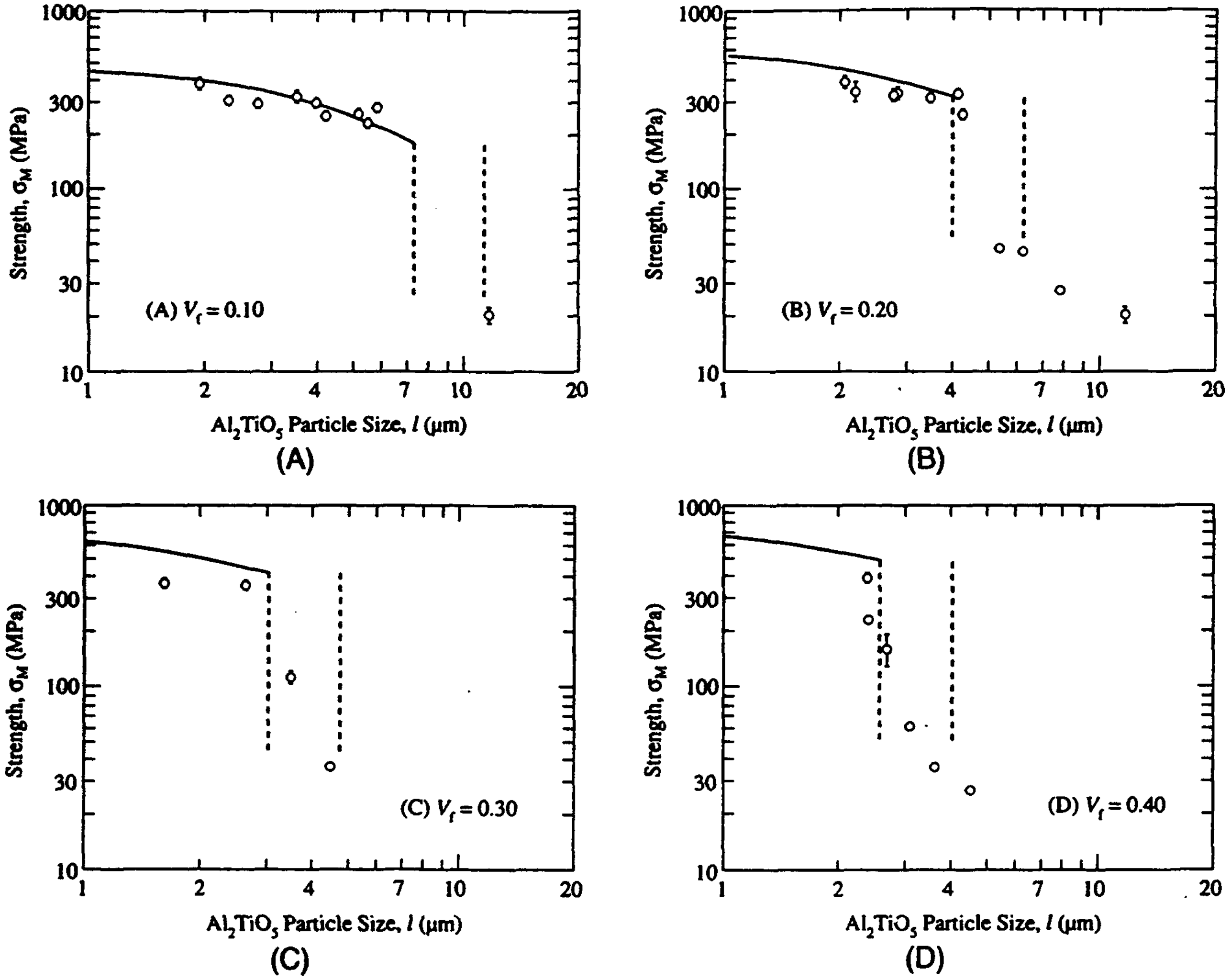

(A) (B)

(C) (D)

Fig. 2. Strength as function of particle size l for Al_2O_3/Al_2TiO_5 composite, for volume fractions (A) $V_f = 0.10$, (B) $V_f = 0.20$, (C) $V_f = 0.30$, (D) $V_f = 0.40$, at fixed indentation load $P = 5$ N. Error bars on datum points are standard deviations; datum points without error bars are individual results. Solid curves are generated from theoretical analysis in Part I. Vertical dashed curves indicate limiting particle sizes l^* and l^{**} evaluated from Eqs. (5) and (7).

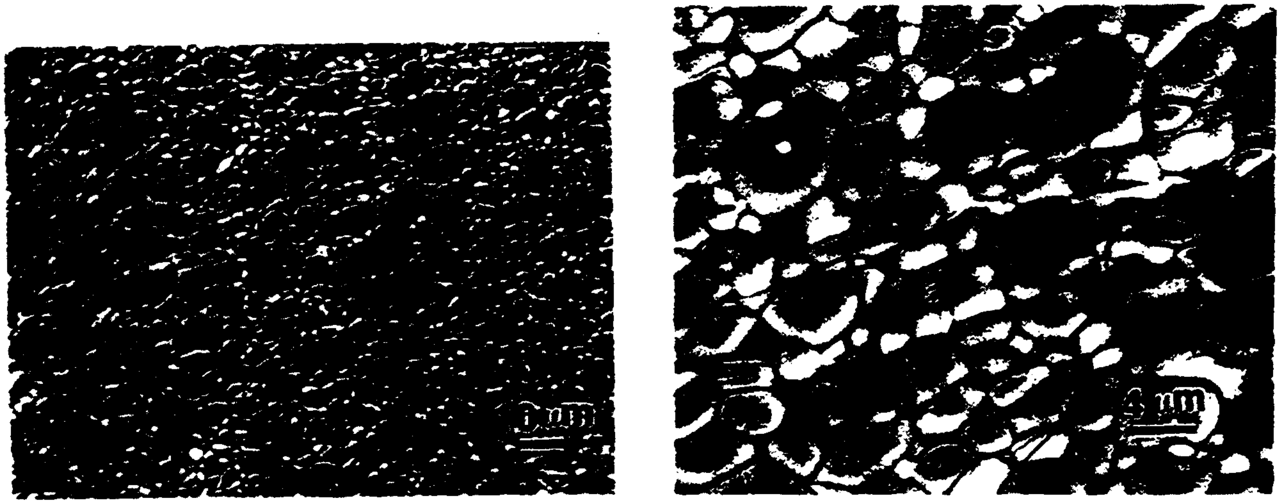

(A) (B)

Fig. 3. SEM micrograph showing bulk microcracking damage in Al_2O_3/Al_2TiO_5 composite, $V_f = 0.30$, $l = 5.0$ μm (cf. Fig. 2(C)). Micrograph (B) is enlargement of portion of (A).

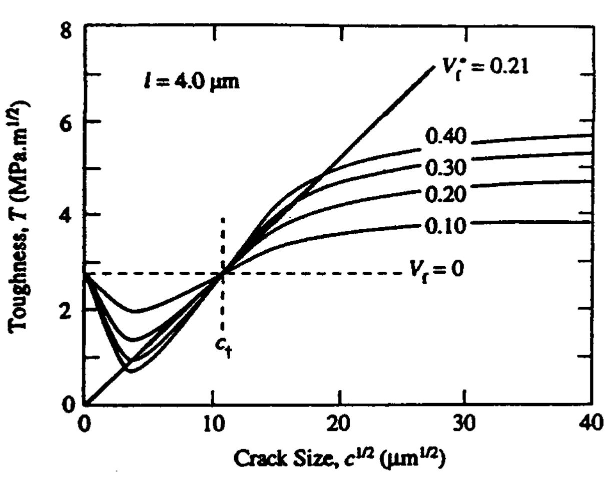

Fig. 4. Predicted T-curves for Al_2O_3/Al_2TiO_5 composites, for specified volume fractions V_f at fixed particle size l = 4.0 μm. Shaded line is K_A-field at $c = c_\dagger, T = T_0$.

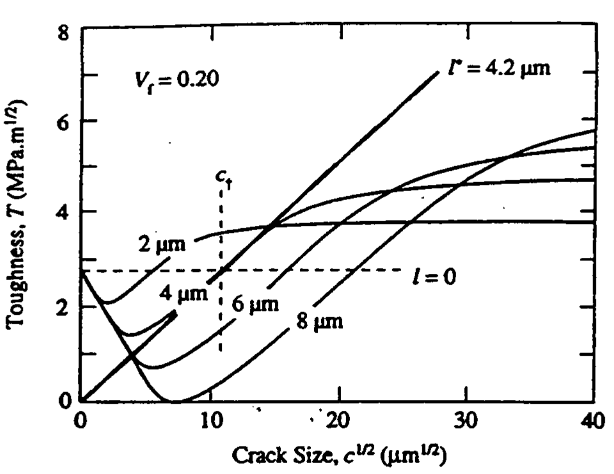

Fig. 6. Predicted T-curves for Al_2O_3/Al_2TiO_5 composites, for specified particle sizes l at fixed volume fraction V_f = 0.20. Shaded line is K_A-field at $c = c_\dagger, T = T_0$.

Note that none of the curves for the l = 4.0 μm material in Fig. 4 intersect the c-axis, nor is there much scope for further increase in volume fraction. Thus, whereas *activated* microcracking occurs at $V_f > 0.21$, *spontaneous* microcracking strictly should not occur in the material at this particle size. However, as indicated in Sect. III(2) above, some premature flaw pop-in may be induced at the higher volume fractions by prolonged exposure to moisture.

The flaw tolerance characteristics implied in Fig. 4 are more clearly demonstrated by calculating strength as a function of initial flaw size, $\sigma_F(c_f)$, using the conventional strength formalism for natural flaws (i.e., Eqs. (13) and (14), Part I, at $\chi = 0$) within the domain $0 < V_f < V_f^*$. Figure 5 shows the results of such calculations for specified values of V_f (l = 4.0 μm). Consistent with the T-curve description, enlarging V_f enhances the "plateau", without affecting the extreme long-crack or short-crack strengths.

(B) Particle Size: Now consider the effect of particle size l on $T(c)$. In Fig. 6 we generate $T(c)$ functions by adjusting λ and Λ for l = 2, 4, 6, and 8 μm using Eq. (3) above, keeping p and q constant at the values determined for V_f = 0.20 (Eqs. (17*a*) and (18*b*), Part I). Observe that the slope of the "linear" region of the T–$c^{1/2}$ plot is now invariant, reflecting the independence of p and q in Eq. (9) of Part I on l. On the other hand, the upper plateau toughness *is* enhanced by increasing the particle size. Most significantly, the linear region of the curve translates to the right of the diagram and extends over a greater range of crack sizes, as l (thus λ and Λ) increases.

Suppose again that a proportion of the population of natural flaws had initial size $c = c_f$ to the right of the minimum of the pertinent curve in Fig. 6. The flaw stability is determined by the disposition of $K_A(c)$ relative to the shaded line at a critical particle size $l = l^*$ = 4.2 μm (V_f = 0.20). Again, we distinguish two regions of material response relative to this transition line:

(i) At $0 < l < l^*$, the equilibrium is unstable, and failure occurs from a single flaw. The strength becomes increasingly insensitive to initial flaw size c_f as l approaches l^*.

(ii) At $l^* < l$, the equilibrium is stable, and the flaws extend at increasing stress up the T-curve to failure at the tangency point. Several flaw sources may be activated. As l increases further, toward and beyond l^{**}, the flaws ultimately coalesce, and strength is degraded.

Figure 7 shows calculated strength as a function of natural flaw size, $\sigma_F(c_f)$, for specified values of l within $0 < l < l^*$ (V_f = 0.20). Enlarging l depresses the strength plateau, but this is compensated by expansion of the "plateau" range, with attendant enhancement of the long-crack strength. A similar tradeoff

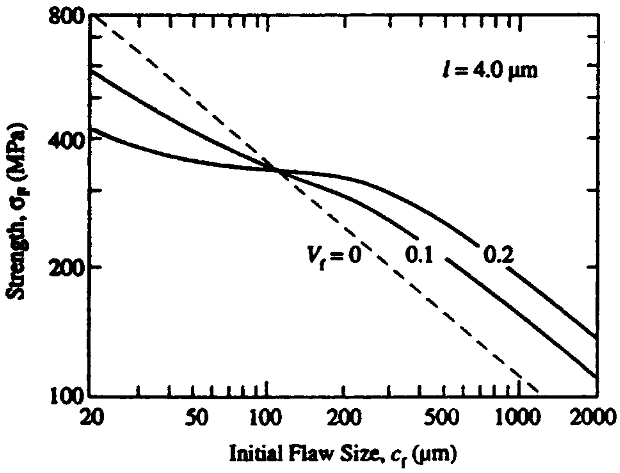

Fig. 5. Predicted strength as function of initial size of natural flaws for Al_2O_3/Al_2TiO_5 composites, for specified volume fractions V_f at fixed particle size l = 4.0 μm.

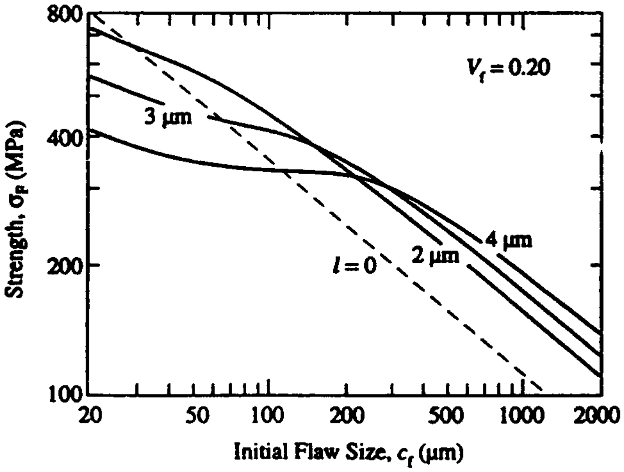

Fig. 7. Predicted strength as function of initial size of natural flaws for Al_2O_3/Al_2TiO_5 composites, for specified particle sizes l at fixed volume fraction V_f = 0.20.

is evident in an earlier study of the effect of grain size on strength in base alumina.[10]

(2) *Microcracking Limits and Design Criteria*

In noting how key microstructural parameters enhance certain characteristics of the T-curve, let us recall an interesting dichotomy foreshadowed in Sect. II(1): an increased volume fraction V_f (or residual stress σ_R) enhances the *slope*, but not the scale (Fig. 4); an increased particle size l enhances the *scale*, but not the slope (Fig. 6). We also recall that excessive increases can lead to bulk microcracking and ultimate strength degradation. It follows that control of these vital microstructural parameters should be an important element in materials design.

In this context, it is useful to consider the *design diagram* in Fig. 8, plotted as $V_f(1 - V_f)\sigma_R$ (governed by stresses p and q) vs l (governed by dimensions λ and Λ). Accordingly, the ordinate measures the *slope* of the T-curve, the abscissa the *scale*. The curves represent the simple inverse relations Eqs. (5) (inner curve) and 7 (outer curve). This diagram may be usefully considered in relation to the three domains of material behavior identified in Sect. II(2).

(A) No Microcracking (NM): Within the subcritical domain $V_f < V_f^*, l < l^*$ in Figs. 4 and 6, failure is unstable from a single flaw at $c = c_f$. However, the traditional "Griffith" condition $\sigma_F \propto c_f^{-1/2}$ is valid only for materials with single-valued toughness, corresponding to the fine-grain matrix material at $V_f = 0$ in Fig. 5 and $l = 0$ in Fig. 7. A true Griffith response is therefore realized only at the origin of Fig. 8. As V_f and l grow larger, the material becomes more flaw-tolerant, in the manner of Figs. 5 and 7, and the composite material migrates away from the origin along an appropriate configurational path in Fig. 8.

(B) Activated Microcracking (AM): For systems just at the critical condition $V_f = V_f^*, l = l^*$ on the inner curve in Fig. 8, the equilibrium is neutral and the critical flaw undergoes precursor extension along the linear portion of the T–$c^{1/2}$ curve, to ultimate failure at $c = \Lambda + \lambda$ (cf. Fig. 1). Now σ_F is altogether independent of c_f. As one progresses further beyond the inner curve and toward the second curve the equilibrium becomes stable, promoting the incidence of multiple flaw extensions. Strength σ_F remains independent of c_f but is compromised by any coalescence. This is the domain of stress-induced damage accumulation.

(C) Spontaneous Microcracking (SM): At $V_f > V_f^{**}, l > l^{**}$, small flaw sources may pop-in spontaneously from the left unstable branch to the right stable branch of the T-curve (e.g., at $l = 8$ μm for the $V_f = 0.2$ material in Fig. 6). Damage is therefore accumulated even in the absence of an external stress. Again, in the presence of moisture, this state may develop prematurely (Sect. III(2)).

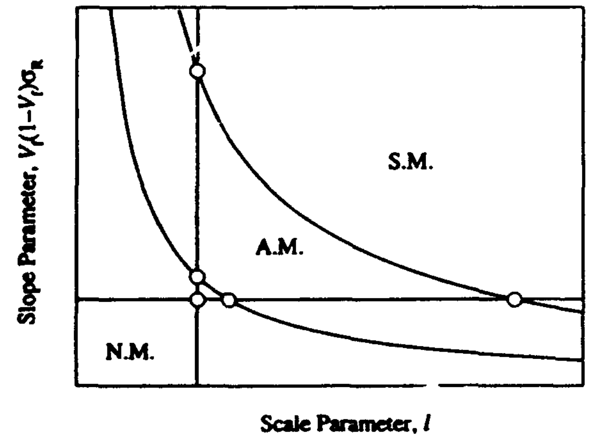

Fig. 8. "Design diagram." Curves are loci of Eqs. (5) and (7), delineating regions of *no* microcracking (N.M.), *activated* microcracking (A.M.), and *spontaneous* microcracking (S.M.). Horizontal shaded line is constant volume fraction and residual stress line; vertical shaded line is constant particle size line.

To illustrate the design utility of Fig. 8, let us consider variations in microstructural states along the two shaded lines. These two shaded lines correspond to the two principal microstructural modifications considered in this study: along the *vertical* line, to volume fraction V_f (or residual stress σ_R), as envisaged in Fig. 4; along the *horizontal* line, to particle *size* l, as envisaged in Fig. 6. In both cases, translation along the line away from the axes corresponds to increased flaw tolerance, limited first by activated then spontaneous microcracking damage as one intersects the two curves. There is a tradeoff here: increasing V_f (or σ_R) progressively restricts the range of l over which flaw tolerance may be achieved, and vice versa.

This latter tradeoff is implicit in the strength vs flaw-size plots for our Al_2O_3/Al_2TiO_5 composites in Figs. 5 and 7. There, we have achieved a degree of flaw tolerance by increasing V_f and l, but the relatively high value of σ_R for this material restricts the range of flaw sizes axis over which the "plateau" strength can be sustained without microcracking.

V. Discussion

The simplistic model presented in Parts I and II of this study provides us with a physical basis for predicting the influence of important microstructural variables, notably volume fraction V_f, particle size l, and thermal expansion mismatch stress σ_R, on toughness-curve and strength properties of two-phase ceramics that exhibit grain-sliding bridging. Especially insightful is the distinction made between the influences of V_f (and σ_R) on the *slope* characteristics (Fig. 4) and l on the *scale* characteristics (Figs. 6 and 7) of the T-curve. This dichotomy may be usefully applied in the microstructural tailoring of optimal flaw-tolerant ceramics for specific structural applications, accordingly to whether the principal requirement is for preservation of plateau strength *level* (increased V_f, Fig. 5) or enhancement of plateau *range* (increased l, Fig. 7).

The analysis also imposes limits on the potential benefits of compositional tailoring by the onset of bulk microcracking. These limits arise naturally in the model from the central role of internal residual mismatch stresses in the bridging micromechanics. They are most usefully demonstrated in the design diagram construction of Fig. 8. In that diagram, the neutral equilibrium state defined by the inner curve represents a locus of optimum flaw tolerance. Beyond that limit, flaw tolerance is retained and damage can accumulate; but strength may be lost, from activation and ultimate coalescence of multiple microcrack sources. Beyond the outer curve in Fig. 8, bulk microcracking occurs spontaneously, and loss of structural integrity may be severe. This takes us into the province of refractories, where the characteristics of individual microcracks (as introduced for example in thermal shock) become subsidiary to those of the integrated, interactive population. There, the stochastics of microcrack sources and mechanisms of coalescence are governing factors.[13,14] In these microcracking domains, the tendency to enhanced local microcracking can be highly deleterious to microfracture-induced wear resistance.[15]

The quantitative capacity of our fracture mechanics model as a predictive tool is limited by approximations in the starting equations. We have mentioned that the elliptical-crack profile relations in Eq. (3) are not self-consistent with the K-field solutions of Sect. III(1) in Part I. A self-consistent solution to the nonlinear displacement-field integral equations[2] could indeed be obtained by direct integration over the constant bridging stress domains of Fig. 3 in Part I, but at the sacrifice of physical insight. Such a solution will inevitably lead to relations for λ and Λ that depend on V_f as well as on l. Under such conditions *slope* and *scale* characteristics of the T-curve may no longer be varied independently via respective adjustments to volume fraction and particle size (as implied, for instance, in Figs. 4 and 6).

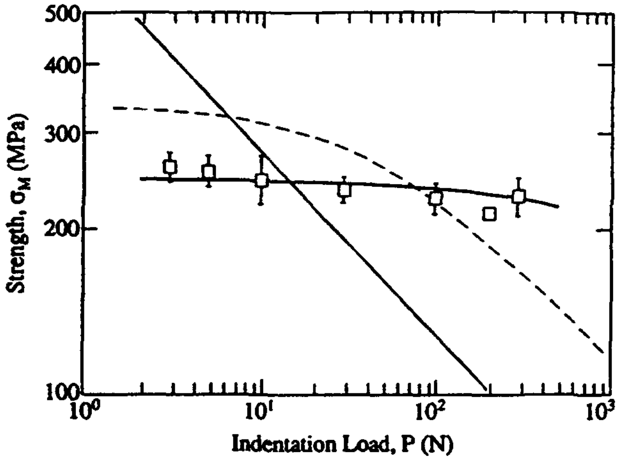

Fig. 9. Indentation–strength data for Al_2O_3/Al_2TiO_5 composite, for volume fraction $V_f = 0.20$ but with exaggerated matrix Al_2O_3 grain size and agglomerated distributions of Al_2TiO_5 particles. Data from Refs. 6 and 16. Solid curve is empirical fit to data. Compare shaded curve for base fine-grain alumina, and dashed curve for homogeneous material at same V_f (from Fig. 6, Part I).

Furthermore, the approximation of constant stress domains in the constitutive stress–separation function $s(u)$ (Fig. 2, Part I) is clearly oversimplistic; in real ceramics, $s(u)$ is tail-dominated.[16] The attendant discontinuities in $s(r)$ at $r = c - \lambda$ and $c - (\Lambda + \lambda)$ (Fig. 3, Part I) could even lead to unphysical, nonunique crack profile solutions.[4,5,17] More detailed analyses will inevitably cause changes in the shapes of the T-curves (Figs. 4 and 6) and the strength plateaus (Figs. 5 and 7). In general, therefore, we must expect the crucial rising portion of the toughness function to be considerably more complex than the "linear" T–$c^{1/2}$ representation of Eq. (9) in Part I. In this context our calibrations of the principal microstructural parameters, stresses p and q and dimensions Λ and λ, are subject to considerable uncertainty. One must exercise due care when using such calibrations as a basis for mechanical design, especially when extrapolating into the short-crack and long-crack regions beyond the data range. On the other hand, these parameters remain useful guides to the strength of the underlying bridging processes responsible for the toughening behavior.

The present study is also subjected to material-specific restrictions, from the imposition of bulk microcracking limits at relatively small particle sizes. These restrictions are attributable to the large residual mismatch stresses in our Al_2O_3/Al_2TiO_5 composites. Consequently, the current examination of flaw tolerance effects have been confined to a small range of particle sizes (Fig. 2). A more comprehensive study calls for material system with greater flexibility in the capacity to vary the microstructural variables. Such a system might include contributions to the T-curve from the matrix itself. In the present case of an alumina matrix, the contributions may become significant for grain sizes above ≈ 10 μm.[10] It has in fact been demonstrated elsewhere that deliberate incorporation of coarse matrix grains into Al_2O_3/Al_2TiO_5 composites can produce further (multiplicative) enhancements of the T-curve.[18] Inhomogeneous distributions of the second phase, e.g., by agglomeration of the aluminum titanate particles, can also enhance the toughness and flaw-tolerance properties. This latter is seen in Fig. 9.[9,19] Such spatial variability in microstructural characteristics might prove to be of even greater importance than variability in flaw size in accounting for observed scatter in strength data in flaw-tolerant ceramics, and thus become a critical issue in the processing of ceramic components for increased reliability.[9]

Acknowledgments: The authors acknowledge stimulating discussions with H. Cai and E. R. Fuller, Jr.

References

[1] B. R. Lawn, N. P. Padture, L. M. Braun, and S. J. Bennison, "Model for Toughness Curves in Two-Phase Ceramics: I, Basic Fracture Mechanics," *J. Am. Ceram. Soc.*, 76 [9] 000–000 (1993).

[2] I. N. Sneddon and M. Lowengrubb, *Crack Problems in the Classical Theory of Elasticity*. Wiley, New York, 1969.

[3] B. Budiansky, J. C. Amazigo, and A. G. Evans, "Small-Scale Crack Bridging and the Fracture Toughness of Particulate-Reinforced Ceramics," *J. Mech. Phys. Solids*, 36 [2] 167–87 (1988).

[4] B. N. Cox and D. B. Marshall, "The Determination of Crack Bridging Forces," *Int. J. Fract.*, 49, 159–76 (1991).

[5] K.-T. Wan and B. R. Lawn, "Effect of Chemical Interaction on Barenblatt Crack Profiles in Brittle Solids," *Acta Metall.*, 40 [12] 3331–37 (1992).

[6] B. R. Lawn, *Fracture of Brittle Solids*. Cambridge University Press, Cambridge, U.K., 1993.

[7] E. Smith, "The Size of the Fully Developed Softening Zone Associated with a Crack in a Strain-Softening Material. I. A Semi-Infinite Crack in a Remotely Loaded Infinite Solid. II. A Crack in a Double-Cantilever Beam Specimen," *Int. J. Eng. Sci.*, 27 [3] 301–307, 309–14 (1989).

[8] F. Erdogan and P. F. Joseph, "Toughening of Ceramics through Crack Bridging by Ductile Particles," *J. Am. Ceram. Soc.*, 72 [2] 262–70 (1989).

[9] J. L. Runyan and S. J. Bennison, "Fabrication of Flaw-Tolerant Aluminum-Titanate-Reinforced Alumina," *J. Eur. Ceram. Soc.*, 7, 93–99 (1991).

[10] P. Chantikul, S. J. Bennison, and B. R. Lawn, "Role of Grain Size in the Strength and *R*-Curve Properties of Alumina," *J. Am. Ceram. Soc.*, 73 [8] 2419–27 (1990).

[11] L. M. Braun, S. J. Bennison, and B. R. Lawn, "Objective Evaluation of Short-Crack Toughness Curves Using Indentation Flaws: Case Study on Alumina-Based Ceramics," *J. Am. Ceram. Soc.*, 75 [11] 3049–57 (1992).

[12] N. P. Padture, "Crack Resistance and Strength Properties of Some Alumina-Based Ceramics"; Ph.D. Dissertation. Lehigh University, Bethlehem, PA, 1991.

[13] G. Sines and T. Okada, "Flaws Responsible for Slow Cracking in the Delayed Fracture of Alumina," *J. Am. Ceram. Soc.*, 66 [3] 228–32 (1983).

[14] T. Okada and G. Sines, "Crack Coalescence and Microscopic Crack Growth in the Delayed Fracture of Alumina," *J. Am. Ceram. Soc.*, 66 [10] 719–25 (1983).

[15] S.-J. Cho, B. J. Hockey, B. R. Lawn, and S. J. Bennison, "Grain-Size and *R*-Curve Effects in the Abrasive Wear of Alumina," *J. Am. Ceram. Soc.*, 72 [7] 1249–52 (1989).

[16] Y.-W. Mai and B. R. Lawn, "Crack-Interface Grain Bridging as a Fracture Resistance Mechanism in Ceramics: II, Theoretical Fracture Mechanics Model," *J. Am. Ceram. Soc.*, 70 [4] 289–94 (1987).

[17] B. N. Cox and D. B. Marshall, "Stable and Unstable Solutions for Bridged Cracks in Various Specimens," *Acta Metall.*, 39 [4] 579–89 (1991).

[18] N. P. Padture, S. J. Bennison, and H. M. Chan, "Flaw-Tolerance and Crack-Resistance Properties of Alumina–Aluminum Titanate Composites with Tailored Microstructures," *J. Am. Ceram. Soc.*, 76 [9] 2312–20 (1993).

[19] S. J. Bennison, N. P. Padture, J. L. Runyan, and B. R. Lawn, "Flaw-Insensitive Ceramics," *Philos. Mag. Lett.*, 64 [4] 191–95 (1991). □

PHILOSOPHICAL MAGAZINE A, 1993, VOL. 68, NO. 5, 1003–1016

Indentation fatigue

A simple cyclic Hertzian test for measuring damage accumulation in polycrystalline ceramics

By FERNANDO GUIBERTEAU†, NITIN P. PADTURE‡, HONGDA CAI‡
and BRIAN R. LAWN
Materials Science and Engineering Laboratory,
National Institute of Standards and Technology,
Gaithersburg, Maryland 20899, USA

[*Received 4 February 1993 and accepted 17 May 1993*]

ABSTRACT

A simple Hertzian contact procedure for investigating cyclic fatigue damage in brittle polycrystalline ceramics is described. Repeat loading of a spherical indenter on a coarse alumina ceramic produces cumulative mechanical damage. The mode of damage is one of deformation-induced intergranular microfracture, leading ultimately at large numbers of cycles and high contact pressures to severe grain dislodgement. In contrast to the classical Hertzian cone cracks that form in more homogeneous materials in the regions of tensile stress *outside* the contact circle, the damage in the coarse-grain alumina develops in a zone of high shear stress and hydrostatic compression *beneath* the contact circle. The fatigue damage is evident in inert environments, confirming the mechanical nature of the process, although exposure to moisture accelerates the effect. The relatively modest degradation in failure stress with number of repeat contacts for indented flexure specimens suggests that conventional strength and toughness testing procedures may not always provide sensitive indications of the extent of damage that can be incurred in concentrated loading.

§ 1. INTRODUCTION

Strength and toughness properties in monotonic loading have been extensively investigated in ceramics. Special interest has recently been shown in polycrystalline materials with enhanced toughening from crack bridging, including various types of monophase and multi-phase composites (Knehans and Steinbrech 1983, Swanson, Fairbanks, Lawn, Mai and Hockey 1987, Bennison and Lawn 1989a, b, Chantikul, Bennison and Lawn 1990, Bennison, Rödel, Lathabai, Chantikul and Lawn 1991, Padture *et al.* 1991, Braun, Bennison and Lawn 1992a, b). Bridging leads to toughness-curve (*T*-curve, or *R*-curve) behaviour, with desirable long-crack flaw tolerance. It is enhanced by internal stresses, e.g. from thermal expansion anisotropy (TEA) mismatch, and is more pronounced in coarser grain microstructures.

However, the same internal stresses responsible for enhanced bridging in the long-crack domain can lead to deleterious short-crack properties, because of premature grain boundary cracking at tensile facets. Wear studies afford an illustrative precedent.

---

† Guest Scientist, from Departamento de Física, Universidad de Extremadura, 06071-Badajoz, Spain.

‡ Guest Scientist, from Department of Materials Science and Engineering, Lehigh University, Bethlehem, Pennsylvania 18015, USA.

In alumina, increasing the grain size increases the long-crack toughness (Chantikul *et al.* 1990), but reduces the resistance to microfracture-assisted wear from multi-pass sliding contacts (Cho, Hockey, Lawn and Bennison 1989, Cho, Moon, Hockey and Hsu 1992). The mechanism of material degradation is an abrupt rise in grain boundary microfracture after an incubation wear period, from the steady augmentation of internal stresses by deformation-accumulation stresses (Ajayi and Ludema 1988, Cho *et al.* 1989). It is not just fracture mechanics, but also precursor damage mechanics, that govern 'failure' events.

These remarks are particularly relevant to the potential response of tough ceramics in repeated loading, i.e. cyclic fatigue (Ritchie 1988, Suresh 1991). Traditional cyclic fatigue tests are conducted on specimens with long cracks. Such tests are expensive, difficult, and labour intensive. They require testing machines with demanding load control over extended periods. An even more compelling criticism is that it is not generally valid to extrapolate long-crack results back to the short-crack region, where *strength is determined*, since for a given material the extreme-region toughness values are often inversely related—i.e. the toughness curves for different grain sizes tend to cross each other (Chantikul *et al.* 1990). This last point is especially pertinent in view of the fact that many ceramic components in service experience concentrated contact stresses (Lawn and Wilshaw 1975) at the microstructural level, rather than macroscopically distributed stresses of the type simulated in conventional crack propagation and strength tests. Questions then arise as to the mechanics of 'failure' in such concentrated loading conditions, and their relevance to fatigue properties.

In this study we propose a simple new procedure for studying the fatigue properties of brittle polycrystalline ceramics. We use an indenter to apply a concentrated load on flat alumina surfaces, and examine the ensuing damage patterns as a function of number of cycles. Some contact damage studies on polycrystalline ceramics have previously been made with 'sharp' fixed-profile indenters (Lawn and Wilshaw 1975) (e.g. Vickers or Knoop pyramids, or Rockwell cones) where the contact pressure (i.e. the 'hardness') is effectively independent of load (Sperisen, Carry and Mocellin 1986, Makino, Kamiya and Wada 1988, 1991, Howes 1990, Reece and Guiu 1991). However, although sharp indenters usefully reveal the microstructural nature of the damage process, they produce virtually 'saturated' deformation at first contact, and are therefore not ideally suited for examining damage *evolution*. Where they have been used in repeated loading (Howes 1990, Reece and Guiu 1991), such indentation experiments reveal only slight fatigue tendencies.

Accordingly, in the present study we use the spherical indenter configuration of fig. 1, where the contact pressure increases monotonically with load from zero at first contact. In its initial stages of loading the stress field is purely elastic, i.e. the classical Hertzian stress field (Hertz 1896, Johnson 1985); the indentation is said to be blunt (Lawn and Wilshaw 1975). Beyond a critical load the material undergoes irreversible deformation and/or fracture. In well-behaved, highly brittle materials like silicate glasses, single crystals, and ultra-fine-grain polycrystals a well-defined cone-shaped crack, the Hertzian fracture, runs around the contact circle and spreads downward and outward into the material. This kind of fracture has received extensive attention in the literature (Frank and Lawn 1967, Lawn 1968, Langitan and Lawn 1969, Lawn and Wilshaw 1975, Lawn and Marshall 1978). In softer, less brittle materials like most metals (Tabor 1951) and lithium fluoride monocrystals (Swain and Lawn 1969) the material deforms plastically beyond the elastic limit; cracks, when they do ultimately develop, take on more of the form of the *radial* and *lateral* geometries characteristic of

Fig. 1

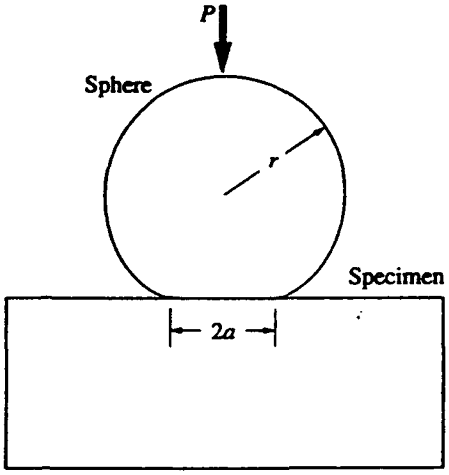

Schematic diagram of indentation with hard elastic sphere of radius r, load P, on flat brittle surface. Loads are made in single (static test) or multiple (fatigue test) cycles.

sharp indenters (Lawn and Swain 1975, Lawn and Wilshaw 1975). This latter kind of deformation-initiated fracture can also be generated in more brittle materials by using indenters of smaller radius (Swain and Hagan 1976)—there is a 'size effect' in the contact process, in which the pattern undergoes a transition from 'blunt' to 'sharp' as the sphere radius is diminished (Lawn and Wilshaw 1975, Lawn 1993).

We shall see that in the tougher, coarser polycrystalline bridging ceramics of interest to us here the fracture pattern is more complex than those discussed above, involving deformation and fracture at the microstructural level. We shall also demonstrate that the spherical-indenter test provides a useful and uncommonly sensitive tool for investigating such damage.

§ 2. EXPERIMENTAL METHOD

The material chosen for the main focus of the present study was a high-purity commercial alumina with grain size 23 μm.† This is sufficiently coarse that the material has a significant toughness-curve (Bennison and Lawn 1989b, Chantikul *et al.* 1990, Braun, Bennison and Lawn 1992a). The material is similar to that used in an earlier fatigue study (Lathabai, Mai and Lawn 1989). In that earlier study the specimens were in the form of discs, each containing a well-developed Vickers indentation crack. Biaxial flexure tests revealed no measurable strength degradation from cyclic loading to $> 10^5$ cycles.‡

A fine-grain alumina (grain size 2·5 μm) with conventional Hertzian fracture properties (§ 3.1.) was used as a control material with an effectively single-valued toughness (Braun *et al.* 1992a).

The alumina specimens were obtained as discs 30 nm diameter and 4 nm thick. Their surfaces were polished to a final finish with 1 μm diamond grit. Indentations were

---

† Vistal grade Al_2O_3, Coors Ceramics Co., Golden CO, USA.

‡ Later tests in a similar alumina of grain sizes 35 μm did reveal a measurable degradation, $< 20\%$, over $> 10^7$ cycles (Lathabai, Rödel and Lawn 1991).

made with tungsten carbide spheres, radii $r = 1{\cdot}98, 3{\cdot}18, 4{\cdot}76, 7{\cdot}94$ and $12{\cdot}70$ mm. Loads in the range $P = 0$ to 3500 N were delivered using crosshead testing machines† at constant displacement rates. The practical loads achievable at smaller radii were ultimately limited by permanent deformation of the WC spheres themselves (see § 3.2). Cycling between zero and specified maximum loads was conducted at frequencies of 1 Hz ('fast cycle') and 0·002 Hz ('slow cycle'). A few control static tests were run over a prolonged hold time at maximum load. The indentation test environment was either nitrogen gas (relative humidity $< 1{\cdot}5\%$), laboratory ambient (humidity 40–50%), or water. Some specimens were coated with gold *prior* to indentation so that the contact radius might be determined as a function of applied load from the residual surface trace, and the contact pressure thereby determined (§ 3.2.).

Reflection optical microscopy was use to examine the indented surfaces. The presence of surface damage was detected by coating the surfaces with gold *after* indentation and viewing in Nomarski interference contrast. Subsurface damage in the translucent coarse alumina was most readily observable in dark-field illumination. Some specimens were sectioned through the indentations to examine the extent of the subsurface damage, by cutting adjacent to the indentation sites and grinding and polishing down to the contact diameter.

Flexure tests were carried out on a batch of indented discs to determine the effect of cyclic degradation on strength. In these tests each disc contained a single cyclic Hertzian indentation at its centre. The discs were broken in biaxial flexure, using a flat circular punch of diameter 6 mm on a three-point support of diameter 22 mm. Prior to flexure the indentations were covered with a drop of silicone oil, and the specimens broken within a load time < 10 ms, to determine 'inert strengths'.

§ 3. RESULTS

3.1. *Damage of indented alumina surfaces*

The evolution of cyclic indentation damage in the coarse grain alumina specimens for indentations in nitrogen gas is apparent in the sequence of fig. 2. The sequence represents an increasing number of cycles, $n = 1, 10, 100, 1000$ and $10\,000$, at frequency 1 Hz, sphere radius $r = 3{\cdot}18$ mm and maximum load $P = 1000$ N. These indentation conditions correspond to the first detectable onset of single-cycle damage. A progressive accumulation of damage with number of cycles is evident in the sequence. Since dry nitrogen is an effectively inert environment, one may assert that the cumulative damage process is driven essentially by *mechanical* forces, as distinct from *chemical* forces. Nevertheless fig. 3, which shows micrographs taken under the same indentation conditions as in fig. 2 (*e*) (i.e. $n = 10\,000$ cycles) but in air and water, indicates that the role of chemistry, while not primary, is not benign in the final damage evolution.

Closer inspection of the micrographs in figs. 2 and 3 provides some insight into the nature of the damage. At some of the indentations, segmented circular crack traces are apparent in the outer regions of the damage pattern, indicative of the formation of 'partial' cone fractures outside an expanding contact circle (final diameter indicated by marker in figs.) (Lawn and Wilshaw 1975). The incidence of these fractures does not increase markedly with the number of cycles. On the other hand the damage within the inner contact area, manifested macroscopically as an ever-deepening residual contact

---

† Instron Universal Screw-Driven Testing Machine 1122 (slow-cycle tests) and Digital Servo-Hydraulic Testing Machine 8502 (fast-cycle tests), Instron Corp., Canton, MA, USA.

Fig. 2

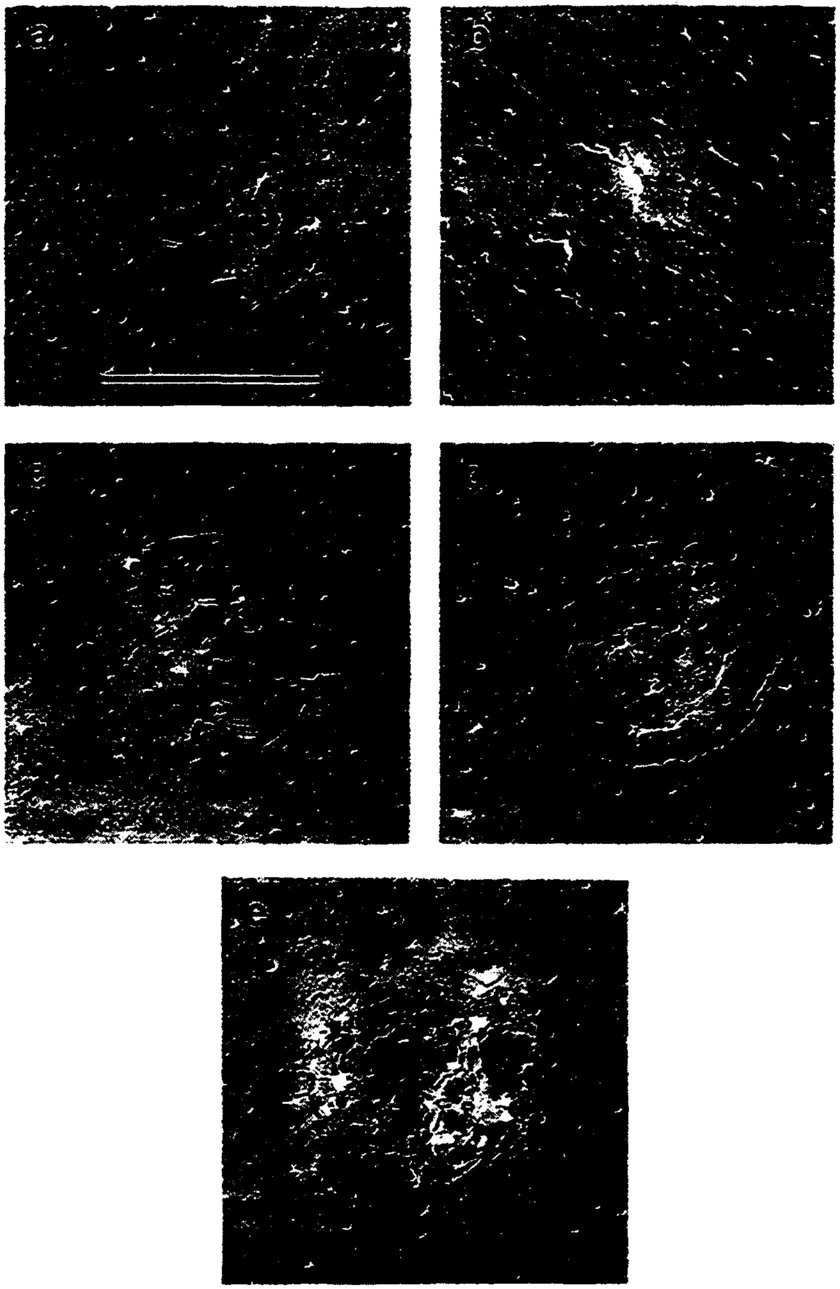

Micrographs of surface damage in coarse alumina (grain size 23 μm) from indentation by WC sphere, radius $r = 3{\cdot}18$ mm, at load $P = 1000$ N, in dry nitrogen gas. Number of cycles n, (*a*) 1, (*b*) 10, (*c*) 100, (*d*) 1000, (*e*) 10000, frequency 1 Hz. Surfaces gold coated after indentation, viewed in Nomarski interference illumination. Marker denotes contact diameter, $2a = 454$ μm.

Fig. 3

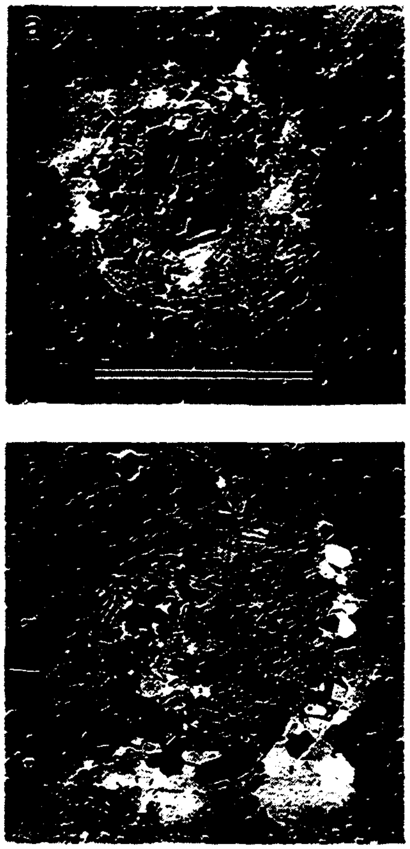

Micrographs of surface damage in coarse alumina from indentation by WC sphere, radius $r = 3{\cdot}18$ mm, load $P = 1000$ N, $n = 10\,000$ cycles, frequency 1 Hz. Tests in (*a*) air, (*b*) water. Surfaces gold coated after indentation, viewed in Nomarski interference illumination. Note enhancement of damage relative to nitrogen test in fig. 2(*e*). Marker denotes contact diameter, $2a = 454\ \mu$m.

impression, does increase with number of cycles. This enhanced damage is characterized by *inter*grain boundary microcracking, and associated *intra*grain deformation in the form of twin or slip bands. Hence it would appear that the fatigue process involves deformation-induced crack initiation at the microstructural level, rather than enhanced propagation of well-developed Hertzian cracks.

As we shall see in the following subsection, an increase in indentation pressure may be rendered by increasing the contact load or reducing the sphere radius. Figure 4 shows indentations made at a higher maximum load $P = 2000$ N and smaller sphere radius $r = 1{\cdot}98$ mm, for $n = 1$ (fig. 4(*a*)) and 10 (fig. 4(*c*)), at frequency 0·002 Hz, in water. For comparison, the figure includes an indentation held at maximum load for an extended duration equal to the total time taken by ten normal cycles (fig. 4*b*)). We observe a conspicuous enhancement in surface damage after the cyclic loading, but *not* after the static loading. This sequence reaffirms the existence of a true mechanical fatigue effect—the results cannot be simply interpreted as the integration over time-

Fig. 4

Micrographs of surface damage in coarse alumina, WC sphere radius $r = 1{\cdot}98$ mm, load $P = 2000$ N, in water: (*a*) 1 cycle at 0·002 Hz; (*b*) static test at same peak load with hold time equal to total duration of test (*c*); (*c*) 10 cycles at 0·002 Hz. Surfaces gold coated after indentation, viewed in Nomarski interference illumination. Marker denotes contact diameter, $2a = 500$ μm.

dependent slow crack growth, because the prolonged hold time at maximum load does not significantly enhance the damage relative to the cyclic test.

The cause of the residual impression is evident in the dark field micrographs of fig. 5 (upper views), of indentations in air at $n = 1$, 100, 10 000 cycles. The micrographs show enhanced specular scattering from below the contact area, indicating the presence of a pervasive subsurface microcracking crush zone. Section views through such indentations (lower views) indicate that the microcrack zones initiate beneath the actual contact surface and, with increasing load, extend upward to the surface and downward

Fig. 5

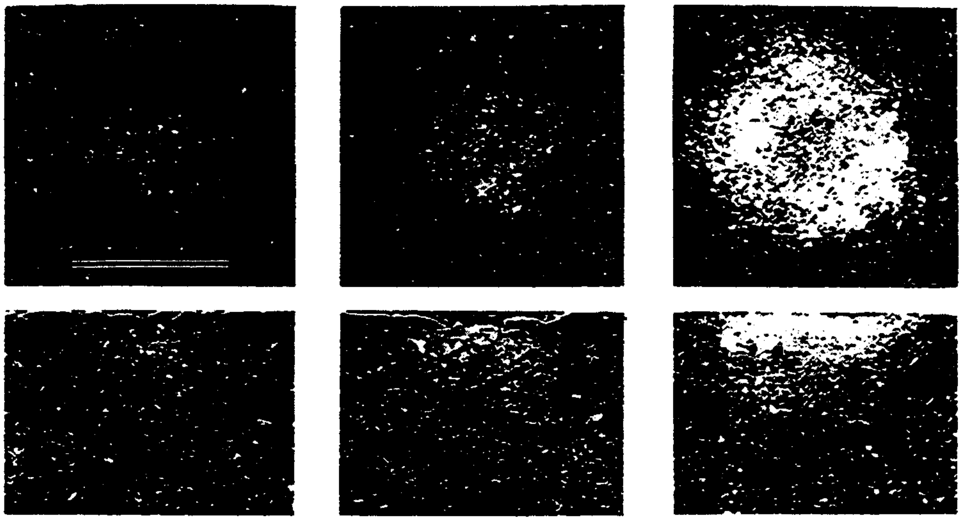

(*a*) (*b*) (*c*)

Damage in coarse alumina, WC sphere radius $r=3{\cdot}18$ mm, load $P=1000$ N: (*a*) 1, (*b*) 100, (*c*) 10 000 cycles, frequency 1 Hz, in air. Upper micrographs surface views, lower micrographs section views, in dark field illumination. Marker denotes contact diameter, $2a=454\,\mu$m.

to a depth of order one contact diameter. Similar subsurface damage zones have been observed in silicon nitride ceramics (Makino *et al.* 1991).

An indentation damage pattern in the fine-grain *control* alumina, for $n=10\,000$ cycles at 1 Hz, $r=3{\cdot}18$ mm and $P=1000$ N, in air, is shown in fig. 6. Relative to its coarse-grain counterpart in fig. 3 (*a*), the damage is slight. The incidence of any damage at all becomes apparent only after several thousand cycles; and, when it does occur, assumes the classical Hertzian cone geometry. There is no detectable microcracking within the contact area up to the 10 000 cycle limit in our experiments. There is therefore a clear implication of a microstructure size effect in the damage process responsible for the fatigue behaviour.

3.2. *Indentation stress–strain curve*

Consider again the sphere, radius *r*, load *P*, on a flat specimen surface, in the schematic diagram of fig. 1. We can define useful scaling quantities for the contact field, regardless of whether the deformation is elastic or inelastic (Tabor 1951, Swain and Lawn 1969). The magnitude of the stress field scales with the mean indentation pressure,

$$p_0=P/\pi a^2. \qquad (1)$$

Likewise, from geometrical similarity, the magnitude of the strain field scales with a/r. Hence we may determine a characteristic indentation stress–strain curve $p_0(a/r)$ for a given material, independent of sphere size. Such curves have been previously determined for lithium fluoride single crystals (Swain and Lawn 1969) and silicate glasses (Swain and Hagan 1976).

Fig. 6

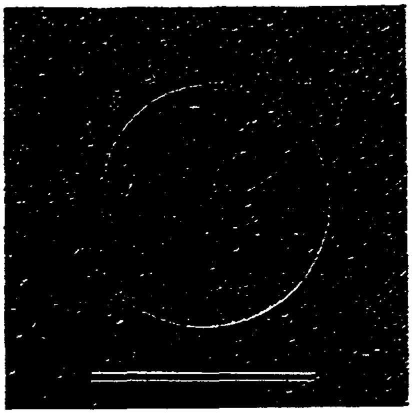

Micrograph of surface damage in fine alumina (grain size 2·5 μm), produced by WC sphere, radius $r = 3{\cdot}18$ mm, at load $P = 1000$ N, $n = 10\,000$ cycles, in air. Surfaces gold coated after indentation, viewed in Nomarski interference illumination. Marker denotes contact diameter, $2a = 454$ μm (cf. fig. 3(*a*)).

Fig. 7

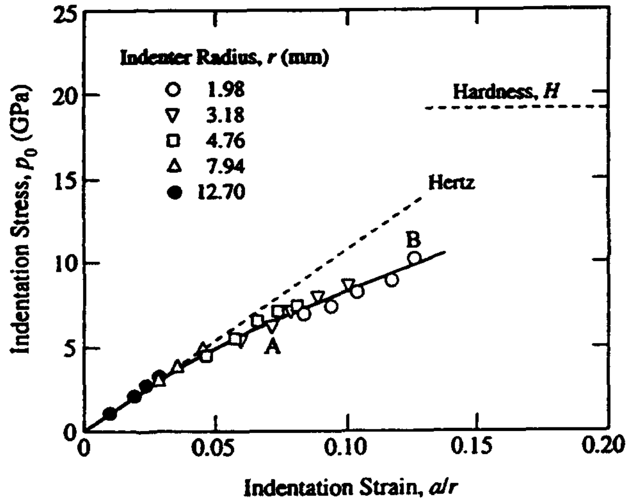

Indentation stress–strain curve for single-cycle contacts in coarse alumina, in air, using spheres of different radius as indicated. Dashed line is Hertzian elastic response, eqn. (2). Point A corresponds to loading conditions in figs. 2 and 3, B to conditions in fig. 4.

We generate appropriate $p_0(a/r)$ data points for our coarse grain alumina in fig. 7, from measurements of a at each value of P from single-cycle tests in air using spheres of specified radii r. We see that for a given sphere radius the indentation pressure initially rises linearly, in accord with the Hertzian theory of elastic contact (Swain and Lawn 1969):

$$p_0 = (3E/4\pi k)(a/r), \tag{2}$$

where $E = 393$ GPa is Young's modulus of the alumina; the constant

$$k = (9/16)[(1 - \nu^2) + (1 - \nu'^2)E/E'] = 0{\cdot}88$$

for tungsten carbide on alumina, with ν Poisson's ratio and the prime notation denoting the indenter material. This relation is represented as the dashed line in fig. 7.

The data deviate below the Hertz line at approximately $p_0 \approx 3$–5 GPa, as indicated by the empirically fitted solid curve. This is the region in which deformation-induced microcracking becomes perceptible in single-cycle loading. For instance, the indentations in figs. 2 and 3 correspond to point A in fig. 7; the indentations in fig. 4 correspond to point B.

Higher stresses than those shown in fig. 7 could not be achieved without permanently deforming the WC spheres. According to Tabor (1951), an isotropic indenting sphere should deform plastically at a contact pressure $\approx 0{\cdot}4$ times the hardness, which corresponds to $p_0 \approx 8$ GPa in fig. 7.

3.3. *Strength degradation*

Results from the measurements of inert strength σ_F as a function of number of cycles n in air are plotted in fig. 8. The indentations in these experiments correspond to the loading conditions A in fig. 7, i.e. just beyond the point of first perceptible deviation from the Hertz line, so as to allow for maximum development of mechanical damage during cycling.

Relative to surfaces *without* indentations (hatched box at left in fig. 8), we see that measurable strength degradation is achieved in the first cycle. For repeat indentations, the degradation relative to specimens with a single cycle is $<30\%$ over 1–10^4 cycles. In view of the strong damage buildup apparent in figs. 2–5, this strength fall-off is relatively modest.

§4. Discussion

We have demonstrated substantial fatigue effects in a coarse alumina ceramic using a Hertzian contact test. Microscopic examination of the contact sites reveals damage

Fig. 8

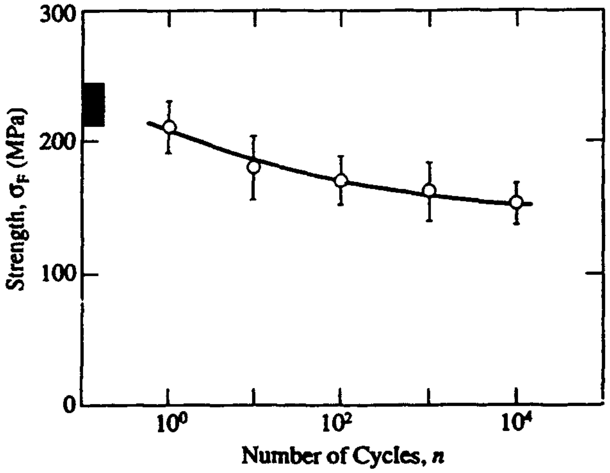

Strength of coarse alumina as function of number of cycles after indentation in air with sphere radius $r = 3{\cdot}18$ mm, load $P = 1000$ N, frequency 1 Hz. Each datum point mean and standard deviation, four specimens. Hatched box at left axis represents breaks from specimens without indentations.

accumulation with increasing number of cycles. The test configuration is simple, requiring only a hard sphere and a smooth flat specimen surface, without the need for the fabrication of expensive, long-crack specimens. One still requires a testing machine for delivering the cyclic loading: however, in favourable cases, e.g. fig. 4, a conventional low-frequency machine may be sufficient to demonstrate the effect.

Strength tests provide a quantitative measure of the severity of accumulated damage. In fig. 8 the degradation relative to first-cycle contact is almost 30% over 10^4 cycles in air. However, strength degradation does not reflect the severity of damage accumulation observed in the micrographs of figs. 2–5.† Strength depends not on the *density*, but rather the *size*, of the flaws; and even this latter dependence is somewhat tempered by the existence of a toughness-curve (Lathabai *et al.* 1989). Flaw density is of much greater influence in wear properties. A similar insensitivity in strength characteristics has been demonstrated in *translating* sphere tests on glass, where an increased friction coefficient produces substantially enhanced contact damage but has relatively small influence on the failure stresses of the contacted surfaces (Lawn, Wiederhorn and Roberts 1984). Again, the implication is that strength (and, by association, toughness) measurements may not always be the most practical measure of damage accumulation in contact fatigue configurations. In this context, it may be noted that the present concentrated-load tests deliver much higher stresses over a much smaller area (typically 5 GPa over 0·1 mm^2) than in conventional strength tests (typically 500 MPa over 100 mm^2). Alternative tests for quantifying accumulated damage during contact history, e.g. acoustic emission (Sperisen *et al.* 1986), might provide more relevant quantitative information.

As to indenter geometry, the 'blunt' contact typified by the Hertzian configuration is especially favoured for following the evolution of damage, because the contact pressure increases monotonically up the $p_0(a/r)$ curve in fig. 7, from linear elastic to the onset of first deformation and microcracking through to the fully elastic–plastic region. The same is not true of 'sharp' contacts with fixed-profile indenters, e.g. Vickers, ıse the contact pressure saturates at the hardness value H (load/projected contact horizontal dashed line in fig. 7) virtually at first contact.‡

he question as to the mode of cyclic fatigue in the alumina remains to be answered. ears to be primarily mechanical rather than chemical. An important ingredient of atigue mode is the existence of some 'kinematic irreversibility of microscopic mation' (Suresh 1991), so that hysteresis exists in the applied load–displacement ion. In the present case the onset of intragrain deformation, coupled with ensuing microcracking, would appear to constitute the necessary basis for such irreversibility. But what are the basic elements of the deformation, and what stresses are needed to activate these elements? In single crystal sapphire, twinning and high-stress slip can occur at room temperature (Hockey 1971, Cannon 1984, Chan and Lawn 1988); in polycrystals, grain boundary stress concentrations from these shear elements, in combination with pre-existing thermal anisotropy stresses, can lead to premature grain

---

† This degradation is nevertheless considerably greater than that observed in a previous study on the same alumina in cyclic flexure testing *after* introduction of a single-cycle Vickers indentation (Lathabai *et al.* 1989).

‡ At the same time, the facility remains for the Hertzian test to simulate the broader features of sharp-indenter patterns, by virtue of an intrinsic size effect in the critical stress relation for cone fracture initiation: at sufficiently small sphere radius, the classical cone fracture is suppressed in favour of subsurface deformation, resulting in a kind of blunt–sharp, brittle–ductile transition (Lawn and Wilshaw 1975, Puttick 1979, Lawn 1993).

Fig. 9

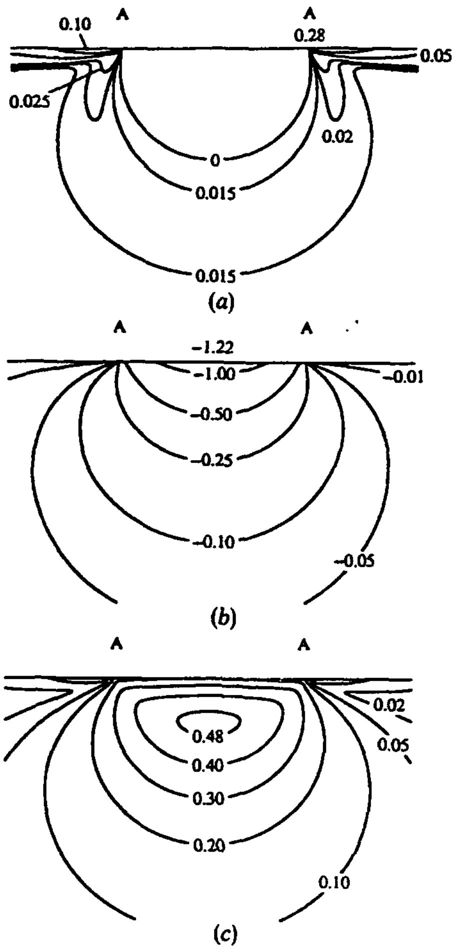

Stress contours in Hertzian contact field, normalized by p_0. (*a*) Principal tensile stress σ_1, (*b*) hydrostatic stress $\frac{1}{3}(\sigma_1+\sigma_2+\sigma_3)$, and (*c*) principal shear stress $\frac{1}{2}(\sigma_1-\sigma_3)$. Calculated using Poisson's ratio $\nu=0{\cdot}22$ for alumina. AA denotes contact diameter.

boundary microcracking. Again, wear studies with translating or rotating spherical indenters provide a precedent for this mechanism (Cho *et al.* 1989, 1992).

There is also the issue as to which stress component of the Hertzian field is responsible for initiating the damage. Recall in fig. 5 that the damage zone is located in a confined region beneath the contact area. An indication of the active component may be obtained from the Hertzian (elastic) stress field plots (Frank and Lawn, 1967, Lawn, Wilshaw and Hartley 1974, Lawn and Wilshaw 1975, Johnson 1985) in fig. 9. This diagram plots stress contours of the principal tensile stress $[\sigma_1]$, hydrostatic stress $[\frac{1}{3}(\sigma_1+\sigma_2+\sigma_3)]$, and principal shear stress $[\frac{1}{2}(\sigma_1-\sigma_3)]$. Whereas the cone crack segments in figs. 2 and 3 form outside the contact area, i.e. where the normal stresses in fig. 9 (*a*) are mildly tensile (maximum $\approx 0{\cdot}28p_0$ at contact circle), the subsurface microcrack zones form beneath the contact area, where the hydrostatic stresses in fig. 9 (*b*) are highly compressive (maximum $\approx -1{\cdot}22p_0$ at the contact centre). However, the shear stresses in fig. 9 (*c*) also attain significant levels beneath the contact area (maximum $\approx 0{\cdot}50p_0$ at depth 0·5*a* along contact axis). It is therefore most likely that those subsurface deformation processes (twinning and slip) ultimately responsible for the microcracking seen in fig. 5 are governed by the shear component of the stress field. Once such a deformation occurs, of course, the Hertzian elastic field description no longer prevails, and one must take into account the effect of irreversible processes on the stress–strain characteristics of the material (Lawn and Wilshaw 1975). In particular, the incidence of microcracking will inevitably dilate the material in the deformation zone, especially if local tensile TEA stresses are relaxed, setting up conditions for continued irreversibility in cyclic loading (Suresh 1991). The intrusion of water into the microcracks will only serve to enhance such irreversibility.

What are the materials implications of the observations in this study? How general are our results on coarse alumina? The comparatively small amount of damage observed in the fine-grain alumina in our studies implies the existence of potentially strong size effects from microstructural scaling. There is again the useful precedent from earlier wear studies on alumina using rotating spherical indenters, where the incubation time to effect a transition from deformation- to microfracture-controlled surface removal was found to increase dramatically at finer grain sizes (Cho *et al.* 1989). It would appear that the highest resistance to fatigue from damage accumulation may be achieved by refining grain size and by avoiding excessive internal residual stresses. Once more, such material requirements may well run counter to those for improving long-crack toughness (Bennison *et al.* 1989b, Chantikul *et al.* 1990, Lawn, Padture, Braun and Bennison 1993, Padture, Runyan, Bennison, Braun and Lawn 1993).

ACKNOWLEDGMENTS

Thanks are due to J. D. Sibold of Coors Ceramics Co. for providing the materials. Funding for this study was provided by the U.S. Air Force Office of Scientific Research. Financial support for F. G. from the Ministerio de Educación y Ciencia (DGICYT), Spain, is gratefully acknowledged.

REFERENCES

AJAYI, O. O., and LUDEMA, K. C., 1988, *Wear*, **124**, 237.

BENNISON, S. J., and LAWN, B. R., 1989a, *J. mater. Sci.*, **24**, 3169; 1989b, *Acta metall.*, **37**, 2659.

BENNISON, S. J., RÖDEL, J., LATHABAI, S., CHANTIKUL, P., and LAWN, B. R., 1991, *Toughening Mechanisms in Quasi-Brittle Materials*, edited by S. P. Shah (Dordrecht: Kluwer), p. 209.

BRAUN, L. M., BENNISON, S. J., and LAWN, B. R., 1992a, *J. Am. Ceram. Soc.*, **75**, 3049; 1992b, *Ceramic Engineering and Science Proceedings*, Vol. 13 (Westerville, Ohio: The American Cermaic Society), p. 156.

CANNON, R. M., 1984, *Advances in Ceramics Structure and Properties of MgO and Al_2O_3 Ceramics*, edited by W. D. Kingery (Columbus, Ohio: The American Ceramic Society), p. 818.

CHAN, H. M., and LAWN, B. R., 1988, *J. Am. Ceram. Soc.*, **71**, 29.

CHANTIKUL, P., BENNISON, S. J., and LAWN, B. R., 1990, *J. Am. Ceram. Soc.*, **72**, 2419.

CHO, S.-J., HOCKEY, B. J., LAWN, B. R., and BENNISON, S. J., 1989, *J. Am. Ceram. Soc.*, **72**, 1249.

CHO, S.-J., MOON, H., HOCKEY, B. J., and HSU, S. M., 1992, *Acta metall.*, **40**, 185.

FRANK, F. C., and LAWN, B. R., 1967, *Proc. R. Soc. Lond.* A, **299**, 291.

HERTZ, H. H., 1896, *Hertz's Miscellaneous Papers* (London: Macmillan), chaps. 5, 6.

HOCKEY, B. J., 1971, *J. Am. Ceram. Soc.*, **54**, 223.

HOWES, V. R., 1990, *J. hard Mater.*, **1**, 95.

JOHNSON, K. L., 1985, *Contact Mechanics* (Cambridge University Press).

KNEHANS, R., and STEINBRECH, R. W., 1983, *Science of Ceramics*, Vol. 12, edited by P. Vincenzini (Imola, Italy: Ceramurgica), p. 613.

Langitan, F. B., and Lawn, B. R., 1969, *J. appl. Phys.*, **40**, 4009.

Lathabai, S., Mai, Y. W., and Lawn, B. R., 1989, *J. Am. Ceram. Soc.*, **72**, 1760.

Lathabai, S., Rödel, J., and Lawn, B. R., 1991, *J. Am. Ceram. Soc.*, **74**, 1340.

Lawn, B. R., 1968, *J. appl. Phys.*, **39**, 4828; 1993, *Fracture of Brittle Solids* (Cambridge: Cambridge University Press).

Lawn, B. R., and Marshall, D. B., 1978, *Fracture Mechanics of Ceramics*, Vol. 3, edited by R. C. Bradt, D. P. H. Hasselman and F. F. Lange (New York: Plenum), p. 205.

Lawn, B. R., Padture, N. P., Braun, L. M., and Bennison, S. J., 1993, *J. Am. Ceram. Soc.*, in press.

Lawn, B. R., and Swain, M. V., 1975, *J. Mater. Sci.*, **10**, 113.

Lawn, B. R., Wiederhorn, S. M., and Roberts, D. E., 1984, *J. mater. Sci.*, **19**, 2561.

Lawn, B. R., and Wilshaw, T. R., 1975, *J. mater. Sci.*, **10**, 1049.

Lawn, B. R., Wilshaw, T. R., and Hartley, N. E. W., 1974, *Int. J. Fract.*, **10**, 1.

Makino, H., Kamiya, N., and Wada, S., 1988, *J. mater Sci. Lett.*, **7**, 475; 1991, *Proceedings of the First International Symposium on the Science of Engineering Ceramics*, edited by S. Kimura and K. Niihara (Koda, Japan: Aichi-Prefecture), p. 229.

Padture, N. P., Bennison, S. J., Runyan, J. L., Rödel, J., Chan, H. M., and Lawn, B. R., 1991, *Ceramic Transactions*, Vol. 19, edited by M. D. Sacks (Westerville, Ohio: The American Ceramic Society), p. 715.

Padture, N. P., Runyan, J. L., Bennison, S. J., Braun, L. M., and Lawn, B. R., 1993, *J. Am. Ceram. Soc.* in press.

Puttick, K. E., 1979, *J. Phys.* D, **12**, L19.

Reece, M., and Guiu, F., 1991, *J. Am. Ceram. Soc.*, **74**, 148.

Ritchie, R. O., 1988, *Mater. Sci. Engng*, A, **103**, 15.

Sperisen, T., Carry, C., and Mocellin, A., 1986, *Fracture Mechanics of Ceramics*, Vol. 8, edited by R. C. Bradt, A. G. Evans, D. P. H. Hasselman and F. F. Lange (New York: Plenum), p. 69.

Suresh, S., 1991, *Fatigue of Materials* (Cambridge: Cambridge University Press).

Swain, M. V., and Hagan, J. T., 1976, *J. Phys.* D, **9**, 2201.

Swain, M. V., and Lawn, B. R., 1969, *Phys. Stat. sol.*, 35, 909.

Swanson, P. L., Fairbanks, C. J., Lawn, B. R., Mai, Y.-W., and Hockey, B. J., 1987, *J. Am. Ceram. Soc.*, **70**, 279.

Tabor, D., 1951, *Hardness of Metals* (Oxford: Clarendon).

Journal of the European Ceramic Society 13 (1994) 149–157

Flaw Tolerance and Toughness Curves in Two-Phase Particulate Composites: SiC/Glass System

Hongda Cai,* Nitin P. Padture,* Bryan M. Hooks** & Brian R. Lawn

Materials Science and Engineering Laboratory, National Institute of Standards and Technology, Gaithersburg, Maryland 20899, USA

(Received 11 March 1993; accepted 10 September 1993)

Abstract

Flaw-tolerance and associated toughness-curve (T-curve) characteristics in SiC/glass particle/matrix composites are studied. Two glass compositions, chosen to produce composites at extremes of high (H) and low (L) thermal expansion mismatch relative to the SiC particles, are investigated. In-situ observations of crack extension from indentation flaws reveal widely different responses: in the L composite the path is relatively undistorted from the planar geometry, with trans-particle fractures; in the H composite the path deflects strongly around the particles, with consequent interfacial bridge formation and activity in the crack wake. Surface fracture patterns produced by spherical indenters confirm the implied transition from trans-particle to inter-particle fracture with increasing internal residual stress, and point to a potential degradation in short-crack properties like wear and fatigue. Indentation–strength measurements also show different characteristics in the two composites: minor flaw tolerance in the L material, consistent with a single-valued, 'rule of mixtures' toughness; major tolerance in the H material, consistent with a pronounced T*-curve. The* T*-curves themselves are deconvoluted from the indentation–strength data for each composite and analyzed.*

*Fehlertoleranz und damit verbundene Charakteristika der Rißwiderstandskurven (*R*-Kurven) von SiC/Glas (Teilchen/Matrix) Verbundwerkstoffen wurden untersucht. Zwei Glaszusammensetzungen, die so gewählt wurden, daß der thermische Ausdehnungskoeffizient entweder extrem groß (H) oder klein (L) im Vergleich zu dem der SiC-Teilchen war, wurden untersucht. In-situ Beobachtung der Rißausbreitung ausgehend von Defekten verursacht durch Eindrücke zeigen stark unterschiedliche Verhaltensweisen: in den L-Verbundwerkstoffen weight der Rißpfad relativ wenig von ebener Geometrie ab, die Risse Verlaufen transgranular; in dem H-Verbundwerkstoff wird der Rißpfad um die Teilchen herumgelenkt, was zur Folge hat, daß zwischen den Grenzflächen Brücken gebildet werden und Wechselwirkungen zwischen den Rißflanken entstehen. Oberflächenbruchspiegel, die durch Kugeleindrücke erzeugt wurden, bestätigen den Übergang von transgranularem zu intergranularem Rißwachstum bei zunehmenden inneren Spannungen und weisen auf eine mögliche Verschlechterung der Verschleiß- und Ermüdungseigenschaften hin. Festigkeitsmessungen an mit Härteeindrücken versehenen Proben zeigen ebenfalls unterschiedliche Eigenschaften der beiden Verbundwerkstoffe: geringere Fehlertoleranz im L-Material, konsistent mit der 'Mischungsregel'; größere Toleranz im H-Material, konsistent mit einer ausgeprägten* R*-Kurve. Die* R*-Kurven werden aus den Härteeindruck–Festigkeit-Daten für jeden Verbundwerkstoff analysiert.*

On étudie la tolérance aux défauts et les caractéristiques associées de la courbe de ténacité dans des composites de verre à particules de SiC. On s'intéresse à deux compositions de verres, choisis afin d'obtenir des désaccords dus à l'expansion thermique extrême, l'un élevé (H), l'autre faible (L). L'observation in situ de l'extension des fissures à partir de marques d'indentation rélèvent des comportements très différents: dans le composite L, la trajectoire de la fissure est pratiquement planaire, avec fracture transgranulaire des particules; dans le composite H, la trajectoire est fortement défléchie autour des particules, et il y a donc formation de ponts de liaison aux interfaces ainsi que de l'activité dans le sillon de la fissure. Les motifs des surfaces de fractures produits par des indenteurs sphériques confirment qu'il y a transition d'un mode de

---

* Guest Scientist from: Department of Materials Science and Engineering, Lehigh University, Bethlehem, PA 18015, USA.

** Present address: Harvard University, Cambridge, MA 02138, USA.

fracture transparticulaire à un mode interparticulaire lorsque la contrainte résiduelle interne augmente, et montre qu'il peut alors y avoir dégradation des propriétés du matériau liées aux fissures courtes, comme le comportement à l'usure ou en fatigue. Les expériences d'indentation et de résistance présentent des caractéristiques différentes pour les deux composites: une tolérance faible aux défauts dans le matériau L, cohérente avec une valeur unique de la ténacité qui suit une 'loi des mélanges', une tolerance élevée dans le matériaux H, correspondant à une courbe de ténacite prononcée. Les courbes de ténacité elles-mêmes ont été déconvoluées à partir des données d'indentation et de tests de résistance, et analysées.

1 Introduction

It is now well established that the existence of crack-size-dependent toughness functions, i.e. toughness curves (*T*-curves, or *R*-curves), in non-transforming monophase ceramics is primarily attributable to grain bridging in the crack wake.[1-12] An important manifestation of *T*-curve behavior is 'flaw tolerance', i.e. a relative insensitivity of strength to initial flaw size.[11,13,14] Designers of high reliability ceramic materials with superior long-crack toughness seek to optimize such flaw-tolerance characteristics.

More recently, this connection of the *T*-curve and its associated flaw tolerance with crack bridging has been shown to extend to particle-reinforced ceramics.[15,16] Fracture mechanics modeling of bridging in two-phase ceramics identifies the *T*-curve with key microstructural variables like volume fraction, particle size and residual thermal expansion mismatch stress.[17,18] To date, Al_2TiO_5/Al_2O_3 has been the material system of choice for analysis, because of the strong *T*-curve enhancement associated with its inordinately high mismatch stresses. However, those same high residual stresses impose severe limits on the capacity of the experimentalist to investigate the role of microstructural variables:[18] the material undergoes bulk microcracking at relatively small volume fraction and particle size, and the residual stress itself for this system is not subject to variation.

In the present paper these limitations are rectified by studying the *T*-curve and flaw-tolerance characteristics of model two-phase particulate ceramic composites of SiC particles in a compositionally variable silicate glass matrix. A major advantage of the proposed SiC/glass system, apart from ease of fabrication, is the facility to control and vary the microstructural parameters. In particular, the internal residual stress can be prescribed by adjusting the glass matrix composition. In-situ microscopic observations of crack extension from indentation flaws are used to provide direct evidence of inter-particle fracture and ensuing bridge formation as a dominant fracture mode in a SiC/glass composite with high internal stresses. By contrast, similar observations in a composite with *low* internal stresses reveal primarily trans-particle fracture, with comparatively little bridging. Hertzian indentation tests confirm this difference in fracture mode, with implications concerning prospective wear and fatigue properties. Indentation–strength tests confirm the predicted correlation between flaw tolerance and internal stress, and enable determinations of the underlying *T*-curves.

The use of model two-phase ceramic/matrix systems in the study of brittle fracture is not new. Compelling evidence for strength and toughness enhancements from incorporation of second-phase particles has been presented in several earlier studies.[19-26] However, little effort was made in those earlier studies to consider the enhancements in relation to a systematically varying toughness curve. Nor was any direct (in-situ) identification made of the responsible agents of crack inhibition; thus, whereas crack deflection, crack pinning and bowing, and frontal-wake zone microcracking have been variously proposed as toughening mechanisms, crack–interface bridging has, until recently, passed unnoticed.

2 Experimental Procedure

2.1 Materials

Composites of SiC particles in silica glass matrices were fabricated for fracture studies. Two glass compositions with different thermal expansion mismatch relative to SiC were chosen to provide high (H) and low (L) levels of compression stress in the SiC particles, Table 1. Glass L, an alkaline-earth aluminosilicate, was obtained commercially as slabs (Glass Code 1723, Corning Inc., Corning, NY). Glass H, a sodium–magnesium silicate, was prepared in the authors' laboratories from reagent-grade raw materials (60% SiO_2, 25% Na_2O, 15% MgO, Fisher Scientific, Fair Lawn, NJ), as described in the following paragraphs. The SiC particles were obtained commercially as abrasive grit, mean diameter 30 μm (37 Crystolon, Norton Company, Worcester, MA).

With glass H, a 300 g batch of blended powder was dry-blended and melted in a platinum crucible at 1500°C for 2 h. The melt was continuously stirred with a platinum rod to ensure homogeneity. One portion of the melt was quenched in water. The remaining portion was cast into a slab and annealed at 500°C for 1 h, followed by slow cooling.

The quenched portion of glass H and as-received slabs of glass L were separately pulverized in a

Table 1. Constituent properties of the SiC-particle/glass–matrix composites

	Expansion coefficient α $(10^{-6\circ}C^{-1})$	*Young's modulus* E *(MPa)*	*Hardness* H *(GPa)*	*Cooling temperature* ΔT (°C)	*Residual stress*[a] σ_R *(MPa)*	*Toughness* T_0 $(MPa\,m^{1/2})$
SiC	4·5[b]	436	24	—	—	4·0[e]
Glass H	12·7[c]	63	5·0	419	308	0·75[f]
Glass L	4·6[d]	90	6·0	685	8	0·91[f]

[a] Computed from $\sigma_R = (\alpha_0 - \alpha_P)\Delta T/[(1+\nu_0)/2E_0 + (1-2\nu_P)/E_P]$ for particle P in matrix 0.[27]

[b] Ref. 28.

[c] Ref. 29.

[d] Corning Glass works, Material Information, 1984.

[e] Refs 30 and 31.

[f] Ref. 32.

zirconia ring mill and sieved (No. 320 mesh). Each glass was mixed with 20 vol.% SiC particles in methanol and Teflon media in polyethylene bottles. The mixtures were then blended in a ball mill for 24 h to form consistent slurries. These were poured into Teflon beakers and dried while continuously stirring on a hot plate. The resulting powders were calcined at 375°C for 24 h. A 60 g batch of each powder composition was rolled in a plastic bag to break up any agglomerates, before transferring to a graphite die. Hot pressing was then carried out in a vacuum hot press (Vacuum Industries, Nashua, NH) at a pressure 10 MPa for 30 min, at temperatures 650°C for composite H and 980°C for composite L, to form disks 75 mm diameter by 6 mm thickness. The hot-pressing temperatures were chosen to correspond to a viscosity of 0·1 MPa s, somewhat higher than the softening points of glasses H[29] and L (Corning Glass Works, Material Information, 1984). The disks were cooled to 50°C above the annealing point at a cooling rate of 10°C min^{-1}, and subsequently to room temperature at 2°C min^{-1}.

Flexure bar specimens 25 × 4 × 4 mm were cut from the hot-pressed composites and the base glass slabs for indentation–strength tests. The specimen edges were chamfered (10 μm diamond grinding wheel) and polished (6 μm diamond paste), to minimize edge failures. The prospective tensile faces of all specimens were given a final polish to 1 μm.

Some polished specimens were etched in 5% hydrofluoric acid solution to check for the presence of microcracks.

2.2 Hertzian indentation tests

Simple Hertzian tests were made on some of the polished surfaces of the high-internal-stress (H) and low-internal-stress (L) SiC/glass composites, as well as on the base glasses as controls. The indenters were made with tungsten carbide spheres, radius 1·98 mm, load 500 N. All tests were carried out in laboratory air, relative humidity 40–50%, under which conditions moisture may assist in fracture initiation.[33]

The presence of surface cracking at the indentation sites was revealed by coating the contacted surfaces with gold and viewing in Nomarski interference contrast.

2.3 In-situ tests

Selected specimens of each of the H and L SiC/glass composites were indented at their polished-face centers with a Vickers diamond pyramid, at fixed load 100 N, with the radial crack arms aligned parallel and perpendicular to the bar edges. Each indentation site was covered with a drop of dry silicone oil, to minimize subsequent moisture-assisted slow crack growth, plus a glass cover slip, to facilitate clear observation of the surface cracks.

A loading fixture mounted onto the stage of an optical microscope was used for in-situ observations of radial crack responses in four-point flexure.[34] The indented specimens were loaded slowly using a piezoelectric driver, and the ensuing crack growth relative to the particulate composite microstructure monitored on a videocassette recorder and intermittently photographed.

2.4 Indentation–strength tests

Each remaining flexure specimen was Vickers indented at its polished-face center, at a prescribed load within the range 3 to 300 N. Care was again taken to align the radial cracks along the specimen edges. All indentations were made in the laboratory ambient, allowed to stand for 5 min, and then covered with a drop of dry silicone oil to minimize environmental effects in the ensuing strength tests.

The indented specimens were tested in a four-point bend fixture (outer span 20 mm, inner span 10 mm) mounted on a universal testing machine (Model 1122, Instron Corp., Canton, MA). The fracture times were kept below 50 ms, to ensure near 'inert' testing conditions. Failed specimens were examined in an optical microscope to confirm that the failures originated from the indentations. Specimens that failed from the other sources were included in the data pool for unindented specimens.[13,30]

3 Qualitative results

3.1 Hertzian tests

Micrographs of Hertzian indentations on L and H SiC/glass surfaces are shown in Fig. 1. The damage in the low-internal-stress composite L, Fig. 1(A), is typical of the classical Hertzian cone fracture,[35–37] i.e. near-circular surface traces. These traces do not deviate substantially from those observed in control tests on the base L glass itself (not shown here), indicating that the crack paths within the radial tensile stress field around the contact circle[35,36] are relatively undistorted by the SiC particulate phase. The pattern is indicative of a material with trans-particle fracture characteristics.

The damage in the high-internal-stress composite H, Fig. 1(B), shows a very different response. The Hertzian fracture is comparatively ill-defined, consisting more of linked-up particle-initiated microcracks than regular circular macrocracks. These microcracks are not oriented normally to the contact radial direction in the manner of classical Hertzian fractures, indicating that the crack driving forces are now dominated by the residual internal tensile stresses.[38] In this case the damage may be more properly characterized in terms of *inter*-particle fracture. Note that individual microcracks extend only over a few inter-particle dimensions, implying that the superimposed microstructural field contains compressive stresses as well as tensile. The interplay between tensile and compressive internal stresses is an important ingredient of grain- or particle-interlock bridging.[11]

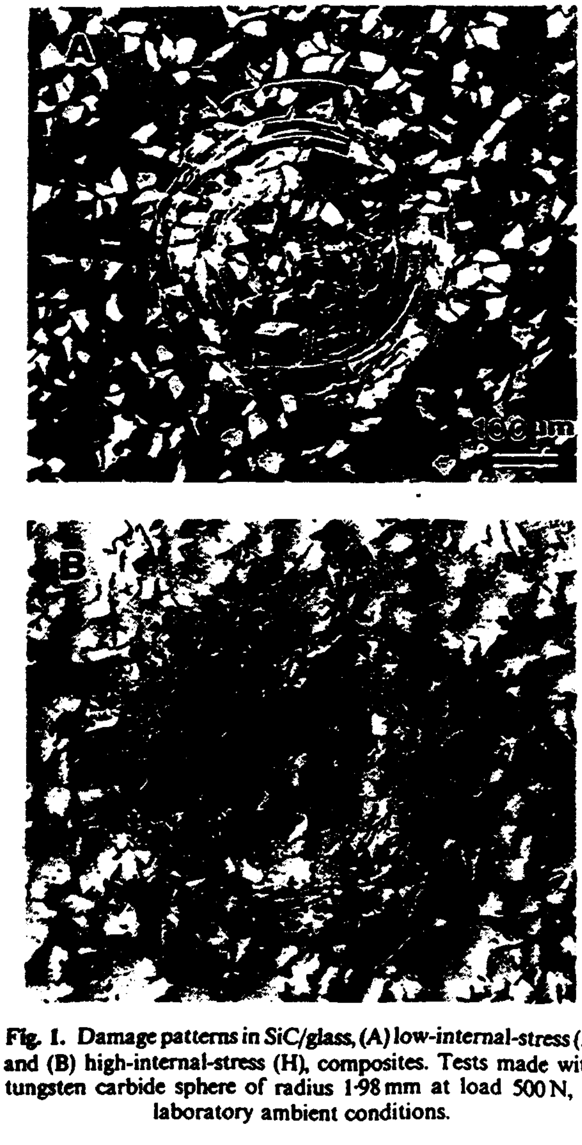

Fig. 1. Damage patterns in SiC/glass, (A) low-internal-stress (L) and (B) high-internal-stress (H), composites. Tests made with tungsten carbide sphere of radius 1·98 mm at load 500 N, in laboratory ambient conditions.

3.2 In-situ observations of Vickers cracks

Optical micrographs of the wake regions of cracks grown from Vickers indentations under applied flexure stresses in the low-internal stress (L) and high-internal-stress (H) composites are shown in Fig. 2. The ultimate stress levels correspond to ≈70% of the strength in both cases.

In composite L, Fig. 2(A), the cracks follow more or less straight, classical radial trajectories. In-situ observations of the crack evolution up to this point revealed intermittent interruption of the extension by the SiC particles. When such interruption did occur, further increase in the applied load was necessary to force the crack through the arresting particle. At such points the crack 'popped in', occasionally propagating through the next two or three particles in the immediate path. Once broken, the obstructing grains rarely appeared to provide any further resistance to the extension; i.e. bridges were not formed, except perhaps when the advancing crack intersected the particle/matrix interface at an unusually oblique angle of incidence. On further stressing beyond the configuration in Fig. 2(A) the crack grew to failure along essentially the same crack plane.

By contrast, the fracture in composite H, Fig. 2(B), shows an entirely different behavior. The cracks often emerge away from the indentation corners and trace a much more disruptive path, again suggestive of a dominant role by local residual stresses. In-situ observations revealed a highly erratic evolution at the microscopic level in this material. Under increasing applied stress the crack popped in from particle to particle, deviating markedly from segment to segment, yet all the while remaining highly stable at the macroscopic level. At some points the crack reinitiated abruptly on the far side of an arresting particle. At others an isolated microcrack appeared to form at a particle some distance ahead of the primary crack tip, with abrupt coalescence at

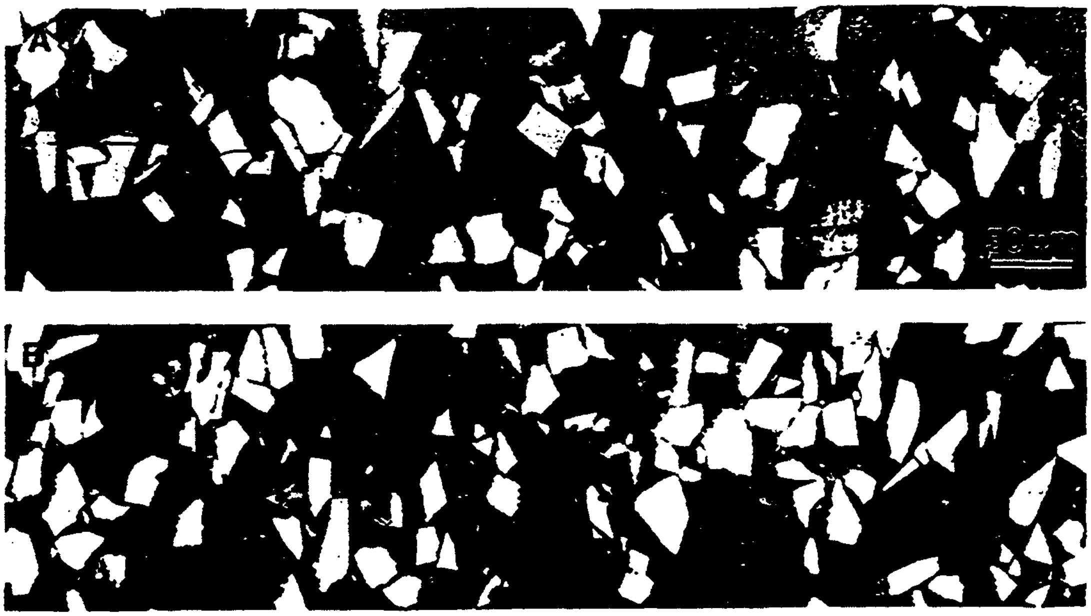

Fig. 2. In-situ optical micrographs of Vickers radial cracks in SiC composites under flexure stress, (A) composite L, (B) composite H. Indentation impression formed at load 100 N, outside field of view at left.

some increment in the load. Notwithstanding the fact that previous investigations in alumina ceramics[2] suggest that such apparently isolated microcracks may well be pre-connected to the primary crack in the subsurface, such geometrical deflections are especially conducive to the formation of particulate bridges at the crack interface. The in-situ observations confirmed the existence of several persistently active bridge sites in Fig. 2(B), up to distances ≈ 1 mm behind the crack tip.

On further stressing, the crack in Fig. 2(B) continued its erratic growth until, ultimately, it spanned almost the entire specimen width. During these final loading stages microcracks began to pop in over the entire surface of the glass matrix. Similar applied-stress-induced microcracking has been reported in the Al_2TiO_5/Al_2O_3 system.[39] Such observations indicate that composite H is close to the limit for spontaneous microcracking. In fact, stress-free specimens left lying in the laboratory ambient conditions for periods of several weeks gradually developed extensive networks, as seen in the etched surface of Fig. 3. On the other hand, no distinctive frontal-wake microcrack cloud was observed at any stage of the crack propagation in the experiments.

3.3 Indentation–strength

Strength–indentation load data for the low-internal-stress (L) and high-internal-stress (H) systems are plotted in Figs 4 and 5, respectively. Each data point with error bar is the mean and standard deviation of 4 to 6 specimens. In these diagrams the upper data set represents the composite, the lower data set the base glass. The hatched regions at left represent breaks from other failure sources, edge flaws in the base glasses and SiC particles in the composites.

It is immediately clear that, within the given indentation load range, the addition of SiC particles substantially improves the stress-bearing capacity of the materials. Both base glasses show a classical flaw sensitivity in the strength characteristics ($P^{-1/3}$ load dependence—Section 4). In composite H, the improvement is manifested primarily as an enhanced flaw tolerance, with a modest 'plateau' strength. In composite L, the improvement is more in the form of a uniformly enhanced strength over the indentation load (indentation flaw size) range, with minimal development of flaw tolerance. Therefore,

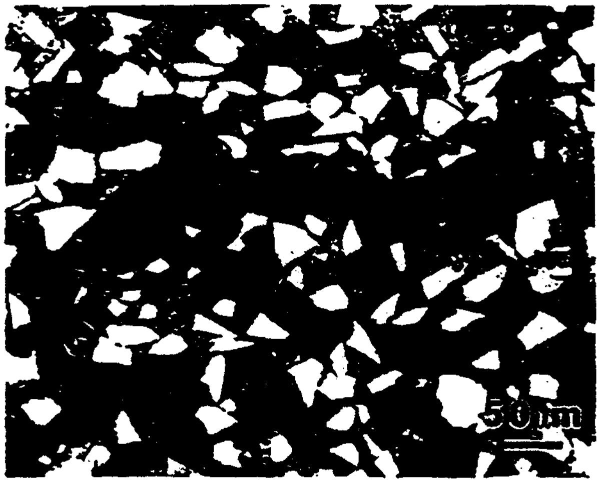

Fig. 3. Etched surface of SiC glass composite H, after prolonged exposure (4 weeks) to laboratory ambient conditions. Note moisture-enhanced development of microcrack network.

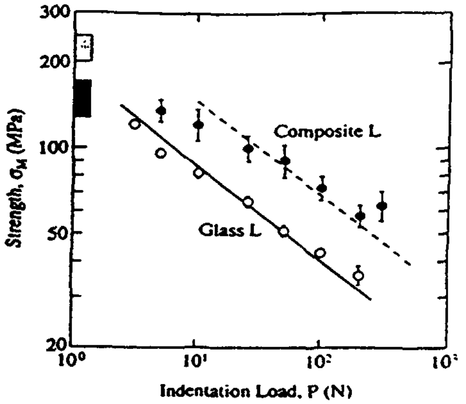

Fig. 4. Indentation–strength data for glass L and corresponding SiC/glass composite L. Each datum point represents mean and standard deviation of strengths from 4 to 6 specimens. The light and dark shaded areas at left represent strengths of unindented specimens for the glass and the composite, respectively. Solid line through glass data is fit to eqn (3) using single-valued toughness for glass L. Dashed line is prediction for SiC/glass composite L, using single-valued toughness from rule of mixtures.

extrapolating beyond the data range, it may be concluded that composite H demonstrates superior toughness properties at high indentation loads (long-crack region), but inferior toughness properties at low indentation loads (short-crack region).

4 Quantitative Evaluation of *T*-Curves

Now the *T*-curve function $T(c)$, with c the crack size, is deconvoluted from the indentation–strength data.[34] At equilibrium, the 'global' K-field for a radial crack system formed at contact load P and subjected to subsequent applied stress σ_A can be expressed as

$$K_A'(c) = K_A(c) + K_R(c) = \psi\sigma_A c^{1/2} + \chi P/c^{3/2} = T(c) \tag{1}$$

where ψ is a crack geometry coefficient and χ is a residual-contact-field coefficient. For a given P, failure occurs at that value of applied stress $\sigma_A = \sigma_M$ that satisfies the 'tangency conditions'[40]

$$dK_A'(c)/dc = dT(c)/dc \tag{2}$$

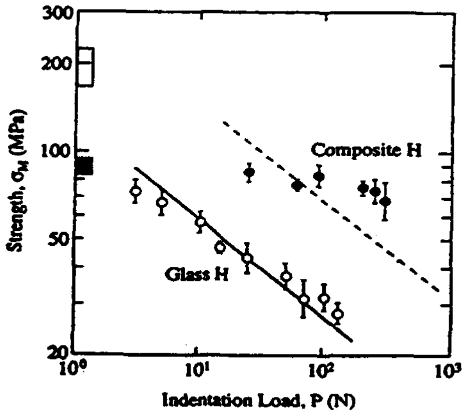

Fig. 5. Indentation–strength data for glass H and corresponding SiC/glass composite H. Each datum point represents mean and standard deviation of strengths from 4 to 6 specimens. The light and dark shaded areas at left represent strengths of unindented specimens for the glass and the composite, respectively. Solid line through glass data is fit to eqn (3) using single-valued toughness for glass H. Dashed line is prediction for SiC/glass composite H, using single-valued toughness from rule of mixtures.

It follows that the *T*-curves for the composites can be determined as the envelopes to the families of $K_A'(c)$ curves constructed from the (σ_M, P) data sets in Figs 4 and 5.[34]

In order to construct such $K_A'(c)$ curves, it is necessary first to 'calibrate' the coefficients ψ and χ in eqn (1) for the matrix glasses. The key to a simplified calibration is the single-valuedness of the matrix toughness, $T = T_0$ for these homogeneous materials.[34] Inserting $T = T_0$ into eqns (1) and (2) then yields the familiar analytical strength–load relation[37,41]

$$\sigma_M = (3T_0/4\psi)(T_0/4\chi P)^{1/3} \tag{3}$$

Hence values for the compound parameter $T_0^4/\psi\chi^{1/3}$ may be obtained from best fits to the data for the base glasses in Figs 4 and 5. It is assumed here that ψ is a material-independent crack geometry coefficient, and the value $\psi = 0{\cdot}77$ obtained previously from data on a fine-grain alumina is retained.[34] Then, using the T_0 values from Table 1, $\chi = 0{\cdot}024$ for glass L and $\chi = 0{\cdot}035$ for glass H are obtained.

Next consider the effect of adding the SiC phase. It has already been intimated that the geometrical coefficient ψ is not sensitive to material variations. The coefficient χ, on the other hand, varies with $(E/H)^{1/2}$, where E is Young's modulus and H is the hardness.[42] Using the rules of mixtures for a 'Voigt' two-phase particle/matrix (P/0) composite (C) with volume fractions $V_0 + V_P = 1$,

$$E_C = V_0E_0 + V_PE_P \tag{4a}$$

$$H_C = V_0H_0 + V_PH_P \tag{4b}$$

it may be verified from Table I that the changes in E/H from addition of 20 vol.% SiC amount to less than 10% for each glass. To a first approximation, therefore, the coefficients ψ and χ may be considered essentially unchanged by addition of the second phase.

Families of $K_A'(c)$ curves for the L and H SiC/glass composites are plotted in Figs 6 and 7 using the (σ_M, P) data from Figs 4 and 5. The fitted *T*-curves are envelopes of tangency points to these families of curves. The lower dashed lines are toughness values T_0 for the base glasses. The upper dashed lines are 'rule-of-mixtures' toughness values T_C for the

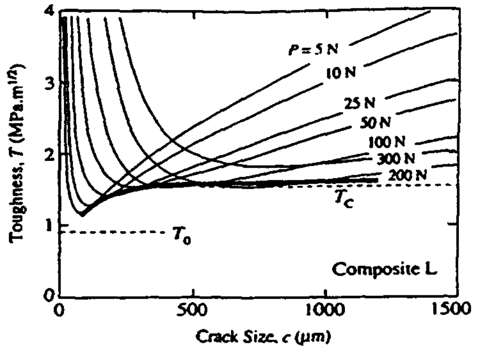

Fig. 6. *T*-curve construction for SiC/glass composite L. Solid curves are plots of global *K*-field function $K'_A(c)$ in eqn (3), evaluated for each strength $\sigma_A = \sigma_M$ and load P in Fig. 4. Shaded band is an empirically fitted *T*-curve envelope.[34] Lower horizontal dashed line is toughness T_0 for base glass; upper horizontal dashed line is rule-of-mixtures toughness T_c for the composite.

composites, evaluated for an ideal planar crack intersecting the second-phase particles in the absence of bridging or other extraneous energy absorbing process; these values are calculable from Table 1 by writing an expression for the reversible work to separate unit area of crack plane,

$$R_C = V_0 R_0 + V_P R_P \tag{5}$$

and invoking the familiar plane stress relation $R = T^2/E$[37] along with eqn (4a) to obtain

$$T_C = [V_0(E_C/E_0)T_0^2 + V_P(E_C/E_P)T_P^2]^{1/2} \tag{6}$$

For the low-internal-stress composite L in Fig. 6 the shaded *T*-curve envelope is fitted empirically to the $K'_A(c)$ curves.[34] This fitted curve virtually overlaps the $T = T_C$ line at $c > 200\,\mu$m, and deviates slightly below T_C at $c < 200\,\mu$m. Thus the toughness behavior of the L composite is consistent with a predominantly trans-particle mode of fracture (Figs 1(A) and 2(A)).

The response is markedly different for the *high*-internal-stress composite H in Fig. 7. In this case the *T*-curve crosses the $T = T_C$ line at $c \approx 400\,\mu$m, and extends well above this line in the long-crack region. This highly enhanced long-crack toughness is consistent with a predominantly inter-particle (Fig. 1(B)), strong-bridging (Fig. 2(B)) mode of fracture. Accordingly, the *T*-curve in Fig. 7 has been plotted using an analytical expression for $T(c)$ derived for the simple bridging model in Fig. 8:[17,18]

$$T(c) = T_0 - \psi q c^{1/2} \qquad (0 \leq c \leq \lambda) \tag{7a}$$

$$T(c) = T_0 + \psi p c^{1/2} \times \{1 - [1 - (1 - \lambda/c)^2]^{1/2}\} - \psi q c^{1/2}[1 - (1 - \lambda/c^2)]^{1/2} \qquad (\lambda \leq c \leq \Lambda + \lambda) \tag{7b}$$

$$T(c) = T_0 + \psi p c^{1/2} \times \{[1 - (1 - \Lambda/c - \lambda/c)^2]^{1/2} - [1 - (1 - \lambda/c^2)]^{1/2} - \psi q c^{1/2}[1 - (1 - \lambda/c)^2]^{1/2} \qquad (\Lambda + \lambda \leq c) \tag{7c}$$

where p and q are averaged long-crack closing and short-crack opening stresses from the matrix/particle mismatch acting over characteristic bridging zone dimensions λ and Λ; the fit corresponds to parameter adjustments $p = 66$ MPa, $(p + q)(2\lambda)^{1/2} = 0{\cdot}40$ MPa m$^{1/2}$ and $\Lambda = 840\,\mu$m.[17]

It is noteworthy that the bridging model of Fig. 8, with its assumption of a crack always constrained to the matrix (implicit by the appearance of T_0 rather than T_C as the base toughness in eqn (7)), could not be made to provide a satisfactory fit to the L composite data in Fig. 6.

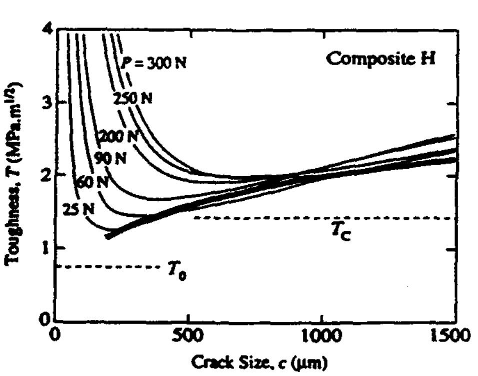

Fig. 7. *T*-curve construction for SiC/glass composite H. Solid curves are plots of global *K*-field function $K'_A(c)$ in eqn (3), evaluated for each strength $\sigma_A = \sigma_M$ and load P in Fig. 5. Shaded curve is fitted *T*-curve from the bridging model, eqn (7). Lower horizontal dashed line is toughness T_0 for base glass; upper horizontal dashed line is rule-of-mixtures toughness T_C for the composite.

5 Discussion

The present study has demonstrated that thermal expansion mismatch can have a dominant influence in the toughness and strength properties of two-phase ceramics, first by controlling the genesis and second by controlling the effectiveness of crack/interface bridging. As shown in the micro-

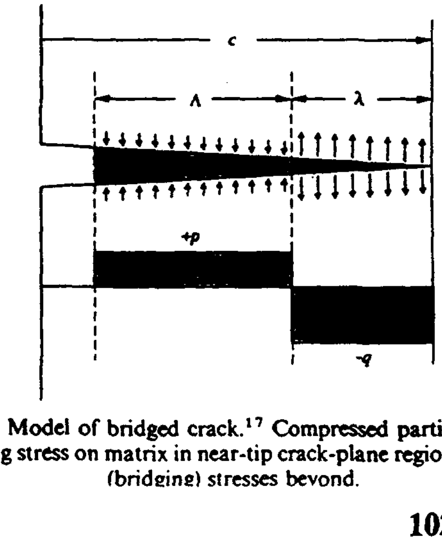

Fig. 8. Model of bridged crack.[17] Compressed particles exert opening stress on matrix in near-tip crack-plane region, closure (bridging) stresses beyond.

graphs of cracks in SiC/glass composites in Figs 1 and 2, increasing the residual stress from low level (composite L) to high level (composite H) results in a transition from predominantly trans-particle to predominantly inter-particle fracture. Inter-particle fracture is promoted by an increase in stress-directed crack deflection, which enhances bridge formation, and in particle/matrix pullout friction, which inhibits bridge rupture.[17,18] The end result is an enhanced *T*-curve for the H composite, Fig. 7, relative to the L composite, Fig. 6.

This *T*-curve enhancement from bridging in two-phase composites is manifested most compellingly in the indentation–strength characteristics of Figs 4 and 5. Composite L in Fig. 4 shows relatively little flaw tolerance, consistent with a single-valued, rule-of-mixtures toughness. Composite H in Fig. 5 shows substantially greater flaw tolerance, with strengths higher than the simple rule-of-mixtures prediction over most of the load range covered. On the other hand, extrapolation of the composite H strength data into the low-load region implies a depressed *T*-curve, with the suggestion of diminished short-crack properties. Hence while increased internal-stress-enhanced bridging results in higher long-crack toughness, tensile components of the same internal-stress field conversely lead to lower practical strength. These same tensile stresses also greatly increase the susceptibility to local microfracture, as in Fig. 1(B), and thence to brittle wear[38] and fatigue.[43] A long-crack/short-crack tradeoff is in effect here. One might attempt to explain any such tradeoff from incorporation of a second phase in terms of a traditional 'critical flaw' argument: short-crack strength is decreased by introducing larger flaws; long-crack toughness is increased by providing geometrical 'obstacles' to crack propagation, e.g. by crack deflection, crack pinning and bowing (Section 1). However, the simple 'obstacle' concept can not account for the improvement in flaw tolerance with increase in thermal mismatch—it contains no provision for a cumulative *T*-curve.[37] In this context it may be recalled that no evidence for the existence of a detached microcrack cloud, which might alternatively account for the *T*-curve, was found in the H composite.

The last point pertaining to microcracking warrants comment in the context of microstructural design. It is clear from the present study that one may control the toughness and strength properties, and even the mode of crack propagation, by tailoring the composite microstructure. In particular, increasing the thermal mismatch between particles and matrix (as well as particle size and volume fraction[17,18]) enhances the bridging long-crack toughness, and hence the flaw tolerance. However, beyond a certain limit this increase in thermal mismatch (or particle size or volume fraction) generates critical local tensile fields, initiating bulk microcracking and, ultimately, degrading the strength.[44] It is clear from Fig. 3 that the materials processor who seeks to optimize microstructures for long-crack toughness should pay due attention to such limits, with additional allowance for the deleterious time-dependent effects of moisture.

Acknowledgements

The authors thank Prabhat Gupta for useful advice on the glass compositions, Dale Kauffman for assistance with the glass melting procedures, and Linda Braun for assistance with the in-situ experiments. Funding for this work was provided by the US Air Force Office of Scientific Research.

References

1. Knehans, R. & Steinbrech, R., Memory effect of crack resistance during slow crack growth in notched Al_2O_3 bend specimens. *J. Mater. Sci. Lett.*, **1** (1982) 327–9.
2. Swanson, P. L., Fairbanks, C. J., Lawn, B. R., Mai, Y.-W. & Hockey, B. J., Crack–interface grain bridging as a fracture resistance mechanism in ceramics: I. Experimental study on alumina. *J. Am. Ceram. Soc.*, **70** (1987) 279–89.
3. Mai, Y.-W. & Lawn, B. R., Crack–interface grain bridging as a fracture resistance mechanism in ceramics: II. Theoretical fracture mechanics model. *J. Am. Ceram. Soc.*, **70** (1987) 289–94.
4. Steinbrech, R. W., Reichl, A., Deuerler, F. & Schaarwachter, W., Correlation of crack opening displacement and crack resistance curve of alumina. *Sci. Ceram.*, **14** (1987) 659–64.
5. Swanson, P. L., Crack-interface traction: A fracture-resistance mechanism in brittle polycrystals. In *Fractography of Glasses and Ceramics*, Vol. 22, American Ceramic Society, Columbus, OH, 1988, pp. 135–55.
6. Reichl, A. & Steinbrech, R. W., Determination of crack bridging forces in alumina. *J. Am. Ceram. Soc.*, **71** (1988) C299–C301.
7. Sakai, M., Yoshimura, J., Goto, Y. & Inagaki, M., *R*-Curve behavior of a polygranular graphite; microcracking and grain bridging in the wake region. *J. Am. Ceram. Soc.*, **71** (1988) 609–16.
8. Beauchamp, E. K. & Monroe, S. L., Effect of crack–interface bridging on subcritical crack growth in ferrites. *J. Am. Ceram. Soc.*, **72** (1989) 1179–84.
9. Bennison, S. J. & Lawn, B. R., Role of interfacial grain-bridging sliding friction in the crack-resistance and strength properties of nontransforming ceramics. *Acta Metall.*, **37** (1989) 2659–71.
10. Rödel, J., Kelly, J. & Lawn, B. R., In situ measurements of bridged crack interfaces in the SEM. *J. Am. Ceram. Soc.*, **73** (1990) 3313–18.
11. Chantikul, P., Bennison, S. J. & Lawn, B. R., Role of grain size in the strength and *R*-curve properties of alumina. *J. Am. Ceram. Soc.*, **73** (1990) 2419–27.
12. Vekinis, G., Ashby, M. F. & Beaumont, P. W. R., *R*-curve behaviour of Al_2O_3 ceramics. *Acta Metall.*, **38** (1990) 1151–62.
13. Cook, R. F., Lawn, B. R. & Fairbanks, C. J., Microstructure–strength properties in ceramics: I. Effect of crack size on toughness. *J. Am. Ceram. Soc.*, **68** (1985) 604–15.

14. Cook, R. F., Fairbanks, C. J., Lawn, B. R. & Mai, Y.-W., Crack resistance by interfacial bridging: its role in determining strength characteristics. *J. Mater. Res.*, 2 (1987) 345–56.
15. Bennison, S. J., Padture, N. P., Runyan, J. L. & Lawn, B. R., Flaw-insensitive ceramics. *Phil. Mag. Lett.*, 64 (1991) 191–5.
16. Padture, N. P., Chan, H. M., Bennison, S. J., Runyan, J. L., Rödel, J. & Lawn, B. R., Flaw Tolerant Al_2O_3–Al_2TiO_5 composites. In *Ceramic Transactions*, Vol. 19, ed. M. D. Sacks. American Ceramic Society, Columbus, OH, 1991, pp. 715–21.
17. Lawn, B. R., Padture, N. P., Braun, L. M. & Bennison, S. J., Model for toughness-curves in two-phase ceramics: I. Basic fracture mechanics. *J. Am. Ceram. Soc.*, 76 (1993) 2241–7.
18. Padture, N. P., Runyan, J. L., Bennison, S. J., Braun, L. M. & Lawn, B. R., Model for toughness-curves in two-phase Ceramics: II. Microstructural variables. *J. Am. Ceram. Soc.* 76 (1993) 2235–40.
19. Hasselman, D. P. H. & Fulrath, R. M., Proposed fracture theory of a dispersion-strengthened glass matrix. *J. Am. Ceram. Soc.*, 49 (1966) 68–72.
20. Frey, W. J. & Mackenzie, J. D., Mechanical properties of selected glass–crystal composites. *J. Mater. Sci.*, 2 (1967) 124–30.
21. Lange, F. F., Fracture energy and strength behavior of a sodium borosilicate glass–Al_2O_3 composite system. *J. Am. Ceram. Soc.*, 54 (1971) 614–20.
22. Green, D. J. & Nicholson, P. S., Fracture of brittle particulate composites. In *Fracture Mechanics of Ceramics*, Vol. 4, ed. R. C. Bradt, D. P. H. Hasselman & F. F. Lange. Plenum Press, NY, 1978, pp. 945–60.
23. Swearengen, J. C., Beauchamp, E. K. & Eagan, R. J., Fracture toughness of reinforced glasses. In *Fracture Mechanics of Ceramics*, Vol. 4, ed. R. C. Bradt, D. P. H. Hasselman & F. F. Lange. Plenum Press, NY, 1978, pp. 973–87.
24. Faber, K. T. & Evans, A. G., Crack deflection processes: II. Experiment. *Acta Metall.*, 31 (1983) 577–84.
25. Miyata, N., Ichikawa, S., Monji, H. & Jinno, H., Fracture behavior of brittle matrix, particulate composites with thermal expansion mismatch. In *Fracture Mechanics of Ceramics*, Vol. 7, ed. R. C. Bradt, A. G. Evans, D. P. H. Hasselman & F. F. Lange. Plenum Press, NY, 1986, pp. 87–102.
26. Donald, I. W., Review—methods of improving the mechanical properties of oxide glasses. *J. Mater. Sci.*, 24 (1989) 4177–208.
27. Selsing, J., Internal stresses in ceramics. *J. Am. Ceram. Soc.*, 44 (1961) 419.
28. Hecht, N. L., McCullum, D. W. & Graves, G. A., Investigation of selected silicon nitride and silicon carbide ceramics. *Ceram. Eng. Sci. Proc.*, 9 (1988) 1313–32.
29. Bansal, N. P. & Doremus, R. H., *Handbook of Glass Properties*, Academic Press, Orlando, 1986.
30. Chantikul, P., Anstis, G. R., Lawn, B. R. & Marshall, D. B., A critical evaluation of indentation techniques for measuring fracture toughness: II. Strength method. *J. Am. Ceram. Soc.*, 64 (1981) 539–43.
31. Anstis, G. R., Chantikul, P., Marshall, D. B. & Lawn, B. R., A critical evaluation of indentation techniques for measuring fracture toughness: I. Direct crack measurements. *J. Am. Ceram. Soc.*, 64 (1981) 533–8.
32. Wiederhorn, S. M., Fracture surface energy of glass. *J. Am. Ceram. Soc.*, 52 (1969) 99–105.
33. Langitan, F. B. & Lawn, B. R., Effect of a reactive environment on the Hertzian strength of brittle solids. *J. Appl. Phys.*, 41 (1970) 3357–65.
34. Braun, L. M., Bennison, S. J. & Lawn, B. R., Objective evaluation of short-crack toughness-curves using indentation flaws: case study on alumina-based ceramics. *J. Am. Ceram. Soc.*, 75 (1992) 3049–57.
35. Frank, F. C. & Lawn, B. R., On the theory of Hertzian fracture. *Proc. Royal Soc. London*, A299 (1967) 291–306.
36. Lawn, B. R. & Wilshaw, T. R., Indentation fracture: principles and applications. *J. Mater. Sci.*, 10 (1975) 1049–81.
37. Lawn, B. R., *Fracture of Brittle Solids*. Cambridge University Press, Cambridge, 1993.
38. Cho, S.-J., Hockey, B. J., Lawn, B. R. & Bennison, S. J., Grain-size and *R*-curve effects in the abrasive wear of alumina. *J. Am. Ceram. Soc.*, 72 (1989) 1249–52.
39. Braun, L. M., Bennison, S. J. & Lawn, B. R., Short-crack *T*-curves and damage tolerance in alumina-based composites. *Ceram. Eng. Sci. Proc.*, 13 (1992) 156–63.
40. Mai, Y.-W. & Lawn, B. R., Crack stability and toughness characteristics in brittle materials. *Ann. Rev. Mater. Sci.*, 16 (1986) 415–39.
41. Marshall, D. B., Lawn, B. R. & Chantikul, P., Residual stress effects in sharp-contact cracking: II. Strength degradation. *J. Mater. Sci.*, 14 (1979) 2225–35.
42. Lawn, B. R., Evans, A. G. & Marshall, D. B., Elastic/plastic indentation damage in ceramics: the median/radial crack system. *J. Am. Ceram. Soc.*, 63 (1980) 574–81.
43. Guiberteau, F., Padture, N. P., Cai, H. & Lawn, B. R., Indentation fatigue: a simple cyclic Hertzian test for measuring damage accumulation in polycrystalline ceramics. *Phil. Mag. A*, 68 (1993) 1003–16.
44. Runyan, J. L. & Bennison, S. J., Fabrication of flaw-tolerant aluminium-titanate-reinforced alumina. *J. Eur. Ceram. Soc.*, 7 (1991) 93–9.

journal

J. Am. Ceram. Soc., 77 [7] 1825-31 (1994)

Effect of Grain Size on Hertzian Contact Damage in Alumina

Fernando Guiberteau,[*,†] Nitin P. Padture,[*,‡] and Brian R. Lawn[*]

Materials Science and Engineering Laboratory, National Institute of Standards and Technology,
Gaithersburg, Maryland 20899

The role of microstructural scale on deformation–microfracture damage induced by contact with spheres is investigated in monophase alumina ceramics over a range 3–48 μm in grain size. Measurement of a universal indentation stress–strain curve indicates a critical contact pressure ≈5 GPa, above which irreversible deformation occurs in alumina. A novel sectioning technique identifies the deformation elements as intragrain shear faults, predominantly crystallographic twins, within a confining subsurface zone of intense compression–shear stress. The twins concentrate the shear stresses at the grain boundaries and, above a threshold grain size, initiate tensile intergranular microcracks. Below this threshold size, classical Hertzian cone fractures initiate outside the contact circle. Above the threshold, the density and scale of subsurface-zone microcracks increase dramatically with increasing grain size, ultimately dominating the cone fractures. The damage process is stochastic, highlighting the microstructural discreteness of the initial deformation field; those grains which lie in the upper tail of the grain-size distribution and which have favorable crystallographic orientation relative to local shear stresses in the contact field are preferentially activated. Initial flaw state is not an important factor, because the contact process creates its own flaw population. These and other generic features of the damage process will be discussed in relation to microstructural design of polycrystalline ceramics.

I. Introduction

Surfaces of ceramic components in service are commonly subjected to concentrated loads, from contact bearings or spurious impacts with foreign bodies. The stresses from such contacts can introduce localized structural damage, which in turn can degrade the strength[1,2] or erode the surface.[3] Depending on the contact geometry, individual cracks may initiate from preexisting flaws or from precursor "plastic" deformation.[4,5] In polycrystalline ceramics, the nature of the fracture damage can be controlled by events at the microstructural level. There is then a need to focus on the "short-crack" aspects of fracture. This need has been foreshadowed in toughness-curve (*T*-curve, or *R*-curve) studies on alumina and other ceramics that exhibit grain-interlock bridging.[6–15] Thus, whereas increasing the grain size of alumina enhances the long-crack toughness, it simultaneously diminishes the strength[16] and wear resistance.[17] Grain size might therefore be expected to play a vital role in determining the nature and degree of contact damage.

In a recent paper,[18] the nature of contact-induced damage in a "coarse" (grain size 23 μm) alumina was studied using the Hertzian test. The Hertzian geometry, in which a spherical indenter is used to deliver concentrated stresses over a small area of specimen surface, usefully simulates "blunt" in-service contact conditions.[4] In addition, because the contact pressure increases monotonically with applied load, the geometry allows one to trace the "indentation stress–strain" response of a material, from initial elastic contact through first irreversible deformation to a final "fully plastic" state.[19] In that earlier study on alumina,[18] damage was found to initiate in the subsurface region of high compression–shear *beneath* the contact instead of in the surface region of weak tension *outside* the contact. Intragrain shear–fault deformation, specifically crystallographic twinning and slip in the alumina, was identified as the primary stage of damage. Grain boundary microcracking at the ends of the constrained shear faults was identified as the secondary stage. Repeat contacts revealed severe mechanical fatigue;[18] in severe cases grain boundary microcracks coalesced into a fragmentation zone, resulting in the detachment of grains from the surface. Some comparative experiments on a "fine" alumina (grain size 2.5 μm) showed no detectable microcracking, suggesting that microstructural scale plays a critical role in the contact damage process.

In this paper we examine more systematically the role of grain size on contact damage from single-cycle Hertzian contacts in polycrystalline alumina. We find that above a contact pressure ≈5 GPa, independent of grain size or sphere size, the contact deviates from an ideal Hertzian elastic response, indicating the onset of "plasticity." We also examine more closely the nature of the subsurface deformation–microcrack damage, using a novel sectioning technique, and monitor the damage rate during the load–unload cycle, using acoustic emission. Our experiments indicate that twin/slip shear faults within individual grains do indeed play a controlling precursor role in the initiation of grain-boundary microcracks, that the bulk of the microcrack initiation occurs during the latter part of the *loading* half-cycle, and that the damage process has a strong stochastic element in the polycrystalline structure. The experiments also indicate the existence of a threshold grain size ≈20 μm for initiation; on traversing this threshold, the microcrack density increases with grain size. Finally, we consider some of the broader implications of our observations on alumina in relation to microstructural design of structural ceramics for contact-related applications.

II. Experimental Procedure

Polycrystalline aluminas with mean grain sizes 3, 9, 15, 21, 35, and 48 μm were obtained from an earlier study on toughness curves.[16] The processing of those aluminas was carried out in a class A-100 clean room to minimize impurity content. The resulting microstructures were fully dense and uniform, with a narrow size distribution of equiaxed grains[§] and small flaw population. In contrast, the commercial material used in our earlier

---

M. V. Swain—contributing editor

Manuscript No. 194390. Received July 14, 1993; approved September 30, 1993.

Supported by the U.S. Office of Naval Research. Special financial support was received for F. Guiberteau from the Ministerio de Educación y Ciencia (DGICYT), Spain.

[*] Member, American Ceramic Society.

[†] Guest Scientist from Departamento de Física, Universidad de Extremadura, 06071, Badajoz, Spain.

[‡] Guest Scientist from Department of Materials Science and Engineering, Lehigh University, Bethlehem, PA 18015.

[§] In accordance with the "Hillert criterion" (maximum diameter < twice mean diameter).

Hertzian contact fatigue experiments[18] had a much wider grain size distribution and a higher population of pores, inclusions, and grain boundary triple-point flaws.

Bar specimens 20 mm × 2.5 mm × 2.5 mm of each grain size alumina were diamond polished to 1-μm grade finish. Some specimens were used for indentation stress–strain measurements. The polished surfaces of these specimens were coated with gold *prior to indentation*. Normal indentations were made in a universal testing machine (Model 1122, Instron, Canton, MA) at constant crosshead speed (1.67 $\mu m \cdot s^{-1}$) over a load range $P = 0$ to 2000 N, using tungsten carbide spheres of radii $r = 1.98, 3.18, 4.76, 7.94$, and 12.7 mm, in air. The contact radius a for each indentation was measured from residual impressions left in the gold coating, to enable evaluations of contact pressure ($p_0 = P/\pi a^2$) and indentation strain (a/r) (see Sect. III(1)). In the inelastic region, the contact radius always exceeded the maximum grain size by at least an order of magnitude.

Subsurface indentation damage could be seen below the contacts of uncoated specimens in dark-field illumination, especially in the coarser aluminas.[18] In the present study an alternative, more revealing observational technique was developed, following a precontact section procedure originally used by Mulhearn[20] and others,[21] as follows:

(i) Polished surfaces of two specimens were bonded face-to-face under clamping pressure with a thin layer (<10 μm) of adhesive (Loctite, Newington, CT).

(ii) A surface perpendicular to the bonded interface was ground and polished along the length of the specimen.

(iii) The newly polished surface was indented symmetrically across the surface trace of the interface (Fig. 1). Since the principal stresses directly beneath the contact area are highly compressive,[4] the opposite surfaces in the region of subsurface damage are constrained from moving apart, precluding potential artifacts associated with free surface effects.[22]

(iv) The two halves of the indented bar were separated by dissolving the glue in acetone, cleaned, gold-coated, and viewed using Nomarski interference illumination.

With this procedure, shear fault features not evident in conventional polished sections were readily visible in the Nomarski contrast as shallow surface offsets on the separated free surfaces.

Acoustic emission experiments were performed to quantify the sequence of damage evolution during indentation. Acoustic activity was recorded during the load–unload indentation cycle using a piezoelectric transducer attached to the specimen indentation surface with rubber cement (LOCAN 320, Physical Acoustics, Princeton, NJ). Data were recorded as accumulated signal energy vs elapsed time at constant crosshead displacement speed.

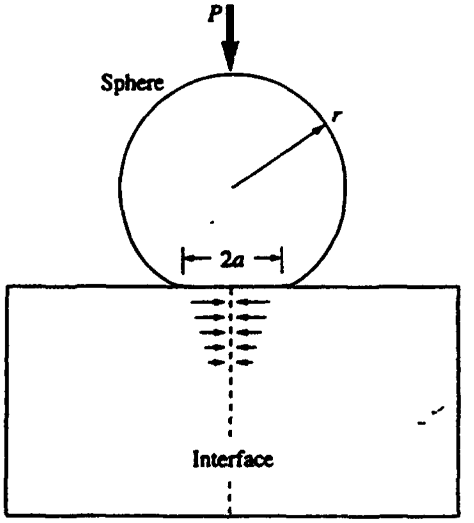

Fig. 1. Hertzian test geometry, for bonded-interface specimen. Sphere radius r delivers load P over contact radius a. Specimen consists of two polished halves glued together across interface. Compressive stresses beneath contact (arrows) maintain contact between specimen halves during indentation.

Some dummy indentation stress–strain tests were made on a tungsten carbide plate cut from one of the larger spheres, to examine the limiting contact conditions for purely reversible deformation of the indenting spheres.

III. Results

(1) *Indentation Stress–Strain Curve*

The Hertzian test can be used to obtain an indentation stress–strain curve[19,23] for deformable solids which would otherwise, in more uniformly tensile loading geometries, behave in a perfectly brittle manner. Measurements of contact radius a, sphere radius r, and indentation load P (Fig. 1) enable one to evaluate

$$\text{Indentation stress} \quad p_0 = P/\pi a^2 \qquad (1a)$$

$$\text{Indentation strain} \quad a/r \qquad (1b)$$

Indentation stress–strain functions $p_0(a/r)$ have been previously measured for lithium fluoride,[23] silicate glasses,[24] and zinc sulfide;[21] more recently, curves have been obtained for a commercial alumina (grain size 23 μm)[18] and a glass-ceramic.[25]

Indentation stress–strain data for the *finest* and *coarsest* of the aluminas investigated in the present study (grain sizes 3 and 48 μm) are plotted in Fig. 2. The results for the two grain sizes are indistinguishable within the experimental scatter. Also included as the solid curve in Fig. 2 is an empirical data fit from our earlier study on a commercial alumina with *intermediate* grain size.[18] The dashed lines represent asymptotic limits for the indentation stress–strain curve: the lower inclined dashed line is the linear relation for purely elastic contacts from Hertzian theory[23]

$$p_0 = (3E/4\pi k)(a/r) \quad \text{(elastic)} \qquad (2)$$

where $E = 393$ GPa is Young's modulus of the alumina and $k = 0.88$ for tungsten carbide on alumina;[18,26,27] the upper horizontal dashed line is an indentation hardness $H = 19.0 \pm 2.0$ GPa, common to all grain sizes, obtained from Vickers tests.[16]

The overlap in data in Fig. 2 suggests the existence of a "universal" stress–strain curve for alumina, implying a critical stress condition for deformation independent of grain size or preexisting flaw state. The data deviate below the Hertzian line at pressures above $p_0 \approx 5$ GPa, marking the onset of "yield." Independent stress–strain tests using tungsten carbide spheres on plates of the same material show deviations above ≈6 GPa, indicating that part of the deviation at the higher stress end of the curve in Fig. 2 could be due to deformation of the sphere.

(2) *Optical Microscopy*

Optical microscopy confirms that the above-mentioned deviation from Hertzian behavior in Fig. 2 (sphere deformation notwithstanding) is due to the onset of indentation damage in the alumina. The nature of this damage can be deduced from the micrograph sequences in Figs. 3 and 4, obtained using the bonded-interface section technique described in Sect. II. Figure 3 shows how the subsurface damage develops in the coarsest (48 μm) alumina as one proceeds up the stress–strain curve in Fig. 2. Thus, the sequence A-B-C-D shows section views at increasing indentation pressure. The initiation of the deformation–microfracture subsurface damage zone, and subsequent expansion of this zone, are immediately apparent from the free-surface relief displacements revealed by the Nomarski contrast. At $p_0 = 5.3$ GPa in A, i.e., just above the elastic limit in Fig. 2, just 3 to 4 grains have deformed. At increased pressures, $p_0 = 6.2$ GPa in B and 7.0 GPa in C, the number of

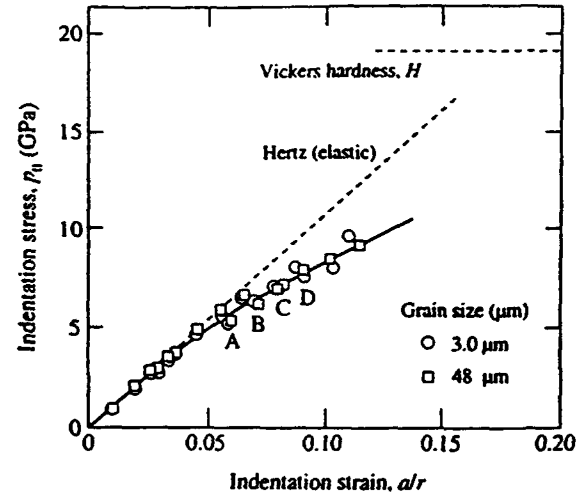

Fig. 2. Indentation stress–strain curve. Data are for aluminas of 3- and 48-μm grain size. Inclined dashed line is Hertzian elastic response, and upper horizontal dashed line is hardness (averaged over all grain sizes). A, B, C, and D correspond to micrographs in Fig. 3. Solid curve is an empirical fit to the data for a commercial alumina (grain size 23 μm) from a previous study.[18]

deformed grains increases, and the damage zone expands toward the surface. At p_0 = 8.0 GPa in D, the damage is more profuse and begins to take on the appearance of the well-developed, near-hemispherical deformation zone expected from continuum plasticity models.[19]

The presence of shear faults traversing the width of some of the deformed grains is clearly evident as deformation (presumably twin) lamellae in the micrographs. Microcracks extending along those grain boundaries intersected by the lamellae are also evident, by virtue of greatly enhanced interference contrast from attendant surface-grain displacements and rotations. At the higher pressures these microcracks tend to link up with neighbors. The microcracks appear to be associated *only* with deformed grains, suggesting that the shear faults are a necessary precursor to fracture damage in these materials. We note also the variability in orientation of the lamellae, indicating strong crystallographic features in the damage pattern.

The set of micrographs in Fig. 4 shows both half-surface (upper) and section views (lower) of indentations for each of the aluminas, at indentation pressure p_0 = 8.0 GPa. Again, the damage is confined within a relatively well-defined hemispherical deformation zone below the contact circle. Note that the section views reveal the subsurface damage more clearly than the half-surface views, reinforcing the utility of the bonded-interface sectioning technique. The apparent universality of the stress–strain curve for the two grain sizes in the indentation stress–strain curve of Fig. 2 (together with the common Vickers hardness value for all grain sizes) suggests that the net plastic

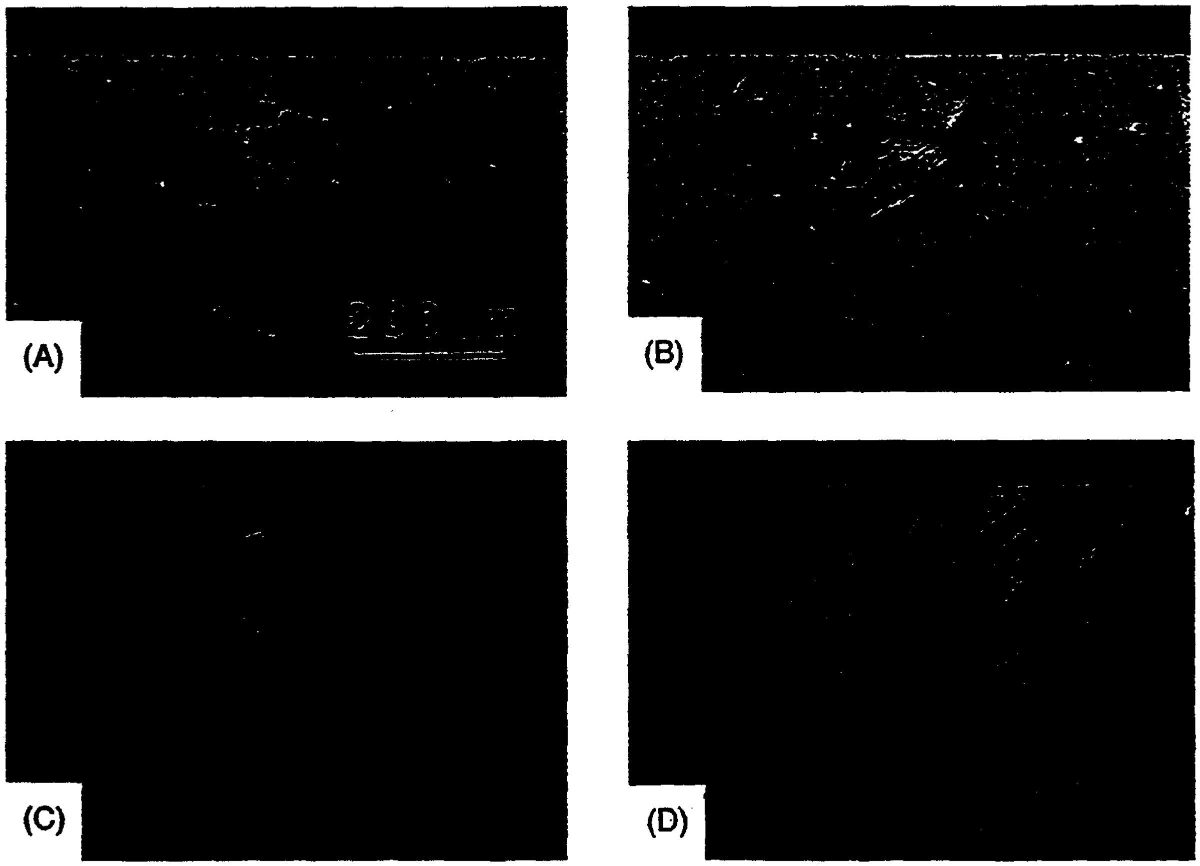

Fig. 3. Optical micrographs in Nomarski illumination showing section views of indentation sites in alumina of grain size 48 μm. Indentations made with WC ball of radius r = 3.18 mm, at increasing contact pressures p_0: (A) 5.3, (B) 6.2, (C) 7.0, and (D) 8.0 GPa (cf. points A–D in Fig. 2).

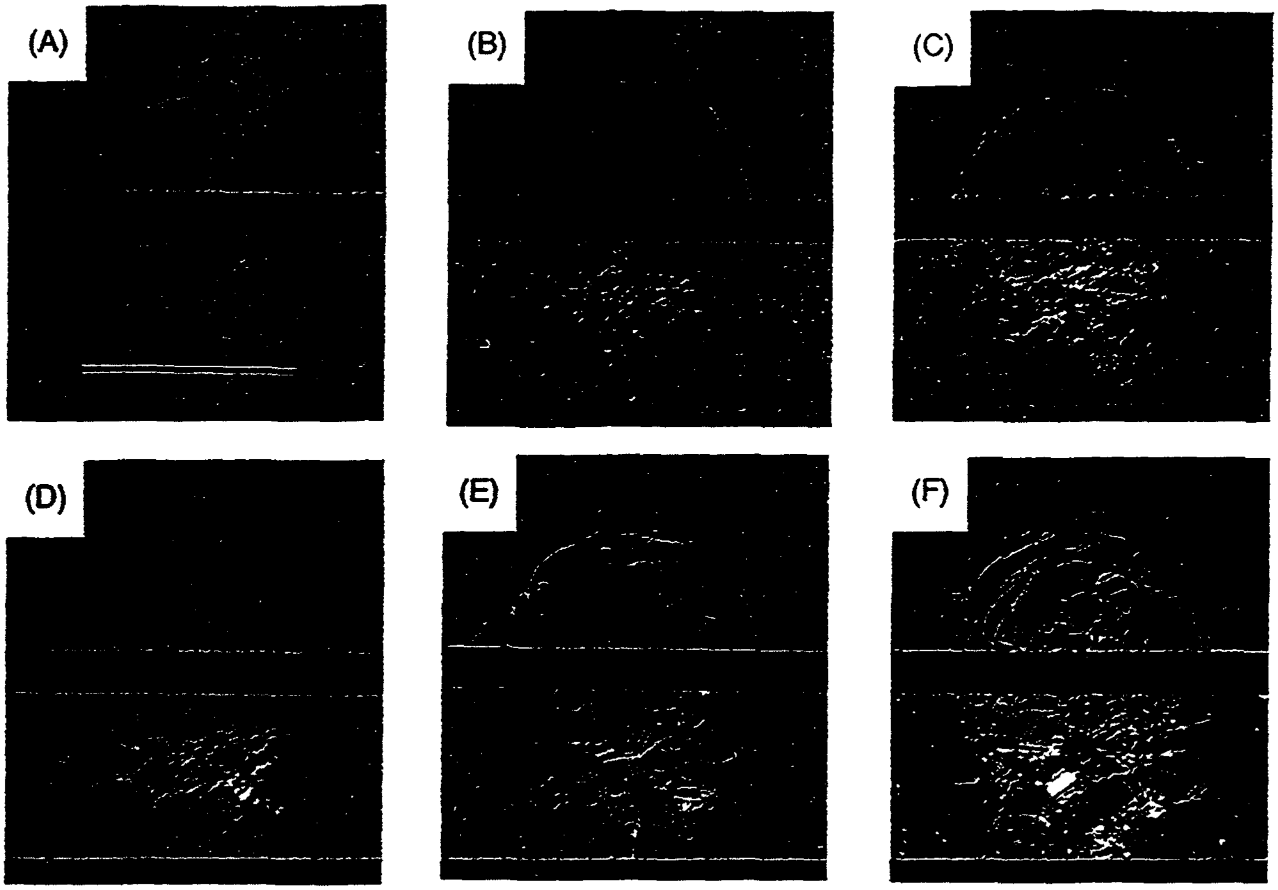

Fig. 4. Optical micrographs in Nomarski illumination showing half-surface (top) and section (bottom) views of indentation sites in aluminas with grain size (A) 3 μm, (B) 9 μm, (C) 15 μm, (D) 21 μm, (E) 35 μm, and (F) 48 μm. Indentations made at a fixed indentation pressure p_0 = 8.0 GPa, using WC sphere of radius r = 3.18 mm at load P = 2000 N (cf. point D in Fig. 2). Marker in (A) represents contact diameter $2a$ = 550 μm.

deformation within this subsurface zone should be the same for all the aluminas. This is not clear from the micrographs. Indeed, with the finest (3 μm) material in Fig. 4(A) there is no obvious indication of any plastic deformation at all; however, the reduction in attendant microcracking inevitably diminishes the surface displacements, and thence the interference contrast. Moreover, at this level we are approaching the limits of spatial resolution of optical microscopy.

Again, confined, shear-fault-initiated microfracture damage *beneath* the contact circle is clearly evident in the coarsest (48 μm) material (Fig. 4(F)), but appears to diminish progressively with decreasing grain size in Fig. 4. There are indications of a threshold in the crack initiation process. This trend to diminished microfracture damage with diminishing grain size is accompanied by an increasing tendency to macrocrack formation *outside* the contact circle; in the finest (3 μm) material (Fig. 4(A)), the fracture pattern closely resembles the classical Hertzian cone crack in ideally homogeneous solids.[4] Cone fracture is inhibited in the coarser materials by the larger scale of crack deflections, particularly in the subsurface Hertzian field where enforced deflection from the principal stress trajectory surface results in a rapid build-up of compressive stresses.[28,29] Thus, for the coarsest alumina, the partial cone crack at lower right in Fig. 4(F) arrests at the very first subsurface grain boundary intersection.

Another feature in Figs. 3 and 4 that warrants special comment is the stochastic nature of the deformation–microfracture damage pattern. It is clear that not all grains in the active deformation zone participate in the damage process. The shear faults in those grains that do deform show wide variability in planar orientation within the Hertzian field. Note further that the damage patterns in Figs. 3(D) and 4(F) differ considerably from each other, although the loading conditions were identical. Grain orientation, as well as size, is clearly an important factor.

(3) Acoustic Emission

Plots of cumulative acoustic energy versus elapsed time during load–unload indentation cycles for the six aluminas for a fixed sphere size (r = 3.18 mm) are shown in the upper diagram of Fig. 5. The corresponding indentation pressure (at constant crosshead displacement rate), to a maximum value p_0 = 8 GPa, is included in the lower diagram.

From the plots in Fig. 5 it is evident that all six aluminas show acoustic activity. There is an initial inactivity as the pressure builds up and ultimately exceeds the elastic limit. We note that the bulk of the activity occurs toward the end of the loading half-cycle, as the system traverses the upper reaches of the data in Fig. 2. Relatively minor activity is observed during the unloading half-cycle. There is a clear discreteness in the acoustic traces, indicating the existence of well-defined local instabilities in the deformation–fracture process.

A systematic trend to increased activity is apparent with increasing grain size. Fewer, but larger, discrete jumps are observed in the finer aluminas (3, 9, and 15 μm) during the loading half-cycle. These jumps correlate with the pop-in of Hertzian cone cracks (Figs. 4(A–C)). More frequent, but smaller, jumps are observed in the coarser aluminas (21, 35, and 48 μm). The bulk of the activity in these latter cases appears to correlate with progressive initiation of the subsurface microfracture damage (Figs. 3(A–D)), although the underlying source of the emissions (e.g., crack pop-in) is not unequivocally

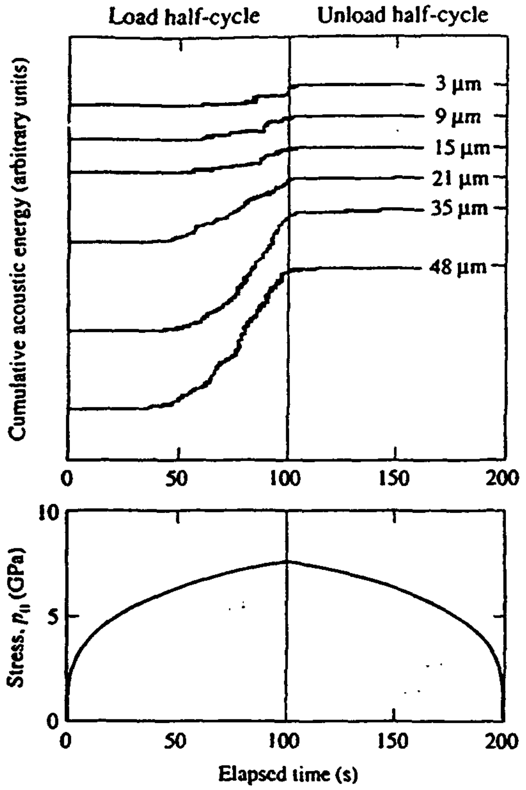

Fig. 5. Plots of cumulative acoustic energy (arbitrary linear scale) versus elapsed time during single load–unload indentation cycle at constant crosshead speed in alumina specimens (upper diagram), using WC sphere of radius r = 3.18 mm. Variation of contact pressure with time indicated (lower diagram).

identified in our tests. Note also that the onset of acoustic activity occurs earlier in the load cycle with increasing grain size. To show the scaling trend more clearly, we plot in Fig. 6 the cumulative energy over the full load–unload cycle as a function of grain size. There is a distinctive, although not abrupt, transition in the integrated signal at grain size ≈20 μm. These results suggest the existence of a grain-size threshold (vertical dashed line in Fig. 6) above which copious new sources of acoustic emission are activated.

IV. Discussion

In this paper we have used Hertzian indentation to investigate the deformation and microfracture in polycrystalline aluminas over a range of grain sizes. Our results reveal departures from an ideally brittle response, as measured on a nonlinear indentation stress–strain curve. Such departures are associated with the generation of a deformation–microfracture damage zone, here revealed by a novel sectioning technique, in the confined region of strong compression and shear stresses *beneath* the indenter.[18] The fully developed damage zone is made up of an accumulation of microstructurally discrete events, each consisting of some kind of intragrain shear faulting accompanied by intergrain microcracking. This cumulative damage zone is quite different from the continuous Hertzian cone fracture that occurs in the weak tensile region *outside* the contact circle in classically homogeneous brittle materials.[4,5,28] The alumina microstructure imposes itself strongly on the contact damage pattern.

The issue of primary interest here in relation to this departure from classical Hertzian cone fracture toward cumulative subsurface microcracking is the effect of grain size. Recall the dramatic enhancement of this transition with progressive microstructural coarsening in Fig. 4. Now, size effects are not

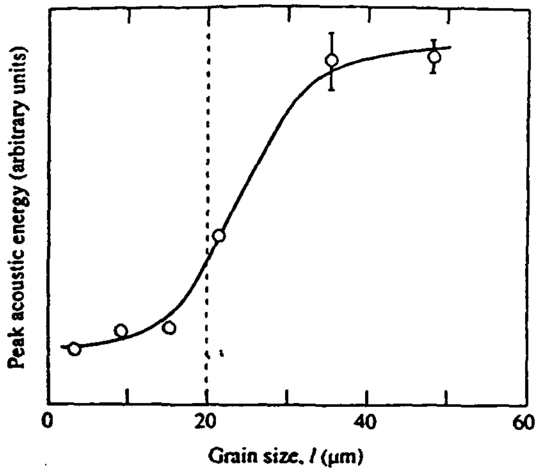

Fig. 6. Plot of peak acoustic energy (i.e., cumulative energy at end of load–unload cycle) as a function of grain size, for data obtained using ball of radius r = 3.18 mm, at peak contact pressure p_0 = 8.0 GPa (cf. Fig. 5).

uncommon in brittle cracks where some kind of competition between deformation (volume-controlled) and fracture (area-controlled) is involved.[5,30–32] This is true even of Hertzian tests in *homogeneous* solids (e.g., glasses and single crystals), where the use of ever-smaller spheres suppresses cone fracture in favor of subsurface shear-fault deformation, reflecting the well-documented transition in indentation response from "blunt" to "sharp."[4,5,24] In Fig. 4, however, the indenter radius is held fixed, so we are dealing here exclusively with microstructural scaling.

It is therefore of interest to consider the nature of the deformation–microfracture pattern more closely in this context of microstructural scaling.

(1) *Deformation*

The existence of a universal nonlinear stress–strain curve in Fig. 2 for alumina, *independent* of grain size, reflects an intrinsic "plasticity" in the mechanical response at high contact pressures. The curve deviates from the Hertzian elastic prediction above $p_0 \approx 5$ GPa, corresponding to an "indentation yield stress" for the material.[19,23] This deviation, together with the observation in Fig. 3 that the damage initiates *beneath* the contact in the region of maximum shear, implies that the deformation component is governed by some critical faulting stress.[18] The micrographs in Figs. 3 and 4 show the subsurface faults in the alumina to be in the form of twin/slip bands contained within individual grains, arrested at their ends by the grain boundaries. The characteristic scale of individual faults within each grain is therefore governed by the grain size. On the other hand, the apparent universality of the curve and hardness values for the aluminas in Fig. 2 indicates that the *net* deformation is not limited by the grain size, i.e., that the integrated volume of deformed material over the contact zone is microstructurally invariant.

Positive identification and detailed analysis of the fundamental microshear processes responsible for the contact deformation in the aluminas, particularly at the finer grain sizes, are issues for further study.

(2) *Microfracture*

On the other hand, grain size has a strong effect on the microcracking damage. This is reflected most dramatically in the acoustic emission data in Fig. 5. Close inspection of the micrographs in Figs. 3 and 4 indicates that the microcracks initiate from the lamella shear faults and extend over one to three grain facets. The lack of any acoustic activity during *un*loading suggests that microcrack *pop-in* occurs only during the loading half-cycle. However, such microcracks will be subject to intense constraining hydrostatic compression at full load, so a significant proportion of the extension may actually take place *stably* (and *quietly*) on *release* of the compression during unloading (cf. growth of lateral cracks during unloading in sharp-indenter fields.[4,33]) The amount of extension from each microcrack nucleus will depend critically on the sign and intensity of residual thermal expansion anisotropy stresses at the grain boundary; clearly, the greatest extension will occur from those facets that experience tensile stresses. These same stresses will also limit the extension of the microcracks, as they encounter compressive facets and become increasingly subject to grain-bridging tractions.[12]

This deformation–microfracture description allows us to construct a simplistic model for the influence of grain size on contact-induced microfracture in alumina. Consider a volume element in the compression–shear deformation zone beneath the contact circle, as shown in the schematic of Fig. 7. Here, $-\sigma_1$ and $-\sigma_3$ are principal compression stresses in the Hertzian field. Those compression stresses are generally unequal, so there is a component of shear acting on planes inclined to the principal axes, attaining a maximum value $\frac{1}{2}(\sigma_1 - \sigma_3)$ at 45°. The shear component initiates intragrain faults FF, which arrest at the weak grain boundaries and generate stress intensities there. If the stress intensities exceed a critical level, microcracks FC pop in. A critical condition for such pop-in may be determined by regarding the faults FF as shear cracks with net shear tractions $S = |\tau| - \mu|\sigma| - \tau_F$ at their interfaces.[34,35] τ and σ are resolved shear and (compressive) normal components of the contact stress field at the fault plane, directly proportional to the mean contact pressure p_0; μ is a coefficient of sliding friction between contacting surfaces; and τ_F is an intrinsic fault cohesion (e.g., twinning) stress. A minimum requirement for crack initiation is that the yield point on the indentation stress–strain curve in Fig. 2 should be exceeded, corresponding to $S = S_Y$, with S_Y a material constant. Then one may write a stress-intensity factor $K = \psi S_Y l^{1/2}$ for the shear fault, with l a grain dimension and ψ a crack geometry term dependent on the angle between FF and FC.[5] Microcrack initiation occurs along FC when the stress intensity equals the grain boundary toughness, i.e., $K = T_0$, corresponding to a critical grain size

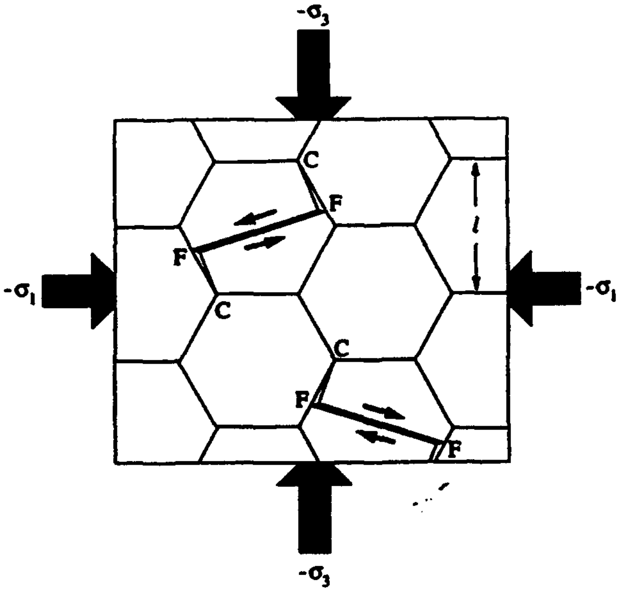

Fig. 7. Schematic of deformation–microfracture damage in polycrystalline alumina ceramic, grain size l. Volume element is subjected to compressive normal stresses $-\sigma_1$ and $-\sigma_3$ along contact axis below spherical indenter. Shear stresses (arrows) initiate intragrain lamellae FF, which pop-in intergrain microcracks FC at their ends.

$$l_C = (T_0/\psi S_Y)^{1/2} \tag{3}$$

A more comprehensive analysis of microcrack initiation, including a description of the subsequent propagation into the adjacent microstructure, will be given elsewhere.[36]

Two aspects of the deformation–microfracture observations reported in Sect. III that warrant special consideration are *stochastics* and *flaw sensitivity*. The stochastic nature of the microstructurally discrete damage alluded to in Sect. III(2) appears to be the result of a complex interplay of statistical variation in both relative size and crystallographic orientation of individual grains. Even the most uniform polycrystals, including the aluminas used in the present study, are characterized by a distribution of grain sizes about a mean; and twin/slip deformation of alumina occurs only on certain preferred crystallographic planes.[37] Hence the largest, "correctly" oriented grains in the Hertzian compression–shear zone will deform first, resulting in a grain-by-grain activation within the ultimate deformation zone as one progresses up the indentation stress–strain curve. This stochastic element will inevitably reflect in Eq. (3), accounting for the lack of an abrupt grain size cutoff (vertical dashed line) in Fig. 6.

Flaw sensitivity is of interest in relation to the susceptibility of polycrystalline ceramics to damage accumulation in contact stress fields. Of particular interest is the issue of preexisting (e.g., processing) flaws vs contact-induced flaws. In Fig. 2, stress–strain data from the present study obtained on equiaxed, homogeneous, "defect-free" aluminas[16] overlap (at least within experimental scatter) the solid curve from a previous study on a nonequiaxed, inhomogeneous, commercial alumina with a relatively high density of large processing flaws.[18] This implies that preexisting defect populations are not of great consequence to contact damage of the kind observed in Figs. 3 and 4. The contact process generates its own flaw population, via the precursor shear faulting.

These results have important implications concerning the microstructural design of ceramics for improved contact-damage resistance. Most obvious is the refinement of grain size, to minimize the prospect of microcrack initiation. Such an approach is not inconsistent with precedent work on the wear of ceramics, where decreased grain size leads to demonstrably reduced removal rates.[17,38–40] However, the insensitivity of contact damage to preexisting flaws suggests processing strategies quite different from the traditional ones in which preexisting flaw populations are painstakingly eliminated.[41] Instead, the emphasis shifts to refining the grain-size distribution, to avoid the occasional large grain or grain cluster. Again, we would emphasize that some of these strategies may run counter to those required for improved long-crack toughness, especially in ceramics that exhibit toughening by grain-interlock bridging.[6–15]

Another interesting materials design aspect pertains to the effect of environment-assisted slow-crack growth, particularly from atmospheric water, on contact damage.[18] Since the contact deformation initiates in the *subsurface* Hertzian field, the ensuing microcracks do not have access to the external chemical environment, at least not until the damage zone becomes sufficiently large that it intersects the contact surface. This suggests that the effect of slow-crack growth may play no role in the early developmental stages of the deformation–microfracture process. Under such conditions the observation of damage *accumulation* in *repeated* contacts[18] can be attributed to a true mechanical fatigue process.

Although we have focused our attention here exclusively on alumina, the basic features of the Hertzian deformation–microfracture damage process envisaged in Fig. 7 may be considered generic to heterogeneous ceramics. Key to this kind of damage is the existence of weak planes in the microstructure, either intragrain or intergrain, so that some kind of easy shear faulting may occur in the subsurface compression–shear zone. In the case of alumina, the faulting is in the form of crystallographic lamellae within individual grains. Intersection of the lamellae with the weak grain boundaries allows for a concentration of stress intensity, which in turn facilitates intergranular microcracking. Other faulting mechanisms are identified in other ceramic types: in softer monophase polycrystals, e.g., magnesium oxide, straightforward crystallographic slip;[42] in silicate glasses, a breakdown of the network structure at the theoretical cohesive shear stress;[43–46] in machinable glass–ceramics, sliding at weak interfaces between crystallized mica flakes and the glass matrix;[25] in complex rocks, a multiplicity of intrinsic and extrinsic frictional sliding defect planes.[34] This suggests that, while fine details of the slip process may be material-specific, the larger concept of deformation-induced damage in Hertzian contact fields is broadly applicable.

It is therefore evident that the Hertzian test offers certain benefits as a means for investigating the general deformation and fracture properties of brittle ceramics. Some of this information, in particular that relating to the deformation component, is not accessible using conventional strength and toughness tests, because in those tests the inevitable dominance of tensile stresses promotes the propagation of a single well-developed crack at the expense of potentially competitive shear processes. To obtain information on such shear processes it is necessary to contrive a test procedure with a high component of hydrostatic compression to suppress or restrict the fracture, as in the traditional (but complex) confined-pressure apparatus used by geophysicists.[34] Vickers (or Knoop) hardness indentation is the one routine form of mechanical testing used by ceramists that does provide the necessary high shear component for activation of irreversible deformation. The relative advantage of the Hertzian test is that one can study the *evolution* of the damage pattern, from initial elastic to final fully plastic contact, providing information on the short-crack microfracture processes that control fundamental fatigue and wear properties of brittle ceramics.

Acknowledgments: We thank H. Cai and M. A. Stevens Kalceff for fruitful discussions and S. J. Bennison and P. Chantikul for providing the alumina specimens.

References

[1] S. M. Wiederhorn and B. R. Lawn, "Strength Degradation of Glass Resulting from Impact with Spheres," *J. Am. Ceram. Soc.*, 60 [9–10] 451–58 (1977).

[2] B. R. Lawn and D. B. Marshall, "Indentation Fracture and Strength Degradation in Ceramics"; pp. 205–29 in *Fracture Mechanics of Ceramics*, Vol. 3. Edited by R. C. Bradt, D. P. H. Hasselman, and F. F. Lange. Plenum, New York, 1978.

[3] S. M. Wiederhorn and B. J. Hockey, "Effect of Material Parameters on the Erosion Resistance of Brittle Materials," *J. Mater. Sci.*, 18 [3] 766–80 (1983).

[4] B. R. Lawn and T. R. Wilshaw, "Indentation Fracture: Principles and Applications," *J. Mater. Sci.*, 10 [6] 1049–81 (1975).

[5] B. R. Lawn, *Fracture of Brittle Solids*. Cambridge University Press, Cambridge, U.K., 1993.

[6] R. Knehans and R. Steinbrech, "Effect of Grain Size on the Resistance Curves of Al$_2$O$_3$," *Sci. Ceram.*, 12, 613–19 (1983).

[7] F. Deuerler, R. Knehans, and R. Steinbrech, "Testing Methods and Crack Resistance Behaviour of Al$_2$O$_3$," *Sci. Ceram.*, 13, C-617–C-621 (1986).

[8] M. V. Swain, "*R*-Curve Behaviour in a Polycrystalline Alumina Material," *J. Mater. Sci. Lett.*, 5, 1313–15 (1986).

[9] P. L. Swanson, C. J. Fairbanks, B. R. Lawn, Y.-W. Mai, and B. J. Hockey, "Crack-Interface Grain Bridging as a Fracture Resistance Mechanism in Ceramics: I. Experimental Study on Alumina," *J. Am. Ceram. Soc.*, 70 [4] 279–89 (1987).

[10] P. L. Swanson, "Crack-Interface Traction: A Fracture-Resistance Mechanism in Brittle Polycrystals"; pp. 135–55 in Advances in Ceramics, Vol. 22, *Fractography of Glasses and Ceramics*. Edited by J. Varner and V. D. Frechette. American Ceramic Society, Columbus, OH, 1988.

[11] R. W. Steinbrech and O. Schmenkel, "Crack Resistance Curves of Surface Cracks in Alumina," *J. Am. Ceram. Soc.*, 71 [5] C-271–C-273 (1988).

[12] S. J. Bennison and B. R. Lawn, "Role of Interfacial Grain-Bridging Sliding Friction in the Crack-Resistance and Strength Properties of Nontransforming Ceramics," *Acta Metall.*, 37 [10] 2659–71 (1989).

[13] G. Vekinis, M. F. Ashby, and P. W. R. Beaumont, "*R*-Curve Behaviour of Al$_2$O$_3$ Ceramics," *Acta Metall.*, 38 [6] 1151–62 (1990).

[14] N. Ramachandran and D. K. Shetty, "Rising Crack-Growth-Resistance (*R*-Curve) Behavior of Toughened Alumina and Silicon Nitride," *J. Am. Ceram. Soc.*, 74 [10] 2634–41 (1991).

[15] L. M. Braun, S. J. Bennison, and B. R. Lawn, "Objective Evaluation of Short-Crack Toughness Curves Using Indentation Flaws: Case Study on Alumina-Based Ceramics," *J. Am. Ceram. Soc.*, 75 [11] 3049–57 (1992).

[16] P. Chantikul, S. J. Bennison, and B. R. Lawn, "Role of Grain Size in the Strength and *R*-Curve Properties of Alumina," *J. Am. Ceram. Soc.*, 73 [8] 2419–27 (1990).

[17] S.-J. Cho, B. J. Hockey, B. R. Lawn, and S. J. Bennison, "Grain-Size and *R*-Curve Effects in the Abrasive Wear of Alumina," *J. Am. Ceram. Soc.*, 72 [7] 1249–52 (1989).

[18] F. Guiberteau, N. P. Padture, H. Cai, and B. R. Lawn, "Indentation Fatigue: A Simple Cyclic Hertzian Test for Measuring Damage Accumulation in Polycrystalline Ceramics," *Philos. Mag. A*, 68 [5] 1003–16 (1993).

[19] D. Tabor, *Hardness of Metals*. Clarendon, Oxford, U.K., 1951.

[20] T. O. Mulhearn, "The Deformation of Metals by Vickers-Type Pyramidal Indenters," *J. Mech. Phys. Solids*, 7, 85–96 (1959).

[21] S. v. d. Zwagg, J. T. Hagan, and J. E. Field, "Studies of Contact Damage in Polycrystalline Zinc Sulphide," *J. Mater. Sci.*, 15, 2965–72 (1980).

[22] N. P. Padture, "Postfailure Subsidiary Cracking from Indentation Flaws," *J. Mater. Res.*, 8 [6] 1411–17 (1993).

[23] M. V. Swain and B. R. Lawn, "A Study of Dislocation Arrays at Spherical Indentations in LiF as a Function of Indentation Stress and Strain," *Phys. Status Solidi*, 35 [2] 909–23 (1969).

[24] M. V. Swain and J. T. Hagan, "Indentation Plasticity and the Ensuing Fracture of Glass," *J. Phys. D: Appl. Phys.*, 9, 2201–14 (1976).

[25] H. Cai, M. A. Stevens Kalceff, and B. R. Lawn, "Deformation and Fracture of Mica-Containing Glass–Ceramics In Hertzian Contacts," *J. Mater. Res.*, 9 [3] 762–70 (1994).

[26] H. Hertz, *Hertz's Miscellaneous Papers*; Ch. 5 and 6. Macmillan, London, U.K., 1896.

[27] K. L. Johnson, *Contact Mechanics*. Cambridge University Press, London, U.K., 1985.

[28] F. C. Frank and B. R. Lawn, "On the Theory of Hertzian Fracture," *Proc. R. Soc. London, A*, 299 [1458] 291–306 (1967).

[29] B. R. Lawn, "Hertzian Fracture in Single Crystals with the Diamond Structure," *J. Appl. Phys.*, 39 [10] 4828–36 (1968).

[30] B. R. Lawn and D. B. Marshall, "Hardness, Toughness, and Brittleness: An Indentation Analysis," *J. Am. Ceram. Soc.*, 62 [7–8] 347–50 (1979).

[31] K. E. Puttick, "Energy Scaling, Size Effects and Ductile–Brittle Transitions in Fracture," *J. Phys. D: Appl. Phys.*, 12, L19–L23 (1979).

[32] K. Puttick, "The Correlation of Fracture Transitions," *J. Phys. D: Appl. Phys.*, 13, 2249–62 (1980).

[33] B. R. Lawn and M. V. Swain, "Microfracture beneath Point Indentations in Brittle Solids," *J. Mater. Sci.*, 10 [1] 113–22 (1975).

[34] J. C. Jaeger and N. G. W. Cook, *Fundamentals of Rock Mechanics*. Chapman and Hall, London, U.K., 1971.

[35] H. Horii and S. Nemat-Nasser, "Compression-Induced Microcrack Growth in Brittle Solids: Axial Splitting and Shear Failure," *J. Geophys. Res.*, 90 [B4] 3105–25 (1985).

[36] B. R. Lawn, N. P. Padture, F. Guiberteau, and H. Cai, "A Model for Microcrack Initiation and Propagation beneath Hertzian Contacts in Polycrystalline Ceramics," *Acta Metall. Mater.*, in press (1994).

[37] M. L. Kronberg, "Plastic Deformation of Single Crystals of Sapphire," *Acta Metall.*, 5 [9] 507–24 (1957).

[38] C. C. Wu, R. W. Rice, D. Johnson, and B. A. Platt, "Grain-Size Dependence of Wear in Ceramics," *Ceram. Eng. Sci. Proc.*, 6 [7–8] 995–1011 (1985).

[39] R. W. Rice, "Micromechanisms of Microstructural Aspects of Ceramics Wear," *Ceram. Eng. Sci. Proc.*, 6 [7–8] 940–58 (1985).

[40] S.-J. Cho, H. Moon, B. J. Hockey, and S. M. Hsu, "The Transition from Mild to Severe Wear in Alumina during Sliding," *Acta Metall.*, 40 [1] 185–92 (1992).

[41] F. F. Lange, "Powder Processing Science and Technology for Increased Reliability," *J. Am. Ceram. Soc.*, 72 [1] 3–15 (1989).

[42] T. L. Johnston, R. J. Stokes, and C. H. Li, "Crack Nucleation in Magnesium Oxide Bicrystals under Compression," *Philos. Mag.*, 7, 23–34 (1962).

[43] J. T. Hagan and M. V. Swain, "The Origin of Median and Lateral Cracks at Plastic Indents in Brittle Materials," *J. Phys. D: Appl. Phys.*, 11 [15] 2091–102 (1978).

[44] A. Arora, D. B. Marshall, B. R. Lawn, and M. V. Swain, "Indentation Deformation/Fracture of Normal and Anomalous Glasses," *J. Non-Cryst. Solids*, 31 [3] 415–28 (1979).

[45] J. T. Hagan, "Shear Deformation under Pyramidal Indenters in Soda–Lime Glass," *J. Mater. Sci.*, 15, 1417–24 (1980).

[46] B. R. Lawn, T. P. Dabbs, and C. J. Fairbanks, "Kinetics of Shear-Activated Indentation Crack Initiation in Soda–Lime Glass," *J. Mater. Sci.*, 18 [9] 2785–97 (1983). □

Reprinted from The Journal of the American Ceramic Society, Vol. 77, No. 2, February 1994

journal

J. Am. Ceram. Soc., 77 [2] 519–23 (1994)

In Situ-Toughened Silicon Carbide

Nitin P. Padture[*,†]

Materials Science and Engineering Laboratory, National Institute of Standards and Technology,
Gaithersburg, Maryland 20899

A new processing strategy based on atmospheric pressure sintering is presented for obtaining dense SiC-based materials with microstructures consisting of (i) uniformly distributed elongate-shaped α-SiC grains and (ii) relatively high amounts (20 vol%) of second-phase yttrium aluminum garnet (YAG). This strategy entails the sintering of β-SiC powder doped with α-SiC, Al_2O_3, and Y_2O_3. The Al_2O_3 and Y_2O_3 aid in the liquid-phase sintering of SiC and form *in situ* YAG, which has a significant thermal expansion mismatch with SiC. During a subsequent grain-growth heat treatment, it is postulated that the α-SiC "seeds" assist in controlling *in situ* growth of the elongated α-SiC grains. The fracture pattern in the *in situ*-toughened SiC is intergranular with evidence of copious crack-wake bridging, akin to toughened Si_3N_4 ceramics. The elongate nature of the α-SiC grains, together with the high thermal-residual stresses in the microstructure, enhance the observed crack-wake bridging. This bridging accounts for a measured twofold increase in the indentation toughness of this new class of *in situ*-toughened SiC relative to a commercial SiC.

I. Introduction

Silicon carbide can be pressureless sintered with the aid of C and B to near full density at temperatures in excess of 2100°C.[1] The resulting SiC materials, which have fine-grain equiaxed microstructures (grain size 1 to 4 μm), show improved high-temperature creep and oxidation resistance.[2,3] However, the low fracture toughness (3 to 4 $MPa{\cdot}m^{1/2}$)[2] and highly flaw-sensitive strength[4] of those SiC materials at room temperature limit their use in many potential structural applications.

It has been demonstrated that sintering of SiC can be achieved at relatively lower temperatures (1850° to 2000°C) with the addition of small quantities of Al_2O_3[5] and Al_2O_3 + Y_2O_3 (or rare-earth oxides)[6-12] via the liquid-phase-sintering mechanism. The resulting materials have equiaxed fine-grain microstructures with second phases located at triple junctions of SiC grains.[10,12,13] Transmission electron microscopy (TEM) studies suggest that the two-grain junctions in some of those SiC materials are free of any intergranular phases, which makes those materials creep resistant.[5] Therefore, without sacrificing the high-temperature properties, the processing temperatures of SiC can be reduced by choosing liquid-phase sintering over solid-state sintering. However, the room-temperature fracture toughness of the available liquid-phase-sintered SiC materials remains low.[9] In one instance, high toughness in fine-grain (~2-μm grain size) liquid-phase-sintered SiC/YAG has been reported.[14] However, in that study the details of processing and microstructure development have not been presented, and the explanation offered for the observed toughening is open to question.

In the present study we have used pressureless liquid-phase sintering to process SiC-based ceramics and have achieved considerable increase in the room-temperature fracture toughness. We use the toughening mechanism of crack bridging by grains in the wake of the crack tip. The crack-wake bridging approach has been successfully applied to many ceramics with equiaxed coarse-grain microstructures.[15,16] It has also been demonstrated that the efficacy of crack-wake bridging can be augmented by both introducing elongate-shape reinforcements (whiskers,[17] grains[18]) and increasing the thermal-expansion-mismatch stress by including an appropriate second phase[19,20] in the microstructure. Here we are able to form *both* the elongated SiC grains and the high thermal-expansion-mismatch second phase $Y_3Al_5O_{12}$ (yttrium aluminum garnet or YAG) ($\Delta\alpha \sim 5.1 \times 10^{-6}\ {}^{\circ}C^{-1}$) *in situ* during processing, instead of by the more conventional route of processing toughened ceramics, viz, addition of whiskers/platelets/particles followed by hot-pressing. Our approach is analogous to the *in situ* toughening in gas-pressure-sintered Si_3N_4-based ceramics,[18,21] but with the added advantage in our case of sintering at atmospheric pressure in an ordinary graphite furnace.

The *in situ*-toughening route has several advantages over the conventional route, viz, no health hazard associated with whiskers, potential to fabricate complex shapes and large size components, atmospheric pressure sintering, and high reinforcement-phase volume fraction. All those advantages can contribute to considerable saving in the cost of a component, making the *in situ* approach an attractive one for SiC.

In this paper we describe a processing strategy, using β-SiC starting powder doped with α-SiC, Al_2O_3, and Y_2O_3 powders, to achieve microstructures consisting of uniformly distributed 80 vol% elongated α-SiC grains and 20 vol% second-phase YAG. We also present evidence for copious crack-wake bridging in those SiC materials, along with some preliminary indentation-toughness measurements.

II. Experimental Procedure

Submicrometer size powders of β-SiC, α-SiC, Y_2O_3 (H. C. Starck, Berlin, Germany; B10, A10, Fine-Grade, respectively), and Al_2O_3 (AKP-30, Sumitomo Chemicals, Tokyo, Japan) were used as starting materials.[‡] Six batches of powder were mixed, each containing 80 vol% SiC (α- and/or β-) and Al_2O_3:Y_2O_3 in molar ratio 3:5 to yield 20 vol% YAG. The relative content of α-SiC powder in those batches was 0, 0.1, 0.2, 0.5, 1.0, and 100 vol%. Individual powder batches were blended intimately by wet-ball-milling in methanol for 24 h. All individual slurries were then stirred while drying on a hot plate.

Individual powder batches (~7 g) were placed in polyethylene bags and deagglomerated by crushing with a roller. Those powder batches were uniaxially pressed into pellets (25-mm

---

D. B. Marshall—contributing editor

Manuscript No. 194577. Received May 11, 1993; approved July 28, 1993.

Supported by the U.S. Air Force Office of Scientific Research and the National Institute of Standards and Technology (NIST).

[*] Member, American Ceramic Society.

[†] Guest Scientist, on leave from Department of Materials Science and Engineering, Lehigh University, Bethlehem, Pennsylvania 18015.

[‡] The use of any products in this work does not imply their endorsement by NIST.

diameter × 7-mm thickness) at 50 MPa pressure in a graphite die, followed by cold isostatic pressing at 350 MPa.

All the green pellets were packed in loose SiC powder (600 grit Crystolon, Norton, Worcester, MA) in a graphite crucible with a screwable lid. Layers of Al_2O_3 powder (15-μm size, Buehler, Lake Bluff, IL) were placed inside the crucible near the bottom and the top of the crucible cavity. The crucible was then closed tightly and placed in a graphite furnace (Astro Industries, Santa Rosa, CA) for sintering. All pellets were given a base sintering heat treatment of 1900°C for 0.5 h in a flowing argon gas atmosphere, using heating and cooling rates of 600°C/h and 1200°C/h, respectively. Some of the as-sintered pellets were again packed in SiC powder in the graphite crucible, but this time without any Al_2O_3 in the packing powder. They were then given a second grain-growth heat treatment of 2000°C for 2, 3, or 4 h (same conditions as before). The rationale for using Al_2O_3 in the packing powder and the proper closure of the crucible is discussed in Sect. III(1).

Dimensions of all individual pellets were measured before and after each heat treatment to compute shrinkages. Densities of some pellets ground to a thickness of ~2.5 mm were measured using the Archimedes principle.[22] X-ray diffraction using $CuK\alpha$ radiation (Philips, Mahwah, NJ) was performed on all the ground specimens. Cross sections of the pellets were polished to 1 μm using routine ceramographic techniques, and were gold-coated prior to observation in a scanning electron microscope (SEM) equipped with an energy-dispersive spectrometer (EDS) (1830, Amray, Bedford, MA).

A polished section of a selected *in situ*-toughened (IST) SiC specimen was indented using a Vickers diamond pyramid at loads ranging from 5 to 200 N. For comparison, a pressureless sintered commercial SiC (Hexoloy SA, Carborundum, Niagara Falls, NY) (HSA), with the same percent theoretical density (97%) as that of IST and an average grain size of 4 μm, was also indented. Lengths of the surface traces of well-defined radial cracks from five indentations per indentation load were measured for the two materials, using an optical microscope (Epiphot, Nikon, Tokyo, Japan).

III. Results

(1) *Processing*

Density and shrinkage for the specimens made from the six different starting powders that underwent only the base sintering heat treatment were found to be independent of the powder composition. The densities in each case were >99.5% of the theoretical limit of 3.484 g/cm^3 (calculated using density values of 3.217 g/cm^3 for SiC and 4.553 g/cm^3 for YAG). Diametric and axial shrinkages for all those specimens were determined to be ~13% and ~16%, respectively. All specimens were found to be composed primarily of β-SiC (except for the specimen made with all-α-SiC starting powder) and YAG, using X-ray diffraction. The microstructures for all the specimens consisted of fine equiaxed SiC grains (average size ~2 μm) and the surrounding YAG phase.

Cordery *et al.*[10] have demonstrated that the presence of Al_2O_3 in the green pellet is essential for the successful sintering of SiC. However, during the sintering heat treatment, the Al_2O_3 from the pellet volatilizes rapidly, resulting in incomplete densification. This problem was overcome by creating an excess pressure of aluminum oxide gas species (AlO, Al_2O) around the pellet by including Al_2O_3 in the packing powder and suitably enclosing the crucible cavity.[10] The second grain growth heat treatment was carried out on as-sintered pellets which did not require Al_2O_3 in the packing powder.

Now consider the sintered specimens that underwent the second grain-growth heat treatment. During that heat treatment, regardless of the powder composition and heat-treatment time, no further shrinkage was observed. However, the second heat treatment (independent of the heat-treatment time) resulted in a considerable decrease in the density from the as-fired level of 99.5%. Figure 1(A) shows such a result for a heat treatment of 2000°C for 3 h. From Fig. 1(A) it can also be seen that the density increases with increasing α-SiC seed content, with the exception of the specimens made with all-α-SiC starting powder. At a fixed α-SiC seed content, the overall densities were found to decrease with increasing heat-treatment time. Figure 1(B) illustrates that trend for specimens containing 0.5 vol% α-SiC seeds.

All heat-treated specimens were found to be composed primarily of α-SiC and YAG, by X-ray diffraction analysis. However, the presence of small quantities of yttrium aluminosilicates could not be ruled out.

Figures 2(A) and (B) show representative microstructures of specimens, heat treated at 2000°C for 3 h, with all-β-SiC and all-α-SiC starting powders, respectively. Note the nonuniform grain structure (5 to 300 μm) in the all-β-SiC starting powder specimen (Fig. 2(A)). In contrast, the specimen with all-α-SiC starting powder shows a uniformly distributed equiaxed fine-grained structure (average size ~ 5 μm) (Fig. 2(B)).

Figures 3(A *to* C) show representative microstructures of specimens containing 0.5 vol% α-SiC seeds heat-treated at 2000°C for 2, 3, and 4 h, respectively. Comparison of Figs. 2(A) and (B) with Fig. 3(B) highlights the effect of seeding on the microstructure; note the relatively uniform distribution of elongated shaped α-SiC grains (2 to 8 μm wide, 5 to 40 μm long) in Fig. 3(B). Note also the increase in the scale of the microstructure from Fig. 3(A) (2 *to* 4 μm wide, 5 *to* 20 μm

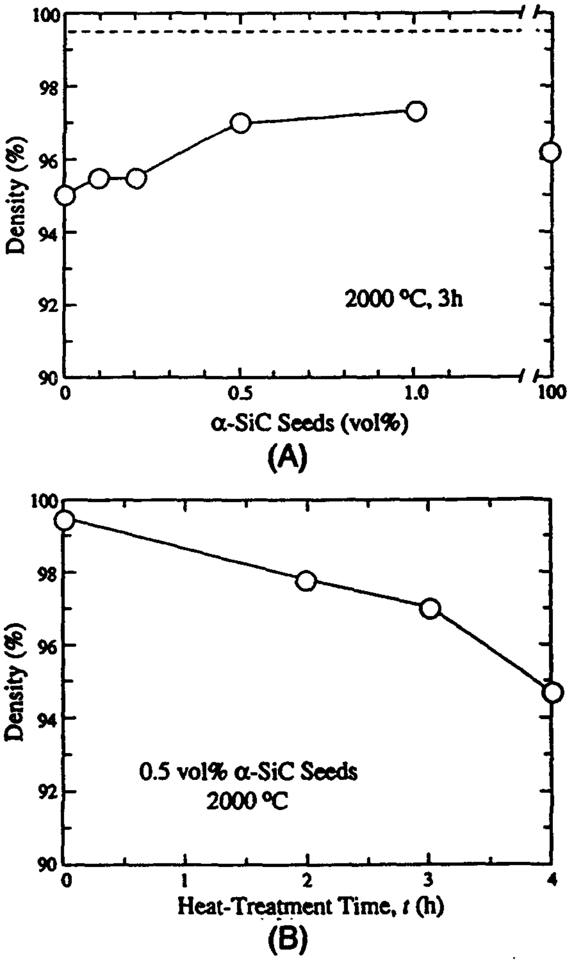

Fig. 1. (A) Plot of density versus α-SiC seed content for postsintering heat treatment of 2000°C for 3 h. The top dashed lines represent as-sintered density (99.5%). (B) Plot of density versus postsintering heat-treatment time at 2000°C for material with 0.5 vol% α-SiC seeds.

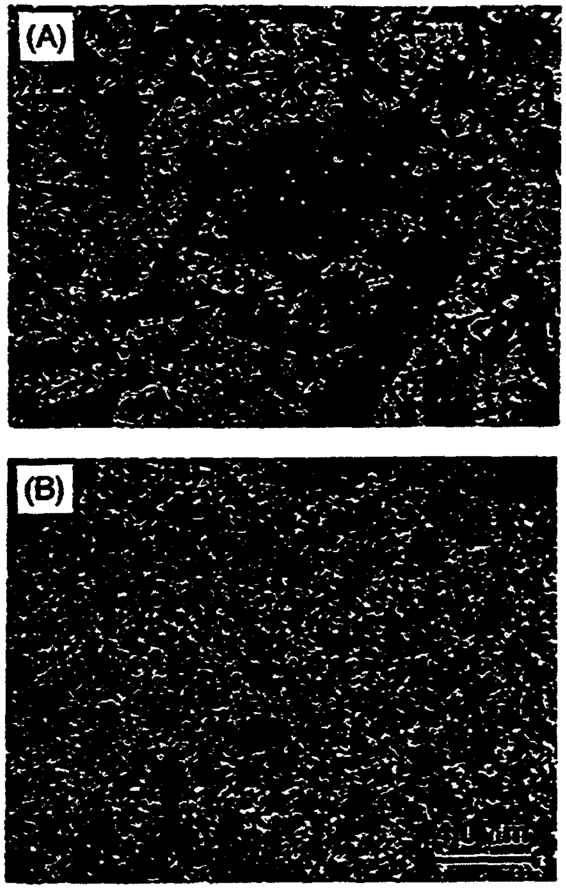

Fig. 2. SEM (backscattered electrons) microstructures of materials with postsintering heat treatment of 2000°C for 3h: (A) all-β-SiC starting powder and (B) all-α-SiC starting powder. Gray phase is SiC, white phase is YAG, and the black region is porosity and/or grain pullout.

long) to Fig. 3(C) (4 to 12 μm wide, 5 to 100 μm long). The microstructures in Figs. 3(A to C) show a bimodal distribution of α-SiC grains. However, the grain growth in those seeded specimen appears to occur in a self-similar manner.

(2) *Mechanical Behavior*

A specimen with 0.5 vol% α-SiC seeds heat-treated for 2000°C for 3 h (IST) (Fig. 3(B)) was chosen for preliminary toughness evaluation. That choice was based on the trade-off between density and microstructural coarseness (Fig. 1(B) and Figs. 3(A to C)). Qualitative observations of Vickers indentation crack patterns revealed that the most extensive crack-wake bridging occurred in specimens with relatively high density and intermediate microstructural coarseness. Figure 4(A) shows a plot of indentation load versus crack length for materials HSA and IST.

The toughness is evaluated using the equilibrium relation for *K*-field generated by the elastic–plastic contact of a Vickers indentation on a brittle solid for radial crack geometry:[23]

$$K_R = \chi P / c^{3/2} = T \tag{1}$$

where T is the toughness, χ is the indentation contact-field parameter (which depends on the square root of the ratio of elastic modulus to hardness E/H), P is the indentation load, and c is the crack length. Fits to Eq. (1) (solid lines in Fig. 4(A)) pass through the data points, implying cracks of radial geometry.[23] Since the E/H ratios for HSA (16.5, Ref. 2) and IST (17.0, this study) are similar, and the density for both materials is 97%, it can be assumed that the χ values are the same for the two materials. Therefore, the toughness of IST relative to HSA

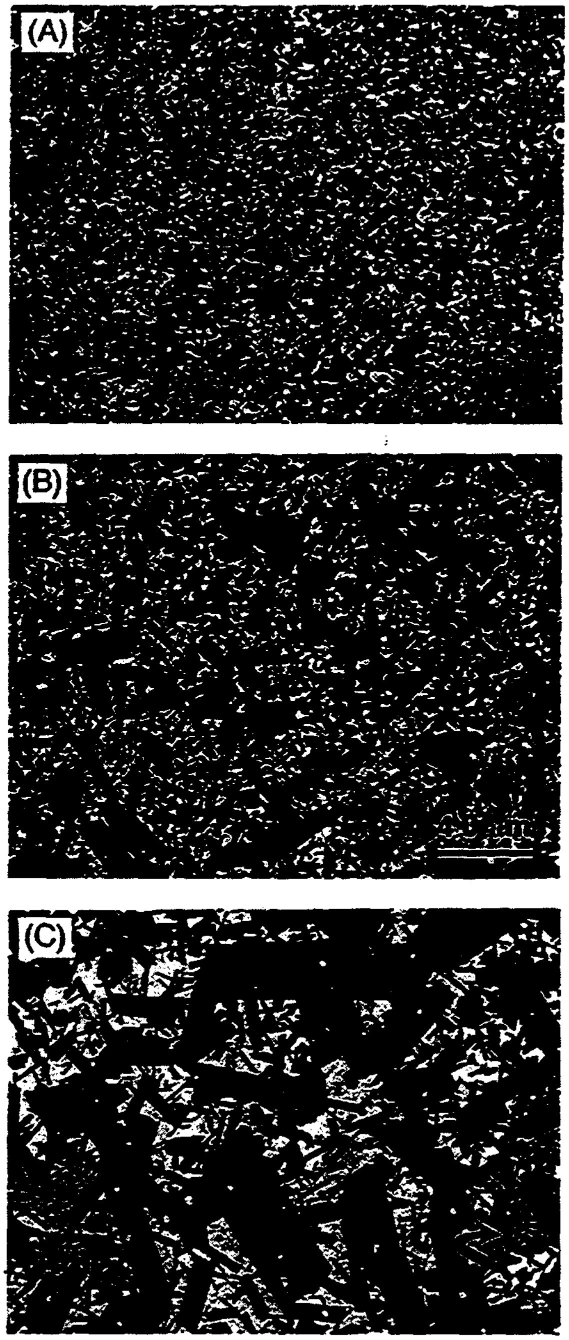

Fig. 3. SEM (backscattered electrons) microstructures of materials containing 0.5 vol% α-SiC seeds with postsintering heat treatments of 2000°C for (A) 2 h, (B) 3 h, and (C) 4 h. (Cf. Fig. 1(B).) Phase denotations same as in Fig. 2. The arrow in (C) indicates grayish Y-, Al-, and Si-containing region.

is determined by the relative positions of the two data on the c–P plot in Fig. 4(A). It is seen that at any given indentation load the crack lengths for our IST are smaller than that for HSA (Fig. 4(A)), implying toughening of IST. The relative toughness of IST, T_{IST}/T_{HSA}, for each indentation load, which is given by $(c_{HSA}/c_{IST})^{3/2}$, is plotted in Fig. 4(B) (right axis represents absolute toughness, using the toughness value of 4.0 MPa·m$^{1/2}$ for HSA[2]). Note the almost twofold increase in the toughness of IST.

Figures 5(A) and (B) show typical crack patterns from the corner of 200-*N* indentations in HSA and IST, respectively.

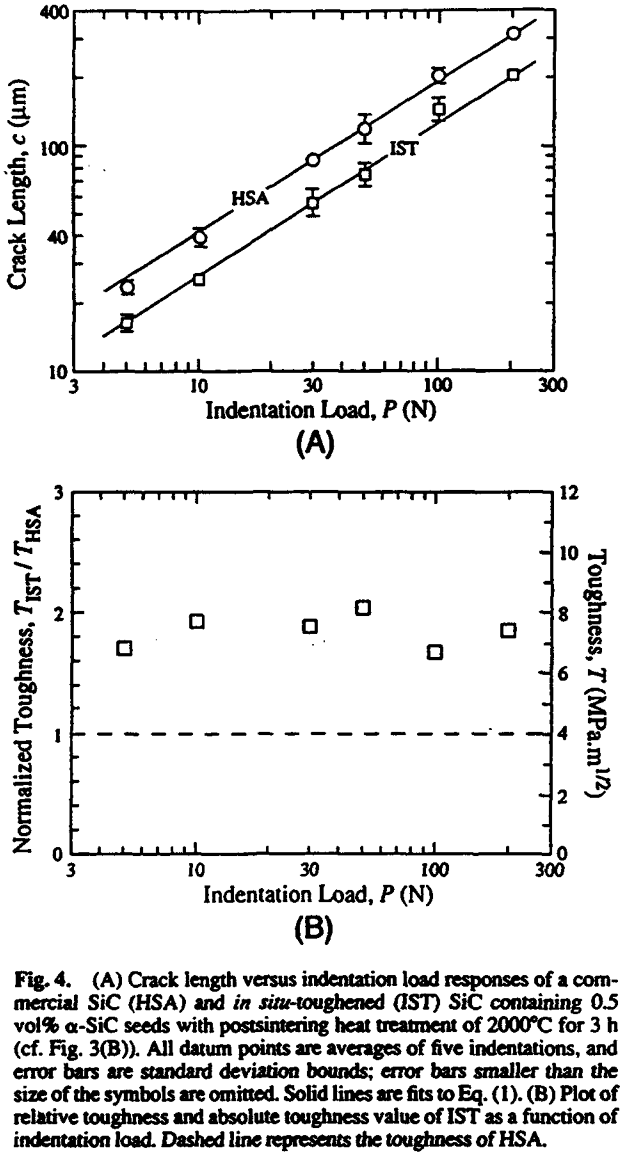

Fig. 4. (A) Crack length versus indentation load responses of a commercial SiC (HSA) and *in situ*-toughened (IST) SiC containing 0.5 vol% α-SiC seeds with postsintering heat treatment of 2000°C for 3 h (cf. Fig. 3(B)). All datum points are averages of five indentations, and error bars are standard deviation bounds; error bars smaller than the size of the symbols are omitted. Solid lines are fits to Eq. (1). (B) Plot of relative toughness and absolute toughness value of IST as a function of indentation load. Dashed line represents the toughness of HSA.

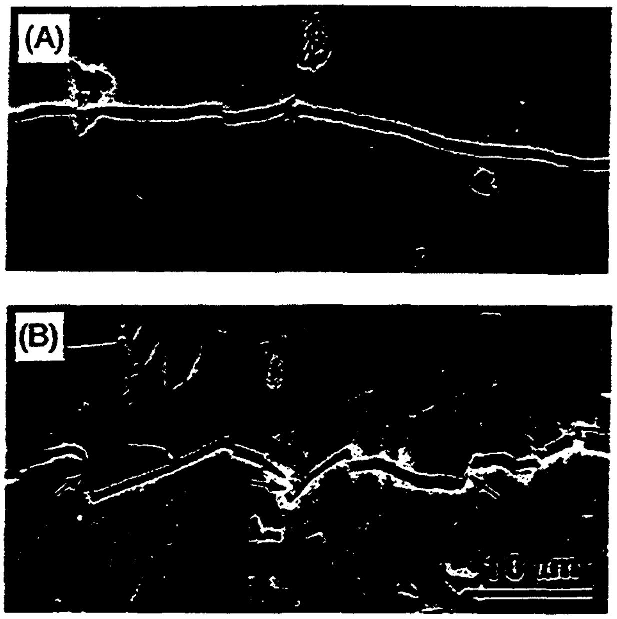

Fig. 5. SEM (secondary electron) images of cracks (running from left to right) from the corners of 200-*N* indentations in (A) HSA and (B) IST. Arrows in 5(B) indicate crack-wake bridging sites. Phase denotation same as in Fig. 2.

From Fig. 5(A) it can be seen that the crack in HSA is relatively straight, with a traction-free wake. On the other hand, in Fig. 5(B) IST shows a tortuous fracture path with several instances of crack-wake bridging by elongated SiC grains (arrows).

IV. Discussion

In this paper we have demonstrated the feasibility of a new processing technique for obtaining dense SiC-based ceramics with unique microstructures and enhanced toughness. Liquid-phase sintering of those SiC ceramics was carried out with the aid of Al_2O_3 and Y_2O_3. Based on thermodynamical calculations, the ability of Al_2O_3 and Y_2O_3 in aiding liquid-phase sintering of SiC[6-12] has been attributed to the lack of decomposition of SiC by those oxides in the temperature range 2027° to 2127°C.[24] However, the mechanism(s) of the sintering remains unclear. Recently, it has been proposed that Ostwald ripening by solution and reprecipitation controls the sintering mechanism in the SiC/YAG system.[13] In most of the aforementioned liquid-phase-sintering studies[6-10,12-14] (and solid-state-sintering studies[25]) of SiC, the starting powder used was α-SiC.[§] This is because α-SiC is the most stable form of SiC at both low and high temperatures and usually results in fine-grain equiaxed microstructures (Fig. 2(B)). The use of β-SiC as the starting powder also results in fine-grain equiaxed microstructures, provided the sintering temperature is low (1850° to 1900°C, as in the case of liquid-phase sintering). Heat treatment at higher temperatures (>1950°C) results in the β ⟶ α transformation, which is accompanied by exaggerated grain growth of elongated α-SiC grains (Fig. 2(A)). It is presumed that those exaggerated α-SiC grains grow from the preexisting α-SiC trace impurities in the otherwise pure β-SiC.

By deliberately adding a predetermined amount of α-SiC seeds, *uniformly distributed elongated grain microstructures* can be obtained (Figs. 3(A to C)). It is clear that the α-SiC seeds assist in the control of grain growth.[¶] The mechanism by which that control occurs remains to be determined. The seeding technique for microstructural control during solid-state sintering in SiC has been previously used.[27] However, the addition of α-SiC seeds to β-SiC in that study resulted in porous (80% to 85% dense) microstructures. Note that in the solid-state-sintering case, due to the high temperatures employed (2110°C), sintering and β ⟶ α transformation occur simultaneously, resulting in the formation of a rigid network of elongated α-SiC grains and preventing full densification.[27] In contrast, in the liquid-phase-sintering case, the sintering occurs first at a lower temperature (1900°C), while the β ⟶ α transformation is allowed to occur later in as-sintered specimens during subsequent high-temperature heat treatments.

From Figs. 1(A) and (B) it was seen that the density decreased during the grain growth heat treatments. It was noted that specimens heat-treated at 2000°C for 4 h revealed isolated macrosize pore channels running through them. Also, the formation of Y-, Al-, and Si-containing regions were detected (arrow in Fig. 3(C)) in those specimens. Those observations

---

[§] The crystal structure of SiC exhibits many polytypes. Most of those polytypes have a hexagonal structure and are collectively referred to as α-SiC; the cubic variation is referred to as β-SiC.

[¶] Successful use of seeding in the control of microstructural evolution in oxide ceramics has been demonstrated by Messing *et al.*[26]

suggest that prolonged exposure to high temperatures may favor reactions between SiC and YAG forming escaping gaseous species, leading to the decrease in the density (Figs. 1(A) and (B)). At this time we do not have an explanation for the dependence of density on the α-SiC seed content (Fig. 1(A)).

It is acknowledged that elongated-grain structures in SiC are not uncommon.[25,28] However, the fracture mode in those other materials is almost invariably transgranular,[28] precluding any possibility of crack-wake bridging. It is suggested that in our IST SiC the presence of a relatively high volume fraction of YAG (20 vol%) results in relatively weak interphase boundaries and high internal residual stresses, the essential ingredients for intergranular fracture, which is a prerequisite for the formation of bridges in the crack wake.[29]

The almost twofold increase in the toughness of IST relative to HSA was seen in Figs. 4(A) and (B). That increase in the toughness is attributed to the toughening mechanism of crack-wake bridging in IST SiC, which is clearly absent in HSA (Figs. 5(A) and (B)).

Ceramics with crack-wake bridging usually exhibit *R*- or *T*-curve behavior in which the toughness is a function of crack size. From Fig. 4(B), *T*-curve in IST is not apparent; the relative toughness is constant at ~2. That may be due to the limitation of the indentation toughness technique in discerning *T*-curve behavior. Recently, other tests such as indentation-strength and toughness measurement have shown *T*-curve behavior in our IST SiC, which is the subject of a separate publication.[30]

Finally, *in situ*-toughened SiC may have significant potential as a technologically important ceramic. Also, the thermal stability and creep resistance of both SiC and YAG may have significant implications on the high-temperature performance of the *in situ*-toughened SiC. Sintering, microstructure development, and fracture in this new class of toughened SiC ceramics are far from well understood, which presents an interesting scientific challenge.

Acknowledgments: *The author is greatly indebted* to Brian Lawn for his continued encouragement and support during the course of this work, and critically reading *the manuscript. Fruitful* discussions with E. R. Fuller, Jr., D. E. Niesz, and J. S. Wallace are gratefully acknowledged.

References

[1] S. Prochazka, "The Role of Boron and Carbon in the Sintering of Silicon Carbide"; pp. 171–81 in *Special Ceramics 6*. Edited by P. Popper. The British Ceramic Research Association, Stoke-on-Trent, UK, 1975.

[2] N. L. Hecht, D. E. McCullum, and G. A. Graves, "Investigation of Selected Nitride and Silicon Carbide Ceramics," *Ceram. Eng. Sci. Proc.*, 9 [9–10] 1313–32 (1988).

[3] D. E. McCullum, N. L. Hecht, L. Chuck, and S. M. Goodrich, "Summary of Results of the Effects of Environment on Mechanical Behavior of High-Performance Ceramics," *Ceram. Eng. Sci. Proc.*, 12 [9–10] 1886–913 (1991).

[4] P. Chantikul, G. R. Anstis, B. R. Lawn, and D. B. Marshall, "A Critical Evaluation of Indentation Techniques for Measuring Fracture Toughness: II. Strength Method," *J. Am. Ceram. Soc.*, 64 [9] 539–43 (1981).

[5] K. Suzuki and M. Sasaki, "Pressureless Sintering of Silicon Carbide"; pp. 75–87 in *Fundamental Structural Ceramics*. Edited by S. Somiya and R. C. Bradt. Terra Scientific Publishing Company, Tokyo, Japan, 1987.

[6] M. Omori and H. Takei, "Pressureless Sintering of SiC," *J. Am. Ceram. Soc.*, 65 [6] C-92 (1982).

[7] M. Omori and H. Takei, "Composite Silicon Carbide Sintered Shapes and Its Manufacturing," U.S. Pat. No. 4 502 983, 1985.

[8] M. Omori and H. Takei, "Method for Preparing Sintered Shapes of Silicon Carbide," U.S. Pat. No. 4 564 490, 1986.

[9] R. A. Cutler and T. B. Jackson, "Liquid Phase Sintered Silicon Carbide"; pp. 309–18 in *Ceramic Materials and Components for Engines, Proceedings of the Third International Symposium*. Edited by V. J. Tennery. The American Ceramic Society, Westerville, OH, 1989.

[10] L. Cordery, D. E. Niesz, and D. J. Shanefield, "Sintering of Silicon Carbide with Rare-Earth Oxide additions"; pp. 618–36 in *Sintering of Advanced Ceramics*, Vol. 7. Edited by C. A. Handwerker, J. E. Blendell, and W. A. Kaysser. The American Ceramic Society, Westerville, OH, 1990.

[11] M. A. Mulla and V. D. Krstic, "Low-Temperature Pressureless Sintering of β-Silicon Carbide with Aluminum Oxide and Yttrium Oxide Additions," *Am. Ceram. Soc. Bull.*, 70 [3] 439–43 (1991).

[12] D.-H. Kim, C.-W. Jang, B.-H. Park, and S.-G. Baik, "Pressureless-Sintering of Silicon Carbide with Additions of Yttria and Alumina," *J. Korean Ceram. Soc.*, 26 [2] 228–34 (1989).

[13] L. S. Sigl and H.-J. Kleebe, "Core/Rim Structure of Liquid-Phase-Sintered Silicon Carbide," *J. Am. Ceram. Soc.*, 76 [3] 773–76 (1993).

[14] K. Y. Chia and S. K. Lau, "High Toughness Silicon Carbide," *Ceram. Eng. Sci. Proc.*, 12 [9–10] 1845–61 (1991).

[15] F. Deuerler, R. Knehans, and R. W. Steinbrech, "Testing Methods and *R*-Curve Behavior of Al_2O_3," *J. Phys. (Les Ulis, Fr.)*, 47 [C1] 617–21 (1986).

[16] P. Chantikul, S. J. Bennison, and B. R. Lawn, "Role of Grain Size in the Strength and *R*-Curve Properties of Alumina," *J. Am. Ceram. Soc.*, 73 [8] 2419–27 (1990).

[17] P. F. Becher, "Microstructural Design of Toughened Ceramics," *J. Am. Ceram. Soc.*, 74 [2] 255–69 (1991).

[18] C.-W. Li and J. Yamanis, "Super-Tough Silicon Nitride with *R*-Curve Behavior," *Ceram. Eng. Sci. Proc.*, 10 [7–8] 632–45 (1989).

[19] S. J. Bennison, N. P. Padture, J. L. Runyan, and B. R. Lawn, "Flaw-Insensitive Ceramics," *Philos. Mag. Lett*, 64 [4] 191–95 (1991).

[20] N. P. Padture, "Crack Resistance and Strength Properties of Some Alumina-Based Ceramics"; Ph.D. Thesis. Lehigh University, Bethlehem, PA, 1991.

[21] E. Tani, S. Umbebayashi, K. Kishi, K. Kobayashi, and M. Nishijima, "Gas-Pressure Sintering of Si_3N_4 with Concurrent Addition of Al_2O_3 and 5 wt% Rare Earth Oxide: High Fracture Toughness Si_3N_4 with Fiber-Like Structure," *Am. Ceram. Soc. Bull.*, 65 [9] 1311–15 (1986).

[22] E. C. M. Pennings and W. Grellner, "Precise Nondestructive Determination of the Density of Porous Ceramics," *J. Am. Ceram. Soc.*, 72 [7] 1268–70 (1989).

[23] G. R. Anstis, P. Chantikul, D. B. Marshall, and B. R. Lawn, "A Critical Evaluation of Indentation Techniques for Measuring Fracture Toughness: I. Direct Crack Measurements," *J. Am. Ceram. Soc.*, 64 [9] 533–38 (1981).

[24] K. Negita, "Effective Sintering Aids for Silicon Carbide Ceramics: Reactivities of Silicon Carbide with Various Additives," *J. Am. Ceram. Soc.*, 69 [12] C-308–C-310 (1986).

[25] W. Böcker and H. Hausner, "The Influence of Boron and Carbon Additions on the Microstructure of Sintered Alpha Silicon Carbide," *Powder Metall. Int.*, 10 [2] 87–89 (1978).

[26] G. L. Messing, M. Kumagai, R. A. Shellman, and J. L. McArdle, "Seeded Transformations for Microstructural Control in Ceramics"; pp. 259–71 in *The Science of Ceramic Chemical Processing*. Edited by L. L. Hench and D. R. Ulrich. Wiley, New York, 1986.

[27] C. A. Johnson and S. Prochazka, "Microstructure of Sintered SiC"; pp. 366–78 in *Ceramic Microstructures '76*. Edited by R. M. Fulrath and J. A. Pask. Westview Press, Boulder, CO, 1977.

[28] S. Prochazka and R. J. Charles, "Strength and Microstructure of Dense Hot-Pressed Silicon Carbide"; pp. 579–98 in *Fracture Mechanics of Ceramics*, Vol. 2. Edited by R. C. Bradt, D. P. H. Hasselman, and F. F. Lange. Plenum Press, New York, 1974.

[29] B. R. Lawn, *Fracture of Brittle Solids—Second Edition*. Cambridge University Press, Cambridge, U.K., 1993.

[30] N. P. Padture and B. R. Lawn, "Short-Crack Properties of *in Situ* Silicon Carbide with Heterogeneous Microstructure," *J. Am. Ceram. Soc.*, in press. □

Reprint Series
25 February 1994, Volume 263, pp. 1114–1116

SCIENCE

Making Ceramics "Ductile"

Brian R. Lawn,* Nitin P. Padture,† Hongda Cai,† and Fernando Guiberteau‡

Making Ceramics "Ductile"

Brian R. Lawn,* Nitin P. Padture,† Hongda Cai,†
Fernando Guiberteau‡

Distributed irreversible deformation in otherwise brittle ceramics (specifically, in silicon carbide and micaceous glass-ceramic) has been observed in Hertzian contacts. The deformation takes the form of an expanding microcrack damage zone below the contact circle, in place of the usual single propagating macrocrack (the Hertzian "cone fracture") outside. An important manifestation of this deformation is an effective "ductility" in the indentation stress-strain response. Control of the associated brittle-ductile transition is readily effected by appropriate design of weak interfaces, large and elongate grains, and high internal stresses in the ceramic microstructure.

Ceramics have been cited as the "materials of the future." However, ceramics are also notoriously brittle and are subject to catastrophic failure from the growth of a single dominant crack (*1*). They are limited in their use as load-bearing materials by a low intrinsic toughness and, correspondingly, a lack of ductility to absorb mechanical energy. Of the various mechanisms that have been advocated for imparting toughness to ceramics (*1*), the most widespread and practical is that of "bridging," in which frictional pullout of interlocking grains and second-phase particles retards crack-wall separation (*2, 3*). Toughness then becomes a rising function of crack size [so-called toughness-curve, or resistance-curve, behavior (*1*)]. A most important element in the enhancement of bridging is the controlled introduction of weak interfaces on the microstructural scale, to deflect the primary crack and thereby generate a more effective interlocking structure. One can also enhance bridging by coarsening and elongating the grain structure and by incorporating internal mismatch stresses (*1, 4, 5*). Thus to gain toughness in ceramics, one builds in microstructural heterogeneity. However, there is a price to pay. Toughness is improved, but only in the "long-crack" region. In the "short-crack" region, built-in weakness can enhance fracture at the microstructural level, reducing laboratory strength (*6*) and increasing the susceptibility to wear and erosion (*7, 8*).

In view of this tendency toward countervailing interrelations in toughness properties, surprisingly little effort has been made to understand the seemingly deleterious short-crack properties of heterogeneous ceramics. We argue that these same seemingly deleterious properties also have potential benefits. The impetus for this assertion comes from our recent contact study on a moderately tough, coarse-grain alumina (*9*). Our test uses the classical Hertzian configuration of an indenting sphere on a flat specimen surface (*10*). A rich literature exists for Hertzian tests on homogeneous brittle solids, notably glass, in which a cone-shaped crack (the Hertzian fracture) forms in a region of weak surface tensile stress outside the contact circle (*11–16*). No such literature exists for analogous tests on heterogeneous tough ceramics. In our study on coarse alumina, we found no well-defined cone crack but rather a damage zone of distributed intergranular microfractures in a region of high shear stress below the contact circle. Stress-induced intragrain twins appeared to act as essential crack precursors in the alumina by concentrating stresses at the weak grain boundaries. The subsurface microfracture damage zone expanded with repeat loading, indicating a pronounced "fatigue" characteristic.

We have performed Hertzian tests on ceramic systems whose microstructural heterogeneity was tailored by heat treatments. In their base homogeneous forms, these ceramics are classically brittle and exhibit the familiar cone fractures. In their heterogeneous forms, however, these same ceramics are subject instead to subsurface microfracture, leading to an effective "ductile" response in the contact behavior. The results have profound implications concerning the capacity of brittle solids to sustain mechanical damage and absorb energy. Most important, the results suggest ways in which such radical "brittle-ductile transitions" in the mechanical response of ceramics may be effected by controlled microstructural modifications.

In our Hertzian test, a hard sphere of radius r was loaded onto a flat specimen surface. From the load P and contact radius a, we plot indentation stress $p_0 = P/\pi a^2$ versus indentation strain a/r (*17*) to produce an indentation stress-strain curve. A special specimen configuration, consisting

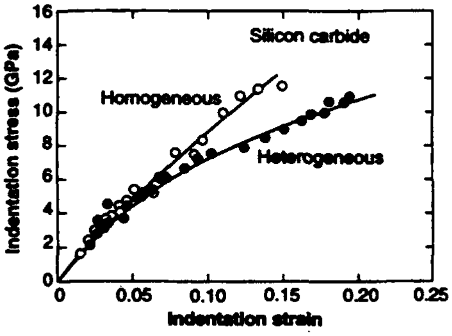

Fig. 1. Indentation stress-strain curve for silicon carbide in homogeneous fine-grain and heterogeneous coarse-grain forms. Data taken with tungsten carbide spheres in the radius range r from 1.58 to 12.7 mm.

Materials Science and Engineering Laboratory, National Institute of Standards and Technology, Gaithersburg, MD 20899, USA.

*To whom correspondence should be addressed.

†Guest scientist from the Department of Materials Science and Engineering, Lehigh University, Bethlehem, PA 18015, USA.

‡Guest scientist from the Departamento de Física, Universidad de Extremadura, 06071—Badajoz, Spain.

of two polished rectangular half-blocks bonded together with thin adhesive, allowed us to obtain section as well as surface views of the contact damage (*18*). Indentations were placed symmetrically across the surface trace of the bonded interface on the top surface. After indentation, the adhesive was dissolved and the half-blocks separated to reveal the subsurface damage. The top and side surfaces of a given half-block were then coated with gold and viewed in Nomarski illumination.

In our first example, we compared two forms of silicon carbide, a ceramic traditionally known for its innate hardness and brittleness. The first form, a commercially available monophase material (*19*), had a fine, equiaxed, well-bonded microstructure (grain size ≈ 4 μm). The second form, a material we developed by incorporating an yttrium-aluminum-garnet (YAG) sintering agent and subjecting the sintered material to a grain-growth heat treatment (*20*), had a coarsened, elongated microstructure (grains ~3 μm thick and 25 μm long) with weakened interfaces between matrix grains and boundary phases. The microstructural conditions in the second form were conducive to enhanced grain bridging and therefore to enhanced long-crack toughness.

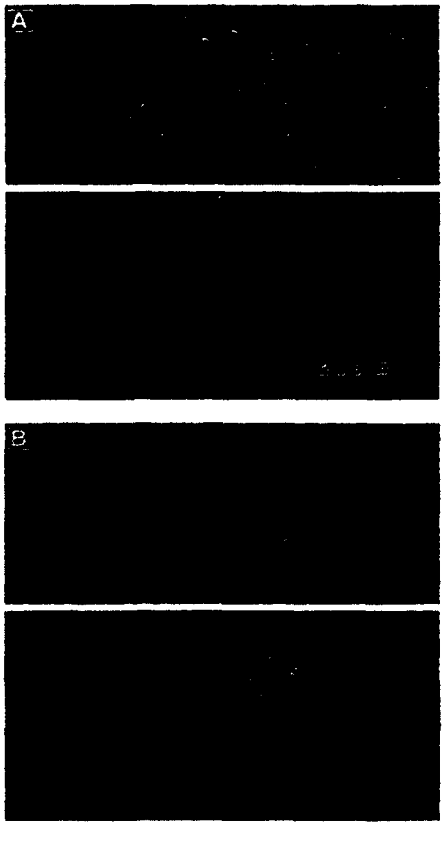

Fig. 2. Half-surface (top) and section (bottom) views of Hertzian contact damage in silicon carbide, from a tungsten carbide sphere of radius r = 3.18 mm at load P = 2000 N. (**A**) Homogeneous fine-grain form showing well-defined cone crack (stress p_0 = 7.44 GPa); (**B**) heterogeneous coarse-grain form showing distributed subsurface damage (stress p_0 = 7.20 GPa).

The indentation stress-strain curve for the homogeneous form (Fig. 1, open circles) shows little nonlinearity, indicating essentially elastic-brittle behavior. By contrast, the curve for the heterogeneous form (Fig. 1, filled circles) tends toward a "yield" response, more characteristic of ductile solids. In micrographs of the contact damage, we observe a transition from well-defined cone fracture (Fig. 2A) to distributed subsurface microfracture (Fig. 2B) with the increase in microstructural heterogeneity. Higher magnification reveals a relatively uninterrupted (transgranular) crack path in Fig. 2A and locally deflected (intergranular) microfractures along the weak interphase boundaries in Fig. 2B.

An even more striking illustration of the effect of microstructural heterogeneity on the intrinsic mechanical response is afforded by a micaceous glass-ceramic (*21*). This ceramic has a respectable long-crack toughness (*22*). It conversely has a low short-crack toughness, a notable consequence of which is that the material is readily machinable (*23*). In its base glass state, the material is effectively homogeneous on the microscale. A controlled heat treatment crystallizes mica flakes (~1 μm thick and 10 μm long) in the glass matrix, with weak interphase boundaries, to produce the glass-ceramic. Whereas the indentation stress-strain curve for the base glass shows little nonlinearity, the curve for the crystallized glass-ceramic shows a dramatic yield turnover (Fig. 3). Half-surface and section micrographs of the contact damage in the base glass (Fig. 4A) reveal classical Hertzian cone fracture. In the glass-ceramic (Fig. 4B), the damage is contained wholly subsurface and has the macroscopic appearance of a plastic zone in metals (*18*). Higher magnification of the areas within the subsurface damage zones revealed local shear fractures along the mica-glass interfaces, with some linkage and coalescence in the glass matrix at heavier loads.

The distinctive change from classical cone fracture to distributed microfracture damage with increased microstructural heterogeneity (Figs. 2 and 4) denotes a new kind of brittle-ductile transition in ceramic materials. This transition is apparent as an increased nonlinearity and a correspondingly greater work of penetration in the indentation stress-strain functions (Figs. 1 and 3). It foreshadows a greater resistance to strength degradation and an enhanced capacity for energy absorption from spurious contacts and impacts.

Microscopically, the subsurface damage responsible for the ductility originates from some local shear-driven deformation process. The nature of this process is fundamentally different from the dislocation processes that operate in metals (*17*). Instead, the deformation originates at "shear faults" in the grain microstructure. The key is the presence of intrinsically weak interfaces to create and arrest the faults, and perhaps

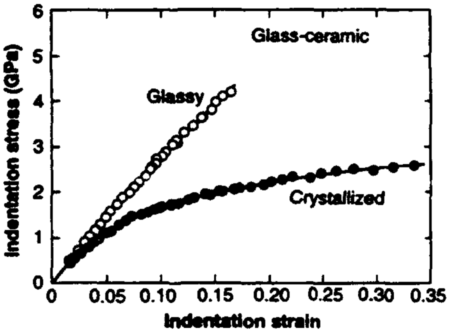

Fig. 3. Indentation stress-strain curve for glass-ceramic in base glass and crystallized forms. Data taken with tungsten carbide spheres in the radius range r from 0.79 to 12.7 mm.

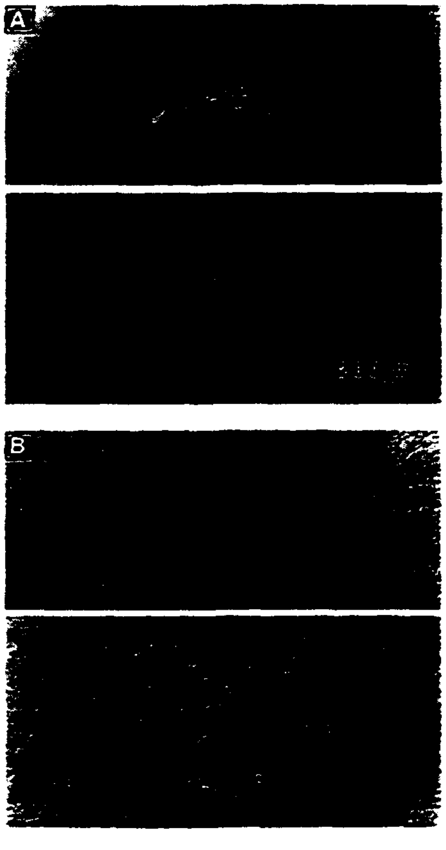

Fig. 4. Half-surface (top) and section (bottom) views of Hertzian contact damage in glass-ceramic, from a tungsten carbide sphere of radius r = 3.18 mm at load P = 1000 N. (**A**) Base glass form showing well-defined cone crack (stress p_0 = 2.88 GPa); (**B**) partially crystallized form showing distributed subsurface damage (stress p_0 = 1.87 GPa).

also to provide favored paths for ensuing extensile microcracks at the fault edges, within the subsurface Hertzian stress field. In the silicon carbide (Fig. 2), the shear faults form at the interfaces between the matrix grains and the grain boundary (YAG) phases. In the glass-ceramic (Fig. 4), they form at the mica-glass interface. This transition to apparent ductility in otherwise highly brittle ceramics is attributable to the large compressive component of contact stress fields (*13*, *16*). The deflection of any downward propagating surface ring cracks along grain or interface boundaries away from the tensile stress trajectories (*13*) suppresses the development of a single cone crack, and at the same time, the action of strong shear stresses on the weak planes in the confining subsurface zone promotes the development of a population of highly stabilized microcracks. The latter kind of distributed damage has been widely considered in the fracture of rocks (*24*), where hydrostatic compressive fields are the norm, but not in advanced ceramics, whose design has hitherto been based predominantly on single-crack mechanics.

Our results are of special relevance to the mechanical response of ceramics where highly localized mechanical or thermal stresses are likely (*10*), such as in bearings, local impact conditions, refractories, and medical implants (for example, tooth restoratives). The implication is that one may design ceramic microstructures to change the very nature of the damage behavior and so optimize the mechanical response to suit particular applications.

REFERENCES AND NOTES

1. B. R. Lawn, *Fracture of Brittle Solids* (Cambridge Univ. Press, Cambridge, ed. 2, 1993).
2. P. L. Swanson, C. J. Fairbanks, B. R. Lawn, Y.-W. Mai, B. J. Hockey, *J. Am. Ceram. Soc.* 70, 279 (1987).
3. P. L. Swanson, in *Fractography of Glasses and Ceramics*, V. Frechette and J. Varner, Eds., vol. 22 of *Advances in Ceramics* (American Ceramic Society, Columbus, OH, 1988), pp. 135–55.
4. B. R. Lawn, N. P. Padture, L. M. Braun, S. J. Bennison, *J. Am. Ceram. Soc.* 76, 2235 (1993).
5. N. P. Padture, J. L. Runyan, S. J. Bennison, L. M. Braun, B. R. Lawn, *ibid.*, p. 2241.
6. P. Chantikul, S. J. Bennison, B. R. Lawn, *ibid.* 73, 2419 (1990).
7. S.-J. Cho, B. J. Hockey, B. R. Lawn, S. J. Bennison, *ibid.* 72, 1249 (1989).
8. S.-J. Cho, H. Moon, B. J. Hockey, S. M. Hsu, *Acta Metall.* 40, 185 (1992).
9. F. Guiberteau, N. P. Padture, H. Cai, B. R. Lawn, *Philos. Mag. A* 68, 1003 (1993).
10. K. L. Johnson, *Contact Mechanics* (Cambridge Univ. Press, London, 1985).
11. H. Hertz, *Hertz's Miscellaneous Papers* (Macmillan, London, 1896), chaps. 5 and 6.
12. F. C. Roesler, *Proc. Phys. Soc. London Sect. B* 69, 981 (1956).
13. F. C. Frank and B. R. Lawn, *Proc. R. Soc. London Ser. A* 299, 291 (1967).
14. F. B. Langitan and B. R. Lawn, *J. Appl. Phys.* 40, 4009 (1969).
15. T. R. Wilshaw, *J. Phys. D* 4, 1567 (1971).
16. B. R. Lawn and T. R. Wilshaw, *J. Mater. Sci.* 10, 1049 (1975).
17. D. Tabor, *Hardness of Metals* (Clarendon, Oxford, United Kingdom, 1951).
18. T. O. Mulhearn, *J. Mech. Phys. Solids* 7, 85 (1959).
19. Hexoloy SA, Carborundum, Niagara Falls, NY.
20. N. P. Padture, *J. Am. Ceram. Soc.* 77, 519 (1994).
21. Macor, Corning, Inc., Corning, NY.
22. C. J. Fairbanks, B. R. Lawn, R. F. Cook, Y.-W. Mai, *Microstructure and the Strength of Ceramics*, vol. 8 of *Fracture Mechanics of Ceramics*, R. C. Bradt, A. G. Evans, D. P. H. Hasselman, F. F. Langes, Eds. (Plenum, New York, 1986), pp. 23–37.
23. K. Chyung, G. H. Beall, D. G. Grossman, in *Proceedings of 10th International Glass Congress*, M. Kunugi, M. Tashiro, N. Saga, Eds. (Ceramic Society of Japan, Tokyo, Japan, 1974), pp. 33–40.
24. J. C. Jaeger and N. G. W. Cook, *Fundamentals of Rock Mechanics* (Chapman & Hall, London, 1971).

25. Funding provided by the U.S. Air Force Office of Scientific Research. Financial support for F.G. from the Ministerio de Educación y Ciencia (DGICYT), Spain, is gratefully acknowledged.

19 November 1993; accepted 12 January 1994

Deformation and fracture of mica-containing glass-ceramics in Hertzian contacts

Hongda Cai,[a] Marion A. Stevens Kalceff,[b] and Brian R. Lawn
Materials Science and Engineering Laboratory, National Institute of Standards and Technology, Gaithersburg, Maryland 20899-0001

(Received 2 August 1993; accepted 29 October 1993)

The Hertzian indentation response of a machinable mica-containing glass-ceramic is studied. Relative to the highly brittle base glass from which it is formed, the glass-ceramic shows evidence of considerable "ductility" in its indentation stress-strain response. Section views through the indentation sites reveal a transition from classical cone fracture outside the contact area in the base glass to accumulated subsurface deformation-microfracture in the glass-ceramic. The deformation is attributed to shear-driven sliding at the weak interfaces between the mica flakes and glass matrix. Extensile microcracks initiate at the shear-fault interfaces and propagate into the matrix, ultimately coalescing with neighbors at adjacent mica flakes to effect easy material removal. The faults are subject to strong compressive stresses in the Hertzian field, suggesting that frictional tractions are an important element in the micromechanics. Bend-test measurements on indented specimens show that the glass-ceramic, although weaker than its base glass counterpart, has superior resistance to strength degradation at high contact loads. Implications of the results in relation to microstructural design of glass-ceramics for optimal toughness, strength, and wear and fatigue properties are discussed.

I. INTRODUCTION

Hertzian indentation of homogeneous brittle materials, such as glasses and single crystals, has received extensive attention in the literature.[1–20] Above a critical load, a ring crack initiates in the weakly tensile region just outside the circle of contact with the indenting sphere, propagates downward as a surface-truncated cone, and finally arrests at a depth approximately equal to the contact radius.[6,15] This is the so-called Hertzian cone crack.[21] Hertzian fracture is of interest to materials scientists for its uncommon insight into the stability of strength-degrading flaws[6,20] and for its intrinsic relation to material toughness.[6,15]

Few Hertzian indentation studies have been made of the newer generation of tougher polycrystalline and two-phase ceramics, where microstructure plays a critical role in the fracture behavior. Some cone fracture observations have previously been reported on low-toughness fine-grain monophase ceramics[15,22] and brittle lithium-silicate glass-ceramics.[23,24] Higher long-crack fracture toughness occurs in those ceramics with larger grains and greater internal mismatch stresses[25,26] and is attributable most commonly to crack-interface "bridging" from interlocking grains or particles.[20,27–31] Recently, examination of Hertzian indentations in a coarse-grain polycrystalline alumina[32] has revealed a radical departure from the classical fracture pattern; the cone crack is suppressed in favor of distributed damage in a zone of high compression-shear beneath the contact circle, more reminiscent of deformable solids. The subsurface damage takes the form of deformation-microfracture by precursor intragrain twin/slip and subsequent grain-localized intergranular microfracture. Repeat loading exacerbates the extent of the subsurface damage, leading to microcrack coalescence and ultimately surface removal.[32] The transition from cone fracture to accumulated damage zone occurs above a threshold grain size, indicating a microstructural scaling effect.[33] Thus, the same microstructural elements responsible for the enhanced toughness properties change the entire nature of the fracture damage process.

One class of ceramics that has received considerable attention for use as model two-phase systems as well as in practical applications is glass-ceramics.[34] A system of particular interest is that of a glass matrix containing crystallized mica platelets, the size and density of which may be readily controlled by simple heat treatments.[35–37] Mica-containing glass-ceramics are best known for their easy machinability,[37–39] an attractive quality for forming operations used in dental restorations[40] and other applications. Yet these same glass-ceramics have

---

[a] Guest Scientist on leave from Department of Materials Science and Engineering, Lehigh University, Bethlehem, Pennsylvania 18015.

[b] Guest Scientist on leave from Department of Applied Physics, University of Technology, Sydney, New South Wales 2007, Australia.

respectable long-crack toughness.[37,39,41] Such countervailing responses in the short-crack and long-crack regions raise questions as to the role of the mica-matrix microstructure in the micromechanisms of deformation and fracture.

In this paper we study the Hertzian indentation response of one mica-containing machinable glass-ceramic, "Macor", using comparison tests on the precursor "green" glass to establish a baseline brittle state. We will show that in the Macor, as in coarse-grain alumina, well-defined cone fracture is supplanted by accumulated subsurface deformation-microfracture damage. This transition is quantified on an indentation stress-strain curve. The deformation takes the form of shear faulting along weak mica-glass interfaces. Microcracks extend from the ends of these faults into the glass matrix, and ultimately coalesce with their neighbors to effect material fragmentation and removal. The shape of the macroscopic damage zone is discussed in relation to the distribution of shear stresses beneath the contact area, with due allowance for sliding friction tractions at the compressively closed faults. Strength degradation associated with the damage is measured as a function of indentation load for both the crystallized and green Macor, and is discussed in terms of the relative toughness properties.

II. EXPERIMENTAL

The material used in this study was a commercial mica-containing glass-ceramic, produced under the trade name Macor (Corning Inc., Corning, NY). Macor composition in weight % is 46% SiO_2, 14% MgO, 16% Al_2O_3, 10% K_2O, 8% B_2O_3, and 6% F). In its final heat-treated form, Macor exists in a partially crystallized state, with composition ≈55% fluorophlogopite mica and ≈45% borosilicate glass. Specifically, the microstructure consists of a network of randomly oriented interlocking mica flakes.[35–38] The individual flakes are approximately 10 μm in surface dimension parallel to the cleavage basal plane, and 1 to 2 μm thick normal to this plane. Simplistically, the network of closely packed planes of weakness, i.e., mica basal cleavage and mica-glass interfaces, facilitates easy fracture in the short-crack domain, thereby accounting for the machinability.[35] At the same time, once a crack develops over a scale large relative to the microstructure the mica flakes act as effective bridges across the separation plane, giving rise to a progressively rising toughness curve and enhancing the long-crack toughness.[41]

The "green" glass from which the final crystallized form of Macor is derived was used as a reference material for baseline comparison. This base glass has an opalescent white color, due to the presence of submicrometer-scale fluorine-rich droplets from liquid phase separation during the original glass-forming process.[35] The droplets comprise nucleation centers for the ultimate formation of mica phases in the crystallization heat treatments.[35–37]

Plate specimens 25 mm square and 4 mm thick were cut from billets of mica-containing Macor and base glass. Surfaces for indentation stress-strain testing were polished with diamond paste to 1 μm finish, and then coated with gold. Indentations were made using tungsten carbide spheres of radii $r = 0.79$, 1.19, 1.98, 3.18, 4.76, 7.94, and 12.70 mm, over a load range $P = 0$ to 2000 N using a universal testing machine (Instron Model 1122, Instron Corp., Canton, MA). Residual traces in the gold layer enabled determinations of contact radius a at each applied load,[32] and thence contact pressure ($p_0 = P/\pi a^2$) as a function of indentation strain (a/r) (see Sec. III).

For detailed microscopic investigation of the subsurface damage, a special bonded-interface specimen configuration was employed,[33] following a procedure first described by Mulhearn.[42] In this configuration, shown in Fig. 1, two half-specimens with polished surfaces were clamped together with a thin layer (≈1 μm) of a cyanoacrylate-based adhesive (SuperBonder, Locite Corp., Newington, CT) to form a bonded interface. The

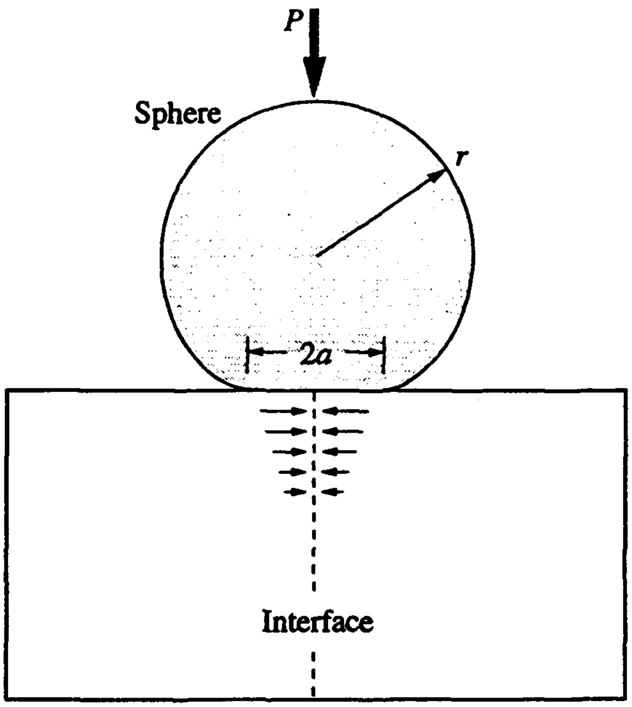

FIG. 1. Hertzian test geometry for bonded-interface specimen. Sphere, radius r, delivers load P over contact radius a. Specimen consists of two polished halves bonded across the interface. Compressive stresses beneath contact (arrows) and from external clamping (not shown) maintain contact between specimen halves during indentation.

ultimate indentation test surface was then ground and polished perpendicular to the bonded interface. A sequence of indentations was subsequently made along the interface trace at the test surface, taking special care to keep the contacts centered across this trace. It was found beneficial to apply a clamping stress normal to the interface during indentation to minimize intersurface separation. After indentation, the interface specimens were soaked in acetone to dissolve the adhesive and to separate the specimens into their two halves. After cleaning the surfaces, reflection optical microscopy in Nomarski interference contrast was used to examine the subsurface deformation and fracture patterns in section view.

Some Vickers indentations were made to measure the hardness of the base glass and the mica-containing glass-ceramic.

Bars 48 × 6 × 4 mm were machined for measurement of strength degradation from Hertzian contact damage. The prospective test faces and sides of these bars were polished to 3 μm finish. All specimens were chamfered at their edges and acid-etched in 2% HF solution for 15 min to minimize edge failures in the ensuing strength tests. The strength tests themselves were conducted in four-point bending. An indentation was made at the center of each polished surface at a specified contact load, using a sphere of radius 3.18 mm at a loading/unloading rate 100 $\mathrm{N \cdot s^{-1}}$. At low loads in the base glass, multiple indentations were made in order to ensure the most favorable conditions for cone fracture. Some specimens were left unindented to measure "natural" strengths.[43] A drop of silicone oil was placed on the indentation sites prior to flexure, and the tests conducted in rapid loading (<50 ms failure time) to minimize effects of slow crack growth from environmental moisture. Broken specimens were examined to ensure that the fracture originated from the indentation sites. Those that did not were included in the data pool for unindented specimens because fracture originated from "natural" flaws in those specimens.

III. RESULTS

A. Indentation stress-strain curves

Indentation stress-strain data for the Macor mica-containing glass ceramic and the base glass are shown in Fig. 2. The responses were obtained by monitoring mean contact pressure

$$p_0 = P/\pi a^2 \tag{1}$$

as a function of the geometrical ratio a/r, with P the indentation load, a the radius of contact, and r the sphere radius. The data for each material fall on a universal curve, independent of r, consistent with the principle of geometrical similarity.[10,16,44] In the low-strain elastic region prior to irreversible deformation, the data lie close to the inclined dashed lines representing the classical Hertzian relation[20,45]:

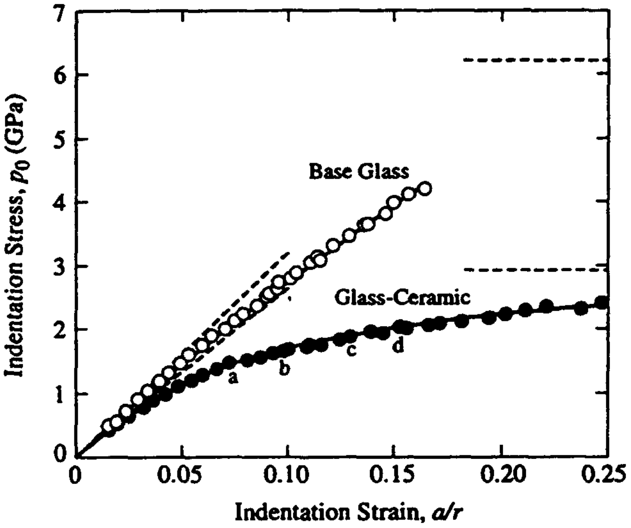

FIG. 2. Indentation stress-strain curves for Macor mica-containing glass-ceramic and base glass, using WC spheres of radii $r = 0.79$, 1.19, 1.98, 3.18, 4.76, 7.94, and 12.70 mm (not distinguished on data points). Solid curves are empirical fits to the data. Inclined dashed lines are Hertzian elastic responses computed from Eq. (2) using Young's modulus from independent ultrasonic measurement and Poisson's ratio from manufacturer's specifications as follows: $E_S = 614$ GPa and $\nu_S = 0.22$ for WC spheres; $E = 77$ GPa and $\nu = 0.29$ for base glass (upper dashed line); and $E = 63$ GPa and $\nu = 0.29$ for Macor (lower dashed line). Horizontal dashed lines indicate Vickers hardness for base glass (upper) and Macor (lower). Points a, b, c, and d on Macor curve correspond to pressures used later in sequence in Fig. 4.

$$p_0 = (3E/4\pi k)(a/r), \tag{2}$$

where E is Young's modulus of the specimen material; $k = (9/16)[(1 - \nu^2) + (1 - \nu_S^2)(E/E_s)]$ is a dimensionless constant of each indenter/specimen combination, with ν Poisson's ratio and subscript S designating the sphere material. Young's moduli used in our evaluations of Eq. (2) were determined from independent ultrasonic measurements on the Macor and base glass, and are included in the caption to Fig. 2. In the high-strain region the data approach the hardness values from the Vickers tests.

We note the clear distinction in stress-strain response between the crystallized Macor and precursor base glass. The base glass behaves in an ideal brittle manner, with near-linear response over the data range. By contrast, the mica-containing Macor deviates dramatically from the linear response at a relatively low indentation stress. It is evident that crystallization of the mica phase has conferred a degree of "plasticity" to the glass-ceramic, more like a ductile metal than a brittle ceramic.

B. Microscopic observations of subsurface damage

Half-surface and side views of Hertzian indentations in the base glass are shown in Fig. 3. Classical concentric cone cracks[4,6,15,46,47] are observed. The contact radius at maximum pressure lies just within the outermost surface ring in Fig. 3, confirming that the cone fractures form in the region of weak tension outside the subsurface compression-shear zone.[15] Note that there is no detectable deformation beneath the contact circle; essentially, the material behaves as an ideally homogeneous solid.

Analogous half-surface and side views for the mica-containing glass-ceramic are shown in Fig. 4, as a sequence of increasing indentation pressures. In these micrographs the mica flakes in the glass matrix are readily observable in the Nomarski illumination. Cone fracture outside the contact area is now inactive. Instead, the indentation takes on the appearance of a "plastic" impression, reminiscent of the subsurface plasticity zone beneath contacts in ductile metals.[42] The evolution of the damage is most clearly revealed in the section views. In Fig. 4(a), the damage starts subsurface and gradually progresses in Figs. 4(b) and 4(c) to the surface until, in Fig. 4(d), the "plastic zone" is fully developed. Note that there is a near-surface region immediately below the contact area where damage appears to be suppressed, even in the more advanced stages of impression in Figs. 4(c) and 4(d).

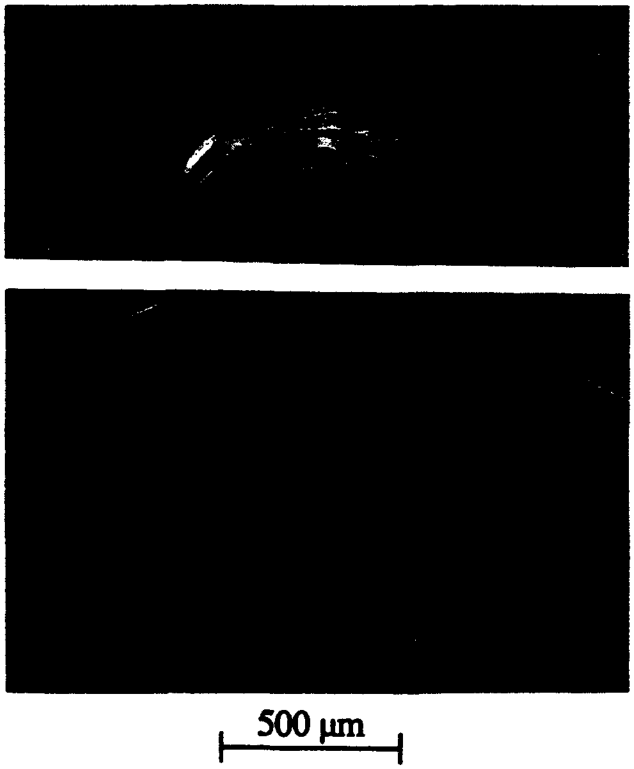

FIG. 3. Optical micrographs of indented base glass, showing half-surface (top) and section (bottom) views of Hertzian cone fracture in bonded-interface specimen, WC sphere radius $r = 3.18$ mm at contact pressure $p_0 = 2.88$ GPa, corresponding to contact radius $a = 330$ μm at load $P = 1000$ N. Viewed in Nomarski interference illumination.

Higher magnification views of the subsurface damage zones in Fig. 5 reveal interrelations between the damage process and the mica plate structure more clearly. The micrograph in Fig. 5(a) is from a region of relatively low damage, point A in Fig. 4(c). Discrete microcracks appear along the interfaces between glass matrix and mica plates. The micrograph in Fig. 5(b) is from a region of higher damage, point B in Fig. 4(d). It shows microcracks extending from individual mica plates into the glass matrix and linking up with neighbors to form coalesced fracture arrays. No microcracking was observed outside the damage zone.

C. Strength degradation

Results from the Hertzian-indentation/inert-strength tests for the Macor mica-containing glass ceramic and the base glass are plotted in Fig. 6. In this diagram the error bars are standard deviations for an average of 4 specimens per data point. The hatched boxes at left indicate strengths of specimens that broke away from indentation sites. Solid curves are empirical fits to the data.[18]

The curves in Fig. 6 show some interesting contrasts, not least the fact that they cross each other. For the Macor glass-ceramic, the strength shows a steady decline with load above the cutoff strength level for failures from natural flaws. This response is characteristic of materials with a low damage threshold but moderate toughness. For the base glass, the strength maintains its high value for natural surfaces up to the critical indentation load for cone fracture, above which it drops precipitously and thereafter declines with increasing load. This response is characteristic of materials with a high damage threshold but low toughness. Thus, although the Macor in its crystallized form may appear to have inferior laboratory strength relative to its base glass counterpart, its ultimate resistance to strength loss from sustained damage is markedly superior, except perhaps at extreme high loads.

IV. DISCUSSION

We have demonstrated that Macor, a mica-containing machinable glass-ceramic, undergoes extensive irreversible damage under Hertzian indentations. The nature of the damage is radically different from the classical cone fracture that forms outside the contact circle in brittle glasses and single crystals. Macroscopically, the damage pattern resembles the form of the continuous plastic zones that form in the subsurface slip-line fields beneath indentations in ductile metals.[42] One may

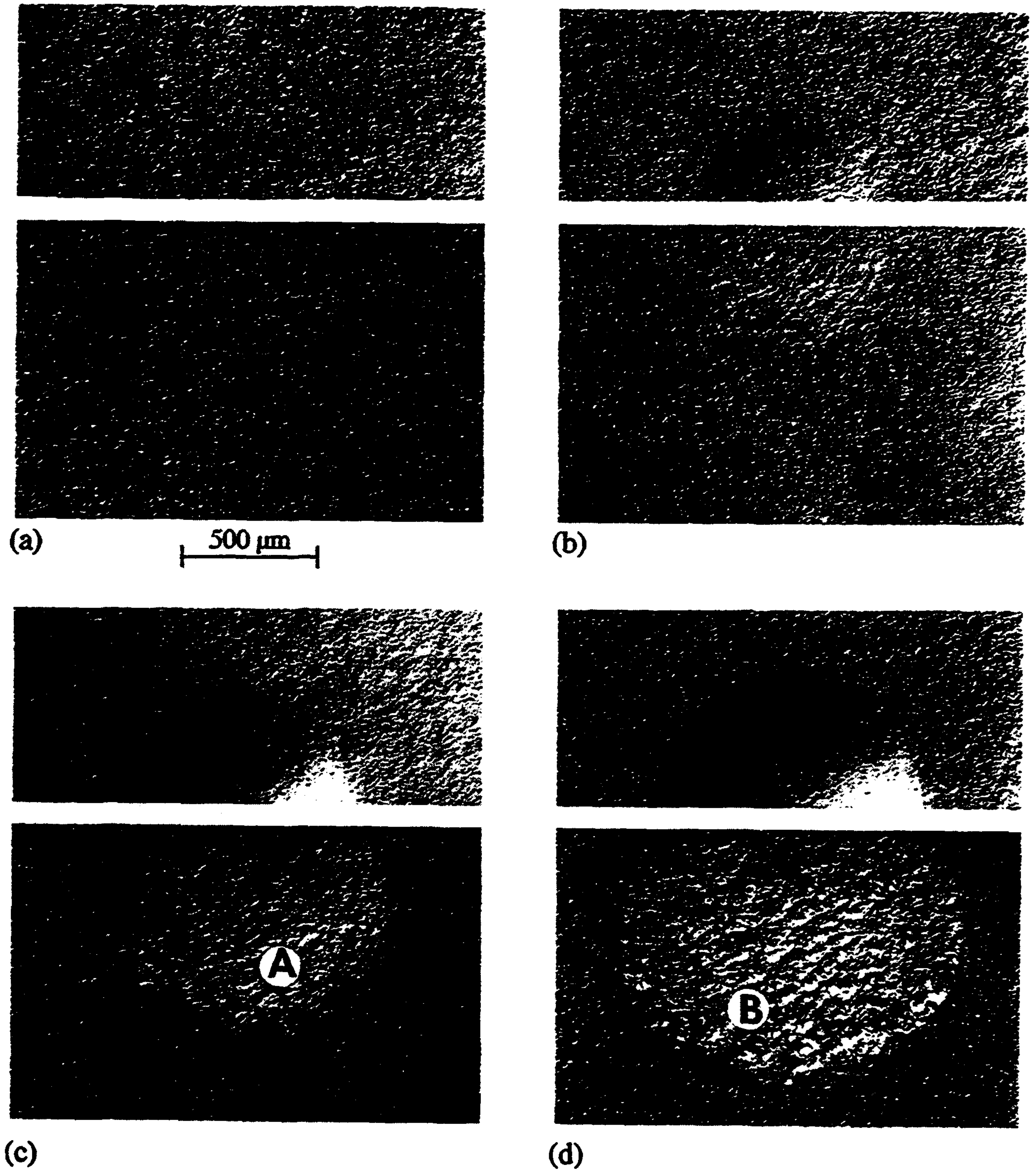

FIG. 4. Optical micrographs of indented Macor glass-ceramic, showing half-surface (top) and section (bottom) views of subsurface deformation-microfracture damage evolution in bonded-interface specimens, at indentation stress (a) $p_0 = 1.46$ GPa, (b) 1.63 GPa, (c) 1.87 GPa, and (d) 2.02 GPa. The corresponding indentation loads are $P = 250$, 500, 1000, and 1500 N. WC sphere radius $r = 3.18$ mm. Viewed in Nomarski interference illumination. Locations A in (c) and B in (d) expanded in Fig. 5.

accordingly regard the observed change in indentation response in the glass-ceramic as akin to a brittle-ductile transition, although the deformation micromechanism differs fundamentally from the traditional dislocation flow process. Microscopically, the damage bears a strong resemblance to the discrete microslip-microfracture

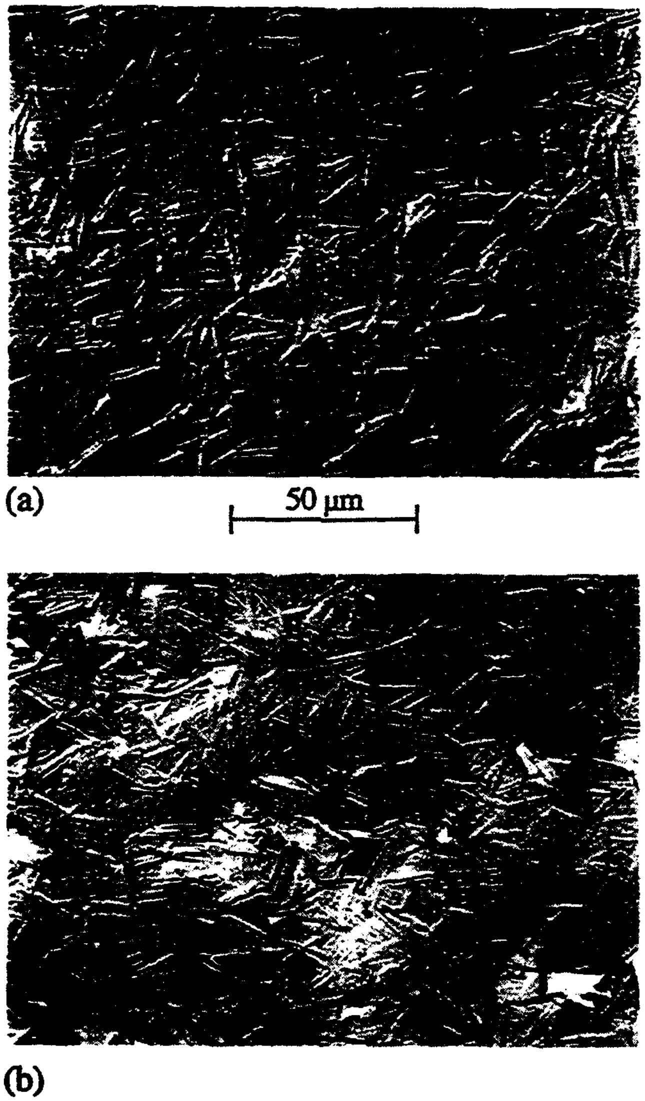

FIG. 5. Enlarged optical micrographs showing subsurface damage in Macor glass-ceramic showing microcracks: (a) individual microcracks at mica-glass interfaces in low damage area [location A in Fig. 4(c)]; and (b) coalesced microcracks in high damage area [location B in Fig. 4(d)]. Viewed in Nomarski interference illumination.

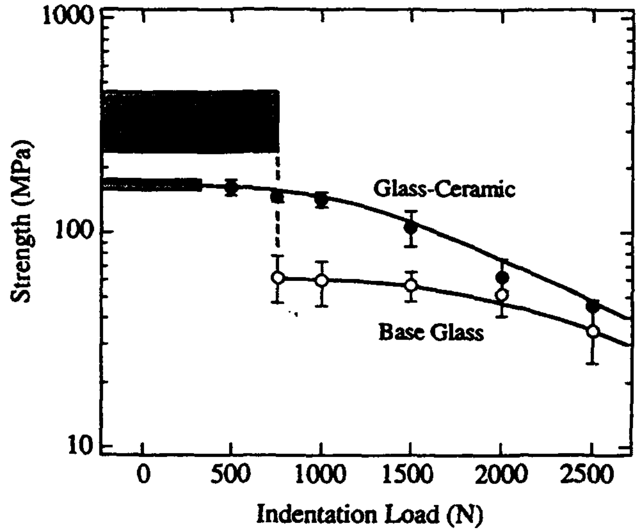

FIG. 6. Inert strength of Macor mica-containing glass-ceramic and base glass after indentation with WC sphere, radius $r = 3.18$ mm, as a function of indentation load. Solid curves are empirical curve fits. Note that curves cross each other. Shaded regions at left represent standard deviation limits for all breaks away from indentation sites. Vertical dashed line for base glass data indicates approximate threshold load for cone crack formation.

patterns observed in rocks subjected to confining pressures.[48–51] Similar discreteness in subsurface damage patterns has also been reported in zinc sulfide polycrystals[52] beneath Vickers hardness impressions.

The indentation stress-strain curve in Fig. 2 is a simple methodology for quantifying the deformation response. In particular, the extreme nonlinear curve in the glass-ceramic is a graphic measure of the "ductility" that results from the crystallization process. It also allows for specification of such useful material parameters as "yield stress"[44] not otherwise accessible by conventional tensile testing routines used to determine mechanical responses of highly brittle solids.

The bonded-interface indentation experiment used in Figs. 3 and 4 is particularly effective for revealing the subsurface damage. This effectiveness is attributable to the detectability of very small (nanometer-scale) shear offsets at the separated free surfaces by Nomarski interference contrast. Polished sections are much less informative, because the very act of polishing removes these offsets. Indeed, polishing away less than 1 μm of the newly separated surfaces is sufficient to render much of the detail in Figs. 3 and 4 invisible. It is acknowledged that the presence of the interface in the experimental configuration of Fig. 1 could influence the observations, by relaxing the stresses on the median plane. However, Mulhearn's earlier definitive studies found no such relaxation effect in metals.[42] Moreover, the damage occurs in the immediate subsurface zone where the opposing surfaces are maintained in mutual contact by compressive stresses (arrows in Fig. 1). In some of our initial experiments certain artifacts (e.g., detachment of the material within the deformation zone) were indeed observed if the specimen was not constrained, especially at higher indentation loads; however, this problem could be avoided by applying clamping stresses as described in Sec. II.

The explicit nature of the deformation mechanism in the mica-containing glass-ceramic is not completely resolved in our observations, but most certainly involves some kind of discrete shear faulting of the weak interfaces.[35] Again, the rock mechanics literature provides rich precedent for the existence of such shear failures.[48–51] Individual microcracks develop at these interfaces on loading and unloading the indenter

[Fig. 5(a)], and ultimately coalesce to form shear-damage bands [Fig. 5(b)]. The microcracking appears to occur along the mica-glass interface rather than along the low-energy cleavage plane of mica, suggesting that the mica cleavage planes are stronger than the mica-glass interfaces. We note that the mica flakes in the subsurface deformation zone are not exposed to the external environment [at least not until the damage bands in Fig. 5(b) intersect the surface], and that the cleavage energy of mica remains relatively high unless exposed to moisture (>2000 mJ · m$^{-1/2}$ in "dry" environments vs ≈ 500 mJ · m$^{-1/2}$ in laboratory air[53–55]). High thermal expansion mismatch stresses may augment the interfacial microcracking[35]; such augmented microcracking has indeed been observed at Hertzian contacts in composites of silicon carbide particles in glass matrices, where the mismatch stresses are enhanced by adjusting the glass composition.[26]

The notion of shear faulting at the weak mica-glass interfaces is consistent with the shape of the deformation zone in the Hertzian stress field. Compression stresses act normal to the fault planes,[32] thereby maintaining the sliding surfaces in intimate contact during the indentation process. Friction must, therefore, be a key element of the micromechanical description. Accordingly, we may write the *net* shear stress S on a mica-glass interface in the generic form:

$$S = |\tau_F| - \mu|\sigma_F| \tag{3}$$

where τ_F and σ_F are the local shear and compressive stresses on the fault plane and μ is the coefficient of sliding friction. The condition for sliding is that $S > 0$, so subzero values of S are inadmissable in Eq. (3).[48,49,51,56] Contours of S for faults oriented for maximum local shear at each point within the Hertzian field[45] are plotted in Fig. 7 for specified values of μ and a Poisson's ratio $\nu = 0.29$ for the glass-ceramic. These contours appear to reflect the broad geometrical features of the evolving deformation zone in Fig. 4. Note the development of a near-surface domain (shaded) within which S is effectively zero, corresponding to faults for which the closure stress is so high as to preclude any sliding in Eq. (3). This zone increases with friction coefficient until, at $\mu = 1$, it occupies virtually the entire subsurface region. Such a zone of zero net shear stress is consistent with the observations of a region of suppressed damage immediately below the contacts in Fig. 4.

The manner in which microcracks extend in extensile mode from the edges of the faults and eventually link up is a complex problem in damage mechanics. Once more, interfacial friction must play a pivotal role in any fracture mechanics model.[56,57] A generic treatment of this problem in the special context of Hertzian contacts will be presented elsewhere.[58]

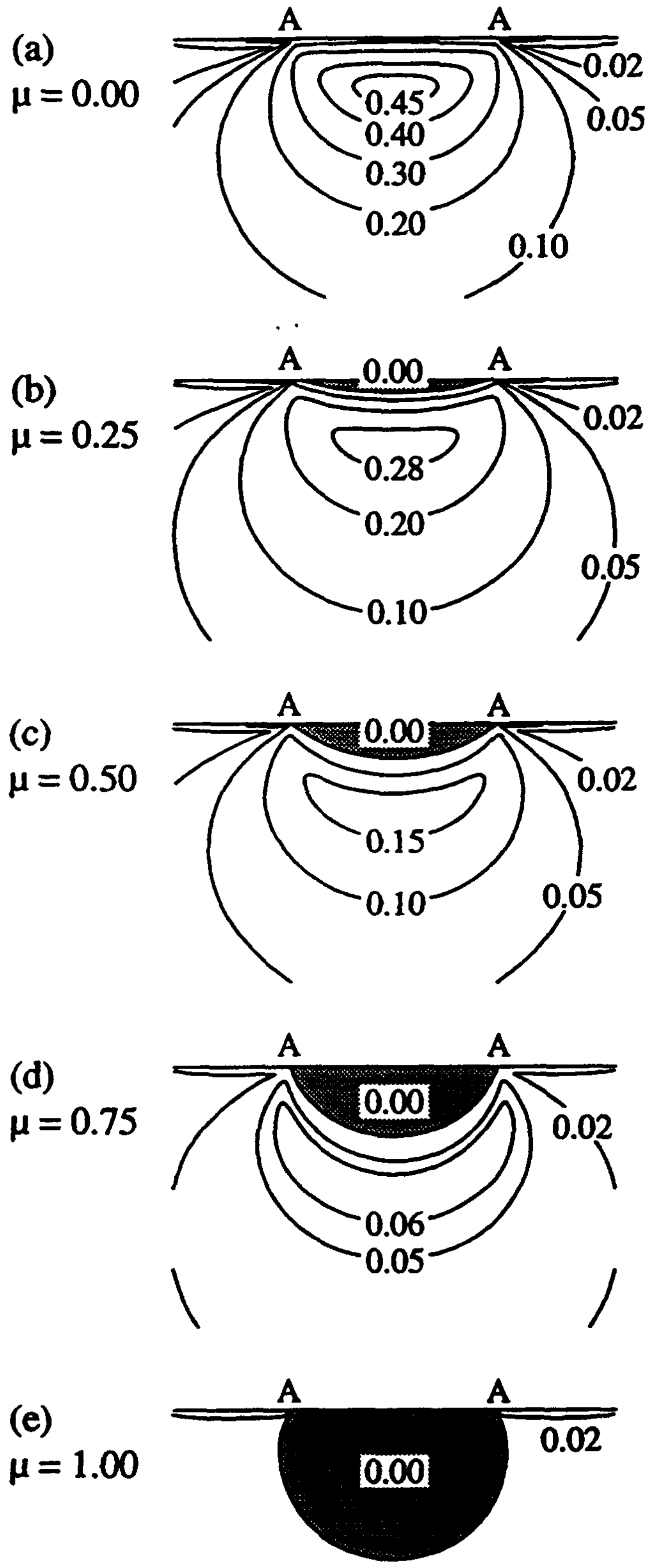

FIG. 7. (a–e) Contours of net shear stress S within Hertzian field for different friction coefficients μ in Eq. (3) and for Poisson's ratio 0.29 for Macor. Note strong suppression in stress levels as μ increases.

The results presented here bear on a broad range of mechanical properties, particularly in relation to the issue of toughness-curve behavior.[20] We commented on the interrelation between contact damage and strength in Sec. III.C. The data in Fig. 6 demonstrate that a material with relatively low laboratory strength (due to the presence of weak mica-glass interfaces as in this case of crystallized Macor) may nevertheless be more immune to degrading contact damage in service conditions. Although relative to the base glass the Macor has a lower short-crack toughness, it also has greater long-crack toughness; the toughness-curves for the Macor and the base glass cross each other.[41,59,60] As we have already mentioned, it is this relative weakness in the short-crack domain that accounts for the machinability of the Macor. Accordingly, following the experience with coarse-grain aluminas,[32,33] we may expect the crystallized Macor to have an entirely different fatigue response to that of the base glass.[61] It is most likely that, under cyclic fatigue loading, the microcrack faces slide and wear against each other, resulting in frictional attrition[62] and thereby causing microcracks to extend and ultimately coalesce.

Finally, there are strong implications in the present work concerning the microstructural design of materials systems for optimal mechanical properties. In the case of glass-ceramics the deformation and fracture responses can be altered through the controlled crystallization of a second phase in the glass matrix by heat treatment. The optimum treatment for a specific application will inevitably depend on an appropriate balance between the countervailing requirements of long-crack toughness, intermediate-crack strength, and short-crack wear and fatigue resistance.

ACKNOWLEDGMENTS

The authors thank F. Guiberteau and N.P. Padture for fruitful discussions, B.M. Hooks and M. Hill for experimental assistance, and K. Chyung of Corning Inc. for supplying the mica-containing Macor and "green" Macor materials for this study. Funding was provided by the United States Office of Naval Research.

REFERENCES

1. V.R. Howes and S. Tolansky, Proc. R. Soc. London A **230**, 287–293 (1955).
2. V.R. Howes and S. Tolansky, Proc. R. Soc. London A **230**, 294–301 (1955).
3. J.P. Tillett, Proc. Phys. Soc. London B **69**, 47–54 (1956).
4. F.C. Roesler, Proc. Phys. Soc. London B **69**, 981 (1956).
5. B.R. Lawn and H. Komatsu, Philos. Mag. **14**, 689–699 (1966).
6. F.C. Frank and B.R. Lawn, Proc. R. Soc. London A **299**, 291–306 (1967).
7. B.R. Lawn, J. Appl. Phys. **39**, 4828–4836 (1968).
8. F.B. Langitan and B.R. Lawn, J. Appl. Phys. **40**, 4009–4017 (1969).
9. F.B. Langitan and B.R. Lawn, J. Appl. Phys. **41**, 3357–3365 (1970).
10. M.V. Swain and B.R. Lawn, Phys. Status Solidi **35**, 909–923 (1969).
11. A.G. Mikosza and B.R. Lawn, J. Appl. Phys. **42**, 5540–5545 (1971).
12. T.R. Wilshaw, J. Phys. D: Appl. Phys. **4**, 1567–1581 (1971).
13. J.S. Nadeau, J. Am. Ceram. Soc. **56**, 467–472 (1973).
14. M.V. Swain, J.S. Williams, B.R. Lawn, and J.J.H. Beek, J. Mater. Sci. **8**, 1153–1164 (1973).
15. B.R. Lawn and T.R. Wilshaw, J. Mater. Sci. **10**, 1049–1081 (1975).
16. M.V. Swain and J.T. Hagan, J. Phys. D: Appl. Phys. **9**, 2201–2214 (1976).
17. A.G. Evans and T.R. Wilshaw, Acta Metall. **24**, 939–956 (1976).
18. B.R. Lawn and D.B. Marshall, in *Fracture Mechanics of Ceramics*, edited by R.C. Bradt, D.P.H. Hasselman, and F.F. Lange (Plenum, New York, 1978), Vol. 3, pp. 205–229.
19. R. Warren, Acta Metall. **26**, 1759–1769 (1978).
20. B.R. Lawn, *Fracture of Brittle Solids* (Cambridge University Press, Cambridge, 1993).
21. H. Hertz, *Hertz's Miscellaneous Papers*, Chaps. 5 and 6 (Macmillan, London, 1896).
22. K. Zeng, K. Breder, and D.J. Rowcliffe, Acta Metall. **40**, 2601–2605 (1992).
23. J.S. Nadeau and A.S. Rao, J. Can. Ceram. Soc. **41**, 63–67 (1972).
24. B.R. Lawn, T.R. Wilshaw, T.I. Barry, and R. Morrell, J. Mater. Sci. **10**, 179–182 (1975).
25. P. Chantikul, S.J. Bennison, and B.R. Lawn, J. Am. Ceram. Soc. **73**, 2419–2427 (1990).
26. H. Cai, N.P. Padture, B.M. Hooks, and B.R. Lawn, J. European Ceram. Soc. (in press).
27. F. Deuerler, R. Knehans, and R. Steinbrech, in *Science of Ceramics 13*, Journal de Physique, Paris (1986), pp. C1-617–621.
28. P.L. Swanson, C.J. Fairbanks, B.R. Lawn, Y-W. Mai, and B.J. Hockey, J. Am. Ceram. Soc. **70**, 279–289 (1987).
29. P.L. Swanson, in *Fractography of Glasses and Ceramics* (The American Ceramic Society, Westerville, OH, 1988), Vol. 22, pp. 135–155.
30. E.K. Beauchamp and S.L. Monroe, J. Am. Ceram. Soc. **72**, 1179–1184 (1989).
31. P.F. Becher, J. Am. Ceram. Soc. **74**, 255–269 (1991).
32. F. Guiberteau, N.P. Padture, H. Cai, and B.R. Lawn, Philos. Mag. A **68**, 1003–1016 (1993).
33. F. Guiberteau, N.P. Padture, and B.R. Lawn, J. Am. Ceram. Soc. (in press).
34. P.W. McMillan, *Glass-Ceramics* (Academic Press, London, 1979).
35. C.K. Chyung, G.H. Beall, and D.G. Grossman, in *Electron Microscopy and Structure of Materials*, edited by G. Thomas, R.M. Fulrath, and R.M. Fisher (University of California Press, Berkeley, CA, 1972), pp. 1167–1194.
36. K. Chyung, G.H. Beall, and D.G. Grossman, in *Proceedings of 10th International Glass Congress, No. 14* (The Ceramic Society of Japan, Tokyo, Japan, 1974), pp. 33–40.
37. K. Chyung, in *Fracture Mechanics of Ceramics*, edited by R.C. Bradt, D.P.H. Hasselman, and F.F. Lange (Plenum Press, New York, 1974), Vol. 2, pp. 495–508.
38. G.H. Beall, in *Advances in Nucleation and Crystallization in Glasses*, edited by L.L. Hench and S.W. Freiman (The American Ceramic Society, Westerville, OH, 1972), pp. 251–261.
39. T. Uno, T. Kasuga, and K. Nakajima, J. Am. Ceram. Soc. **74**, 3139–3141 (1991).

40. D. G. Grossman, in *Proceedings of the International Symposium on Computer Restorations*, edited by W. H. Mörmann (Quintessence Publishing Co., Chicago, IL, 1991), pp. 103–115.
41. C. J. Fairbanks, B. R. Lawn, R. F. Cook, and Y-W. Mai, in *Fracture Mechanics of Ceramics*, edited by R. C. Bradt, A. G. Evans, D. P. H. Hasselman, and F. F. Lange (Plenum, New York, 1986), Vol. 8, pp. 23–37.
42. T. O. Mulhearn, J. Mech. Phys. Solids 7, 85–96 (1959).
43. R. F. Cook, B. R. Lawn, and C. J. Fairbanks, J. Am. Ceram. Soc. **68**, 604–615 (1985).
44. D. Tabor, *Hardness of Metals* (Clarendon, Oxford, 1951).
45. K. L. Johnson, *Contact Mechanics* (Cambridge University Press, London, 1985).
46. J. J. Benbow, Proc. Phys. Soc. London 75, 697–699 (1960).
47. J. S. Williams, B. R. Lawn, and M. V. Swain, Phys. Status Solidi A 2, 7–29 (1970).
48. J. C. Jaeger and N. G. W. Cook, *Fundamentals of Rock Mechanics* (Chapman and Hall, London, 1971).
49. M. S. Paterson, *Experimental Rock Deformation–The Brittle Field* (Springer-Verlag, Berlin, 1978).
50. R. L. Kranz, Tectonophysics **100**, 449–480 (1983).
51. L. R. Myer, J. M. Kemeny, Z. Zheng, R. Suarez, R. T. Ewy, and N. G. W. Cook, Appl. Mech. Rev. **45**, 263–280 (1992).
52. S. van der Zwagg, J. T. Hagan, and J. E. Field, J. Mater. Sci. **15**, 2965–2972 (1980).
53. K-T. Wan, N. Aimard, S. Lathabai, R. G. Horn, and B. R. Lawn, J. Mater. Res. 5, 172–182 (1990).
54. K-T. Wan and B. R. Lawn, Acta Metall. **38**, 2073–2083 (1990).
55. K-T. Wan, D. T. Smith, and B. R. Lawn, J. Am. Ceram. Soc. **75**, 667–676 (1992).
56. H. Horii and S. Namat-Nasser, J. Geophys. Res. **90**, 3105–3125 (1985).
57. M. F. Ashby and S. D. Hallam, Acta Metall. Mater. **34**, 497–510 (1986).
58. B. R. Lawn, N. P. Padture, F. Guiberteau, and H. Cai, Acta Metall. (in press).
59. B. R. Lawn, N. P. Padture, L. M. Braun, and S. J. Bennison, J. Am. Ceram. Soc. **76**, 2235–2240 (1993).
60. N. P. Padture, J. L. Runyan, S. J. Bennison, L. M. Braun, and B. R. Lawn, J. Am. Ceram. Soc. **76**, 2241–2247 (1993).
61. H. Cai, M. A. Stevens Kalceff, and B. R. Lawn, J. Mater. Res. (unpublished research).
62. S. Lathabai, J. Rödel, and B. R. Lawn, J. Am. Ceram. Soc. **74**, 1340–1348 (1991).

Pergamon

0956-7151(93)E0068-E

Acta metall. mater. Vol. 42, No. 5, pp. 1683–1693, 1994
Elsevier Science Ltd
Printed in Great Britain
0956-7151/94 $6.00 + 0.00

A MODEL FOR MICROCRACK INITIATION AND PROPAGATION BENEATH HERTZIAN CONTACTS IN POLYCRYSTALLINE CERAMICS

B. R. LAWN, N. P. PADTURE†, F. GUIBERTEAU‡ and H. CAI†

Materials Science and Engineering Laboratory, National Institute of Standards and Technology, Gaithersburg, MD 20899, U.S.A.

(Received 27 September 1993)

Abstract—A fracture mechanics model of damage evolution within Hertzian stress fields in heterogeneous brittle ceramics is developed. Discrete microcracks generate from shear faults associated with the heterogeneous ceramic microstructure; e.g. in polycrystalline alumina, they initiate at the ends of intragrain twin lamellae and extend along intergrain boundaries. Unlike the well-defined classical cone fracture that occurs in the weakly tensile region *outside* the surface contact in homogeneous brittle solids, the fault-microcrack damage in polycrystalline ceramics is distributed within a subsurface shear-compression zone *below* the contact. The shear faults are modelled as sliding interfaces with friction, in the manner of established rock mechanics descriptions but with provision for critical nucleation and matrix restraining stresses. This allows for constrained microcrack pop-in during the loading half-cycle. Ensuing stable microcrack extension is then analyzed in terms of a K-field formulation. For simplicity, only mode I extension is considered specifically here, although provision exists for including mode II. The compressive stresses in the subsurface field constrain microcrack growth during the loading half-cycle, such that enhanced extension occurs during unloading. Data from damage observations in alumina ceramics are used to illustrate the theoretical predictions. Microstructural scaling is a vital element in the microcrack description: initiation is unstable only above a critical grain size, and extension increases as the grain size increases. Internal residual stresses also play an important role in determining the extent of microcrack damage. Implications of the results in the practical context of wear and fatigue properties are discussed.

1. INTRODUCTION

The nature of contact damage beneath an indenting sphere on a brittle surface has been extensively studied in homogeneous, isotropic materials like glasses and single crystals, and in some fine-grain ceramics. In such relatively ideal materials one observes an elastic response up to a critical load, whence a classical "Hertzian cone fracture" suddenly develops outside the contact circle [1–8]. Traditional cone fractures tend to be near-symmetrical and well-defined, and are accordingly amenable to linear elastic fracture mechanics analysis [3]. On the other hand, it is possible under certain circumstances (e.g. softer materials, harder and smaller indenters) to suppress the cone fracture and to induce subsurface deformation, thereby providing information on intrinsic deformation processes in otherwise highly brittle solids [9, 10].

Given this background, it is perhaps surprising that relatively little attention has been given to the nature of Hertzian damage in heterogeneous polycrystalline ceramics. This is especially so in those coarser ceramics where weak interfaces and internal stresses exert a controlling influence on the fracture process, leading to countervailing "toughness-curve" (T-curve, or R-curve) effects [11]. Thus, whereas the toughness in the *long*-crack region is enhanced by grain-interlock bridging [12–16], in the *short*-crack region it is diminished by thermal expansion mismatch stresses at tensile grain or interphase boundaries [15]. Recently, spherical indenter tests on a coarse-grain alumina [17, 18] and a glass–ceramic [19] have revealed a different kind of contact damage, with the following distinctive features:

(i) A well-defined "indentation stress–strain" curve, independent of sphere size, indicating a deviation from the ideal Hertzian elasticity relations toward a "plastic contact" at high indentation pressures.
(ii) Instead of the classical cone fracture *outside* the contact circle, where the stresses are (weakly) tensile, a microfracture initiation and coalescence zone *beneath* the contact circle, where the stresses are (strongly) hydrostatic compressive and deviatoric in nature.
(iii) An indication that each microfracture is preceded by some kind of stress-concentrating

---

†Guest Scientist, from Department of Materials Science and Engineering, Lehigh University, Bethlehem, PA 18015, U.S.A.

‡Guest Scientist, from Departamento de Fisica, Universidad de Extremadura, 06071-Badajoz, Spain.

"constrained shear fault" (e.g. twin lamella, in the case of alumina), so that the damage is intrinsic to the microstructure.

In addition, the damage zone expands in repeat contacts, with progressive microcrack coalescence and ultimate material removal, indicating a true mechanical fatigue effect. Such features are of special interest to those concerned with the strength, fatigue and wear of structural ceramics.

In this paper we present a generic fracture mechanics model of the microfracture evolution within the subsurface damage zone in polycrystalline ceramics during a full indentation loading and unloading cycle. The crux of our model is the initiation and subsequent growth of a microcrack from some shear fault within the compressive indentation zone. This evolution is described in terms of a detailed K-field formulation [11]. The envisaged process is loosely based on the "pile-up" concept for crack initiation in semi-brittle solids [11, 20–22]. The process is also reminiscent of the kind of crack initiation that occurs beneath "sharp" (e.g. Vickers) indenters in glasses [23, 24], in rocks and other coarse-grain materials subjected to macroscopic confining pressures [25–29], and in compressively loaded notched ceramics [30–32]. In setting up our model we shall borrow from these earlier research areas, although new elements specifically pertinent to structural ceramics will also be introduced. The scale of individual damage events is determined by a characteristic microstructural dimension, grain size in the case of polycrystalline alumina, which limits the length of the critical shear fault and thereby determines threshold conditions for microcracking. Ideally, the microcracks are assumed to propagate along constrained grain boundaries or other weak interfaces in predominantly extensile mode (i.e. mode I). These microcracks are, by virtue of the compressive nature of the immediate subsurface contact field, highly stable in their subsequent evolution, with continued propagation during unloading. In actuality, the geometrical constraints imposed by the grain boundaries relative to the shear fault and Hertzian field will inevitably result in superposed shear stresses on the microcrack surfaces (i.e. mode II), opening the way to frictional tractions and hence hysteresis during unloading–reloading cycles, i.e. fatigue.

In the interest of mathematical simplicity, we confine ourselves here to mode I microcrack extension. Data from previous studies on polycrystalline alumina will be used to illustrate how one may calibrate K-field parameters in the analysis, and thence evaluate the microcrack development through a complete Hertzian load–unload cycle. In particular, we address the important role of grain size, in special relation to the crack initiation (pop-in) and subsequent propagation. We shall determine that a greater portion of the propagation actually takes place during the unloading half-cycle, although in a highly stable manner.

Whereas we specifically address single-cycle, mode I microfracture here, we foreshadow potential extension of the model to fatigue and wear properties by inclusion of mode II frictional tractions at the closed microcrack interfaces. The mode II component allows for hysteresis in cyclic loading, enabling progressive coalescence of neighboring microcracks and, ultimately, material removal.

2. NATURE OF DAMAGE IN HERTZIAN CONTACT FIELD

2.1. *Background experimental observations on polycrystalline alumina*

The nature of Hertzian contact damage on polycrystalline ceramics has been examined in recent experimental studies on alumina [17, 18] and glass–ceramics [19]. From these studies we identify the following features:

(i) Macroscopically, the damage occurs in a region of intense hydrostatic compression and shear stress, reminiscent of the deformation observed in homogeneous brittle solids in sharp-indenter fields [10, 33–37] and in rocks under confining pressures [25–27]. The extent of deformation can be quantified by departure from the linear Hertzian elasticity relation on an indentation stress–strain diagram, mean contact pressure $p_0 = P/\pi a^2$ vs contact strain a/r [9, 10, 38]. For polycrystalline alumina in Fig. 1 [18], we see that this curve is independent of grain size, indicating a material "yield stress". Note the relatively high values of p_0, up to 10 GPa, typical of contact configurations.

(ii) Microscopically, the contact deformation is associated with the activation of discrete "shear faults", from which microcracks initiate. It is implicit that the shear fault is obstructed in its extension, e.g. by intersection with weak grain boundaries, to

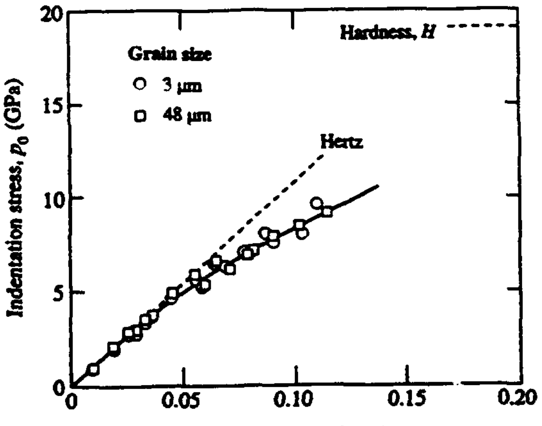

Fig. 1. Indentation stress–strain curve for aluminas, obtained using tungsten carbide (WC) spheres of radius $r = 1.98$–12.70 mm. Inclined dashed line is Hertzian elastic response and upper horizontal dashed line is Vickers hardness (averaged over all grain sizes). Solid curve is an empirical fit to the data. (After [18].)

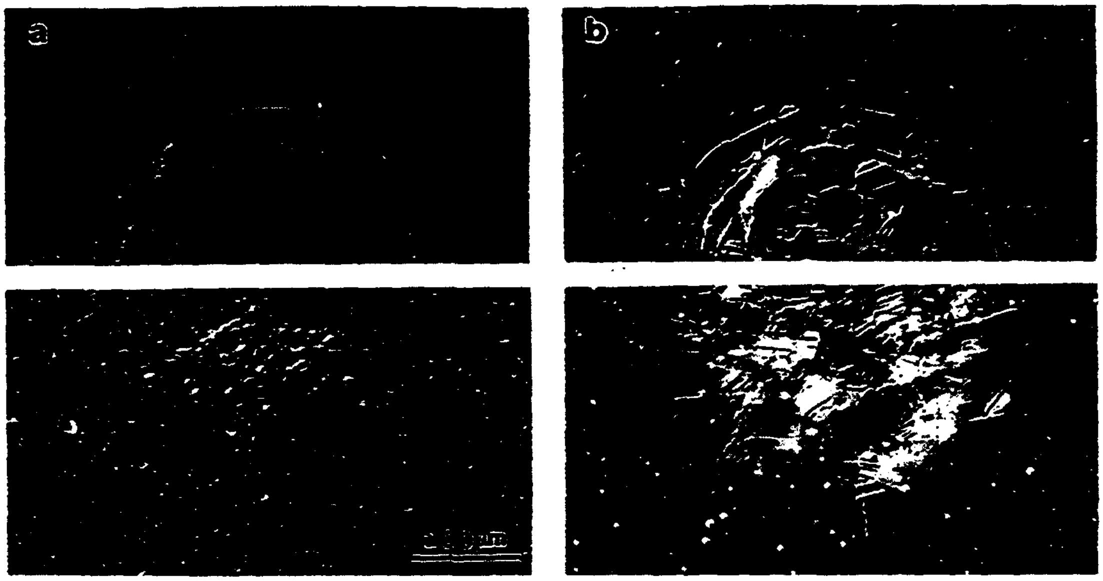

Fig. 2. Optical micrographs in Nomarski illumination showing half-surface (top) and section (bottom) views of indentation sites in aluminas, grain size (a) 9 μm and (b) 48 μm. Indentations made at indentation pressure $p_0 = 8.0$ GPa, using WC sphere of radius $r = 3.18$ mm at load $P = 2000$ N. (After [18].)

produce a local stress concentration [11, 20]. We show representative section views in Fig. 2(a) and 2(b) for aluminas of two grain sizes, "fine" (9 μm) and "coarse" (48 μm), at a contact pressure in the nonlinear indentation stress–strain region. In the fine-grain material we see limited subsurface microcrack damage (section view), along with classical cone crack traces (half-surface view). The extent of subsurface microcracking is much more apparent in the coarse-grain material. In alumina, the shear faults are principally identifiable as intra-grain twins, clearly visible in Fig. 2(b) [17]. Acoustic emission data from load–unload indentation cycles on a broad range of aluminas in Fig. 3 indicates a pronounced increase in damage activity above a grain size $\approx 20\,\mu$m. Note that the bulk of the activity occurs above a contact pressure ≈ 5 GPa during the loading half-cycle.

The features outlined in (i) and (ii) are generic to brittle materials, apart from the underlying sources of the shear faults, which are material-specific (see Section 6).

2.2. *Stress field considerations*

In this subsection we summarize the pertinent characteristics of the Hertzian elastic contact field [3, 6, 39]. The confining principal normal stresses σ_1, σ_2 and σ_3 within the prospective damage zone prior to deformation are so defined that $\sigma_1 > \sigma_2 > \sigma_3$ nearly everywhere (positive stress tensile). Beneath the indentation center the trajectory of maximum compression $-\sigma_3$ runs parallel to the contact axis, and that of minimum compression $-\sigma_1$ (or $-\sigma_2$)

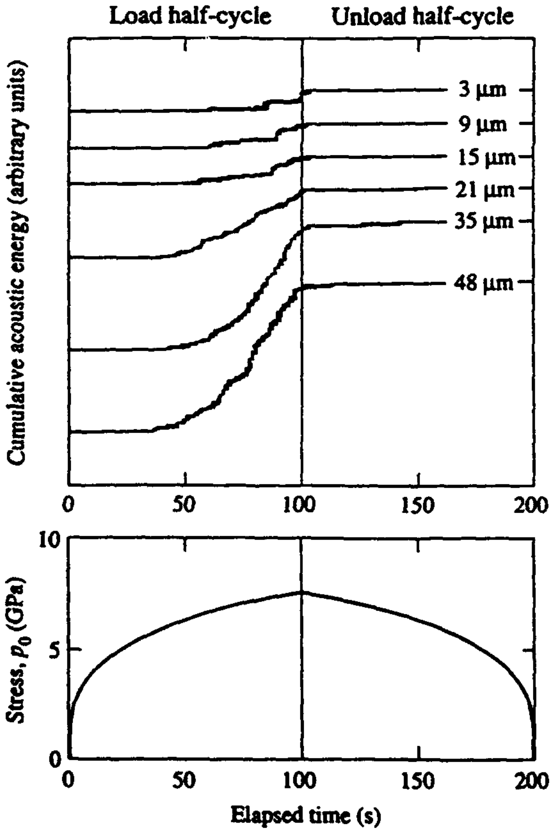

Fig. 3. Plots of cumulative acoustic energy (arbitrary linear scale) vs elapsed time during single load–unload indentation cycle (constant crosshead speed) in alumina specimens (upper diagram), using WC sphere of radius $r = 3.18$ mm. Variation of contact pressure with time indicated (lower diagram). (After [18].)

runs perpendicular to that axis. Figure 4 shows contours of principal normal stresses σ_1 and σ_3 and principal shear stress $\frac{1}{2}(\sigma_1 - \sigma_3)$, here plotted for Poisson's ratio $\nu = 0.22$ (appropriate to alumina). In these plots the contact radius a determines the spatial scale, and contact pressure p_0 the intensity, of the stress field. The tensile stresses $+\sigma_1$, Fig. 4(a), are relatively weak, with a maximum $0.28p_0$ *at* the contact circle and rapid falloff *outside* the contact circle. The shear stresses, Fig. 4(c), are stronger, with maximum $0.49p_0$ along the contact axis at depth $\approx 0.5a$ on planes oriented at 45° to this axis; they are less concentrated than their tensile counterparts, and are confined within a zone of high biaxial hydrostatic compression, $\frac{1}{2}(\sigma_1 + \sigma_3)$.

The damage in Fig. 2 takes place almost exclusively within a drop-shaped zone below the contact, and begins subsurface, indicating that it is the maximum shear stress that primarily initiates the damage [17]. This is in striking contrast with the traditional cone fracture which, we recall, initiates and propagates in the tensile region outside the contact circle in Fig. 4(a) [3, 40]. Of course, once damage does occur the field is no longer purely elastic. However, provided we concern ourselves primarily with conditions for the onset of microcracking from individual shear faults rather than with subsequent damage coalescence and evolution into a full "plastic" zone [38], the Hertzian field may be retained as a useful base for fracture mechanics calculations.

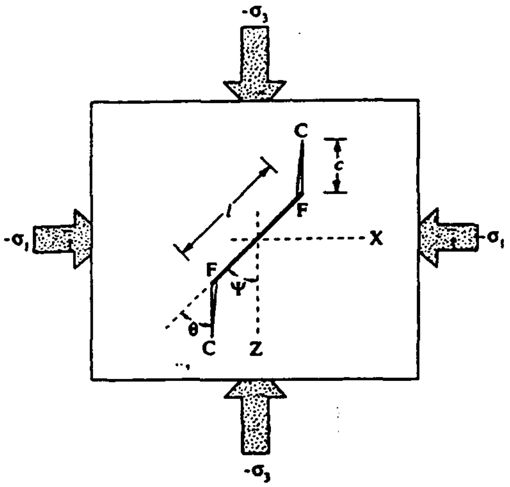

Fig. 5. Deformation-microfracture damage in polycrystalline ceramic, grain size l. Volume element is subjected to compressive normal stresses $-\sigma_1$ and $-\sigma_3$ along contact axis below spherical indenter. Shear stresses initiate intragrain slip bands FF, from which intergrain extensile microcracks FC extend at their constrained ends.

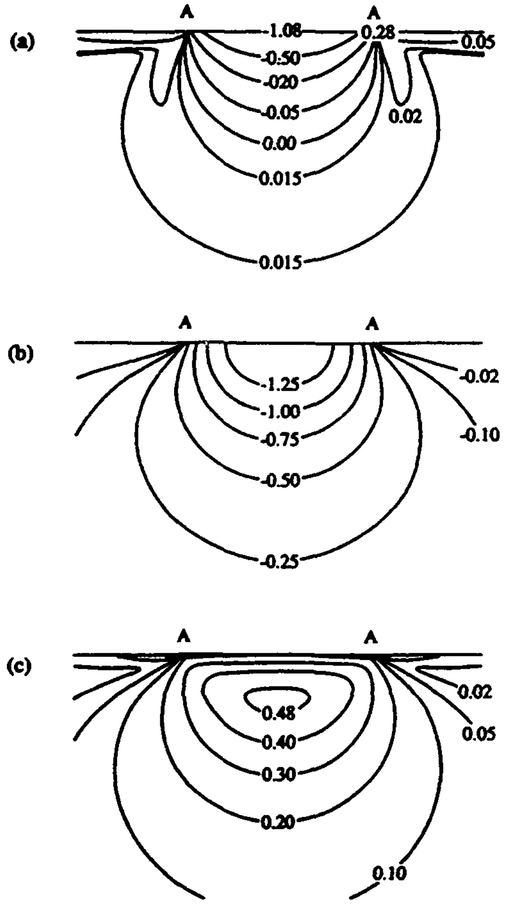

Fig. 4. Stress contours in Hertzian contact field, normalized to p_0. AA denotes contact diameter $2a$. (a) Maximum principal normal stress σ_1, (b) minimum principal normal stress σ_3, and (c) principal shear stress $\frac{1}{2}(\sigma_1 - \sigma_3)$. Note region of high biaxial hydrostatic compression $\frac{1}{2}(\sigma_1 + \sigma_3)$ beneath contact. Calculated using Poisson's ratio $\nu = 0.22$ for alumina.

In accordance with these considerations, we set up the model for microcrack initiation shown in Fig. 5. An incipient shear fault FF is contained in a volume element beneath a spherical indenter in a material of grain size l (Section 3). At their ends the faults are constrained by some microstructural interface, e.g. weak grain boundary, along which microcracks FC ultimately initiate (Section 4). We do not specify the *nature* of the fault, so the model is generic: however, we do specify that the *scale* of the fault is determined by l. In the limit of sufficiently large contacts, $l \ll a$, uniform normal and shear contact stresses

$$\sigma(\Psi) = \tfrac{1}{2}(\sigma_1 + \sigma_3) + \tfrac{1}{2}(\sigma_1 - \sigma_3)\cos 2\Psi \qquad (1a)$$

$$\tau(\Psi) = \tfrac{1}{2}(\sigma_1 - \sigma_3)\sin 2\Psi \qquad (1b)$$

act on the fault plane, where Ψ is the angle between the fault and the σ_3 trajectory. We see directly from eqn. 1b that the fault orientation for maximum shear stress is $\Psi \approx 45°$, as pictured in Fig. 5. The corresponding stresses acting on the extended microcrack plane are

$$\sigma(\Psi - \theta) = \tfrac{1}{2}(\sigma_1 + \sigma_3) + \tfrac{1}{2}(\sigma_1 - \sigma_3)\cos 2(\Psi - \theta) \qquad (2a)$$

$$\tau(\Psi - \theta) = \tfrac{1}{2}(\sigma_1 - \sigma_3)\sin 2(\Psi - \theta). \qquad (2b)$$

Note that in the favored orientation $\Psi \approx \theta \approx 45°$ [28, 29], the shear component in equation (2b) tends to zero.

In typical ceramics, internal mismatch stresses also act at individual grain boundaries, some tensile and some compressive. Predominant in noncubic monophase and two-phase materials are those residual stresses, σ_R, due to thermal expansion mismatch. In alumina these stresses have a value $\sigma_R \approx 200$ MPa [16, 41], i.e. more than an order of magnitude lower than the contact stresses $p_0 \approx 5$–10 GPa in the deformation region of Fig. 1. Microcracks that initiate on tensile grain facets are more likely than those on compressive facets to extend into adjacent grain boundaries. Those extending microcracks that ultimately coalesce with their neighbors (e.g. from contact overloading, fatigue from cyclic loading, or chemical enhancement) will become increasingly subject to sliding friction tractions across the crack interface at adjacent compressive facets, resulting in a progressively increasing toughness by bridging (toughness-curve, or T-curve, behavior) [15]. We shall regard such bridging tractions as secondary elements in the micromechanics in this study.

3. SHEAR-FAULT MICROMECHANICS

Now consider the conditions for activation of the closed shear fault FF in Fig. 5. To do this we resort to the phenomenological constitutive relations adopted by rock mechanists [25, 26], whereby the sliding faces of the fault are subject to resistive tractions. We acknowledge that the normal (N) contact field stresses on the fault (F) plane in the subsurface damage zone will usually be compressive by defining

$$\sigma_F^N = \sigma(\Psi) = -\alpha_F p_0 \tag{3}$$

with $\alpha_F = -\sigma(\Psi)/p_0$ a positive coefficient (p_0 positive). The applied shear (S) stress on the sliding fault will be resisted by internal stresses from the intrinsic cohesion (e.g. twinning stress), τ_F, and frictional sliding, $\mu_F\sigma_F^N$, where μ_F is a fault friction coefficient. Thus, again with due allowance for the negative sign of σ_F^N, and for sign reversal of the resistance stresses on unloading, the net shear stress may be written [25]

$$\begin{aligned}\sigma_F^S &= |\tau(\Psi)| + \mu_F\sigma(\Psi) - \tau_F \\ &= (\beta_F - \alpha_F\mu_F)p_0 - \tau_F, \quad \text{(forward slip)} \quad (4a)\end{aligned}$$

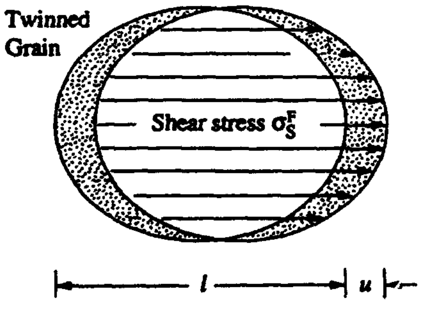

Fig. 6. Twinning slip of grain across shear plane at stress σ_F^S, resulting in strain u/l.

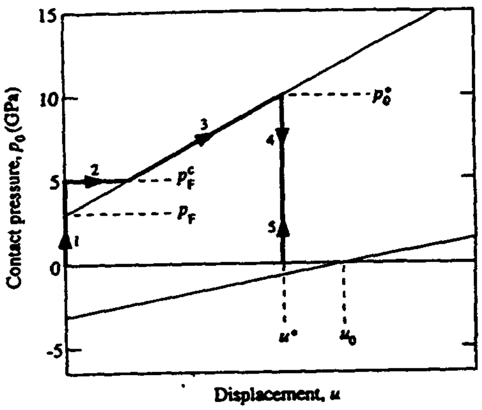

Fig. 7. Plots showing shear displacement u for twinned grain at location of maximum shear stress in Hertzian field at pressure p_0. (Pressure axis "calibrated" from alumina data in Section 5.) Case shown corresponds to zero reverse slip, $u^* < u_0$.

$$\begin{aligned}\sigma_F^S &= |\tau(\Psi)| - \mu_F\sigma(\Psi) + \tau_F \\ &= (\beta_F + \alpha_F\mu_F)p_0 + \tau_F, \quad \text{(backward slip)} \quad (4b)\end{aligned}$$

with $\beta_F = |\tau(\Psi)|/p_0$ another positive coefficient. Note that invariance of the coefficients α_F and β_F through the indentation cycle is contingent on complete reversibility of the stress field.

Accordingly, a necessary requirement for faulting to occur is that $\sigma_F^S > 0$ in equation (4). Where the fault interface has low cohesion but is rough (e.g. debonded interfaces in certain particle–matrix composites), the frictional term will dominate the mechanics. Where the fault must first be initiated (e.g. twinning in alumina), the cohesion term will dominate. In the latter case provision may be necessary to allow for a barrier to fault initiation, e.g. by defining a critical nucleation cohesion stress $\tau_F^c > \tau_F$.

Continued sliding of the fault within a grain confined in the Hertzian field is opposed by the surrounding elastic matrix, which exerts a linear restraining force in proportion to the shear displacement u, Fig. 6. At equilibrium

$$\sigma_F^S = \kappa u \tag{5}$$

where κ is an elastic stiffness term. We may now combine equations (4) and (5) for the contact pressure p_0 as a function of displacement u to produce constitutive equilibrium relations for our shear fault

$$p_0 = (\kappa u + \tau_F)/(\beta_F - \alpha_F\mu_F), \text{ (forward slip)} \tag{6a}$$

$$p_0 = (\kappa u - \tau_F)/(\beta_F + \alpha_F\mu_F), \text{ (backward slip).} \tag{6b}$$

A plot of the function $p_0(u)$ from equation (6) is shown in Fig. 7. In this plot the upper inclined line represents equation (6a), with slope $\kappa/(\beta_F - \alpha_F\mu_F)$ and intercept $\tau_F/(\beta_F - \alpha_F\mu_F)$ on the p_0 axis. Similarly, the lower inclined line represents equation (6b), with slope $\tau_F/(\beta_F - \alpha_F\mu_F)$ and intercept $-\tau_F/(\beta_F + \alpha_F\mu_F)$. The vertical dashed line at $u_0 = \tau_F/\kappa$ represents the intersection of equation (6b) with the u axis.

Consider the potential response for load–unload contact cycles, indicated in the plot by the arrowed solid lines. Let us treat the case in which a critical stress $\tau_F^c > \tau_F$ is needed to nucleate the fault. Initially, the contact pressure p_0 increases without slip along branch (1), at $u = 0$. At a critical pressure $p_0 = p_F^c$ a fault pops in unstably along branch (2), until the upper equilibrium line for forward slip is intersected. Note that in the absence of a critical nucleation condition the fault would initiate stably at the intercept pressure $p_0 = \tau_F/(\beta_F - \alpha_F \mu_F) = p_F < p_F^c$, i.e. without pop-in. Further increase in contact pressure to a maximum value $p_0 = p_0^*$ causes slip to continue stably along branch (3). Now suppose we unload at some displacement $u^* < u_0$. The system traverses branch (4) at $u^* = [(\beta_F - \alpha_F \mu_F)p_0^* - \tau_F]/\kappa =$ constant from equation (6a). Along this unloading branch the fault shear stress $\sigma_F^S = \kappa u^*$ remains constant. At intersection of branch (4) with the u axis at $p_0 = 0$ the system is fully unloaded, so (unless we reverse the contact pressure, i.e. exert an adhesive "contact tension") we can not satisfy equation (6b) for reverse slip. Reloading along (5) then retraces (4), and all further cycles are constrained to this vertical branch. In summary, the fault exerts a monotonically increasing shear stress $\sigma_F^S = \kappa u$ during the loading half-cycle and a persistent shear stress $\sigma_F^S = \kappa u^*$ during (and after) the unloading half-cycle.

Note in Fig. 7 that there is hysteresis in the first cycle, but not in subsequent cycles. The latter kind of hysteresis may occur at "overloaded" contacts, such that the displacement at maximum load satisfies the condition $u^* > u_0$, leading to reverse slip along portion of the lower inclined line to $p_0 = 0$ during the unload half-cycle. Note that reverse slip would also occur if the cohesion were to be zero, i.e. $\tau_F = 0$ in equation (6), regardless of the maximum load, because then both the forward and backward slip lines would intersect the origin in Fig. 7.

4. *K*-FIELD ANALYSIS OF MICROCRACK DEVELOPMENT

Consider now the evolution of a microcrack FC from an edge F of the shear fault FF in Fig. 5. The problem of crack initiation from sliding shear cracks in confining triaxial compressive fields has been considered at some length by the rock mechanics community. Fracture mechanics treatments have been presented by Horii and Nemat-Nasser [28] and Ashby and Hallam [29], specifically for systems with preexisting faults. A characteristic feature of the microfracture in those cases is a highly stabilized extension at all stages of evolution to "failure", on planes closely normal to the least compressive of the principal stresses. In the case of alumina, it is necessary to allow for a potential initiation instability from twin pop-in. The pop-in problem bears striking similarities to that of crack initiation from shear faults in Vickers indentation fields [24], and it is the relatively straightforward stress-intensity factor approach of that analysis that we adopt here.

4.1. Crack-plane stresses

The initial microcrack increment will be governed by the near field associated with the shear fault, and will search for a path of maximum local tension. Ideally, for $\Psi = 45°$ in Fig. 5 (orientation for maximum shear on fault), this initial path corresponds to $\theta = 70.5°$ [29]. As the microcrack extends, it becomes influenced more strongly by the far-field contact stresses; the optimum orientation for maximum tension, again at $\Psi = 45°$, is then $\theta = 45°$. In reality, the fault may be constrained by crystallography at more unfavorable orientations, i.e. $\Psi \neq 45°$. Similarly, the microcrack may be constrained to extend along a grain or interphase boundary within the local shear-fault field, and therefore will not necessarily follow principal stress trajectories. Hence, in general, the microcrack segment will experience both modes I and II (and III, for that matter).

Once the crack path is established, the fracture mechanics are completely determined by the stresses from the contact field plus any internal stresses acting along that path. On the closed-fault (F) segment FF in Fig. 5, resolved normal (compressive) and shear contact-field stresses $\sigma(\Psi)$ and $\tau(\Psi)$ are defined in equations (1a) and (1b), respectively. The key stress that determines subsequent fracture extension during a full load–unload cycle is the *net* shear stress in equation (4a)

$$\sigma_F^S = (\beta_F - \alpha_F \mu_F)p_0 - \tau_F, \text{ (loading)} \tag{7a}$$

$$\sigma_F^S = (\beta_F - \alpha_F \mu_F)p_0^* - \tau_F, \text{ (unloading–reloading)} \tag{7b}$$

recalling that $\alpha_F = -\sigma(\Psi)/p_0$, $\beta_F = |\tau(\Psi)|/p_0$, and p_0^* the contact pressure at maximum loading, with $\sigma_F^S > 0$ always. We note that σ_F^S in equation (7b) remains constant during the unloading and any reloading half-cycles.

Similarly, for the extended open-microcrack (M) segment FC in Fig. 5, resolved contact-field stresses $\sigma(\Psi - \theta)$ and $\tau(\Psi - \theta)$ are defined in equation (2). Thus, normal stresses

$$\sigma_M^N = \sigma(\Psi - \theta) = -\alpha_M p_0 \tag{8}$$

act throughout the loading–unloading cycle, with $\alpha_M = -\sigma(\Psi - \theta)/p_0$ another positive coefficient [cf. equation (3)]. Since this stress component exerts its maximum constraint at peak loading, the cracks will extend during unloading as well as loading, and conversely close during any reloading. Any shear stresses on the otherwise extensile microcrack are again expressible in the form [25]

$$\sigma_M^S = (\beta_M - \alpha_M \mu_M)p_0 - \tau_M, \text{ (loading–unloading)} \tag{9a}$$

$$\sigma_M^S = (\beta_M + \alpha_M \mu_M)p_0 + \tau_M, \text{ (reloading)} \tag{9b}$$

with positive coefficient $\beta_M = |\tau(\Psi - \theta)|/p_0$, crack-interface sliding friction coefficient μ_M and shear "cohesion" stress τ_M [cf. equation (5)]; again, it is required that $\sigma_M^S > 0$ for sliding. As with coefficients α_F and β_F in equations (2) and (3), invariance of α_M and β_M in equations (8) and (9) is contingent on reversibility of the stress field.

In addition, the extensile microcracks in noncubic polycrystals and two-phase materials are subject to thermal expansion mismatch stresses σ_R.

4.2. Stress–intensity factors for Mode I extension

In this section we make simplifying assumptions concerning the fault-microcrack geometry in Fig. 5, to minimize mathematical complexity. Thus in our stress-intensity factors we ignore the deflection of the microcrack from the fault plane by treating the system as a planar penny crack with radial coordinate r, radius $C = c + l/2$, subjected to stress σ_F^S [equation (7)] over $0 \leqslant r \leqslant l/2$ plus stresses σ_M^S, σ_M^N [equations (8, 9)] and σ_R over $l/2 \leqslant r \leqslant C$. Also, we choose the configuration that maximizes the contact field shear on the fault, $\Psi = 45°$, and tension on the developed microcrack, $\theta = 45°$; in this ideal case the shear stress σ_M^S in equation (9) is zero (see below), so the microcrack extends in pure mode I. On the other hand, recognizing that the σ_M^S term may be an essential element of fatigue (e.g. from frictional attrition at the sliding crack interface—Section 6), provision remains in the formalism of Sections 3 and 4 for a more general, mixed-mode analysis.

These geometrical simplifications allow us to calculate the α and β coefficients in the stress terms of Section 4.1. Inserting $\Psi = 45°$ in equation (1) yields fault stresses $\sigma(\Psi) = \frac{1}{2}(\sigma_1 + \sigma_3)$ and $\tau(\Psi) = \frac{1}{2}(\sigma_1 - \sigma_3)$; similarly, inserting $\Psi = 45° = \theta$ in equation (2) yields microcrack stresses $\sigma(\Psi - \theta) = \sigma_1$ and $\tau(\Psi - \theta) = 0$. Now we are concerned with the values of these stresses in the subsurface damage zone, specifically at the point of maximum shear stress at depth $0.5a$ beneath the contact center and for Poisson's ratio $\nu = 0.22$ for alumina. We find $\sigma_1 = -0.25p_0$ [Fig. 4(a)] and $\sigma_3 = -0.74p_0$ [Fig. 4(b)] at this point, yielding $\alpha_F = -\sigma(\Psi)/p_0 = 0.74$ and $\beta_F = |\tau(\Psi)|/p_0 = 0.49$, $\alpha_M = -\sigma(\Psi - \theta)/p_0 = 0.25$ and $\beta_M = |\tau(\Psi - \theta)|/p_0 = 0$. Since negative values of σ_M^S are inadmissable in equation (9a), the zero value of β_M guarantees mode I extension.

To compute K-fields for the extensile microcrack in the domain $C > l/2$, $c > 0$, we resort to standard relations for penny cracks subjected to crack-plane stress distributions $\sigma(r)$ [11, 42]. We obtain the following stress-intensity factors [24]:

(i) Shear-fault stress contribution. The stress σ_F^S [equation (7)] acting uniformly over $0 \leqslant r \leqslant l/2$ on the fault segment contributes

$$K_F(C, l) = \sigma_F^S l^{1/2} f_F(C/l) \tag{10}$$

where the crack-size dependence is contained wholly in the dimensionless function [24, 42]

$$f_F(C/l) = 2(C/\pi l)^{1/2}\{[1 - (1 - l^2/4C^2)^{1/2}] - [\nu/(2-\nu)][1 - (1 - l^2/4C^2)^{3/2}]\}. \tag{11}$$

Note in the limit of large extension, $C \gg l/2$, we have $K_F = [(1-2\nu)/2\pi^{1/2}(2-\nu)]\sigma_F^S l^2/C^{3/2}$, i.e. the system is highly stable with the same $C^{-3/2}$ crack size dependence as indentation cracks [11].

(ii) Microcrack–stress contribution. The uniform contact field stresses σ_M^N [equation (8)] acting over $l/2 \leqslant r \leqslant C$ on the microcrack segment contributes

$$K_M(C, l) = \sigma_M^N l^{1/2} f_M(C/l) \tag{12}$$

with the dimensionless crack size function [24]†

$$f_M(C/l) = 2(C/\pi l)^{1/2}(1 - l^2/4C^2)^{1/2}. \tag{13}$$

Note that K_M is zero for the first microcrack growth increment at $C = l/2$, $c = 0$. Thereafter, since σ_M^N in equation (8) is negative in the damage zone, K_M increasingly constrains the extension.

(iii) Residual-stress contribution. For cracks initiating on a grain boundary facet under the action of a uniform thermal expansion mismatch stress σ_R we have

$$K_R(C, l) = \sigma_R l^{1/2} f_R(C/l) \tag{14}$$

in which the crack-size function

$$f_R(C/l) = 2(C/\pi l)^{1/2}(1 - l^2/4C^2)^{1/2} \tag{15}$$

has the same form as equation (13). As with K_M, the contribution K_R is zero for the first microcrack growth increment. At $C \gg l/2$ we have $K_R = (2/\pi^{1/2})\sigma_R C^{1/2}$, so for tensile facets ($\sigma_R > 0$) K_R is a destabilizing influence in the extension.

The net K-field for microcrack extension is therefore the superposition of the contributions in equations (10–15)

$$\begin{aligned} K_*(C/l) &= K_F + K_M + K_R \\ &= \sigma_F^S l^{1/2} f_F(C/l) + \sigma_M^N l^{1/2} f_M(C/l) \\ &\quad + \sigma_R l^{1/2} f_R(C/l). \end{aligned} \tag{16}$$

Extension then occurs when the crack-tip K-field is just sufficient to overcome the intrinsic (grain or interphase boundary) toughness of the material, i.e. $K_* = T_0$. Given that the dimensionless $f(C/l)$ functions are invariant for geometrically similar microstructures, the quantity $l^{1/2}$ emerges as the key scaling quantity in the K-field formalism.

5. EFFECT OF GRAIN SIZE ON MICROCRACK INITIATION AND EXTENSION IN ALUMINA

Allusion has been made to the role of grain size in determining the microfracture damage in polycrystalline materials, in both the experimental

---

†Calculable directly from the standard stress-intensity factor relation for penny cracks with distributed stresses $\sigma(r)$ [11]

$$K(C) = 2/(\pi C)^{1/2}\int_0^C r\sigma(r)\mathrm{d}r/(C^2 - r^2)^{1/2}.$$

observations referred to in Section 2.1 (e.g. Figs 2 and 3) and the theoretical formalism just described in Section 4.2 [e.g. $l^{1/2}$ term in equation (16)]. In the present section we demonstrate the capacity of our model to provide quantitative information on this critical microstructural scaling effect, with specific reference to alumina.

Accordingly, along with the calibrated α and β coefficients from Section 4.2, we assign the following quantities for insertion into the fracture mechanics analysis, from independent data on alumina:

(i) Grain boundary toughness $T_0 = 2.75$ MPa.m$^{1/2}$, from indentation-strength tests [15]; and thermal expansion mismatch stress $\sigma_R = 200$ MPa, from spectroscopic measurements [41].

(ii) Critical contact stress $p_F^C = 5.0$ GPa (see Fig. 7), corresponding to the nucleation pressure at which faulting is first evident in indentation stress–strain curves (Fig. 1), optical microscopy (Fig. 2) and acoustic emission (Fig. 3) [18].

(iii). Fault intercept quantity $p_F = \tau_F/(\beta_F - \alpha_F\mu_F)$ from Section 3 (see Fig. 7), to evaluate σ_F^S in equation (7). We choose $p_F = 3.0$ GPa to provide sensible values below for the fully extended microcrack dimensions (note that $p_F < p_F^C$, as required in Fig. 7). If we assume that the twinning in alumina is governed entirely by a critical cohesion stress, so that $\mu_F = 0$, we evaluate $\tau_F = \beta_F p_F = 1.4$ GPa.

It is acknowledged that these parameter evaluations are approximate, and that the fracture mechanics formalism embodies many assumptions, so the numerical accuracy of the calculations are open to a degree of uncertainty.

In Fig. 8 we plot the function $K_*(c)$ from equation 16 [in conjunction with equations (7–15)] for a selected alumina grain size $l = 35\,\mu$m, incrementing p_0 to a peak $p_0^* = 10$ GPa in a complete load–unload cycle (cf. Fig. 1). Extension occurs along the horizontal equilibrium line $K_* = T_0$. Because of the dominating influence of the K_F and K_M terms at small c in equation (16), the microcrack is stabilized (i.e. $dK_*/dc < 0$), most strongly in the loading half-cycle. However, at large c the K_R term becomes dominant in equation (16), and the $K_*(c)$ function begins to rise on approaching the final unload state. This indicates that the crack configuration is approaching an instability configuration. If such a configuration were to be achieved (e.g. by admitting water to the subsurface fault–microcrack to promote subcritical extension), the unloaded microcrack would extend unstably into the surrounding microstructure. The material would then be on the verge of spontaneous bulk microfracture, and its structural integrity would be contingent on the arrest of individual microcracks at adjacent grain facet bridges [11, 16].

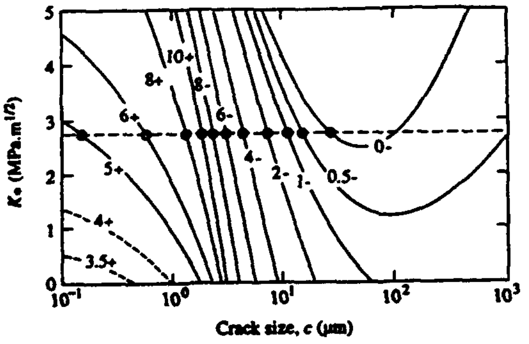

Fig. 8. Plots of function $K_*(c)$ in equation (16) for fault-generated microcracks in alumina of grain size $35\,\mu$m, for indicated values of contact pressure p_0 (GPa) during load (+) and unload (−) half-cycles. Equilibrium condition determined by intersection with horizontal dashed line, representing grain boundary toughness T_0. Dashed curves at contact pressure $p_0 < p_F^C = 5.0$ GPa indicate region prior to fault initiation. At p_F^C microcrack pops in, and thereafter grows stably along $K_* = T_0$ (circles).

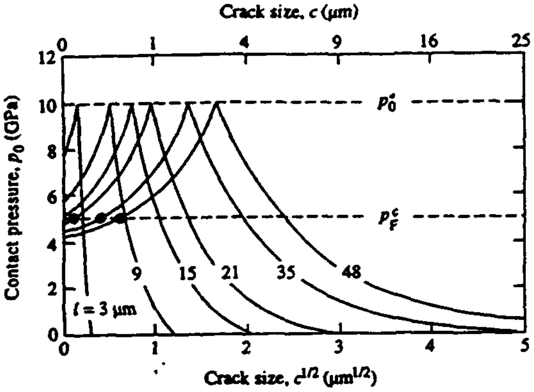

Fig. 9. Plots of function $p_0(c)$ for equilibrium cracks ($K_* = T_0$) for alumina at specified grain sizes (cf. Fig. 3). Horizontal dashed line denotes critical fault pressure $p_F^C = 5.0$ GPa. Intercepts at $c = 0$ represent minimum contact pressures p_M [equation (17)] for extension of existing miocrocrack. For grain sizes $l < 20\,\mu$m, $p_M > p_F^C$, and extension occurs stably at $p_0 = p_M$; for $l > 20\,\mu$m, $p_M < p_F^C$, and microcracks must first pop in at $p_0 = p_F^C$ before stable extension occurs.

It is important to remember that our model presumes the existence of a shear fault. In reality, a microcrack cannot form unless a fault nucleates first, at $p_0 = p_F^C = 5.0$ GPa. At p_F^C the microcrack pops in spontaneously, to $c \approx 0.2\,\mu$m for our $35\,\mu$m grain size alumina in Fig. 8. As the pressure continues to increase beyond p_F^C the microcrack extends stably, to $c \approx 3\,\mu$m at $p_0 = p_0^* = 10$ GPa. On unloading, the microcrack continues in stable growth, at an ever-increasing rate, to its final size $c \approx 23\,\mu$m at $p_0 = 0$, i.e. less than one grain facet for this material.

The grain size effect is more clearly represented by $p_0(c)$ curves for equilibrium microcrack extension, obtainable either directly from equation (16) [again together with equations (7–15)] at $K_* = T_0$ or from intersection points along the horizontal dashed line in Fig. 8. We show such a plot in Fig. 9 for alumina at several grain sizes (cf. Fig. 3), for peak pressure $p_0^* = 10$ GPa. Stable branches during both half-cycles are again evident. The dashed line at

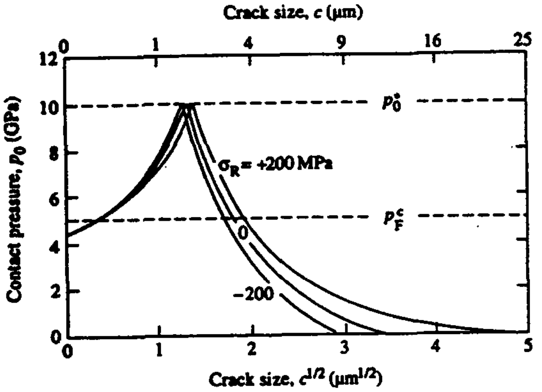

Fig. 10. Plots of $p_0(c)$ for equilibrium cracks for alumina of grain size 35 μm, showing effect of residual thermal expansion mismatch stress σ_R.

$p_0 = p_F^C = 5.0$ GPa represents the critical stress for fault nucleation, independent of grain size l. The intercept $p_0(c) = p_M$ at $c = 0$ $(C = l/2)$ represents the minimum pressure for microcrack extension, and *does* depend on l,

$$p_M(l) = p_F(\pi^{1/2}T_0/2\tau_F l^{1/2} - 1). \tag{17}$$

At grain sizes $l < 20\,\mu$m in Fig. 9, p_M lies above the threshold p_F^C line; in this region p_0 must be increased above this line before a microcrack can extend. When extension does occur, it is stable. At grain sizes $l > 20\,\mu$m, p_M falls below p_F^C, so no fault exists from which extension can occur; in this region, the loading must first be increased to the threshold level. At threshold the microcrack pops in along the $p_0 = p_F^C$ line to the first branch of the $p_0(c)$ curve, producing constrained flaws of dimension $c \approx 0.5\,\mu$m for the largest grain size l in Fig. 9. Through the remainder of the loading–unloading cycle, extension is again stable, with extension to $c > 100\,\mu$m at largest l. We note that the scale of microcrack pop-in increases monotonically with grain size above $l \approx 20\,\mu$m in Fig. 9, consistent with the acoustic emission data in Fig. 3.

In Fig. 10 we plot the $p_0(c)$ curve for alumina at $l = 35\,\mu$m using thermal mismatch stresses $\sigma_R = 200$, 0, and −200 MPa. We note that while σ_R has no bearing on the value of the intercept stress p_M at $c = 0$, it has a pronounced influence on the ultimate microcrack extension. The contrast between final crack sizes $c \approx 23\,\mu$m at the tensile facet and $c \approx 8\,\mu$m at the compressive facet serves to emphasize the important role of internal stresses in the damage susceptibility.

6. DISCUSSION

Hertzian contact presents itself as a powerful test procedure for investigating fundamental deformation-assisted damage properties of otherwise highly brittle polycrystalline materials. Our damage model is based on microcrack extension from stress concentrations at constrained "shear faults". Such faults account for the subsurface "plastic" deformation observed in indentation stress–strain responses, micrographic sections, and acoustic emission records. These experimental elements have been demonstrated for a monophase alumina ceramic in Figs 1–3. In alumina, the shear faults are primarily associated with the activation of intra-grain twinning. In brittle ceramics in general, the stresses required to activate analogous shear faults are characteristically high, often approaching the cohesive shear strength of the material. In glass, shear faults occur along principal shear stress trajectories [23, 35, 43]. In single crystals, e.g. silicon [44] or sapphire [45, 46], they result from "block slip" on low-index crystallographic planes. In multiphase composites [19], including rocks [25, 27], slippage occurs on some incipient weak interface associated with microstructural defects, e.g. sliding grain or interphase boundary facets. In polycrystalline ceramics any one or more of these processes may be active as incipient faults.

The closed-fault model outlined in Section 3 captures the generic essence of the precursor deformation process. While retaining the traditional friction and cohesion stress descriptions of shear-activated faulting in rock mechanics [25], our model allows for fault pop-in by incorporating a fault nucleation stress. It also allows for an additional, constraining effect of the matrix on individual grains within the subsurface Hertzian contact field in Fig. 4. We recall from Fig. 6 that the fault is most commonly expected to be active only in the first load half-cycle, i.e. along branch (2) in Fig. 6. Continued hysteretic activity during subsequent unloading and reloading half-cycles is predicted only in overloaded contacts.

The principal focus of the model is the extension of microcracks from the closed shear faults in the constraining subsurface compressive field, again in the spirit of traditional rock mechanics but here expressed in terms of the K-field formalisms previously used to describe radial crack initiation in sharp-indenter contacts [23, 24, 33, 43, 47, 48]. In its most general form, the model enables one to describe a continuing crack evolution through sequential load–unload contact cycles, with due allowance for a mode II component. However, our specific treatment in Sections 4 and 5 defers consideration of the mode II terms, in the interest of simplicity. The model predicts microcrack pop-in during the loading half-cycle (required to account for acoustic emission data) and enhanced stable extension during the unloading half-cycle, highlighting the stabilizing influence of the compressive field.

We have alluded to the relevance of contact damage to several mechanical properties of brittle ceramics, including damage accumulation [29], material removal and wear [49, 50], and strength degradation [17, 19]. But perhaps the property of greatest practical significance is *fatigue*, e.g. in contact bearings and dental–ceramic restorations

[51]. Experimentally, strong contact fatigue effects have been reported in cyclic tests on coarse-grain aluminas [17]. In such fatigue phenomena, the inbuilt provision for frictional tractions in the crack-plane stresses of Section 4.1, at both the fault and microcrack interfaces, is indispensable. Accordingly, we foreshadow two potential contributions to contact fatigue:

(i) *Individual microcrack evoluation.* Sliding crack interfaces can lead to progressive frictional degradation or wear in continual reversed loading. Direct evidence for interfacial attrition has been reported in the accumulation of wear products and debris at cracked grain boundary interfaces in alumina [30, 52, 53] and rocks [27, 54]. With diminishing values of the friction μ and τ terms in the shear stresses σ_F^S and σ_M^S in Section 4.1, the final crack sizes in Figs 8 and 9 become subject to progressive extension with number of cycles. This raises the prospect of interaction and coalescence of neighboring microcracks [29], leading ultimately to fragmentation [17]. Any such process will be enhanced by the accumulation of debris at the sliding crack interfaces [30, 52].

(ii) *Deformation zone expansion.* It is well known from rock mechanics that the compliance of specimens in compression loading increases significantly with the introduction of closed, but sliding, microcracks [25]. As extending microcracks begin to interact with their neighbors in a confined contact field, the local compliance within the damage zone will increase, with consequent stress transfer to the immediately surrounding matrix. Accordingly, the adjacent matrix grains will bear more of the transmitted contact load, and will themselves become susceptible to faulting. The deformation zone, and thence the microcrack density, will therefore spread outward, exacerbating the fatigue process.

Finally, the fracture mechanics analysis has important implications concerning material characteristics in design:

(i) *Grain size.* As indicated in Section 5, grain size is a critical element in the microcrack evolution, most dramatically in the initiation. This enhancement of fracture susceptibility with microstructural scaling, illustrated dramatically by the contact damage in alumina ceramics (e.g. Figs 2 and 3 [18]), is a widespread phenomenon in brittle fracture [11, 55, 56]. The connotation in the special context of ceramics processing is that minimal susceptibility to damage accumulation requires refinement of mean grain size. In reality, for any given material there may be a *distribution* of grain sizes (as well as of crystal misorientations), so the transition may not be abrupt, especially in inhomogeneous stress fields like that in Fig. 4. The result is then a progressive accumulation of microcracks as the load is increased at given nominal grain size, or as grain size is increased at prescribed load [18]. Hence, not only grain size, but also grain-size *variation*, is subject to refinement.

(ii) *Residual thermal mismatch stress.* Noncubic and two-phase ceramics are subject to thermal expansion and other mismatch stresses at intergrain facets. The tensile component of these stresses greatly enhances final microcrack extension within the contact field. Hence it would appear that microstructures with large mismatch stresses will be most susceptible to contact damage. On the other hand, countervailing compressive stresses at adjacent bridging facets constitute a most effective route to effective crack–interface bridging in the long-crack region [11, 15]. We have omitted considerations of bridging tractions from our analysis, on the grounds that the individual microcracks remain confined to a grain facet or so. However, bridging stresses will become important in the secondary stages of multiple crack coalescence and material removal [29].

(iii) *Nature of strength-degrading flaws.* Polycrystalline ceramics inevitably contain a population of pre-existing *extrinsic* flaws, e.g. from the processing and surface treatments. However, in ceramics like alumina the flaws leading to microfracture may be *activated* by the very contact event itself, via the shear faulting process. Insofar as this shear faulting process occurs at a well-defined contact stress independent of grain size (recall p_F^C in Fig. 9), such flaws are governed by material-*intrinsic* factors. Hence preexisting flaws may be expected to play only a secondary role in the micromechanics of damage accumulation (although they might well exert a dominant influence near the critical grain size for *spontaneous* general microcracking [11, 49, 50]). There is the strong suggestion here that, contrary to common expectation, initial flaw state may not be a decisive factor in determining the resistance of polycrystalline ceramics to contact fatigue.

Acknowledgements—Funding for this study was provided by the U.S. Air Force Office of Scientific Research. Special financial support for FG from the Ministerio de Educación Y Ciencia (DGICYT), Spain, and from NIST, is gratefully acknowledged.

REFERENCES

1. H. Hertz, *Hertz's Miscellaneous Papers*, Chaps 5, 6. Macmillan, London (1896).
2. F. C. Roesler, *Proc. Phys. Soc. Lond.* **B69**, 981 (1956).
3. F. C. Frank and B. R. Lawn, *Proc. R. Soc.* **A299**, 291 (1967).
4. B. R. Lawn, *J. appl. Phys.* **39**, 4828 (1968).
5. F. B. Langitan and B. R. Lawn, *J. appl. Phys.* **40**, 4009 (1969).
6. B. R. Lawn and T. R. Wilshaw, *J. Mater. Sci.* **10**, 1049 (1975).
7. A. G. Evans and T. R. Wilshaw, *Acta metall.* **24**, 939 (1976).
8. B. R. Lawn and D. B. Marshall, *Fracture Mechanics of Ceramics* (edited by R. C. Bradt, D. P. H. Hasselman and F. F. Lange), Vol. 3, p. 205. Plenum Press, New York (1978).
9. M. V. Swain and B. R. Lawn, *Physica status solidi* **35**, 909 (1969).

10. M. V. Swain and J. T. Hagan, *J. Phys. D, Appl. Phys.* **9**, 2201 (1976).
11. B. R. Lawn, *Fracture of Brittle Solids*, 2nd edn. Cambridge Univ. Press (1993).
12. R. Knehans and R. Steinbrech, *Science of Ceramics* (edited by P. Vincenzini), Vol. 12, p. 613. Ceramurgica, Imola, Italy (1983).
13. P. L. Swanson, C. J. Fairbanks, B. R. Lawn, Y.-W. Mai and B. J. Hockey, *J. Am. Ceram. Soc.* **70**, 279 (1987).
14. S. J. Bennison and B. R. Lawn, *J. Mater. Sci.* **24**, 3169 (1989).
15. S. J. Bennison and B. R. Lawn, *Acta metall.* **37**, 2659 (1989).
16. P. Chantikul, S. J. Bennison and B. R. Lawn, *J. Am. Ceram. Soc.* **73**, 2419 (1990).
17. F. Guiberteau, N. P. Padture, H. Cai and B. R. Lawn, *Phil. Mag. A.* **68**, 1003 (1993).
18. F. Guiberteau, N. P. Padture and B. R. Lawn, *J. Am. Ceram. Soc.* In press.
19. H. Cai, M. A. Stevens Kalceff and B. R. Lawn, *J. Mater. Res.* In press.
20. A. N. Stroh, *Adv. Phys.* **6**, 418 (1957).
21. A. H. Cottrell, *Trans. metall. Soc. A.I.M.E.* **212**, 192 (1958).
22. N. J. Petch, *Fracture* (edited by H. Liebowitz), Vol. 1, Chap. 5. Academic Press, New York (1968).
23. B. R. Lawn, T. P. Dabbs and C. J. Fairbanks, *J. Mater. Sci.* **18**, 2785 (1983).
24. S. Lathabai, J. Rödel, B. R. Lawn and T. P. Dabbs, *J. Mater. Sci.* **26**, 2157 (1991).
25. J. C. Jaeger and N. G. W. Cook, *Fundamentals of Rock Mechanics*, Chapman & Hall, New York (1971).
26. M. S. Paterson, *Experimental Rock Deformation—The Brittle Field.* Springer, Berlin (1978).
27. R. L. Kranz, *Tectonophysics* **100**, 449 (1983).
28. H. Horii and S. Nemat-Nasser, *J. Geophys. Res.* **90**, 3105 (1985).
29. M. F. Ashby and S. D. Hallam, *Acta metall.* **34**, 497 (1986).
30. L. Ewart and S. Suresh, *J. Mater. Sci.* **22**, 1173 (1987).
31. S. Suresh and J. R. Brockenbrough, *Acta metall.* **36**, 1455 (1988).
32. S. Suresh, *Fatigue of Materials.* Cambridge Univ. Press (1991).
33. J. T. Hagan, *J. Mater. Sci.* **14**, 2975 (1979).
34. J. T. Hagan, *J. Mater. Sci.* **14**, 462 (1979).
35. J. T. Hagan, *J. Mater. Sci.* **15**, 1417 (1980).
36. S.v.d. Zwagg, J. T. Hagan and J. E. Field, *J. Mater. Sci.* **15**, 2965 (1980).
37. T. P. Dabbs, C. J. Fairbanks and B. R. Lawn, *Methods for Assessing the Structural Reliability of Brittle Materials* (edited by S. W. Freiman and C. M. Hudson), p. 142. A.S.T.M. Special Tech. Publ. 844, Philadelphia, Pa (1984).
38. D. Tabor, *Hardness of Metals.* Clarendon, Oxford (1951).
39. K. L. Johnson, *Contact Mechanics*, Cambridge Univ. Press (1985).
40. T. R. Wilshaw, *J. Phys. D, Appl. Phys.* **4**, 1567 (1971).
41. J. E. Blendell and R. L. Coble, *J. Am. Ceram. Soc.* **65**, 174 (1982).
42. H. Tada, P. Paris and G. R. Irwin, *The Stress Analysis of Cracks Handbook.* Del Research, St. Louis (1985).
43. J. T. Hagan and M. V. Swain, *J. Phys. D* **11**, 2091 (1978).
44. M. J. Hill and D. J. Rowcliffe, *J. Mater. Sci.* **9**, 1569 (1974).
45. B. J. Hockey and B. R. Lawn, *J. Mater. Sci.* **10**, 1275 (1975).
46. H. M. Chan and B. R. Lawn, *J. Am. Ceram. Soc.* **71**, 29 (1988).
47. B. R. Lawn and A. G. Evans, *J. Mater. Sci.* **12**, 2195 (1977).
48. S. Lathabai, J. Rödel, B. R. Lawn and T. P. Dabbs, *J. Mater. Sci.* **26**, 2313 (1991).
49. S.-J. Cho, B. J. Hockey, B. R. Lawn and S. J. Bennison, *J. Am. Ceram. Soc.* **72**, 1249 (1989).
50. S.-J. Cho, H. Moon, B. J. Hockey and S. M. Hsu, *Acta metall. mater.* **40**, 185 (1992).
51. D. G. Grossman, *Proc. Int. Symp. on Computer Restorations* (edited by W. H. Mörmann), p. 103. Quintessence, Chicago, Ill. (1991).
52. S. Lathabai, J. Rödel and B. R. Lawn, *J. Am. Ceram. Soc.* **74**, 1340 (1991).
53. R. H. Dauskardt, *Acta metall. mater.* 41, 2765 (1993).
54. M. L. Batzle, G. Simmons and R. W. Siegfried, *J. Geophys. Res.* **85**, 7072 (1980).
55. B. R. Lawn and D. B. Marshall, *J. Am. Ceram. Soc.* **62**, 347 (1979).
56. K. E. Puttick, *J. Phys. D, Appl. Phys.* **12**, L19 (1979).